






Universitat Autònoma de Barcelona

ADVERTIMENT. L'accés als continguts d'aquesta tesi queda condicionat a l'acceptació de les condicions d'ús establertes per la següent llicència Creative Commons:  http://cat.creativecommons.org/?page_id=184

ADVERTENCIA. El acceso a los contenidos de esta tesis queda condicionado a la aceptación de las condiciones de uso establecidas por la siguiente licencia Creative Commons:  <http://es.creativecommons.org/blog/licencias/>

WARNING. The access to the contents of this doctoral thesis it is limited to the acceptance of the use conditions set by the following Creative Commons license:  <https://creativecommons.org/licenses/?lang=en>

UNIVERSITAT AUTNÒNOMA DE BARCELONA

DOCTORAL THESIS

**Indirect Dark Matter Searches:
MAGIC & CTA**



Joaquim Palacio Navarro
Departament de Física
Universitat Autònoma de Barcelona

A thesis submitted for the degree of
PhilosophiæDoctor

February 5, 2018

Director:

Javier Rico Castro

IFAE

Edifici Cn, UAB

08193 Bellaterra (Barcelona) Spain

enrique.fernandez@ifae.es

Tutor:

Dr. Enrique Fernandez

IFAE & UAB

Edifici Cn, UAB

08193 Bellaterra (Barcelona) Spain

enrique.fernandez@ifae.es

I herewith declare that I have produced this thesis without the prohibited assistance of third parties and without making use of aids other than those specified; notions taken over directly or indirectly from other sources have been identified as such. This paper has not previously been presented in identical or similar form to any other Spanish or foreign examination board.

The thesis work was conducted from January 2014 to February 2018 under the supervision of Javier Rico Castro at Barcelona.

Barcelona, February 5, 2018.

ABSTRACT

Decades of observational evidences have been accumulated to show that Standard Model (SM) particles cannot totally explain the strong gravitational unbalance observed in several astronomical regions, at all cosmological scales, from that of Milky Way satellite galaxies, to that of Cluster of Galaxies. Although some theories argue for the modification of the gravitational laws, the existence of a new massive particle (or a set of them), interacting only weakly with SM particles, provides a preferred explanation. It is estimated that this form of Dark Matter (DM) roughly accounts for 4 times the amount of SM matter, therefore shaping the evolution of cosmic structures along the history of the Universe. A well-motivated general framework for DM is that of a Weakly Interacting Massive Particle (WIMP), generic massive particles with a mass range expected between few GeVs and few hundreds TeV, interaction strengths at the weak scale, and either stable or very long lived. The WIMP paradigm has been long debated, and has the advantage of being at reach by different of the top-class instruments of the current times, so that a putative discovery could be validated independently.

We focus on the indirect search of DM, where annihilating or decaying WIMP are expected to emit gamma rays at energies detectable by Imaging Atmospheric Cherenkov Telescopes (IACTs), as the currently operating Florian Goeble Major Atmospheric Gamma-ray Imaging Cherenkov (MAGIC) telescopes or the future Cherenkov Telescope Array (CTA). The expected DM signal can be moderate extended when compared to IACT Field of View, what challenges the performance of the DM search of these instruments.

In this thesis, I contribute to the MAGIC ongoing efforts on indirect DM searches at different analysis levels. A tool for handling the massive data products generated by current High Energy experiments is developed. More over, a tailored Monte Carlo (MC) for moderate extended sources is proposed as an upgrade of the current general MC for extended sources. Finally, a method to optimize the pointing strategy of IACT while observing moderate extended sources taking into account the off-axis performance of the instrument has also been developed and, implemented for the first time to indirect DM searches on highly DM dominated nearby dwarf Spheroidal galaxy. I also show my contribution to the largest telescope to be part of CTA, the Large Size Telescope, that will dominate the CTA sensitivity for standard WIMP searches.

Constraints on the WIMP thermally averaged cross-section and/or decay life-

time are put with 60 hours of data in the recently discovered dwarf Spheroidal galaxy Triangulum II and 202 hours on the Perseus Cluster of Galaxies. On both searches, we apply a binned likelihood analysis optimized for the spectral and morphological features of gamma-ray signals of DM from annihilating or decaying WIMP. We reach sensitivities to the thermally averaged cross-section of $3 \times 10^{-26} \text{ cm}^3\text{s}^{-1}$ and decay life-times of $0.3 \times 10^{25} \text{ s}$, being this the most constraining MAGIC results on WIMP searches.

PRÒLEG

Després de dècades d'observacions, és evident que les partícules del model estàndard són insuficients per explicar el fort desequilibri gravitacional observat a diverses regions astronòmiques, de diferents escales cosmològiques, des de satèl·lits de la Via Làctia fins a cúmuls de galàxies. Si bé és veritat que algunes teories suggereixen a una modificació de les lleis gravitacionals actuals, l'existència d'una partícula (o un grup de partícules) nova, interaccionant de forma feble amb les partícules del model estàndard està considerada com l'opció més viable. Estimacions recents prediuen que aquest tipus de matèria fosca és 4 vegades més present que la matèria del model estàndard, modelant així la formació de les grans estructures de l'univers al llarg de la vida d'aquest. Un escenari general de la matèria fosca és el dels WIMPs, partícules genèriques massives, amb masses entre pocs GeVs i alguns TeV, interaccions de l'ordre de les interaccions dèbils del model estàndard, i o bé estables o amb temps de vida mitjana prou llargs. L'escenari WIMP ha estat llargament debatut, i té l'avantatge d'estar a l'abast dels instruments més potents construïts a la terra, proporcionant així possibles deteccions independents que podria validar el descobriment.

En particular em centro en cerques indirectes de matèria fosca, on s'espera que WIMPs anihilats o decaïent emetin rajos gamma amb energies detectables per telescopis IACT, com per exemple els telescopis MAGIC, actualment operant des de La Palma o la futura xarxa de telescopis CTA. El senyal esperat de rajos gamma d'aquesta matèria fosca pot ser moderadament extensa, comparada amb el camp de visió dels IACTs, cosa que afegeix certa complexitat a les cerques de matèria fosca realitzades per a aquests telescopis.

En aquesta tesi, he contribuït a l'esforç realitzat per MAGIC en cerques indirectes de matèria fosca a diferents nivells d'anàlisi. He desenvolupat una eina per gestionar volums massius de dades que són típicament generats per MAGIC, però també per tota la comunitat experimental de física d'altres energies. També he desenvolupat un MonteCarlo per a fonts extenses que s'ajusta a l'emissió esperada de la font, obtenint així les funcions correctes de resposta de l'instrument. Finalment, un mètode per a optimitzar la configuració d'apuntat durant les observacions de fonts moderadament extenses amb IACTs ha estat proposat. El mètode té en compte la resposta finita dels IACTs al llarg de tot el camp de visió per a proporcionar la distància òptima a la qual el telescopi ha d'apuntar a la font, així com, quina seria la regió d'integració més adient. Apliquem aquest mètode per primera vegada a cerques de matèria fosca en

galàxies satèl·lits de la Via Làctia. També exposo la meva contribució al telescopi més gran que operarà a CTA, el LST, que dominarà la sensibilitat de cerques de WIMPs estàndard.

Límits a la secció eficaç i/o temps de vida mitjana són imposats mitjançant 60 hores d'observació de la galàxia Triangulum II i 202 hores del cúmulo de galàxies de Perseus. En ambdues cerques, fem ús del mètode de màxima versemblança, optimitzat per a la morfologia espacial i energètica del senyal esperada de rajos gamma. Obtenim sensibilitats a la secció eficaç de $3 \times 10^{-26} \text{ cm}^3\text{s}^{-1}$ i temps de vida mitjana de $0.3 \times 10^{25} \text{ s}$, essent aquests els resultats més restrictius obtinguts amb MAGIC en cerques de WIMPs.

CONTENTS

I	Theoretical/Experimental Framework	1
1	Historical Introduction	3
2	The Dark Matter Problem	7
2.1	Observational Evidences	7
2.1.1	Galactic evidences	7
2.1.2	Extra-galactic evidences	9
2.1.3	Cosmological scale	11
2.2	Dark Matter Candidates	20
2.2.1	Dark Matter candidates within Λ CDM	21
2.2.2	Alternative Cosmologies	22
2.2.3	The WIMP <i>miracle</i>	23
2.2.4	Non-WIMP Dark Matter	30
2.2.5	Gravity induced Dark Matter Candidates	33
2.3	WIMP Searches	33
2.3.1	Production at Particle Colliders	34
2.3.2	Direct Detection	36
2.3.3	Indirect Detection	38
3	Imaging atmospheric Cherenkov Telescopes: MAGIC & CTA	45
3.1	The Imaging Atmospheric Cherenkov Technique	46
3.1.1	Cherenkov Radiation	49
3.1.2	Types of EAS	51
3.1.3	The Imaging Technique	52
3.2	The MAGIC Telescopes	55
3.2.1	Hardware description	56
3.2.2	Data taking	65
3.2.3	Data analysis	67

3.2.4	The full likelihood method	70
3.3	The future Cherenkov Telescope Array (CTA)	75
3.3.1	Large Size Telescope	77
II	Technical Work	83
4	Data Management at PIC: <i>ToMaRe</i>	85
4.1	Introduction	85
4.2	Code Usage	85
4.3	Code Structure	87
4.4	Conclusion	88
5	The Donut MC: Point-like vs Extended MC Simulations	89
5.1	Introduction	89
5.2	MAGIC MC productions	90
5.3	Donut Method procedure	91
5.4	Testing the method	93
6	Pointing optimization for IACTs	99
6.1	Introduction	101
6.2	Off-axis performance	102
6.2.1	Relative Acceptance (ϵ) for real Imaging Atmospheric Cherenkov Telescopes (IACTs)	103
6.3	Quality factor (\mathcal{Q} -factor)	106
6.3.1	$\mathcal{Q}_{\mathcal{A}}$: Finite Acceptance	108
6.3.2	$\mathcal{Q}_{\mathcal{L}}$: Leakage Effect	108
6.3.3	$\overline{\mathcal{Q}}$: “Acceptance + Leakage” Effect	110
6.4	w_{opt} & θ_{opt} for indirect DM searches with dSphs	111
6.4.1	Annihilating WIMP	111
6.4.2	Decaying WIMP	113
6.5	Conclusions and remarks	115
7	LST Camera noise tests	117
7.1	Introduction	117
7.2	Tests CIEMAT	118
7.3	Data Analysis	120
7.3.1	L0 Rate Pedestal Scan	120
7.3.2	L0 Rate Scan with Pulse Injection	121
7.3.3	L1 Rate Pedestal Scan	123
7.3.4	L1 Rate Scan with Pulse Injection	124

7.4	Results	125
7.4.1	L0 Rate Pedestal Scan	125
7.4.2	L0 Rate Scan with Pulse Injection	126
7.4.3	L1 Rate Pedestal Scan	129
7.4.4	L1 Rate Scan with Pulse Injection	130
7.5	Comparison with a linear power supply	133
7.5.1	L0 Rate Scan for Module 15	134
7.5.2	L1 Rate Scan for Module 15	134
7.6	Conclusions of the tests	135
III Indirect Dark Matter Searches with MAGIC		137
8	Triangulum II	139
8.1	Introduction	140
8.2	Dark Matter content	144
8.3	Observation, Data reconstruction and Analysis	145
8.4	Results: Constraints to the cross section	154
8.5	Conclusions and remarks	156
9	The Perseus galaxy cluster	159
9.1	Introduction	160
9.2	Dark Matter content	163
9.3	Observation, Data reconstruction and Analysis	166
9.4	Results: Constraints to the decay life time	174
9.5	Conclusions and remarks	174
10	Summary, conclusions and remarks	185
	List of Figures	189
	List of Tables	193
	Bibliography	195

Part I

Theoretical/Experimental Framework

Chapter 1

HISTORICAL INTRODUCTION

In the mid 1660s, first *Johannes Kepler* and then *Isaac Newton*, provided the tools to understand and predict the motion of the celestial objects through the night sky, making evident for the first time in the human history the concept of *Gravity*. It was in 1859, that Newtonian dynamics failed to explain Mercury's precession in the Solar System, a problem that had to wait until *Albert Einstein* postulated the equations of General Relativity (GR) (Einstein, 1916). This modern view of Gravity action, has extended up to current days, where observations performed at the beginning of the twentieth century, evidences that the luminous components of galaxies are not sufficiently massive to explain their dynamics (Öpik, 1922; Oort, 1932). Oort actually settled that, if gravitational predictions are right, the rotation velocities measured needed to account for a total density of matter of a factor ~ 2 higher than the actual star density measured.

In 1933, using measurements of galaxy velocities in regions of the Coma Cluster of Galaxies (CG) (Hubble and Humason, 1931) and assuming the Virial theorem for galaxy motions, *Fritz Zwicky* calculated the gravitational mass of the galaxies within the CG and inferred the existence of an unseen matter at least 400 times more abundant than expected from the luminosity of the same galaxies, which he referred to as *dunkle Materie* “dark matter” (Zwicky, 1933, 1937). Zwicky postulated for the first time the existence of a new type of matter, that should have been missed in previous experiments. Later observations have confirmed Zwicky's results (e.g: on the Virgo, CG Smith, 1936) and today, over 80 years later, same calculations clearly show that the great majority of matter was correctly inferred to be dark and the concept of Dark Matter (DM) has become an standard in modern physics.

DM is nowadays believed to be the dominant form of matter in the Universe, representing almost 85% of the total mass density. Its existence is supported by abundant observational evidence on all scales. Although some theories argue for the modification of the gravitational laws (Milgrom, 1983), there is a “relatively” large consensus in interpreting DM as a new form of matter filling the Cosmos, whose evidences (apart from the gravitational) remain still today undetected. This view is independently motivated by the theoretical extensions to the Standard Model (SM) of particle physics, which commonly predict the existence of new particles that could fulfill the “characteristics” of DM. The principal detection strategies of the existing experiments after DM are based on (viable) possibilities that the DM particles could be “seen” through some relation with the SM ones: either being created in collisions of hadrons or leptons (production in colliders); or by scattering off nuclei (direct detection); or by annihilation, decay and/or conversion into SM particles (indirect detection).

This thesis is focused on indirect DM searches with IACTs. The outline of this thesis has been structured according to the following parts:

-
- Part I** I introduce the theoretical and experimental framework where the thesis work is sustained, where in **Chapter 2** I introduce the main evidences that motivate the DM paradigm, together it's main candidates and their experimental research lines, giving special emphasis on indirect DM searches; in **Chapter 3** I will introduce the IACT technique and the two instruments with which the work of this thesis is based: the Florian Goeble Major Atmospheric Gamma-ray Imaging Cherenkov (MAGIC) and Cherenkov Telescope Array (CTA).
- Part II** I focus on the technical work I have performed complementing my research line, and the experiments and collaborations I belong. In **Chapter 4** briefly discuss a software development to process large amounts of data within the MAGIC collaboration; in **Chapter 5** I focus on a new Monte Carlo (MC) development for IACTs dedicated moderate extended sources; in **Chapter 7** I go into a characterization of the camera of the largest telescope prototype to form CTA; finally in Chapter 6 I propose a method for optimizing the pointing strategy of general IACTs observations.
- Part III** the main results of the thesis are shown, based on recorded data of the MAGIC telescopes where in **Chapter 8** I search for DM evidences of DM annihilation from the direction of the recently discovered Triangulum II (Tri II) dwarf Spheroidal galaxy (dSph); in **Chapter 9** instead, signatures of decaying DM are searched within the region of the massive CG of Perseus.

Chapter 2

THE DARK MATTER PROBLEM

The notion of Dark Matter (DM) has been present for almost a century, but the question about its nature is still unanswered. Observational evidence and cosmological predictions assure that DM represents almost 85% of the matter content of the Universe, and more than 25% of its total energy budget. Discovering its essence is one of the most important and exciting tasks of modern science. This Chapter is devoted to a brief introduction of the DM concept as well as the experimental results and theoretical predictions that support this paradigm. Additionally, some of the most widely considered candidates for the DM particle are presented.

2.1 OBSERVATIONAL EVIDENCES

Decades of observational evidences have been accumulated to show that SM particles cannot totally explain the strong gravitational unbalance observed in several astronomical regions, at all cosmological scales, from that of Milky Way satellite galaxies, to that of galaxy clusters (Freese, 2009). In this section, a will briefly describe the main evidences we have nowadays of DM that have been classified into *galactic*, *extra-galactic* and *cosmological* evidences, according to the typical scale at which measurements take place.

2.1.1 GALACTIC EVIDENCES

Galaxies are the arena where stars form, evolve and collapse in constant interaction with the Inter-Stellar Medium (ISM), a complex mix of gas and plasma, dust, radiation, Cosmic Rays (CRs) and magnetic fields (Avila-Reese, 2006). Galaxies in the local Universe are mainly conglomerates of hundreds of millions to trillions of stars supported against gravity either by rotation or by random motions. The expected velocities of these stars can be computed based on the

mass distributions around the galaxy. Figure 2.1 shows the *rotational speeds* of stars orbiting around a typical galaxy as a function of the distance to the center of the galaxy.

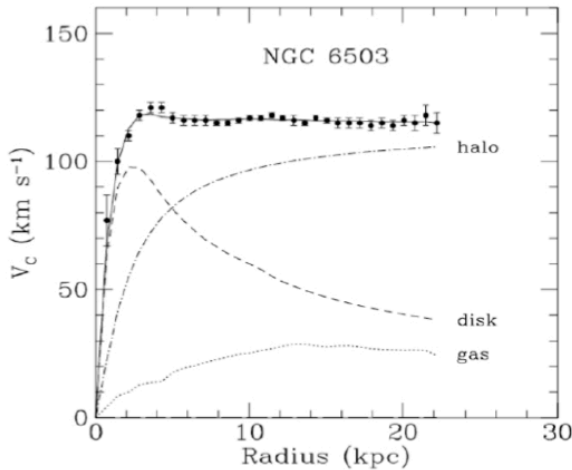


Figure 2.1: Rotation curve of NGC 6503 star-members w.r.t the distance to the center of the galaxy. Figure also show the rotational speeds computed w.r.t types of mass distributions around the galaxy: gas (dotted), disk (dashed) and halo (dot-dashed). (**Figure by Begeman et al., 1991**)

Assuming GR predictions to be correct (as we do unless specifically specified), figure evidences how luminous matter forming the galaxy (mainly *disk+gas*) is insufficient to account for the large angular momentum of stars around the galaxy at large distances. Luminous matter successfully accounts for star rotation in the inner region, but for large radii, an spherical distribution of mass centered in the galaxy (*halo*) linearly combined with *disk+gas* reproduces the data fairly well.

Figure 2.1 is *a typical galaxy*, where observations of these kind are easily reproduced in other galaxies making evident that: 1) Luminous matter forming galaxies is insufficient to reproduce the large angular momentum of star-members. 2) A spherical component of matter center in the galaxy, together with the luminous contribution, successfully reproduces the observed rotational speeds, where at large radii, the halo component is the dominant source of matter keeping the star gravitationally bound to the system; 3) this halo component extends at much larger distance that the luminous matter (the most distant stars), where measurements on on the rotational speed of ISM (through the 21 cm Hydrogen I (HI) line) or satellite galaxies of the *mother* galaxy have also an imprint of the gravitational field of this halo; and 4) smaller galaxies

have a larger fraction of their total mass in the form of this halo.

2.1.2 EXTRA-GALACTIC EVIDENCES

DM evidences have been also seen at larger scales than galaxies. CGs are the largest and most massive gravitationally bound systems in the Universe, with radii of few Mpc and total masses $M \sim (10^{14} - 10^{15}) M_{\odot}$, of which galaxies, gas, and DM contribute roughly for 5%, 15% and 80%, respectively (see Sarazin, 1986; Dai et al., 2007, for a general overview). In the cosmological hierarchic clustering model (as will be introduced in Section 2.1.3), large-scale structure grows hierarchically through merging and accretion of smaller systems into larger ones, and CGs are the latest and most massive objects to form (see Peebles, 1994). CGs are the collapse of the largest gravitationally bound over-densities in the initial density field and its formation, is accompanied by the most energetic phenomena since the *Big Bang*. CGs are thus the crossroads of cosmology and astrophysics and are unique laboratories for testing models of gravitational structure formation, galaxy evolution, thermodynamics of the intergalactic medium, and plasma physics. The full description of cluster formation requires detailed modeling of the non-linear processes of collapse and the dissipative physics of baryons. During this accretion process, the gas filling the Inter-Galactic Medium (IGM) heats to high X-ray emitting temperatures.

ROTATIONAL SPEEDS OF GALAXY MEMBERS

In analogy with galaxies, rotational speeds of galaxy members in CGs can also be used to infer the DM content of CGs, where in this case, DM is filling the space *all the way* between galaxies (note that this is 10 to 100 times larger than the typical galaxy size).

STRONG GRAVITATIONAL LENSING

GR describes how space-time curves under the influence of matter and energy. As particles (including photons) follow geodesics of space-time, light from distant sources will bend when passing around foreground mass-energy concentrations. Consequently, the images of distant galaxies are distorted due to the presence of foreground matter structures, an effect that is known as gravitational lensing (see Figure 2.2). *Strong gravitational lensing* from light from very distant galaxies going through a CG is bent before reaching us, producing this ring effect in the image as shown in Figure 2.3. The amount of mass inferred through this GR effect is larger than the one inferred from the closest galaxies, forming the CG.

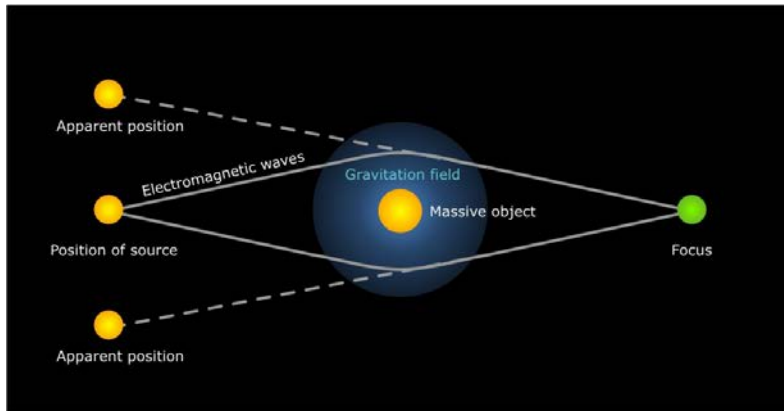


Figure 2.2: Light traveling through a gravitational field is bent, what is called a *strong lensing*, displacing the apparent position of the object seen from the Earth. In case of the bending effect being small, a *weak lensing*, only the apparent shape of the object is altered.



Figure 2.3: The massive foreground cluster (Abell 2218) distorting the images of background galaxies and forming arcs, due to strong gravitational lensing. The arcs align in a way that their ellipticity is oriented tangent to the direction of the foreground mass, in this case the galaxy cluster center. Image credit. NASA/ESA.

THE “BULLET CLUSTER”-LIKE EVIDENCE

One of the most intriguing evidence for DM is shown in Figure 2.4), where a real collision between two CGs, passing each one through each other is shown. Through X-ray measurements, the location of the gas forming both CGs is shown (red), while through lensing effect, the center of gravity of both CGs is also shown (blue). Gas filling both CGs has been slowed down during the collision, while *collision less* matter as DM (galaxies also act as collision less “particles” inside a CG) were not.

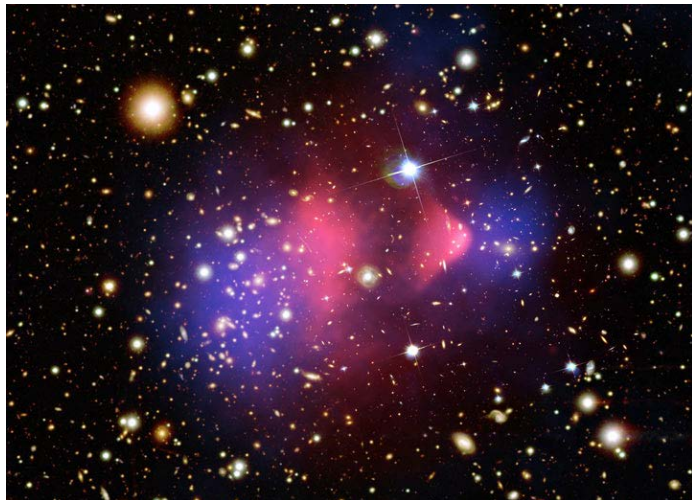


Figure 2.4: The Bullet cluster to cluster collision. In Blue is mapped the gravitational potential extracted from weak lensing and in red the radio emission

SUNYÁEV–ZELDÓVICH EFFECT

Measurements on the Intra-Cluster Medium (ICM) temperature provides an independent confirmation that the depth of the gravitational potential of CGs requires an additional dark component. *Inverse Compton* scattering of Cosmic Microwave Background (CMB) photons (the CMB radiation will be introduced in Section 2.1.3) with the thermal electrons of the hot IGM plasma should lead to distortions in the CMB spectrum Sunyaev and Zeldovich (1970, 1972, 1980). This effect has now been measured in hundreds of clusters (e.g, Carlstrom et al., 2002).

Extra-galactic evidences tell us that DM: 1) should no interact with baryonic matter (these means “neutral” under all SM *charges*) or, if it does, it does in a very weak way; 2) fills all the IGM between galaxies inside a CGs, being the larger amount of matter; 3) no GR extension has been proposed that explains evidences as the on from the *bullet cluster*.

2.1.3 COSMOLOGICAL SCALE

Cosmology, astrophysics, and particle physics intersect in an scenario (but sill not a theory) of cosmic structure formation and evolution called *Lambda* Cold Dark Matter (Λ CDM) model (we will come back to the meaning of this acronym). *Lambda* Cold Dark Matter (Λ CDM) is a model sustained into two main pillars: 1) GR equations and 2) that the Universe is, at large scales,

homogeneous and isotropic (looks the same anywhere and in any direction) commonly referred as the *Cosmological Principle*. Under Λ CDM, the Universe is now ~ 13 Gy old and its evolution has been completely determined by its initial conditions, determined after a first inflationary phase (Guth et al., 2014; Linde, 2015). A detailed view of the processes taking place before this inflationary phase are still a matter of debate, where the current view is that the Universe went through an inflationary epoch lasted from 10^{-36} seconds after the conjectured *Big Bang* singularity to sometime between 10^{-33} and 10^{-32} s after the singularity. During these inflationary phase, the Universe expanded by a factor of at least 10^{26} in which its temperature initially decreases to be immediately after reheated in a process in which SM particles should created (see Figure 2.5).

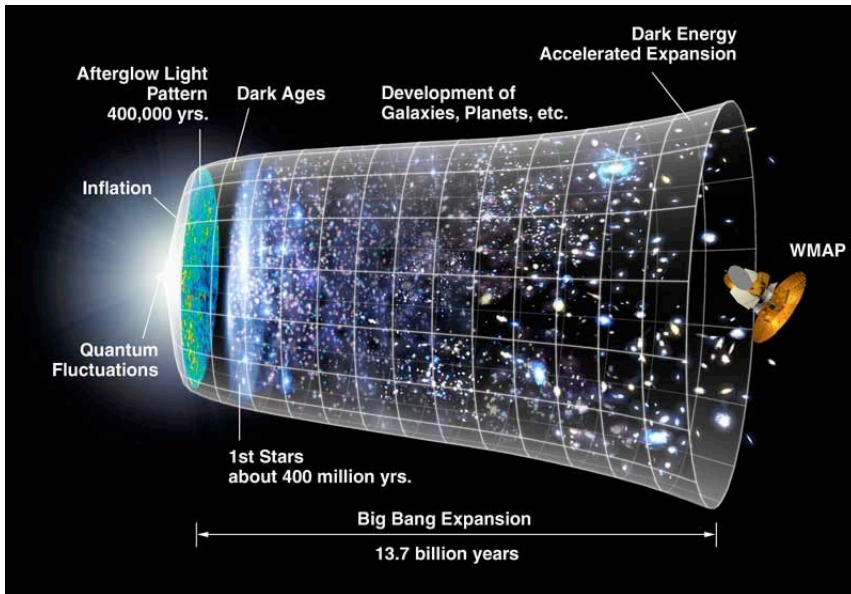


Figure 2.5: A schematic view of the Universe’s history. Time evolution goes in the right direction. In the left side, the first singularity is shown, the Big Bang, were radiation, matter and cosmological constant era go after (in this order).

There is nowadays a large number of independent observables that sustain Λ CDM, all of them converging into a single image in which at the beginning, the Universe was a very hot plasma of particles (mainly electrons, protons and neutrons) in expansion, where high energetic photon radiation prevented complex structures to form, a period typically know as the *radiation dominated era*. As the Universe expanded and cooled, the energy of ambient photons was no longer high enough to ionize Hydrogen, and the mean free path of photons

grew drastically, effectively making the Universe *transparent*. From this point, a *matter dominated era* takes place in which gravity is the main force governing the Universe, and forms the large structures we see now a days (galaxies and CG) by accreting matter from smaller structures into larger ones. During this matter dominated era, the expansion rate of the Universe is slowed down. Finally, in the recent days of our Universe “life”, a new transition phase took place in which the expansion rate of the Universe has started to increase. An unknown form of energy, Dark Energy (DE), is hypothesized to permeate all of space, tending to drive this accelerated expansion. The density of DE ($\sim 7 \times 10^{-30} \text{ g/cm}^3$) is very low, much less than the density of ordinary matter or DM within galaxies. However, it dominates the mass–energy of the Universe because it is uniform across space.

The name of Λ CDM comes from *Cold Dark Matter* component, a non relativistic component dominating the matter era, where Λ is the cosmological constant¹ introduced to explain the accelerated expansion phase we are nowadays. In this context the current view is that the Universe is made of DE, matter in the form of baryonic (ordinary) matter and DM, radiation and an extra component which accounts for the curvature of the universe². The relative contribution of each of these components can be expressed as:

$$\Omega_m + \Omega_r + \Omega_\Lambda + \Omega_k = 1; \quad (2.1)$$

where Ω is the *density parameter* and m , r , Λ and k account for matter (baryonic and DM, $\Omega_m = \Omega_b + \Omega_{dm}$), radiation, DE and curvature.

Current best-fit values of the density parameters are (Ade et al., 2016):

$$\begin{aligned} \Omega_b &= 0.0486 \pm 0.002, \\ \Omega_{dm} &= 0.2647 \pm 0.015, \\ \Omega_\Lambda &= 0.6850^{+0.017}_{-0.016}. \end{aligned} \quad (2.2)$$

In other words, baryon matter and DM account of $\sim 5\%$ and $\sim 25\%$ of the total energy content of the Universe respectively. In the following, I will try to summarize the main evidences that sustain these values.

¹ Introduced by Einstein in his equations.

² This is related to the metric satisfying the *Cosmological Principle*, but is not very relevant for this matter.

THE COSMIC MICROWAVE BACKGROUND

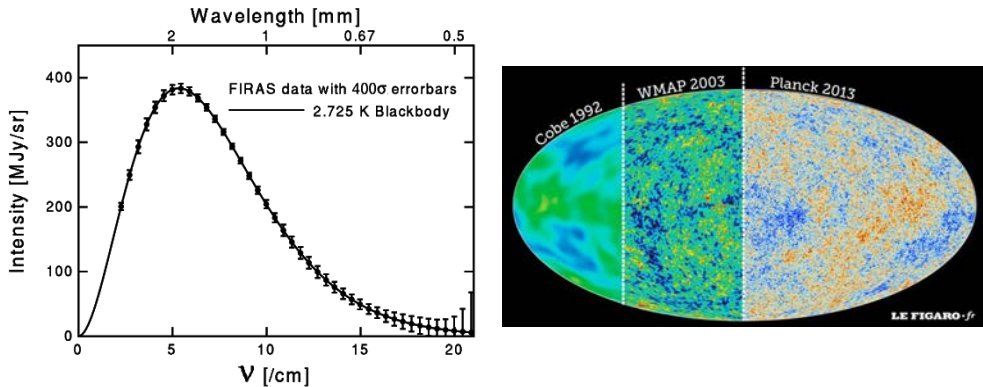


Figure 2.6: (left) Intensity of CMB radiation as a function of frequency (and wavelength) for the COBE FIRAS experiment, showing impressive agreement with a black-body spectrum (note that errorbars are magnified by a factor of 400 in the plot!). (right) Anisotropies in the CMB (color scale shows relative differences of order 10^{-5}) as seen by three different satellites: COBE (Boggess et al., 1992), WMAP (Spergel et al., 2003) and Planck (Ade et al., 2016); clearly apparent is the increase in angular resolution from one experiment to the next.

In the mid twentieth century, cosmologists started looking for the remnants of a radiation released during the transition between the radiation and matter dominated eras, as a proof of the Big Bang theory. The Cosmic Microwave Background (CMB), called like this for its higher intensity in the microwave part of the radio spectrum today, was first detected serendipitously by Penzias and Wilson (1965), in a single wavelength. This first detection was further confirmed by other experiments, but it was the Cosmic Background Explorer (COBE) satellite, launched in 1989, that impressively extended it to a broad range of wavelengths (Mather et al., 1994), confirming its agreement with a black-body spectrum and hence providing direct observational evidence for the Big Bang (see Figure 2.6).

After COBE, many experiments including other satellites like Wilkinson Microwave Anisotropy Probe (WMAP) and more recently Planck have measured and characterized the CMB properties. In detail, now we know that CMB radiation comes from the Universe when it was about 400,000 years old, and its spectrum today corresponds to a black-body at a temperature of $T_0 = 2.72548 \pm 0.00057$ K (Fixsen, 2009). The CMB represents the most precise black-body spectrum in nature, in all directions in sky, and anisotropies found are of the order of 1 part in 10^3 , which corresponds to the *Doppler effect* caused by the movement of the Milky Way with respect to the CMB reference

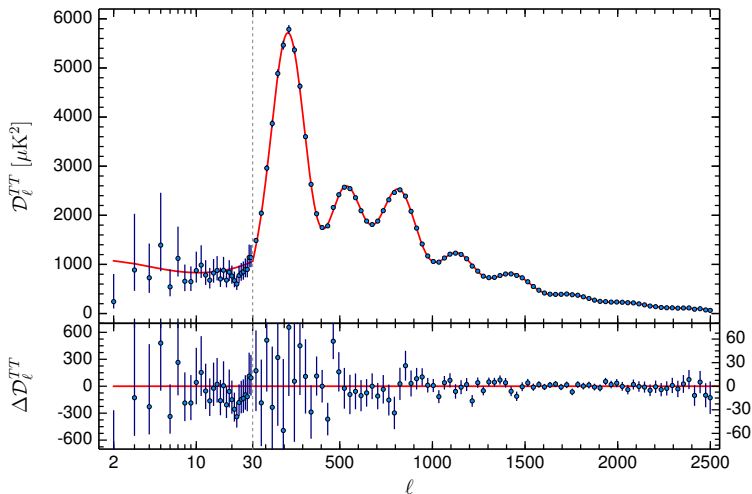


Figure 2.7: (**Figure by Ade et al., 2016, .**) CMB power spectrum (blue dots and error bars), with $D_l \equiv l(l+1)/(2\pi)C_l$, and Λ CDM best-fit model (red line). The upper panel shows the spectrum and the lower panel the residuals. Note the change of scale from logarithmic to linear at the vertical dotted line, $l = 29$, and the change in the residuals y -axis between these two regimes.

rest frame. More interestingly, once the dipole is corrected for, smaller temperature variations at the 1 part in 10^5 level also exist and have been studied in detail. Such anisotropies, first detected by COBE (Smoot et al., 1992), are caused by the density fluctuations in the early Universe, which eventually led to the structures we see today (galaxies, clusters of galaxies, filaments...). In particular, the most important effect comes from oscillations of the coupled baryon-photon plasma in the early Universe. Gravity tries to compress the photon-baryon fluid sitting on primordial gravitational potential wells, while radiation pressure acts in the opposite way, resulting in acoustic (pressure) oscillations. These anisotropies are usually analyzed using a decomposition in spherical harmonics $Y_{l,m}(\theta, \phi)$ such as:

$$\frac{\Delta T(\theta, \phi)}{T_0} = \sum_{l=0}^{\infty} \sum_{m=-l}^l a_{l,m} Y_{l,m}(\theta, \phi), \quad (2.3)$$

where the $a_{l,m}$ coefficients, provided they are independent, can be completely

characterized by what is known as the CMB power spectrum:

$$C_l = \frac{1}{2l+1} \sum_{m=-l}^l |a_{l,m}|^2, \quad (2.4)$$

which describes CMB fluctuations at a given multipole moment, l , corresponding to an angular scale of about $l \sim \pi/\theta$. Figure 2.7 shows the Planck 2015 measured CMB power spectrum and its excellent agreement with the Λ CDM best-fit theoretical model (Ade et al., 2016). The *baryon-photon acoustic oscillations* are responsible for its peak structure, as photons decoupling when a particular mode is in its peak amplitude create resonances which correspond to the different peaks. There are other effects occurring at later times in the Universe which are also imprinted in the CMB, as its photons are free to interact with ionized electrons and they also feel the gravitational fields of the late-time large-scale structure of the Universe. As a consequence of the variety of the physical phenomena involved, the analysis of the CMB power spectrum provides an enormous amount of information about the composition of the Universe and hence about the cosmological parameters defined in (Equation 2.2).

BARYON ACOUSTIC OSCILLATIONS

In analogy to the CMB, the Baryon Acoustic Oscillations (BAO) are regular, periodic fluctuations in the density of the visible baryonic matter of the Universe. In an over-dense region of the primordial plasma (made of DM, baryons and photons) while gravitationally attracts matter towards it, the heat of photon-matter interactions creates a large amount of outward pressure. These counteracting forces of gravity and pressure created oscillations, resulting in a spherical sound wave of both baryons and photons (DM is expected to interact only gravitationally) moving with a relativistic speeds outwards from the over-density. After decoupling the photons were no longer interacting with the baryonic matter and they diffused away leaving behind a shell of baryonic matter at a fixed radius. This radius is often referred to as the sound horizon and can be measured by looking at the Large Scale Structure (LSS) of matter using astronomical surveys (~ 490 million light years in today's Universe, see Figure 2.8).

WEAK LENSING

Similarly to the case of CG, we can extract key information from gravitational lensing, as the distortions in the light are produced by the total matter gravitational field. Then, by quantitatively measuring these distortions we can

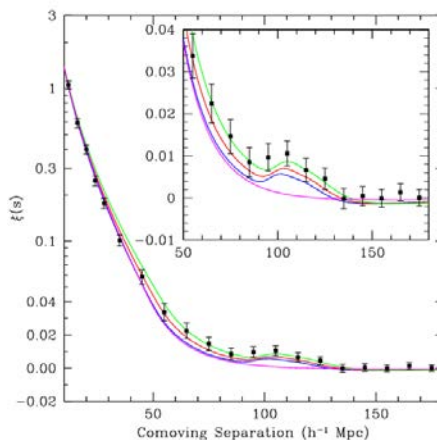


Figure 2.8: The Baryon Acoustic Peak (BAP) in the correlation function – the BAP is visible in the clustering of the Sloan Digital Sky Survey (SDSS) citeAlbareti:2016xlm luminous red galaxies sample, and is sensitive to the matter density. Different lines correspond to different realizations of Λ CDM where the relative contribution of each species changes. Magenta line corresponds to the case where no baryonic matter is presence (and hence, no BAP is present, Bassett and Hlozek, 2009; Eisenstein et al., 2005).

infer information about the mass distribution in the Universe. As introduced before (Section 2.1.2) gravitational lensing, in some extreme cases produce massive distortions. Extracting large-scale structure information from gravitational lensing however, requires the study of faint distortions in the shapes of distant galaxies induced by foreground mass over-densities, where we focus in the large-scale properties of the effect throughout the Universe. Similar to the case of the CMB, we can infer cosmological parameters by measuring the properties of these LSSs.

Current galaxy surveys as (DES, The Dark Energy Survey Collaboration, 2005), provide independent measurements to cosmological parameters as the ones obtained from the CMB physics. Latest results (Abbott et al., 2017), despite being in slight tension with current satellite values (Ade et al., 2016), confirm the current view of the Universe composition.

COSMOLOGICAL SIMULATIONS

Cosmology is an observational science, where only one realization of the Universe is known³ and, a frequentist experimental approach is hence, not always achievable. In order to understand how galaxies form and evolve in their cos-

³ At least up to the day of today, February 5, 2018.

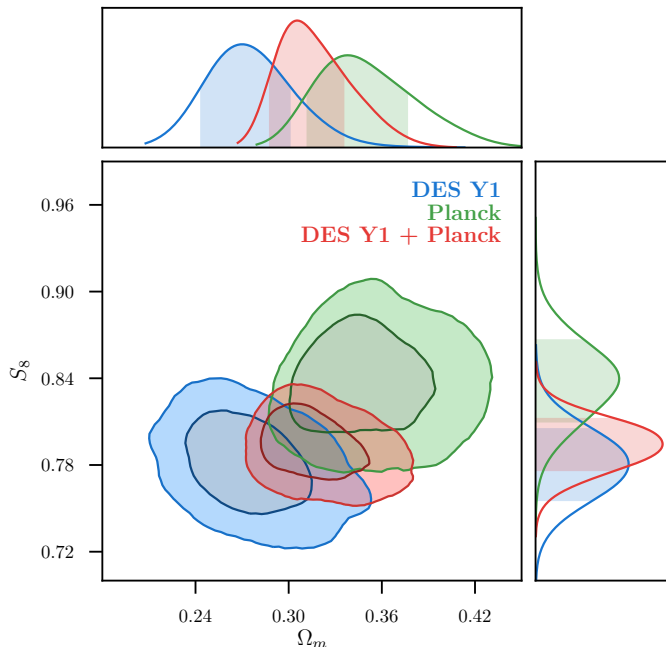


Figure 2.9: **(Figure by Abbott et al., 2017)** Λ CDM constraints from the three combined probes in Dark Energy Survey (DES) year1 (blue), Planck (Ade et al., 2016) with no lensing (green), and their combination (red).

mological context and to understand the properties of dark matter halos over a wide range of physical scales and across virtually all of cosmic history, numerical simulations provide one of the best methods for approaching this problem and have proven invaluable for studying the growth of cosmological structure and, in particular, of DM halos (Kuhlen et al., 2012). Increasing computational power and improved algorithms have led to a steady and rapid increase in the ability of N -body simulations to resolve the detailed internal very large cosmological simulations have focused on larger volumes in order to study topics such as the statistical detection of BAOs or weak lensing shear, or to build mock catalogs for the next generation of galaxy surveys. The opposite regime – smaller volumes with higher mass resolution – is much more computationally demanding but is also of great interest, especially for questions of galaxy formation, where the relevant mass scales are substantially smaller than for large-scale clustering.

Figure 2.10 shows the Projected density field for a thick slice of an N -body simulation from *The Millennium Simulation Project* as a function of the age

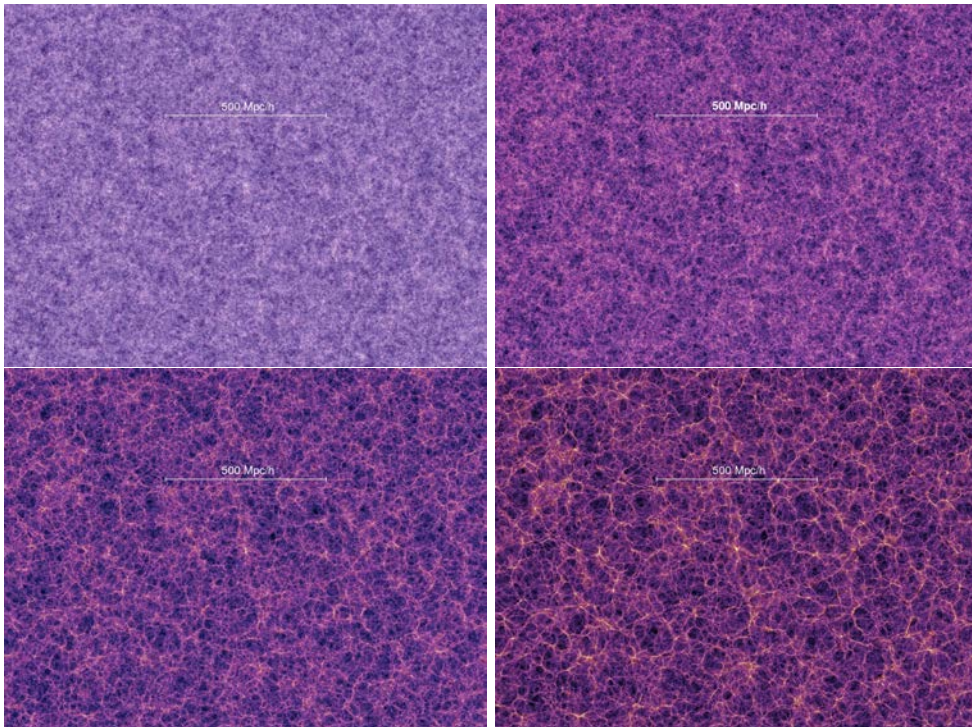


Figure 2.10: Projected density field for a ~ 500 Mpc/h thick slice at the time the Universe was 0.21 (top left), 1.0 (top right), 4.7 (bottom left) and 13.6 Gy (bottom right) old. **Images taken from The Millennium Simulation Project.**

of the Universe. We see, how, as time goes on, the Universe becomes less homogeneous and structures grow, driven by gravity, by accreting smaller over-densities into larger ones. Larger over-densities should give birth to star, galaxy and later to CGs formation, and are the ones hosting those structures nowadays. In order to reproduce the distribution of galaxies and CGs observed in our local Universe (see Figure 2.11), a non negligible fraction of DM needs to be considered.

OTHER EVIDENCES

We only covered so far, a tiny fraction of large variety of evidences that sustain the DM paradigm leaving aside for instance, measurements coming from supernovae rate or Big Bang Nucleosynthesis (BBN), the production of nuclei (other than those of the lightest isotope of hydrogen) during the early phases of the Universe. The most precise determination of the different cosmological parameters is obtained by global analysis of all available independent observables

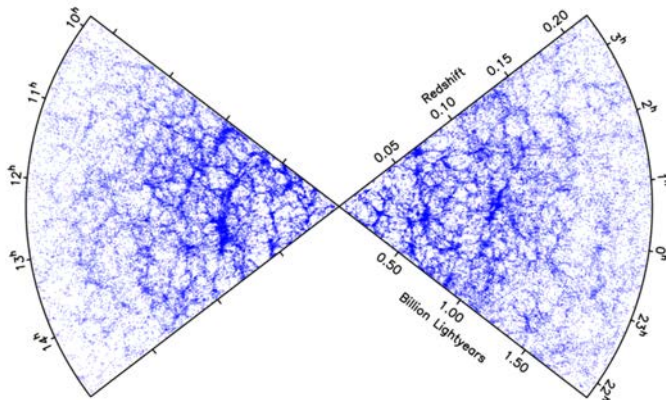


Figure 2.11: The 2dF redshift survey of approximately 220,000 galaxies during 1995 to 2002 (Percival et al., 2001; Cole et al., 2005).

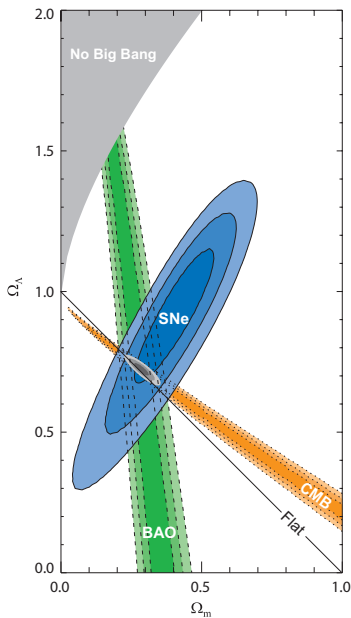


Figure 2.12: Compilation of different bounds on the preferred region in the $\Omega_m - \Omega_\Lambda$ plane (Kowalski et al., 2008). The superimposed black contours are from the Planck measurements. Adapted from Ade et al. (2014).

which confirm the DM paradigm view (see Figure 2.12).

2.2 DARK MATTER CANDIDATES

There are overwhelming observational evidences for the existence of DM however, the nature of its constituent is still unknown. Properties of the DM can be inferred however, from the wealth of recent astrophysical and cosmological data, that imposes significant constraints on it. Some of those evidences where

already introduced in Section 2.1 however, we list the full list of requirements in here⁴.

In context of Λ CDM, the DM particle should:

- be neutral – otherwise, it could couple with photons and therefore would not be dark;
- match the DM relic density (Ω_m);
- be stable on cosmological scales, so that it was present in the early Universe and is still around today;
- interact only weakly and gravitationally: the couplings with electromagnetic sector, as well as strong interactions are highly suppressed by the observations;
- play a leading role in the structure formation in the Universe, as the fluctuations in the DM density are dominating the evolution of the perturbations in the matter dominated era;
- DM density are dominating the evolution of the perturbations in the matter-dominated era;
- be consistent with the BBN and not contradict the observed abundances of light elements;
- not affect the stellar evolution;
- be experimentally verifiable and consistent with the constraints derived by different methods of DM searches (Section 2.3).

This section presents some of the theoretically best-motivated dark matter particle candidates.

2.2.1 DARK MATTER CANDIDATES WITHIN Λ CDM

Among all the (already discovered) SM particles, neutrinos (ν) are the only particles that (almost) fulfill the previous requirements. SM ν s are massless however, measurements on neutrino oscillation (Kajita, 2006; Barenboim et al., 2017)⁵ imply that at least two of the three active neutrino are massive and hence, a possible DM candidate. Current neutrino mass bound are

⁴ Some of the topics, have not been covered in Section 2.1.

⁵ In 2015, Takaaki Kajita and Arthur McDonald, were granted with the Nobel prize for the discovery of Neutrino oscillations.

$m_\nu \leq \text{eV}$ (Otten and Weinheimer, 2008; Lesgourgues and Pastor, 2012) what implies that neutrinos were relativistic at the decoupling (the transition between radiation and matter era) and hence could not account for structure formation within ΛCDM . Tiny neutrino masses challenge the interpretation of neutrinos as the only source of DM for galaxy formation and evolution nowadays, and hence new ideas have arisen in order to account for this extra mass component.

Among all the different, so far, proposed solutions, probably one of the most simple ones has been the postulation of “standard” baryonic matter so far undetected. Such contribution would be made of massive baryonic objects, like unseen astrophysical structures, with masses ranging from very small fractions of M_\odot to well above $100M_\odot$. Examples of these objects could be brown dwarf, Jupiters, black hole remnants of an early generation of stars, and objects that are dark or not bright enough to be revealed by current instruments. Despite it is very challenging to account for all DM evidences with only this component, these objects (named Massive Compact Halo Objects (MACHOs) (Freese et al., 1998), thought to lie in the galactic outskirts) have been investigated by microlensing measurements (Lasserre, 2000) in our Galaxy and Local Universe. Several studies in our Galaxy have ruled out MACHOs as the main component of DM for mass ranges between $\sim 10^{-7}M_\odot$ and $\sim 30M_\odot$. Also at very high masses ($\sim 10^7M_\odot$), the kinematics of the Galactic disk excludes this hypothesis. Moreover, recent studies from compact stellar system in ultra-faint dSph (Brandt, 2016) provide strong limits to fully baryonic DM at intermediate mass values. In summary, existing data from samples of compact ultra-faint dSph appear sufficient to rule out the hypothesis of DM composed exclusively by MACHO for all masses above $\sim 10^{-7}M_\odot$.

2.2.2 ALTERNATIVE COSMOLOGIES

Despite not being the main focus of this thesis, alternative cosmological explanations (alternative to ΛCDM) have also been proposed as possible solutions to the DM problem. Based on the assumptions that DM is not cold or weakly interacting, or even postulating that DM does not exist at all, the majority of these alternative cosmologies provide solutions to singular problems, while at the same time create new inconsistencies. Until date, neither of the proposed cosmologies offers an evolutionary image of the Universe as completely as ΛCDM does. However, for the sake of argument, the best-justified of these alternatives are briefly described.

Modified Newtonian Dynamics (MOND) claims that the law of gravity deviates from the Newtonian one, thus eliminating the need for existence of dark matter (Milgrom, 1983). According to MOND, below a certain gravity scale the effects of the gravitational force are magnified. This would explain the observed flattening of the rotation curves, as well as the Tully-Fisher (McGaugh, 2012) relation. However, MOND fails to explain the dynamics of large objects like CGs, as well as the gravitational lensing effects without adding an additional component of matter. More over, MOND can not account for any relativistic phenomena, and overall, does not provide a satisfactory cosmology.

Tensor-Vector-Scalar (TeVeS) gravity is developed as the relativistic generalization of MOND (Bekenstein, 2004). TeVeS works in the weak-field limit and possesses all good qualities of the MOND theory. In addition, TeVeS can explain gravitational lensing effects, although in a way non- consistent with the galaxy rotation curves. Major drawbacks of the TeVeS gravity model are the incompatibility with stellar evolution theory and the inability to explain the Bullet cluster phenomena (Figure 2.4).

2.2.3 THE WIMP *miracle*

WIMPs are probably the most studied DM candidate. WIMPs are postulated as non-baryonic, stable and weakly interacting particles, but what made them really attractive is that they are found in many DM extensions, and that they naturally produce the correct relic density (what is commonly referred as the *WIMP miracle*). Moreover, WIMPs can be detected in many ways (Hut, 1977; Gelmini and Gondolo, 2010) what makes the WIMP a testable theory.

In the early Universe, WIMPs were in the thermal equilibrium with the primordial plasma; when temperature dropped below the WIMP mass m_χ , these particles decoupled, their production ceased and their number density began to drop exponentially, as $e^{-m_\chi/T}$ (Figure 2.13). However, as the Universe kept expanding, the DM gas became so diluted, that WIMPs could no longer find each other to annihilate. At that point, WIMPs density froze-out, and their number asymptotically approached a constant – their thermal relic density. The fact that this relic abundance is compatible with the estimate of the present DM density is known as the *WIMP miracle*. That is, the relic density today, given as

$$\Omega_\chi h^2 \simeq \frac{10^{-27} \text{cm}^3 \text{s}^{-1}}{\langle \sigma v \rangle} \quad (2.5)$$

where Ω_χ is the WIMP density parameter, h is the scaled Hubble constant

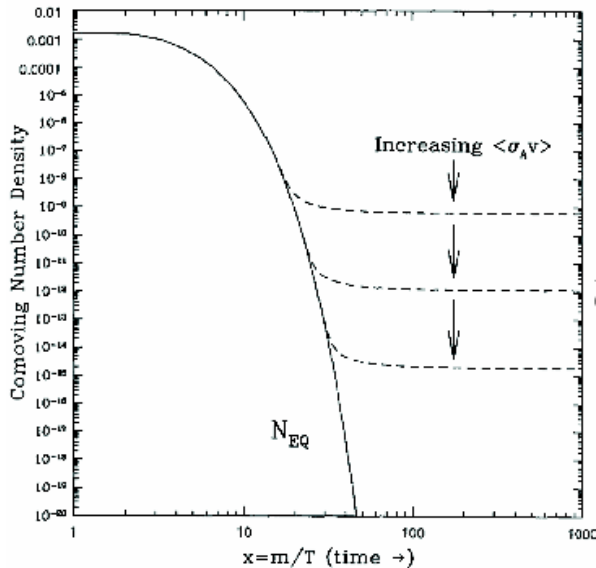


Figure 2.13: The comoving number density (or, in other units, the thermal relic density) of a Weakly Interacting Massive Particle (WIMP) particle as a function of the inverse temperature of the Universe. The solid black line corresponds to the annihilation cross section that yields the correct relic density while the dashed gray line is the number density of a particle that remains in thermal equilibrium. Figure adapted from (Feng, 2010).

and $\langle\sigma v\rangle$ refers to the thermally averaged product of the annihilation cross section and velocity, is naturally produced by a thermal relic with a mass and interaction cross section on the weak scale. For WIMPs, the freeze-out occurred at $T \approx m_\chi/20$, which sets the m_χ value in a few GeV \sim TeV range. Therefore, at the time of decoupling, these particles were non-relativistic, and as such are suitable candidates for the role of *cold* DM. Additionally, as the WIMP number density froze before the BBN epoch⁶, WIMPs are the oldest remnants: if discovered, they would give, for the first time, information on the very earliest stages of the Universe. However, as already mentioned, WIMPs do not exist within the SM framework, and hence, one must go to theories beyond the SM to search for WIMPs. Some of these theories are described below, putting especial accent on those scenarios that are of relevance for this work.

SUPERSYMMETRIC DARK MATTER

SUPerSYmmetry (SUSY) postulates that, for every SM particle there is a new, as-yet-undiscovered partner particle, with the same set of quantum numbers

⁶ Not discussed in this work.

SM particles/fields		SUSY partners			
		Interaction eigenstates		Mass eigenstates	
quark	q	squark	\bar{q}_L, \bar{q}_R	squark	\bar{q}_1, \bar{q}_2
lepton	l	slepton	\bar{l}_L, \bar{l}_R	slepton	\bar{l}_1, \bar{l}_2
neutrino	ν	sneutrino	$\tilde{\nu}$	sneutrino	$\tilde{\nu}$
gluon	g	gluino	\tilde{g}	gluino	\tilde{g}
W-boson	W^\pm	wino	\tilde{W}^\pm	} chargino	$\tilde{\chi}_{1,2}^\pm$
Higgs boson	H^\pm	higgsino	$\tilde{H}_{1,2}^\pm$		
B-field	B	bino	\tilde{B}	} neutralino	$\tilde{\chi}_{1,2,3,4}^0$
Higgs boson	$H_{1,2,3}^0$	higgsino	$\tilde{H}_{1,2}^0$		
W^3 -field	W^3	wino	\tilde{W}^3		

Table 2.1: SM particles and their superpartners in the MSSM model.

and gauge interactions but the spin, which is increased by 1/2. SUSY represents an elegant, theoretically scenario that relates fermions and bosons (see, e.g. Fayet and Ferrara, 1977; Nilles, 1984). More importantly, SUSY provides possible solutions to some of the problems of the SM:

- hierarchy problem, linked to the vast discrepancy between the aspects of the weak nuclear force and gravity, is stabilized with SUSY through cancellation of divergences in the radiative corrections to the Higgs boson mass (Witten, 1981);
- unification of the gauge couplings of the SM is possible if the SUSY particles (*sparticles*) are included in the renormalization-group equations (Ellis et al., 1992);
- natural dark matter candidate is provided by SUSY: the Lightest Supersymmetric Particle (LSP) is expected to be heavy, neutral and stable, thus fitting perfectly in the Λ CDM paradigm as the DM constituent (Ellis et al., 1984).

SUSY Realisations A general SUSY extension contains many unknown parameters. Typically, only specific models in which simplifying assumptions unify many parameters and considered. The Minimal Supersymmetric Standard Model (MSSM)(Fayet, 1976) is the minimal extension that contains all necessary field contents to give rise to all the fields of the SM. The MSSM doubles the SM degrees of freedom, plus two complex Higgs doublets (Table 2.1). Since no sparticle with the same mass as its SM partner has been seen by the accelerator experiments (Section 2.3.1), SUSY has to be broken. Breaking of

the symmetry, on the other hand, produces some critical effects on the proton lifetime, shortening it down to values lower than the age of the Universe, which contradicts the observations. To remedy the issue, a new discrete symmetry, called *R-parity*, is introduced. *R-parity* is defined as $R \equiv (-1)^{3B+2L+2s}$, where B , L and s stand for the baryon, lepton and the spin number, respectively. SM particles have *R-parity* of $+1$, and their SUSY partners of -1 . If *R-parity* is conserved, the sparticles can only be produced/annihilated in pairs, so that the LSP is stable and a viable DM candidate. Still, the MSSM has over 120 free parameters. Further “well-motivated” assumptions are typically taken to reduce even further the available parameter space. The constrained Minimal Supersymmetric Standard Model (cMSSM) (Wess and Bagger, 1992) is often regarded as the most simple and economical SUSY model (reducing the number of needed parameters from 120 to only 5). The fact that no cMSSM has yet been found (i.e. in collider experiments Section 2.3.1), puts this model on the verge of exclusion (ATL, 2012). The Minimal SuperGRAvity Model (mSUGRA) (Chamseddine et al., 1982) is a special case of the cMSSM, where the SUSY breaking is mediated by the gravitational effects. The cMSSM shrinks to the mSUGRA, with the same free parameters but in a reduced hyperspace where those parameters can move. Other MSSM realizations include the non-universal Higgs masses model (the SUSY breaking contributions to the Higgs masses do not have to be universal, Ellis et al., 2003), phenomenological MSSM (based on phenomenology rather than on particular theoretical assumptions, with number of free parameters reduced to 19, Berger et al., 2009), etc.

SUSY dark matter candidates Among the new particles that SUSY introduces, the electrically neutral ones with weak interactions are the natural DM candidates: the spin 3/2 fermion gravitino (G), the spin 1/2 fermions called *neutralinos* ($\tilde{\chi}_1, \tilde{\chi}_2, \tilde{\chi}_3, \tilde{\chi}_4$), and the spin 0 scalars *sneutrinos* ($\tilde{\nu}_e, \tilde{\nu}_\mu, \tilde{\nu}_\tau$). The sneutrinos are not good DM candidates, as both their annihilation and scattering cross sections are large, so they are underabundant or excluded by null results from direct detection experiments, for all masses near m_{weak} . *Gravitinos* (G) qualify as the DM in some particular scenarios, like the gauge mediated SUSY, where they are stable and lightest particles. Although theoretically well-motivated, G may be difficult to detect: as it interacts only gravitationally, the main source of gravitinos would be the decay of the *next-to-lightest* SUSY particles. Neutralinos, on the other hand, are favored as DM constituents. Neutralinos are mass eigenstates produced in mixing of the neutral, spin 1/2 fermions: bino (\tilde{B}), wino (\tilde{W}_3) and two higgsinos (\tilde{H}_1^0 and \tilde{H}_2^0 , Ellis et al., 1984).

With R -parity conserved, the neutralino is the LSP and thus a natural DM candidate, with relic density compatible with bounds from the Planck satellite (Section 2.1.3), a mass at the GeV-TeV scale, and a typical cross section of the order of weak interactions. Being a Majorana fermion (fermions that are their own antiparticle), the neutralino can self-annihilate into (detectable) SM particles, such are:

- *Fermions*: the leading neutralino annihilation channels are into fermion pairs at tree-level, via s -channel through the exchange of Z or Higgs bosons, or via t -channel through sfermion exchange. The dominant final states are composed by heavy particles, like $\tau^+\tau^-$, $b\bar{b}$ and $t\bar{t}$ (for sufficiently high masses).
- *Photons*: direct annihilation into photons can occur at one loop level, as $\chi\chi \rightarrow \gamma X$ where $X = \gamma, Z$ or h . Such process is strongly suppressed, but not impossible; photons produced this way would be detected as sharp lines at energies $E_\gamma \approx_\chi (1 - m_X^2/4m_\chi^2)$, representing an undoubtable evidence of dark matter detection. Photons can also be produced in the so-called internal bremsstrahlung (Bringmann et al., 2008): if neutralinos annihilate into leptons, the annihilation exchange particle is a charged sparticle that can emit a photon. This photon restores the helicity in the annihilation processes of type $\chi\chi \rightarrow l^+l^-\gamma$, thus allowing for otherwise forbidden interactions. Photons produced this way are expected to carry a significant amount of energy ($E_\gamma > 0.6m_\chi$) and to produce a characteristic bump at the end of the differential photon energy spectrum.
- *Gauge bosons*: in the low-velocity regime, pure gaugino-like neutralinos can annihilate into Z and W^\pm bosons via t -channel, while pure higgsino-like and mixed neutralinos would produce these particles via s -channel.
- *Higgs boson*: neutralinos can annihilate into pair of Higgs bosons or a Higgs and a gauge bosons. The most favoured channels are the annihilation into light neutral Higgs and a Z boson ($\chi\chi \rightarrow h^0 Z$), into a heavy Higgs and a Z boson ($\chi\chi \rightarrow H^0 Z$), into a charged Higgs and a W boson ($\chi\chi \rightarrow H^\pm W^\pm$), and into light Higgs and a pseudoscalar Higgs ($\chi\chi \rightarrow h^0 A_0$)

However, long-lived particles can either be due to kinematical or dynamical reasons (in the form of a protecting symmetry), or a combination of both (Catà et al., 2017). Among the vast list of known SM particles, only very few have

lifetimes longer than the age of the Universe. The lightest neutrino, the electron and the proton are long-lived due to the conservation of the *Lorentz symmetry*, the electric charge and the total baryon number, respectively, while the two other neutrino mass eigenstates are long-lived as a consequence of the small neutrino mass splittings, which translates into a tiny phase space available in their decay. In supersymmetric models DM models, the LSP becomes unstable once R-Parity violation (RPV) operators are introduced in the superpotential (Ando and Ishiwata, 2015),

$$W_{\mathcal{R}_p} = \mu_i \hat{L}_i \hat{H}_u + \lambda_{ijk} \hat{Q}_i \hat{L}_j \hat{D}_k^c + \lambda'_{ijk} \hat{L}_i \hat{L}_j \hat{E}_k^c + \lambda''_{ijk} \hat{U}_i^c \hat{D}_j^c \hat{D}_k^c \quad (2.6)$$

where i, j, k are generation indices, \hat{Q}_i (\hat{L}_i) is left-handed quark (lepton), \hat{U}_i^c , \hat{D}_i^c (\hat{E}_i^c) are right-handed up- and down-type quarks (lepton), and \hat{H}_u s up-type Higgs. We use “hat” to represent chiral superfields (superpartners are expressed by using “tilde” in the later discussion). The final state of DM decay depends on which of the above RPV interaction terms are operative. According to the different symmetry breaking mechanisms, there are several models predicting decay DM as wino, sneutrino, gravitino or the *axino* (superpartner of the axion, as introduced below).

The *winos* \tilde{W}^0 are the superpartner of the W -boson, and may be valid DM candidate with a mass of a few hundred GeV or around 3 TeV (Randall and Sundrum, 1999; Giudice et al., 1998), typically annihilating into leptons. Right-handed *sneutrinos*, superpartners of right-handed neutrinos, can also interact with the other particles via the *Yukawa* couplings, and therefore the lightest one can be DM. Right-handed sneutrinos can decay into charged leptons pairs. Another possibility is the *gravitino*. The gravitino $\psi_{3/2}$ has also a large lifetime and therefore it can also be a viable DM candidate (or it can be one of the DM candidates). Main decay products from the gravitino are generally electrons and positrons, protons and antiprotons, and gamma ray (γ ray)s, originating by prompt leptons and W -bosons found in the decay (Buchmuller et al., 2007). In case of mass below a hundred GeV, the gravitino show a prominent decay into a a gamma-ray (γ -ray) line, while above that mass, the preferred decay channels are: $\psi_{3/2} \rightarrow W^\pm l^\mp$ and $\psi_{3/2} \rightarrow Z_0 \nu$. To conclude, also the *photino* has been considered as a DM candidate (Cabibbo et al., 1981).

Details on methods and current progress of the searches for SUSY DM will be presented in Section 2.3. However, it should be mentioned that the latest results from Large Hadron Collider (LHC) (CERN) have struck serious blows to the SUSY credibility. No proof of new physics has been found so

far. The newly discovered Higgs boson (Aad et al., 2012; Chatrchyan et al., 2012) behaves pretty much as the SM predicts, while none of the proposed SM extensions claims a completely “standard” Higgs. Furthermore, no hint of any anomalous behaviour was detected in the extremely rare B_s meson decay (Aaij et al., 2013). Still, not all hope for the SUSY is lost: introduction of new parameters can adjust the model (to a certain extent) to the current experimental constraints.

UNIVERSAL EXTRA DIMENSIONS

An alternative possibility for the new weak-scale physics are extra dimensions. The idea originated from work of *Kaluza* and *Klein* almost a century ago (Kaluza, 1921; Klein, 1926), and since then it acquired many modern descendants, of which the theory of Universal Extra Dimensions (UED) has the strongest foundations (Appelquist et al., 2001). In UED, all particles propagate in flat, compact extra dimensions of size 10^{-18} m or smaller. Every SM particle has an infinite number of partner particles of the same spin, with one at every Kaluza-Klein (KK) level n with mass $\sim nR^{-1}$, with R referring to the compactified radius of the extra dimension. Unlike SUSY, UED do not solve the gauge hierarchy problem; in fact, their couplings become large and nonperturbative at energies far below the Planck scale. However, UED are considered as plausible models under the assumption that they are a low-energy approximation to a more complete theory that resolves the hierarchy problem and is well-defined up to the Planck scale. The simplest UED models preserve a discrete, KK parity, which implies that the lightest Lightest Kaluza-Klein Particle (LKP) is stable and a possible DM candidate. The LKP is typically a B^1 , a level 1 partner of the hypercharge gauge boson. Investigations of the B^1 regions with the correct thermal relic density indicate that the required LKP mass is in the 600 GeV-1.4 TeV range, a slightly heavier than for the neutralino. Other possibilities for the LKP are KK neutron, KK Z and KK Higgs.

OTHER WIMP CANDIDATES

Neutralino can be considered as a prototype of a WIMP, and KK DM an instructive alternative. There are many other examples, however. Some of the electroweak theories and their accompanying WIMP candidates include large extra dimensions with branons as particles (Cembranos et al., 2003), little Higgs theories with T -odd particles (Schmaltz and Tucker-Smith, 2005;

Hirsch et al., 2013)⁷ and warped extra dimensions with excited states (Agashe and Servant, 2004). As with all WIMPs, these DM candidates are produced through thermal freeze-out and are cold and collision-less, but their implications for detection may differ significantly.

2.2.4 NON-WIMP DARK MATTER

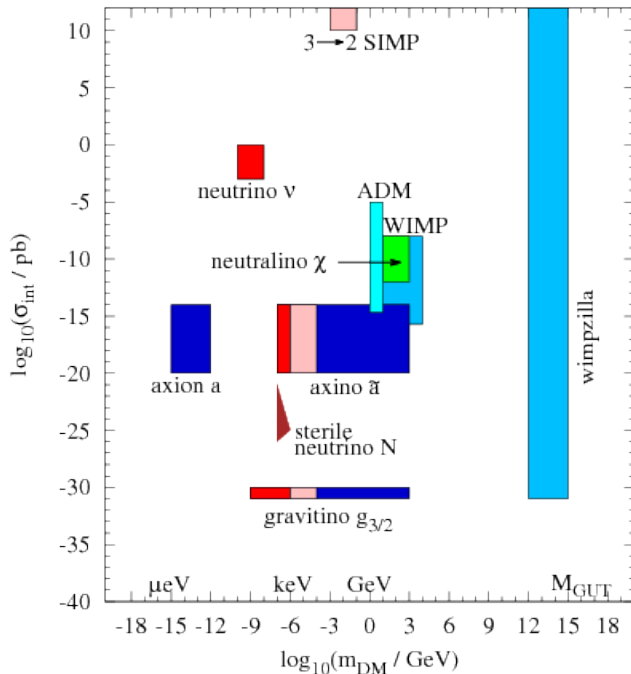


Figure 2.14: Schematic representation of some well-motivated DM candidate particles. σ_{int} represents a typical order of magnitude of the interaction strength with the ordinary matter. The box marked as “WIMP” stands for several possible candidates. Taken from (Baer et al., 2015)

As already mentioned, there is a vast collection of dark matter candidates (Figure 2.14). As this work is focused on the search for WIMP particles, some of these other candidates are only briefly reviewed in this Section.

STERILE NEUTRINOS

The fact that neutrinos have non-zero mass is a solid experimental evidence for new physics beyond the SM. For the neutrinos to get mass through the

⁷J. Palacio is a corresponding author of this publication.

same mechanisms that generate masses for quarks and charged leptons, a new, right-handed neutrinos should be added. These, so-called sterile neutrinos, are *weakly-interacting Majorana* fermions. The lightest of sterile neutrinos, with mass predicted to be in the keV range, is compatible with *warm* DM matter (Section 2.1.3), but could also be considered as cold candidate, depending on the production mechanism. Additionally, sterile neutrinos may provide solution for the baryon asymmetry (Asaka and Shaposhnikov, 2005) and, in the warm DM scenario, the missing satellites problem (Goetz and Sommer-Larsen, 2003). As a consequence of the mixing between the sterile and active neutrinos (ν_s and ν , respectively), the former become unstable. The main decay channel for the lightest sterile neutrino is $\nu_s \rightarrow 3\nu$; from there, assuming the ν_s mass m_{ν_s} of order of 1 keV, the expected lifetime of the sterile neutrinos is estimated to 10^{17} years, meaning that these particles are cosmologically stable (Dolgov and Hansen, 2002). Through the described decay, the sterile neutrinos are extremely difficult to detect, given the low energy of the resulting active neutrinos. An alternative way of detection could be pursued for a subdominant decay channel that can provide a distinctive photon line, $\nu_s \rightarrow \gamma\nu$. Such line would contribute at energies of $E_\gamma = m_{\nu_s}/2$, and it would be broadened due to the velocity dispersion of sterile neutrino population. Therefore, compact regions with significant accumulations of sterile neutrinos could produce a detectable X-ray flux line in the 0.1 – 100 keV energy range.

SUPERWIMPS

In the *superWIMP* framework for DM, WIMPs freeze-out in the early Universe (as described in Figure 2.13), but later decay to superWIMPs, particles that form the DM that exists today (Feng et al., 2003b). Because superWIMPs are very weakly interacting, they have no impact on WIMPs freeze-out and decouple with a thermal relic density $\Omega_\chi \sim \Omega_{dm}$. Assuming that each WIMP decay produces one superWIMP, the relic density of superWIMPs is

$$\Omega_{s\chi} = \frac{m_{s\chi}}{m_\chi} \Omega_\chi \quad (2.7)$$

SuperWIMPs therefore inherit their relic density from WIMPs, and for $m_{s\chi} \sim m_\chi$, the WIMP miracle also applies and the superWIMPs are produced in the desired amount to constitute much or all of DM. Because the superWIMPs are very weakly interacting, they cannot be detected in conventional direct and indirect dark matter searches (Section 2.3). However, their extraordinarily weak couplings suggest that the decays of WIMPs to superWIMPs may have occurred very late, producing an observable impact on the BBN, the Planckian

spectrum of the CMB, small-scale structure and the diffuse photon spectrum, thus possibly providing a way for superWIMP detection. The superWIMP scenario is realized in many particle physics models. The prototypical example is gravitino, which exists in all SUSY theories. Other examples of superWIMP dark matter candidates include KK gravitinos in UED scenarios, axinos and quintessinos in SUSY theories, and many other.

SuperWIMP candidates are also found with finite decay life-times (Chung et al., 1998; Doroshkevich and Naselsky, 2002; Feng et al., 2003a; Chen and Kamionkowski, 2004).

AXIONS

The axion particle was initially proposed as a solution to the strong CP problem of the SM (Peccei and Quinn, 1989). It is a light, neutral and weakly interacting, spin 0 boson that represents a natural DM candidate. For axions to live longer than the age of the Universe, their mass cannot exceed $m_a \leq 20$ eV. Axions can be produced thermally, like light gravitinos and sterile neutrinos, and in that scenario they would be the *hot* DM (Section 2.1.3). However, in order to achieve the correct relic density, the axion mass would have to be $m_a \sim 80$ eV; such particles can not be the bulk of the DM. The alternative is a non-thermal axion production, consequential to the spontaneous Peccei-Quinn (PQ) symmetry breaking. In that case, the axion can be a viable, cold DM particle, with mass in the $10^{-6} - 10^{-2}$ eV range, and with properties dependent on whether the PQ phase transition occurred before or after the inflation epoch. In the presence of electromagnetic fields, axions are predicted to couple with photons, leading to the so-called photon-axion oscillations. This effect may imprint a distinctive signature in the observed spectra of distant γ -ray sources.

It should also be said that, the *axino*, the superpartner of the axion particle (in case of SUSY) can also be a stable DM particle some supersymmetry models. Even in some RPV scenarios, an axino with a mass of $\mathcal{O}10$ GeV) can be long-lived to be DM, long-lived and decaying mainly into quarks (Ishiwata, 2014).

HIDDEN DARK MATTER

Hidden DM is postulated as DM that has no SM gauge interactions (Feng and Kumar, 2008). Hidden sector differs from the visible one, as it can have its own matter content and gauge forces. Therefore, for the correct relic density

to be achieved, for the hidden dark matter the WIMP miracle is generalized to the WIMPless miracle: dark matter naturally has the correct relic density, but does not necessarily have a weak-scale mass or weak interactions. Matter in hidden sector interacts only gravitationally. Still, in the scenarios that involve the existence of connector sectors, that mediate between the SM and the hidden sector, certain (detectable) astrophysical implications are possible (França et al., 2013)⁸.

2.2.5 GRAVITY INDUCED DARK MATTER CANDIDATES

Finally, gravity induced decaying DM candidates also arise from the fact that the stabilizing symmetry is normally imposed on the flat spacetime Lagrangian (Catà et al., 2017, 2016). In the absence of an ultimate theory that unifies SM forces with gravity, this matter is usually ignored, and the question whether the stabilizing mechanism remains operational in the presence of spacetime curvature effects is left opened (Berezinsky and Valle, 1993). After all, all current evidence for dark matter so far comes from its gravitational interactions with ordinary matter.

In conclusion, 80 years after Zwicky’s DM discovery, DM candidates can be found in (almost) all kind of forms (i.e., Ellis et al., 1990; Chen and Kamionkowski, 2004; Asaka et al., 1998; Bi et al., 2004; García-Bellido, 2017), and the kind of phenomenology the produce is extense, where among other things we find SM products.

2.3 WIMP SEARCHES

The last decades have been marked by ever-growing efforts to discover the true nature of DM. Numerous experiments have been devised in attempt to catch a glimpse of the elusive DM, however, to date, no undeniable results can be claimed. Based on the WIMP approach, three main detection techniques can be distinguished (Figure 2.15): *production* of DM in particle accelerators, *direct detection* through DM scattering off ordinary matter, and *indirect detection* of primary or secondary SM particles produced in DM annihilation or decay.

This section describes the basic principles behind each of these approaches, as well as their latest experimental results. As implied from the title of this work, indirect searches will be discussed in more detail – from the technique

⁸J. Palacio is a corresponding author of this publication.

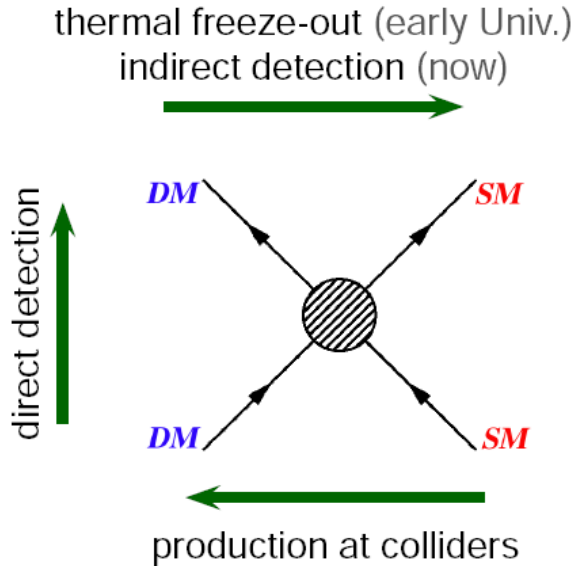


Figure 2.15: WIMP interaction diagram with SM particles. Depending on the orientation the diagram is seen, different processes (and hence, type of searches) are read: Production of DM at colliders (right to left), direct detection (bottom to top), thermal freeze-out and indirect detection (left to right).

and expected spectral signatures, to suitable targets, existing observatories and the most interesting results.

2.3.1 PRODUCTION AT PARTICLE COLLIDERS

Possible detection of new physics in *particle collider experiments* may shed some light on the nature of DM. WIMPs could be created in a collider whose luminosity and center-of-mass energy are sufficiently large. The produced WIMPs would, most probably, be invisible to the detector, but its presence can be deduced indirectly, by measuring the outcome of the collisions (see, e.g. Bertone et al., 2005, and references within). The missing transverse energy refers to the energy carried away by a body leaving the detector unseen. It is reconstructed from the momentum conservation law: the momenta of incoming projectiles in the direction orthogonal to the beam is zero, so the final products of the collision must balance their momenta in the transverse plane. When this does not happen, a possible explanation is the production of DM particles⁹.

⁹ Other explanations include the escape of high energy neutrino or imperfect reconstruction of the momenta of the outgoing particles.

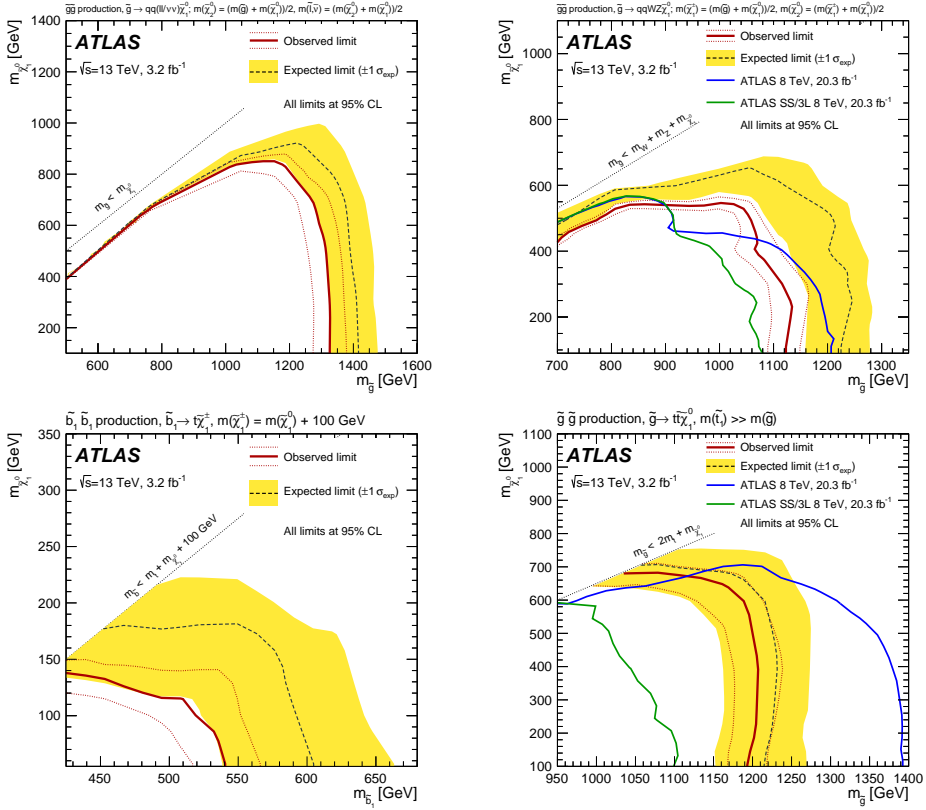


Figure 2.16: (**Figure taken from Aad et al., 2016**) Observed and expected exclusion limits on the \tilde{g} , \tilde{b}_1 and $\tilde{\chi}_1^0$ masses in the context of SUSY scenarios with simplified mass spectra featuring $\tilde{g}\tilde{g}$ or $\tilde{b}_1\tilde{b}_1$ pair production with exclusive decay modes. The signal region used to obtain the limits is specified for each scenario. The contours of the band around the expected limit are the $\pm\sigma$ results, including all uncertainties except theoretical uncertainties on the signal cross-section. The dotted lines around the observed limit illustrate the change in the observed limit as the nominal signal cross-section is scaled up and down by the theoretical uncertainty. All limits are computed at 95% CL. The diagonal lines indicate the kinematic limit for the decays in each specified scenario.

Different mechanisms for WIMP production at colliders have been proposed. In the particular case of SUSY (Equation 2.2.3), the best detection prospects would arise from the creation of heavier superparticles that in turn decay into quark and gluon jets and pair(s) of neutralinos. Such events should be seen at the LHC detectors A Toroidal LHC ApparatuA (ATLAS) (ATLAS) and Compact Muon Solenoid (CMS) (CMS); however, failure to detect them so far has put serious strains on the most simplified SUSY models Figure 2.16. Collider experiments also offer the possibility of probing the UED models (Equation 2.2.3). The expected signatures in this case are remarkably similar to

those of SUSY, and involve jets, leptons and missing energy. In the hypothetical case of the discovery of new physics, SUSY and UED particles would be distinguished by their different spins or by different number of partners for each SM particle (infinite tower of particles for UED versus one partner for SUSY).

Also possible is the direct production of WIMP particle pair accompanied by emission of a photon or a jet from the initial state. Such mono-photon and mono-jet events, respectively, together with the missing transversal energy carried away by the WIMPs, would represent striking signatures of DM presence. In lepton colliders (i.e. the Large Electron–positron Collider (LEP) Acciarri et al., 1995), disentanglement of such signals from the background is possible, as the initial state particles have definite energy and may be polarized, which provides useful diagnostics. For the hadron colliders, however, these features are missing, since energies of the *gluons and quarks* (the SM constituents of protons and anti-protons), that actually interact in the collision, are not fixed. Consequently, in LHC, mono-jet and mono-photon signals are highly obscured by the background. Still, limits for such events can be made, and they are directly comparable to the constraints of direct search experiments.

Production and detection of the DM particle in colliders would reveal significant information, like its mass, annihilation and direct detection cross section, as well as the value of its thermal relic density. Nevertheless, such set of characteristics would have to be independently confirmed by direct and indirect detection experiments before identifying the new particle as DM.

2.3.2 DIRECT DETECTION

WIMP flux expected on Earth is of the order of $10^5 \text{ cm}^{-2} \text{ s}^{-1}$ for a particle of $m_\chi = 100 \text{ GeV}$ (Bertone et al., 2005). This flux is sufficiently large to have a small, but potentially determinable fraction of WIMPs interact with ordinary matter. *Direct detection* experiments aim to discover DM by measuring the nuclear recoils caused by elastic scattering of the WIMPs off baryonic targets. Assuming that the velocity distribution of WIMPs with respect to the Solar System is of order of 100 km s^{-1} , the expected recoil energy, transferred from a GeV-mass WIMP to a heavy nucleus, is typically of order of tens of keV. The energy exchanged in these interactions can be deposited in the detector through ionization, scintillation or heat (*phonon*) production. All the information about DM microscopic properties is codified into the differential elastic scattering cross section, generally separated into a spin-independent and spin-

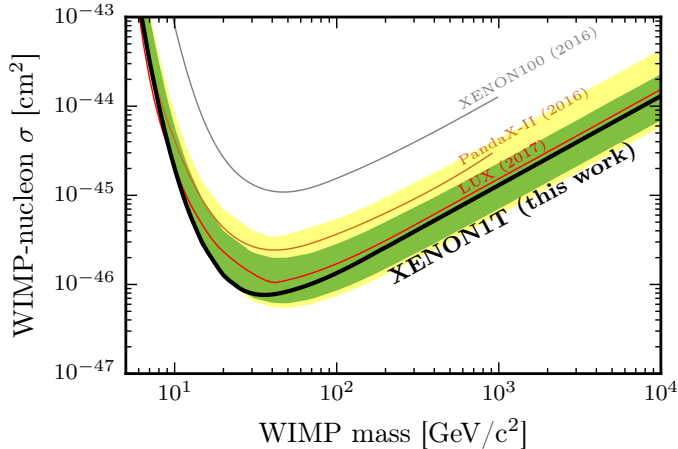


Figure 2.17: **(Figure taken from Aprile et al., 2017)** The spin-independent WIMP-nucleon cross section limits as a function of WIMP mass at 90% confidence level (black) for XENON1T (Aprile et al., 2017). In green and yellow are the 1- and 2σ sensitivity bands. Results from Large Underground Xenon (LUX) (Akerib et al., 2017a) (red), PandaX-II (Tan et al., 2016) (brown), and XENON100 (Aprile et al., 2016) (gray) are shown for reference.

dependent contributions. The spin-independent term comes from scalar and vector couplings to quarks, and its value basically scales as the square number of nucleons. On the other hand, the spin-dependent term comes from axial-vector couplings to quarks, and it is dependent on the nuclear angular momentum. For different DM models relation between these two contributions may differ, and although both have to be taken into account, the scalar component dominates for heavy targets, which is the case for most direct detection experiments. Since the expected elastic cross section is of order of $\sigma \sim 10^{-43} \text{ cm}^2$, the rate of nuclear interactions is extremely low (less than 1 event per kg per day). That makes the background characterization and control the greatest challenges of direct detection experiments. Better performance is ensured by choosing a large detection target, composed of extremely radiopure elements; the same philosophy steers the selection of the rest of the detector parts. Furthermore, the target material is often surrounded by a high-density metal shielding, and special care is taken to minimize the electronic noise. In order to suppress the unwanted background originating from cosmic rays (mainly muons), the installations of the experiments are typically located deep under ground. During the last decade, hints of direct detection of DM have been reported by experiments like *DAMA/Nai* (Bernabei et al., 2003) and *DAMA/LIBRA* (Bernabei et al., 2014), and CoGeNT (Aalseth et al., 2014); however, neither was conclusive enough on its own and could not be

reproduced by other experiments. Moreover, the most stringent limits over the spin-independent interaction cross section, measured by the *XENON1T* experiment (XENON1T) and of order $\sim 10^{-46}$ cm² (Aprile et al., 2017), already exclude both the DAMA/LIBRA and the CoGeNT favored regions (Figure 2.17). Current best sensitivity for the spin-dependent cross section is obtained by LUX that provides 90% CL upper limits to the WIMP-*neutron* (WIMP-*proton*) cross section of $\sigma_n = 1.6 \times 10^{-41}$ cm² ($\sigma_p = 5 \times 10^{-40}$ cm²) at 35 GeV c^{-2} (Akerib et al., 2017b). The future of the direct detection instruments goes along the line of increasing the mass of the target materials above one tone, lowering the ambient temperature down to few mK, and measuring the signals from ionization, scintillation and heat production within the same detector. Efforts on several of such future experiments, like *EURECA* (Kraus and Danevich, 2009), *DARWIN* (Aalbers et al., 2016) and *DarkSide-20k* (Aalseth et al., 2017), are already under way. For more information on direct detection searches, see e.g. (Bertone et al., 2005) and references within.

2.3.3 INDIRECT DETECTION

Indirect detection searches exploit the possibility that DM particles can annihilate or decay, producing SM particles detectable through a variety of modern ground and space-based observatories. The resulting SM products are expected to carry valuable information on the properties of DM particle. Furthermore, indirect searches are probing the astrophysical distribution of DM, which is not possible with direct neither with collider approaches. The main obstacle to this search method is the (usually) overwhelming abundance of astrophysical background, which makes the disentanglement of SM particles that are of DM origin a rather complex task. The premise of DM particle annihilating or decaying is based on the assumption that this particle is not absolutely stable, but stable on cosmological scales, i.e. its lifetime is longer than the age of the Universe and its annihilation/decay rate is sufficiently small so that the total DM budget is not significantly reduced. Indirect searches look for signatures of DM through the stable final SM products: photons, neutrinos, electrons, protons and their corresponding antiparticles. The expected signal depends on the properties of the DM particle, on the resulting final state SM particle, as well as on how and where it was produced. This work focuses on searches for γ -ray signatures of DM annihilation or decay. The remaining of this section describes the calculation of the expected photon flux, the suitable targets and types of γ -ray observatories used for indirect searches. But first, for the sake of completeness, the most relevant detectable products are listed.

MESSENGERS FOR INDIRECT DARK MATTER SEARCHES

Photons are particularly interesting products of DM annihilation or decay, as they travel in straight lines and are “practically” unabsorbed in the local Universe. Because they point back to the place of their creation, astrophysical foregrounds can be significantly reduced by looking for signals in regions with high DM density. Furthermore, the resulting photon spectrum should have some characteristic features (Figure 2.19), unique and universal for DM annihilation or decay, whose detection would represent the “smoking gun” of indirect searches. For WIMP-type DM, emission of photons is expected in the γ -ray energy range. More details on the γ -ray-based searches are provided in the following sections.

Neutrinos, like photons, are not deflected by magnetic fields and thus can be traced back to their source of origin. Neutrinos do not couple with electromagnetic sector and their interactions with matter are weak, however, they could potentially be detected in highly transparent well-shielded deep water (Astronomy with a Neutrino Telescope and Abyss environmental RESearch ANTARES) or ice (IceCube ICECUBE) detectors¹⁰. Neutrinos are expected to be produced in large amounts in DM annihilation or decay. If primary products from these processes are heavy leptons, their consequent decay into lighter ones will be accompanied by neutrino emission. If the primary products are gauge bosons, neutrinos are also produced in their decay into lepton (for W^\pm , Z) and quark pairs (for Z). In addition, if Z boson is among the primaries, it can decay directly into a pair of neutrinos. Direct annihilation into a neutrino pair is possible as well. Neutrinos can also be produced by DM that gets captured by deep gravitational wells, such as the Sun, and that annihilates at significant rate if gathered in great concentrations. Neutrinos can escape compact objects, and a detection of a neutrino excess from the direction of the Sun could indicate DM Aartsen et al. (2017). The same reasoning can be applied to DM captured by the Earth, but the detection prospects are much weaker than in the case of the Sun (Albert et al., 2017a). The currently best limits on DM annihilation cross section from neutrino searches come from IceCube observation of the Galactic Center (Adrian-Martinez et al., 2015; IceCube Collaboration et al., 2017): for $m_\chi \sim 100$ GeV, $\langle\sigma v\rangle$ for direct annihilation into neutrinos is $18 \times 10^{-23} \text{ cm}^3\text{s}^{-1}$, while the lower limit on lifetime of the DM particle is $\tau_\chi \sim 10^{22}$ s (Abbasi et al., 2012).

¹⁰ Despite neutrino astronomy is a very active field, no neutrino source has been firmly detected yet.

Charged cosmic rays diffuse through the galactic magnetic field from their production site to the Solar System, so, unlike photons and neutrinos, they can not be traced back to the place of their origin. It therefore makes sense to search for DM signal as an anomalous component in isotropic cosmic ray spectrum. Given that DM annihilation or decay results is typically expected

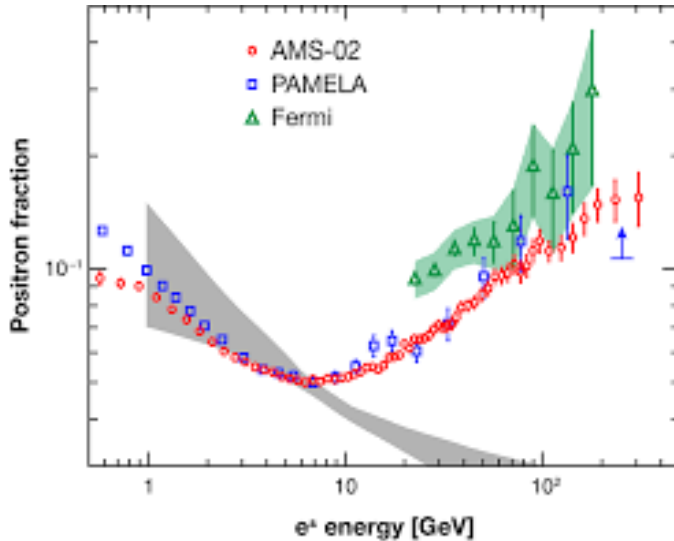


Figure 2.18: The positron fraction in high-energy cosmic rays. The measurement from the Alpha Magnetic Spectrometer (AMS) (Aguilar et al., 2013) extends over a wider energy range and has much lower uncertainty than the earlier measurements from the PAMELA (Adriani et al., 2009) and Fermi-LAT satellites (Abdo et al., 2009). The AMS measurement confirms an excess in the high-energy positron fraction, above what is expected from positrons produced in CR interactions. (The grey band indicates the expected range in the positron fraction, which is based on calculations in Moskalenko and Strong, 1998). Taken from Aguilar et al. (2013).

to create the same amount of matter and antimatter, the “anti-”products are especially attractive from the point of indirect searches, since for them the astrophysical background is much lower but “standard” matter can also be used to search and constrain DM. Recently the (DARK MATTER PARTICLE EXPLORER DAMPE) has provided a direct measurement of the all-electron spectrum with unprecedentedly high energy resolution revealing a spectral break at about 0.9 TeV (Ambrosi et al., 2017), confirming the evidence found by previous indirect measurements (Di Mauro and Vittino, 2016; Abdollahi et al., 2017). All-electron spectrum has also been measured by ground based instruments, although they show a lower performance (Colin, 2011b; Aharonian et al., 2008)

On the “anti-”mater side, distributions of positrons and antiprotons are very

promising places to look for deviations from conventional flux expected from astrophysical processes. In the last years, there have been a number of reports on unusual features in the electron-positron spectrum at high energies. The Payload for Antimatter Matter Exploration and Light-nuclei Astrophysics (PAMELA) found an interesting rise in the positron fraction ($e^+/(e^+ + e^-)$) at energies up to 100 GeV (Adriani et al., 2009), a behaviour in contradiction to the expected decline predicted by traditional models of DM propagation (Moskalenko and Strong, 1998) (Figure 2.18). This result was corroborated by measurements by Fermi-LAT for energies up to 200 GeV (Abdo et al., 2009). The latest news on this subject come from the high-precision results of Alpha Magnetic Spectrometer-02 (AMS-02) that extend up to 350 GeV (Aguilar et al., 2013): these measurements confirm the rise for energies up to ~ 250 GeV, above which there is a hint of spectrum flattening. There are numerous proposed theories involving DM (Cirelli et al., 2009; Ibarra et al., 2010) that can justify the observed excess, however, they are not fully supported by the experimental measurements (for instance, the positron excess should be accompanied by photon excesses at other wavelengths, which is not the case). On the other hand, a more conventional explanation, with particles being accelerated by the nearby pulsars (Hooper et al., 2009), is much more plausible. Another stable product from DM annihilation or decay are the antiprotons.

Antiprotons may also be created from decay of primary products; however, current measurements of the antiproton flux show no deviation from the predictions for local astrophysical sources (Aguilar et al., 2016). *anti deuterons* (*anti-Ds*), is also a possible messenger for indirect DM searches. Anti-*D* are produced by the annihilation of WIMPs, whereas they are rarely produced by CRs below 1 GeV (see, Salati et al., 2010, and references within). The General AntiParticle Spectrometer (GAPS) (Ong et al., 2017), initially configured as a long-duration balloon experiment, will search for anti-*Ds* with an effectively background-free method in a low energy range so far unexplored¹¹. An unambiguous detection of an anti-*D* particle would be by itself of great importance for the field of astrophysics, but could shed light on current evidences of DM detection claimed by ongoing experiments.

PHOTON FLUX FROM DARK MATTER

In order to proceed on details within indirect DM searches with photons, we need to assess first the DM framework. The γ -ray flux from annihilating (or

¹¹ AMS superconducting magnets bend low energetic charged particles outside of the detector.

decaying) WIMPs arriving at Earth from a given region of the sky ($d\Omega$) can be factorized as,

$$\frac{d\Phi(E, \Delta\Omega)}{dE} = \frac{d\bar{\Phi}^{\text{PP}}}{dE} \cdot J(\Delta\Omega), \quad (2.8)$$

where $d\bar{\Phi}^{\text{PP}}/dE$ is called the *particle-physics* factor, and depends on the nature of DM, and $J(d\Omega)$ is called the astrophysical factor (JFactor), and depends on the target distance and its DM distribution. These two factors read:

$$\begin{aligned} \frac{d\bar{\Phi}^{\text{PP}}}{dE} &= (1 + \mathcal{B}) \frac{1}{4\pi} \frac{\alpha}{k} \frac{dN}{m_{\text{DM}}^k dE} \\ J(d\Omega) &= \int_{d\Omega} d\Omega' \int_{\text{l.o.s.}} dl \rho^k(l, \Omega') \end{aligned} \quad (2.9)$$

respectively, with

$$\begin{aligned} \alpha &= \langle\sigma v\rangle, k = 2 \quad , \quad \text{for annihilating DM,} \\ \alpha &= \tau_{\text{DM}}^{-1}, k = 1 \quad , \quad \text{for decaying DM;} \end{aligned}$$

$\langle\sigma v\rangle$, τ_{DM} and m_{DM} are the DM particle velocity-averaged annihilation cross section, lifetime, and mass, respectively; dN/dE the average γ -ray spectrum of a DM annihilation or decay event, obtained from references (Cirelli et al., 2011) and Cirelli (2013); and ρ the DM density at a given sky direction Ω' and distance from Earth l . The integrals in the JFactor run over the region $d\Omega$ (which, in this work, we will assume ρ to be spherically symmetric, $\rho = \rho(r)$) and the line of sight, respectively. Another important quantity we want to define is the differential astrophysical factor ($dJ/d\Omega$) which, from Equation 2.9 can be written as:

$$\frac{dJ}{d\Omega} = \int_{\text{l.o.s.}} dl \rho^k(l, \Omega') \quad (2.10)$$

For the rest of this work we will use acronym of J_{ann} -factor (J_{dec} -factor), or simply $J_{\text{ann}}/J_{\text{dec}}$ for the astrophysical factor for the annihilation (decay) case. Respectively, we will talk about $dJ_{\text{ann}}/d\Omega$ and $dJ_{\text{dec}}/d\Omega$ for the differential JFactor of each case.

The expected signal of DM is described by Equation 2.8. While the particle-physics factor (Equation 2.9, up) encloses all the information on the particle candidate (see Section 2.2), it's annihilation or decay modes and the final spectral information of the γ -ray signal, the JFactor (Equation 2.9, down) encloses the information on how DM is distributed w.r.t. us. The term \mathcal{B} in Equation 2.9, represents possible intrinsic flux boost factors that are not

included in the naive computation shown in here. These can have different contributions, and it will be discussed below.

DM distribution There is a general agreement from N -body simulations (see Section 2.1.3), yet only partially supported with experimental data, that the DM density profile around different classes of DM dominated targets (from dSphs, to galaxies, and to CGs) is substantially universal, and can be expressed by the Zhao-Hernquist (Hernquist, 1990; Zhao, 1996) functional form which reads as:

$$\rho(r) = \frac{\rho_s}{\left(\frac{r}{r_s}\right)^\gamma \left[1 + \left(\frac{r}{r_s}\right)^\alpha\right]^{(\beta-\gamma)/\alpha}} \quad (2.11)$$

where $\rho(r)$ is the DM density in function of the distance r from the DM barycenter, r_s and ρ_s are the characteristic scale radius and density, α, β, γ are free parameters. γ tunes the logarithmic density gradient at small radii, β at large radii, while the third power α controls the rate at which the density profile interpolates between its inner and outer values. Because of the Λ CDM hierarchical structure formation, the total DM profile is the sum of a "smooth" component and a large number of smaller DM substructures (also called clumps, or sub-halos). The effect on the expected fluxes, of these substructures in the DM profile in galaxy clusters has been studied amply in the literature, but mainly for the annihilating-DM case, resulting at first in large discrepancies in the expected "boost" from substructures (the term \mathcal{B} in Equation 2.9). This effect is maximally relevant for the annihilating-DM case because in this case, J_{ann} -factor (in Equation 2.9) is computed as an integral over the *square* of the DM density. However, in the decay case, because of the linear dependence with the DM density in the integral, substructures tend to average out for large integration angles $d\Omega$ and do not add a significant internal boost.

DM particle models As already mentioned, there are in general no absolute theoretical motivations for the nature of the DM particle, neither its main annihilation or decay products. A very pragmatic approach is to divide models into *mainly hadronic*, *mainly leptonic* or a combination of the two, where DM annihilation/decay takes place mainly into SM leptons, hadrons or a mixture between both. Despite begin the real particle (or force) mediator of DM annihilation/decay still a mystery, the assumption of the process happening with a certain strength, allows us to develop further for indirect DM

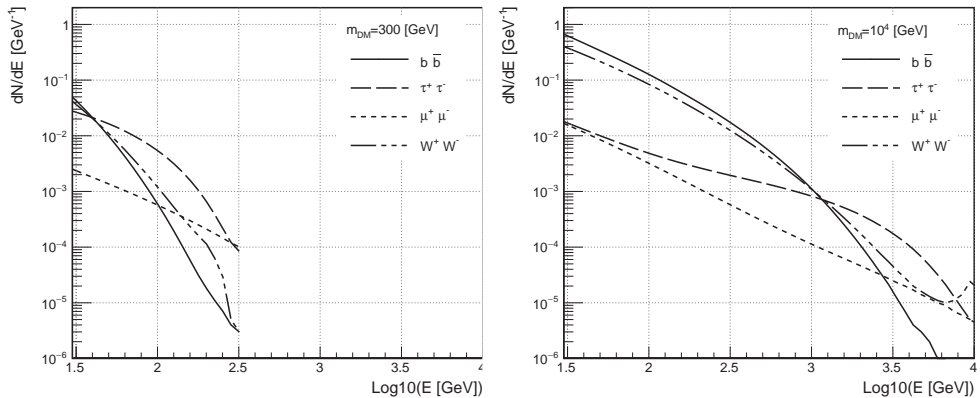


Figure 2.19: Gamma-ray spectra due to prompt emission from different DM annihilation/decay SM pairs. m_{DM} is the mass of the DM particle annihilating ($2m_{\chi}$ for the case of decay).

searches. Suppose a (two) DM particle(s) gravitationally bound annihilating (decaying) into a SM pair. We can assume the process to happen with no momentum w.r.t. the rest frame of the DM halo. Moreover, the kinematical conditions fix the final energy and momentum of the outgoing SM particles, where the further production of γ rays can be assumed to be purely SM driven. Figure 2.19 shows different mean γ -ray spectra due to prompt emission from different DM annihilation/decay SM pairs. For a given DM mass and annihilation/decay mode, they can be obtained by averaging the number of γ rays promptly emitted after many simulations of the defined energy SM pair (Sjöstrand et al., 2015). Note that we don't consider here secondary γ rays that originate from e.g. Inverse Compton scattering on the intra-cluster radiation field, because these are not expected to be significantly contributing in the TeV range (Colafrancesco et al., 2006).

Chapter 3

IMAGING ATMOSPHERIC CHERENKOV TELESCOPES: MAGIC & CTA

IACTs are ground based instruments capable of detecting γ rays with energies from ~ 50 GeV to ~ 100 TeV impinging the Earth's atmosphere. The detection technique is based on an indirect detection of the initial γ ray that, after interacting with the molecules forming the higher layers of the Earth's atmosphere (at ~ 10 km a.s.l), creates a cascade of particles traveling at super-luminical¹ speeds towards the ground, all of them emitting light in a "bluish" wavelength known as Cherenkov radiation (Cherenkov, 1934). IACTs, through the collected Cherenkov light reaching the ground, are able to reconstruct the distribution of particles forming the cascade, and hence, properties of the initial particle colliding with the atmosphere as: the initial incoming direction of the particle; the arrival energy at which the interaction took place; and the nature of the interacting particle, being events usually classified into *gamma*-like (*hadron*-like) showers, where the initial particle is likely to be a γ ray (CR). Typically, only γ -like showers are used to do high-energy astronomy of all kind (the study of super nova remnant, active galactic nuclei, pulsars and among many others, the topic that concerns us here, DM) however, interesting physics can also be studied with hadronic events, despite the directional correlation is lost due to charged induced deflections. The first detection of a VHE γ -ray source by an IACT was announced in 1989 (Weekes et al., 1989). Later instruments as HEGRA (Daum et al., 1997) or CAT (Barrau et al., 1998) were essential as a prove of concept of the technique. In the last decade, the three most sensitive currently operating instruments, VERITAS (Holder et al., 2009), H.E.S.S. (Aharonian et al., 2006) and MAGIC (Aleksić et al., 2016b), have discovered over 150 sources, comprised of a large variety of astronomical

¹ Super-luminical with respect to the speed of light in the medium, in this case the atmosphere.

objects (see de Naurois and Mazin, 2015, for a recent review). The number of entries in the Very High Energy (VHE) source catalogue is expected to increase to ~ 1000 with the future CTA (Actis et al., 2011), which would produce a new turn in the field. In this thesis, we focus on MAGIC, operating from La Palma since 2004 (MAGIC-I) and upgraded into a stereoscopic system of two telescopes in 2009 (MAGIC-II), and in CTA, the next generation ground-based observatory for γ -ray astronomy at very-high energies.

This chapter is structured as follows: in Section 3.1 I briefly discuss the different γ ray detection techniques with special emphasis on IACTs; in Section 3.2 I describe in detail The MAGIC Telescopes, the main instruments used in this thesis, where I go in detail to its hardware and software components, and some of the main instruments complementing MAGIC observations; Finally in Section 3.3 I introduce the next generation of IACTs, CTA, and focus on the biggest telescope kind forming the CTA array, the Large Size Telescope (LST) (currently under construction in La Palma (LP)).

3.1 THE IMAGING ATMOSPHERIC CHERENKOV TECHNIQUE

Astronomy is one of the oldest natural sciences where, applying mathematics, physics, and chemistry, try to explain the origin of celestial objects, phenomena and their evolution. The early civilizations in recorded history (such as the Babylonians, Greeks, Indians, Egyptians, Nubians, Iranians, Chinese, Maya, and many ancient indigenous peoples of the Americas) driven by their craving for knowledge, already performed methodical observations of the night sky. Historically, astronomy has included disciplines as diverse as astrometry, celestial navigation, observational astronomy and the making of calendars, but professional astronomy is now often considered to be synonymous with astrophysics.

Originally, these observations were performed on the visible range of the ElectroMagnetic (EM) spectrum however, astrophysics is nowadays, a much wider field of research, where observations are carried on not only all along the EM spectrum, but also through other SM products and event since very recently, also on gravitation (with the first detection of a Gravitational Waves (GWs) (Abbott et al., 2016a,b)). Among all the particles and radiation reaching constantly the Earth, CRs are the particles with the highest energies known, and their study allows to understand the composition and evolution of the Universe. This kind of radiation, that reaches energies up to 10^{20} eV, is so

3.1 THE IMAGING ATMOSPHERIC CHERENKOV TECHNIQUE

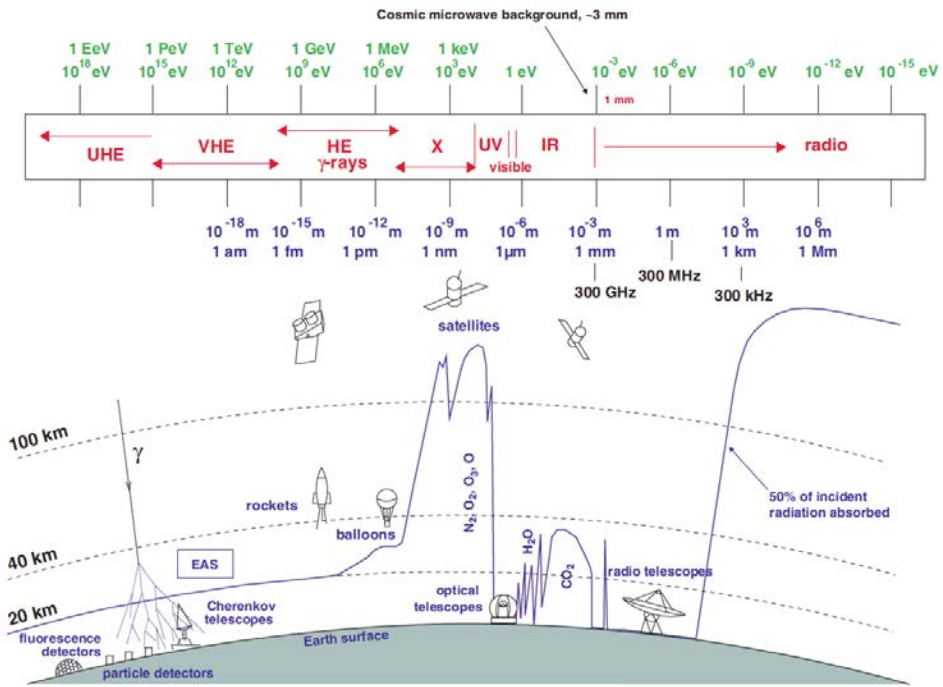


Figure 3.1: The bounds of the EM spectrum (above) as seen from the altitude where photons are fully absorbed in the atmosphere (below). From Longair (1992); Moralejo (2002); Wagner (2006)

energetic that cannot be produced in the thermal processes, otherwise, the temperature of the body producing it would have to be close to that existing in the early stages of the Big Bang. However, since they are charged particles, they are deflected by the randomly oriented magnetic fields they find in their travel to the Earth. This implies that their arrival directions are almost randomly distributed and their origin cannot be traced back. Apart from CRs, one can observe the products of non-thermal processes along the whole EM spectrum, from radio to VHE. Photons are neutral particles and do not suffer from deflections when travelling towards the Earth. This allows photon studies to establish clear relations between the arrival direction and emission site². In the case of DM, the signal of γ rays is expected to correlate with this DM sites, very DM dominated environments where the emission probability is higher (see Chapter 2).

Photons with energies above \sim MeV (γ rays) reaching the Earth's atmosphere,

² This is also valid for neutrinos, but no clear neutrino source has been established so far.

can not penetrate it, and are absorbed before reaching the ground. In order to detect this photons, one needs to go to search it outside the atmosphere. Satellite telescopes are launched in orbit (~ 500 km), where γ rays reaching the instrument are pair converted³ and then absorbed inside the detector. Direction, energy and charge estimation of the incoming particle are estimated through the deposit of energy inside the detector. Among the main advantages of satellite telescopes are the very large duty cycles (can operate almost every day), strong background rejection (thanks to a very good particle identification), large Field of View (FoV) (covering all sky every few hours) and even more important, a very good energy calibration (they are tested on real particle beams before being launched). Their main drawback of satellites is that, due to space science instrumentation limitations on size (and/or weight), typical satellite instrument's size are of the order of the meter cube⁴. Above energies around \sim GeV (typically defined as VHE), most of events are only partially contained within the detector, and angular and energy estimation is very much affected. Even more, size limitation becomes specially critical for even larger energies, (~ 100 GeV), where γ -ray individual source fluxes are typically of the order of $\sim m^{-2}y^{-1}$ (Abdo et al., 2010a).

Above certain energies, γ rays can also be detected from the ground, where ground based instruments have typical *collection areas* ($\sim 10^4 m^2$) much larger than satellite telescopes. The detection principle is based on an indirect detection of the γ ray through the generated products after interacting with the high layers of the atmosphere. VHE γ rays or CRs interacting in the atmosphere generate a cascade of particles moving at relativistic speeds towards the ground. The IACT technique, that will be introduced in Section 3.1.3, is based in the detection of the Cherenkov light emitted by these particles when traveling at speeds faster than the speed of light in the atmosphere towards the ground. As we will see, IACTs have very limited FoV ($\sim 5^\circ$) and can only be operated under *dark* nights in *good weather* conditions (preventing them to observe with strong moon, wind and/or rain). Ultra High Energy (UHE) γ rays ($E > 10$ TeV) produce particle cascades that reach the ground, where they can be detected using different techniques. The most successful one is the water Cherenkov technique, that measures the Cherenkov light produced by the particles forming the cascade as they cross water tanks equipped with PhotoMultiplier Tubes (PMTs). They have higher energy threshold, worst

³ Under certain environments, γ rays tend to generate an electron-positron pairs.

⁴ It is more common to express the effective size of these instruments in units of m^2 , as their *effective area*, a concept similar to the particle physics *cross-sections* that will be introduced later on.

angular resolution ($> 1^\circ$) and worse energy resolutions than the IACTs, but their collection area is larger, therefore they are able to detect the low fluxes at multi TeV energies. These arrays have also larger duty cycles since water tanks are shielded in dark, and hence can operate during day time.

3.1.1 CHERENKOV RADIATION

Cherenkov radiation is electromagnetic radiation emitted when a charged particle (such as an electron) passes through a dielectric medium at a speed greater than the phase velocity of light in that medium. As a charged particle travels, it disrupts the local electromagnetic field in its medium and the medium becomes electrically polarized. If the particle travels slowly, then the disturbance elastically relaxes back to mechanical equilibrium as the particle passes however, when the particle is traveling fast enough, the limited response speed of the medium means that a disturbance is left in the wake of the particle, and the energy contained in this disturbance radiates as a coherent shockwave⁵ (see Figure 3.2, *slow* and *fast*). The number of Cherenkov photons produced by an ultrarelativistic particle as a function of length and wavelength grows inversely proportional with its wavelength (Yao et al., 2006). It is expected hence, that Cherenkov pulses peak at Ultra Violet (UV) regime and, that due to energy losses in the atmosphere (scatter with air molecules and aerosols), a bluish light reaches the ground.

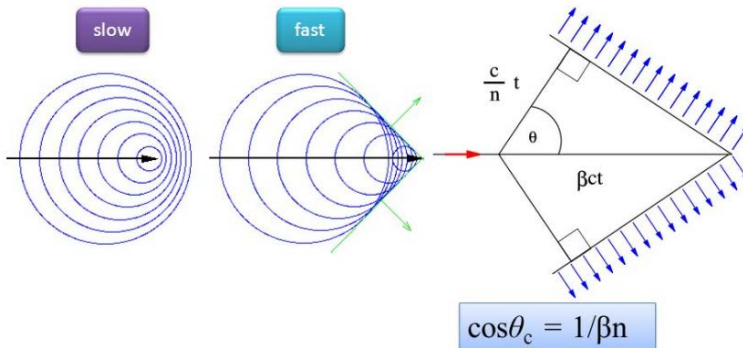


Figure 3.2: Schematic view of the Cherenkov radiation emitted by a charged particle moving through a dielectric medium. v is the velocity of the particle (red arrow), β is v/c , n is the refractive index of the medium. Blue arrows are photons.

Charged particles travelling at superluminal speeds⁶ emit Cherenkov radi-

⁵ A common analogy is the sonic boom of a supersonic aircraft or bullet.

⁶I always mean w.r.t. the speed of light in the medium.

ation in a cone with an aperture angle Θ w.r.t. its direction (the so-called Cherenkov angle; see Figure 3.3 right), given by:

$$\cos\Theta = \frac{c'}{v} = \frac{c}{vn(\lambda)} \quad (3.1)$$

where $c' = c/n$ is the speed of light in the medium and $n(\lambda)$ is the refractive index of the medium, whose value varies with the wavelength (λ) of the Cherenkov light. At a given moment, an ultrarelativistic particle propagating vertically through the atmosphere emits Cherenkov light in a ring that propagates downwards with an angle Θ w.r.t. the initial direction of the particle. The fact that showers produce Cherenkov light was pointed out by Blackett (1948) and later measured by Jelley and Porter (1963). After the interaction of a γ ray with the atmosphere, the contribution of all the involving particles in a Extended Air Shower (EAS), each particle emitting Cherenkov radiation, leads to a full circle on the ground, the so-called Cherenkov light pool (Figure 3.3), where the density of Cherenkov photons is proportional to the energy of the primary particle. Since $(n - 1) \sim \mathcal{O}^{-4}$ in the air, the maximum angle is $\Theta \leq 1$.

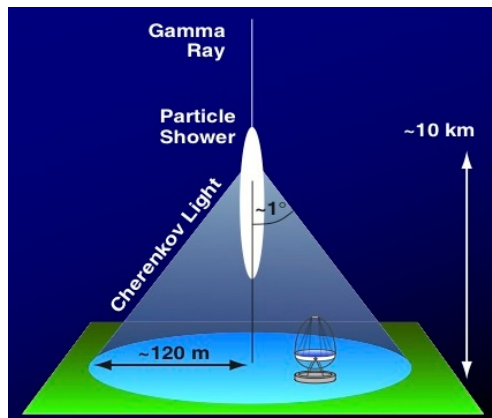


Figure 3.3: The superposition of the Cherenkov light emitted by all particles forming an EAS creates a disk of light reaching the ground, the *Cherenkov pool*.

Although we are interested in EASs initiated by γ rays, cascades induced by hadrons (mainly protons) are much more numerous. Even for strong γ -ray sources, as it is the case of the *Crab Nebula*, the ratio between hadron-induced and γ -ray induced cascades is considerably high, around 1000 hadronic cascades for each electromagnetic shower above 100 GeV. Therefore, hadronic cascades represent the major source of background in our observations. A good

background rejection power relies in a good understanding on both types of EASs.

3.1.2 TYPES OF EAS

Typically for γ -ray astronomy, we are only interested in differentiating between γ ray- (hadron)-like EASs, being the cascade originated by the interaction of a γ ray (CR). Depending on the particle interaction with the atmospheric nuclei, its development along the air is going to be different, and hence the Cherenkov pool imprint at ground level. In the following sections, I will give an overview of the difference between gamma ray- and hadron-induced EAS.

ELECTROMAGNETIC SHOWERS

Gamma rays above a certain threshold energy ($\gtrsim 20$ MeV) can initiate particle cascades through the pair creation process on air nuclei. The electrons and positrons, product of this interaction, emit in turn gamma rays via bremsstrahlung. If photons emitted through bremsstrahlung have enough energy, they undergo pair creation as well, leading to a EM cascade (see Figure 3.4, left). Both

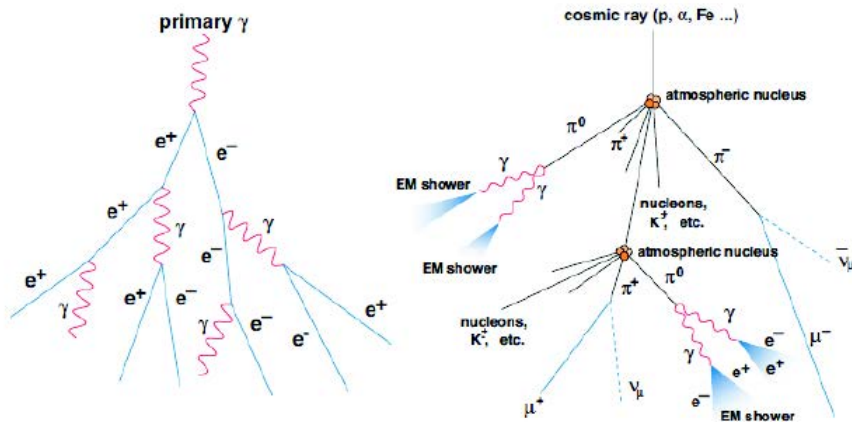


Figure 3.4: Schemes of an EM (*left*) and hadronic (*right*) showers. Credit: Wagner (2006).

bremsstrahlung *radiation length* for electrons and positrons and γ -rays *mean free path* (average distance traveled between collisions) due to pair creation in air are small (and comparable between each other). Consequently, the particles in an EM shower do not scatter too much from the shower axis, leading to a quite symmetric cascade (see Figure 3.5 left). The cross-section for the interaction of γ rays with the atmospheric nuclei is weakly dependent on the

photon energy, and therefore the height of the collision of the primary γ ray is similar for different γ ray energies, being located at $\sim 20\text{--}30$ km above sea level (a.s.l.). In each step of the shower, the number of particles is doubled, while the particle energy halves, until reaching $E_C = 86$ MeV, (below which the ionization energy loss dominates), moment at which the shower is disrupted and the number of particles reaches its maximum. The altitude at which this condition is fulfilled is called *height of the shower maximum* and it is inversely proportional to the logarithm of the primary gamma-ray energy, $H_{max} \propto 1/\ln(E)$.

HADRONIC SHOWERS

Hadronic cascades are those produced by the interaction between a CR and an atmospheric nuclei. Normally, the primary particle of this interaction is a proton which gives rise mostly ($\sim 90\%$) to pions (approximately in the same proportion π^+ , π^- , π^0). Besides pions, these collisions produce kaons and nuclei (Figure 3.4, right). Both hadrons and pions undergo more collisions or decays that generate the shower. The cascade stops when the energy per nucleon is less than ~ 1 GeV, minimum energy needed for pion production. Among all the processes and decays that take place inside hadronic showers⁷, π^0 are mainly going to decay into secondary photons, electrons and positrons, initiating an EM cascade, as a subcascade of the hadronic one. Generally speaking, hadronic showers are wider than the EM ones, because the transversal momentum that the kaons and pions receive. Furthermore, this type of cascades can undergo into more subshowers, leading to a not only wider but more asymmetric EAS. Figure 3.5 presents MC simulations of γ ray- and hadron-induced cascades (left and right respectively), where the shape difference is evident. Due to these population differences, timing development can also be used as a parameter to distinguish between them.

3.1.3 THE IMAGING TECHNIQUE

The the *Imaging Atmospheric Cherenkov Telescope* technique bases its study of γ rays on the indirect observations of the Cherenkov radiation produced in EAS (see Figure 3.6). IACTs consist on very large mirror extensions where, if the telescopes are inside the Cherenkov light pool, part of the Cherenkov light is reflected to be collected in their fast pixelized cameras. The images created are projections of the EASs, from which spatial and timing information is ob-

⁷ We leave aside muon cherenkov traces, very important for the instrument calibration, a topic however not coverer in this thesis.

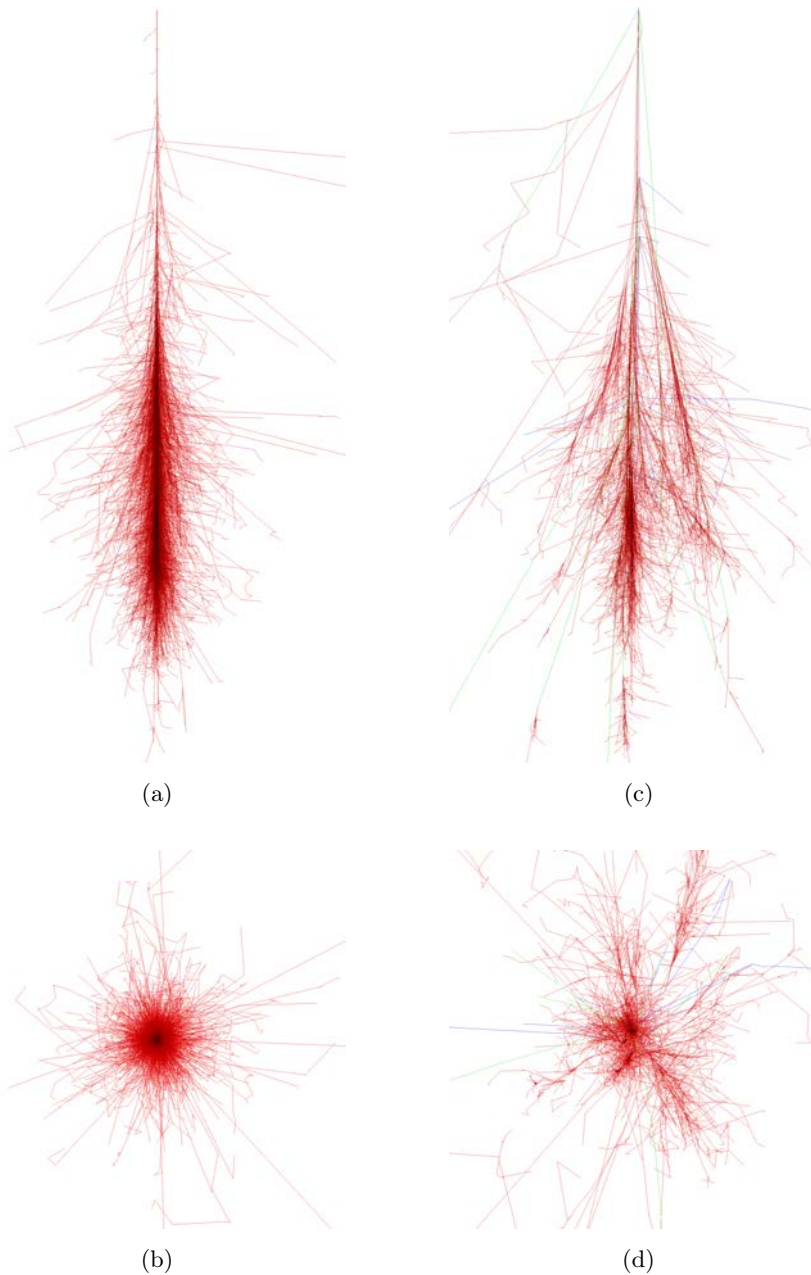


Figure 3.5: *On the left:* MC simulation of an EM cascade initiated by a 100 GeV gamma ray. *On the right:* MC simulation of a hadronic cascade initiated by a 100 GeV proton. Red lines show the gamma-ray, electron and positron tracks, green lines are used for muons and blue ones for hadrons. The upper plots represent the vertical trajectory, while the lower plots represent the transversal planes.

tained. The Cherenkov light density at ground level is used to reconstruct the distribution of the particles forming the cascade, and hence, properties of the initial particle colliding with the atmosphere as: the initial incoming direction of the particle; the arrival energy at which the interaction took place; and the nature of the interacting particle, being events classified into *gamma*-like (*hadron*-like) showers.

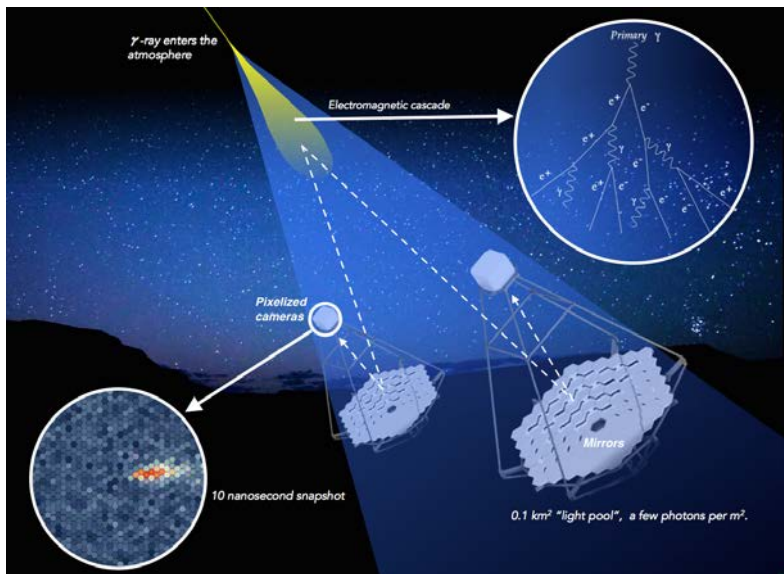


Figure 3.6: Sketch of the IACT technique. The Cherenkov light from the cascade is reflected in the mirrors and collected in the camera. Modified image from www.cta-observatory.org.

Cherenkov pulses from EAS are very fast (~ 3 ns) for which precise and very efficient detectors are needed. PhotoMultiplier Tubes (PMTs) are extremely sensitive detectors of light in the ultraviolet, visible, and near-infrared ranges of the EM spectrum, commonly used in IACTs⁸. These detectors multiply the current produced by incident light by as much as 100 million times, in multiple dynode stages, enabling (for example) individual photons to be detected when the incident flux of light is low. A fast response time is also important to avoid collecting undesirable photons, product of the background sources. As mentioned before, the main background sources are the hadronic showers,

⁸ Silicon PhotoMultiplier (SiPM) tubes are becoming more and more common in the field since they overcome one of the main drawbacks of PMTs, they are much more robust devices and can be exposed to large light fluxes without being damaged. However, SiPM sensors size is $\mathcal{O} \sim \text{cm}^2$, and despite commercial prices are decreasing very fast, covering large extensions ($\mathcal{O} \sim \text{m}^2$) is still challenging.

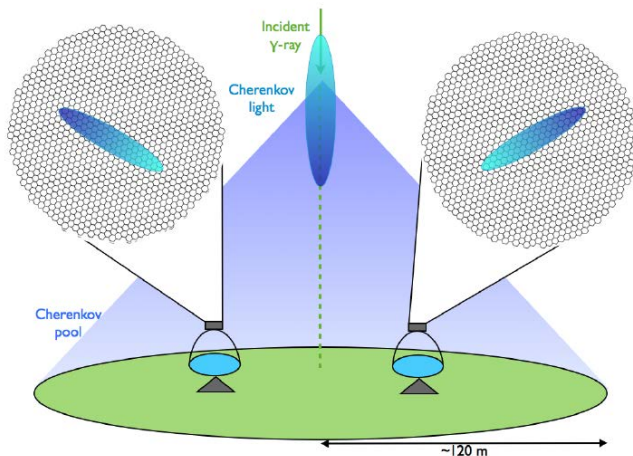


Figure 3.7: Scheme of stereo reconstruction with 2 IACTs. Credit to López-Coto (2015)

from which the EM subcascades act like an irreducible background for the gamma-ray observations. Besides the background from the EASs, optical photons isotropically distributed on the sky can affect the observations as well. This is the so-called Night Sky Background (NSB) that is formed by the stars' light, airglow, polar and zodiacal light and artificial lights. Typically, IACTs are built in arrays of telescopes, where observations are performed stereoscopic mode, such that all instruments forming the array behave as if being only one⁹ (see Figure 3.7). Such operation mode, not only improves the angular resolution of these instruments, as it will be shown in the next section, but acts as a main source of background rejection since EAS events would leave a trace in both telescopes that NSB can not reproduce.

3.2 THE MAGIC TELESCOPES

The MAGIC is a stereoscopic system consisting of two 17 m diameter IACTs located in El Roque de los Muchachos in the Canary island of LP, Spain (28.8deg N, 17.8deg W, 2225 m a.s.l.). MAGIC core science is focused on the study of the CR origin in either galactic or extragalactic targets, but it is well-known that cosmic γ rays constitute also a probe for several fundamental physics quests, including DM (see, e.g. Doro et al. (2013)). Until 2009, MAGIC consisted of just one stand-alone IACT (MAGICI) with an integral flux sensitivity around 1.6% of the Crab Nebula flux in 50 hours of observation

⁹ Similarly as the two eyes of humans.

(Albert et al., 2008a). After autumn 2009, the second telescope (MAGIC II) started operation, reaching in stereo mode an energy threshold of 50 GeV at low zenith angles and a sensitivity of $0.76 \pm 0.03\%$ of the Crab Nebula flux for energies greater than 290 GeV in 50 hours of observation (Carmona et al., 2011). Between summer 2011 and 2012 both telescopes underwent a major upgrade that involved the digital trigger, readout systems and the MAGIC I camera (Aleksić et al., 2016b). After this upgrade, the system achieves, in stereoscopic observational mode, an integral sensitivity of $0.66 \pm 0.03\%$ of the Crab Nebula flux in 50 hours above 220 GeV (Aleksić et al., 2016a). After the major upgrade, both telescopes became almost identical. The data analyzed in this thesis has been taken on stereoscopic observations, before and after the major upgrade however, we focus here to describe only the current status of the instrument (see Figure 3.8).



Figure 3.8: Picture of the MAGIC telescopes at El Roque de los Muchachos. Image taken from <https://magic.mpp.mpg.de/>.

3.2.1 HARDWARE DESCRIPTION

In this section, I will give a description of the main components of MAGIC, mainly composed of a structure, a mirror dish, the camera and other systems that complement MAGIC during operation (see Figure 3.9).

STRUCTURE AND DRIVE

The telescopes structure (that supports the 17 m dish and the camera) is made of light carbon fibre-epoxy tubes. This material is strong enough to support

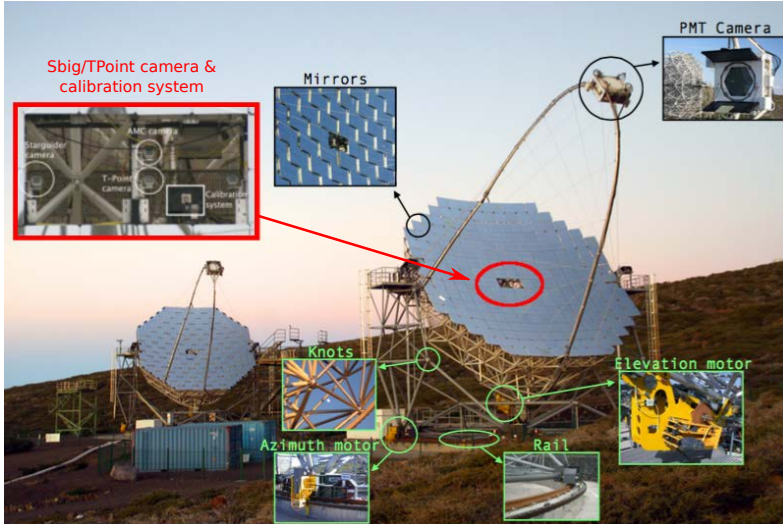


Figure 3.9: Picture of the MAGIC telescopes (MAGICI behind, MAGICII on the front) with some of their hardware subsystems highlighted. Image taken from <https://magic.mpp.mpg.de/>. (Picture edited by Fernández-Barral (2017))

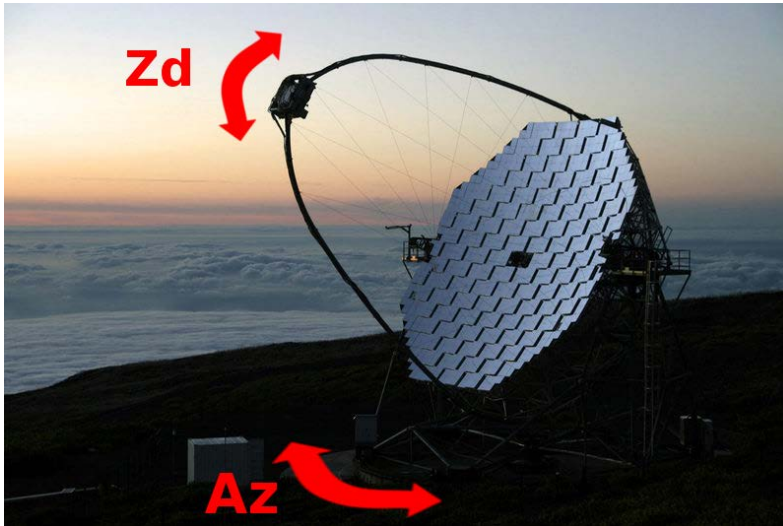


Figure 3.10: Moving degrees of the MAGIC telescope.

the weight and the tensions the telescope is exposed during observations¹⁰ while being at the same time light enough, to allow MAGIC to be fast at reposition (repointing at any direction on the sky can be done in less than ~ 20 s). MAGIC telescopes move in two degrees of freedom (Azimuth angle

¹⁰ Or during strong winds.

(Az) and Zenith distance (Zd), see Figure 3.10), where two drive cabinets move the telescope through a 20 m diameter circular rail and an alt-azimuthal mount takes care on the elevation. The camera is held by an aluminum circular tube secured to the main structure by 20 steel cables. Small bending of the mirror surface during the movement of the telescopes are corrected before (and during) data taking through the Active Mirror Control (AMC) (see Section 3.2.1). As most of subsystems, the drive system of both telescopes can be operated (MI only, MII only or both telescopes at the time) from a central control room, however for safety reasons, the drive system is automatically stopped whenever the fence around each of the telescopes is opened. A Charge-Coupled Device (CCD) camera (the starguider camera) is located at the center of the mirror, looking in the same direction as the telescope (see Figure 3.9, at the center of the dish). Its purpose is to crosscheck where the telescope is looking at. Usually, the Drive system steers the pointing of the telescope pretty well, but to improve the pointing on analysis level, the starguider camera images are analyzed online for stars in its FoV, leading to a correction to the nominal position. Starguider images are taken throughout each measurement, such that the corrections can be interpolated for every single event. The parametrisation of the starguider misspointing in dependence of pointing direction is called *Bending Model*. It can be considered a multi-parameter calibration function, Look Up Tables (LUTs), whose parameters can be derived after comparing cataloged and observed coordinates of bright stars projected in the mirror focus plane (such images are taken with another CCD camera, the *T-Points camera* also located in the dish).

REFLECTOR AND MIRRORS

The $17 \times 17 \text{ m}^2$ mirror dish is made of individual mirrors, $\sim 1 \text{ m}^2$ each. This mirrors are placed in parabolic shape, with a focal length at 17 m (distance at which the camera is placed). Each individual mirror has a spherical surface¹¹, and is automatically aligned through the AMC system. The AMS is a system composed by two actuators installed on the back of each mirror, together with a third mirror subjection to the telescope structure, that allow to move the mirror based on LUTs (binned in Az and Zd) for a correct focusing of all the mirrors. There are several reasons that could cause the miss-alignment of one or several mirrors during operation (change of the mirror's surface due to aging, displacement of the mirror's position after strong winds, wrong or outdated bending model, aging of the mirrors or even very high humidity

¹¹ Easier to produce since all mirrors are equal, and can be easily exchanged or replaced one by another regardless of their position on the dish.



Figure 3.11: Moon filter installation in LP, October 2014.

periods¹²). In case of not being realized, this does not only decrease the fraction of collected Cherenkov light, but potentially focuses NSB light into the camera increasing the noise levels. For that purpose the Point Spread Function (PSF) of the telescope is measured every night of observation, typically ~ 10 mm (atmospheric effects as clouds, humidity or aerosol particles, or even high air mass values can enlarge this value).

CAMERA

The PMT cameras of the telescopes play a key role in the overall instrument. As discussed at the beginning of this chapter, during summers of 2011 and 2012, the MI camera suffered a major upgrade to mimic the MII camera. Both cameras have now a circular shape region with ~ 1.2 m diameter covering 3.5 deg FoV, covered by 1039 PMTs uniformly distributed (with a 0.1° FoV each). In order to detect Cherenkov pulses, High Voltages (HV) are applied to the PMTs, where a Cherenkov photon striking the photocathode material would eject a single electron that would be accelerated several times inside the tube, creating a cascade of electrons easily collectable. In order to collect the highest amount of Cherenkov photons reflected in the mirrors and exclude, in

¹² This issue is still under investigation, however, MAGIC has experienced several times that after very high humidity periods, the focusing accuracy of the instruments takes a few days to recover.

turn, NSB light coming at larger angles, light guides are attached to each PMT, typically (miss-)labelled as *Winston Cones*. PMTs output electrical signal are transported through 162 m optical fibers to the Counting House (CH) where a logical trigger is decided (see Figure 3.2.1). The cameras have a plexiglass window installed in front of the light collectors to protect it from the environment conditions. There are also movable lids that prevents damage on the camera due to strong light (as Sun light) and external agents. PMTs have very low time responses, however, they are very sensitive devices and can only be operated in very dark conditions. In order to enlarge MAGIC duty cycle, several HVs values are used according to the ambient moon light level (Colin, 2011a). Moreover, *Ultra-Violet* filters (see Figure 3.11) have been proposed in MAGIC as an alternative PMT protection for extreme bright conditions (as directly pointing the moon Ahnen et al., 2017c). HVs also prevent PMTs to be exposed to high humidity environments.

CALIBRATION SYSTEM

To flat field the PMT gain, obtain the conversion factor between the counts of the digitizers to number of Photo Electrons (phe) and the conversion between Analog-to-Digital Converter (ADC) timing into an absolute timing, the MAGIC telescope needs a calibration system. It consists on a Nd-YAG laser, operating at 355 nm with 0.7 ns pulse width. To obtain a dynamic range, two rotating filter wheels can attenuate the laser beam, so that the signal produced in a PMT ranges between 1 and 1000 phe. To achieve an homogeneous distribution of the calibration light at the camera plane, the laser beam is diffused using an integrating (Ulbricht) sphere.

RECEIVERS

Trigger, readout electronics and Data Acquisition (DAQ) are placed in a CH. We will describe the electronic chain that is followed by the signals coming from the telescope. The optical signals coming from the telescope through the optical fibers enter the so-called receiver boards, where they are converted back to electric ones by photodiodes. The electric signals are then split into a trigger and a readout branch.

TRIGGER SYSTEM

In order to make an efficient use of the devoted computer resources, only potential γ -ray induced cascades are stored into data, discriminating mainly over NSB. The *trigger* subsystem is a set of logical decisions in order to decide

whether the event has (or not) to be saved. In general words, very conservative trigger systems miss a fraction of the Cherenkov events recorded by the telescopes (specially the low energetic ones) while very permissive settings, are constantly triggering increasing the total data storage and the induced dead-time of the telescope. Each PMT's collected charge is temporary stored in buffers so that, in case a trigger is fulfilled, data acquisition is stopped and the recorded even is downloaded to disk. Currently in MAGIC, trigger decisions are taken in three logical steps: *pixel-wise*, *pixel-group* and *stereo-telescope* trigger (*L0*-, *L1*- and *L3*-trigger respectively).

- **Level 0 (L0) trigger:** This trigger releases a square signal every time the analog signal from an individual PMT overpasses a certain amplitude threshold, the so-called Discriminator Threshold (DT). A dedicated channel rate counter allows to obtain the individual pixel rate on-line (during data taking). The level of this DT is automatically adjusted by the Individual Pixel Rate Control (IPRC), in order to keep the pixel rate within the optimal operation conditions. The operation intervals are adjusted depending on the moonlight or HV settings.
- **Level 1 (L1) trigger:** PMTs are organized into 19 overlapping hexagonal cells, the so-called macrocells. Each macrocell receives the L0 input of all PMTs forming the macrocell. Thus, L1 is used to find spatial and timing coincidence between closer pixels (see Figure 3.12). If a number n of neighboring pixels in any macrocell, defined in MAGIC as n Next Neighboring (NN), have a coincident L0, the L1 trigger releases a signal. 3 NN is a standard for stereoscopic observations in MAGIC however $n=2$, 4 and 5 are also allowed.
- **Level 3 (L3) trigger:** This trigger level only applies for stereo observations, where it searches for a trigger coincident in time in both telescopes. In order to do that, the arrival time of one of the two telescopes needs to be corrected w.r.t. the Az and Zd pointing, and the relative distance between the them (~ 70 m).

For a matter of completeness, let me add that two different new trigger systems are being developed in MAGIC, a new “pixel-group” and a new “stereo-telescope” trigger. The idea behind in both independent efforts is to use our current knowledge on EASs and their expected signal to improve the discrimination power over NSB. A better discrimination lowers the acquisition rates at which data is written into disk, what allows to lower individual pixel DTs to search for lower energy cascades in the most background dominated region.

The data presented in this thesis uses non of these two new triggers. Finally, note that hadronic showers are expected to generate smaller EM showers, which the trigger system can not be able to distinguish. This hadronic cascades are written into disk (they are in fact the dominant fraction of events being written) and are discarded later on during the analysis.

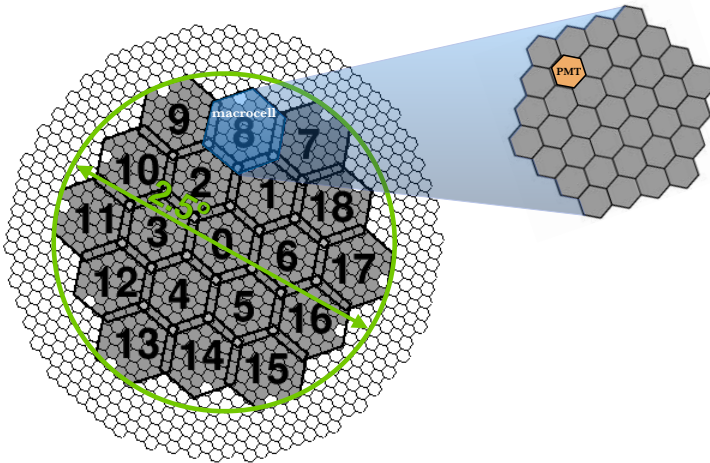


Figure 3.12: Hexagonal L1 macrocells in the current MAGIC camera version, each of which contains 37 PMT (one blind). The numbers on the macrocells are the internal MAGIC identification. The hexagonal shape of the PMT is given by the Winston cones. The trigger FoV is 2.5degdiameter. **Figure taken from Fernández-Barral (2017); López-Coto (2015).**

READOUT

As mentioned before, one of the two signal paths goes to the readout system, responsible for the DAQ. This signal is delayed a few ns in order to wait for the trigger system response, which will determine if an event is produced by a γ ray and hence, has to be recorded by DAQ. During the major upgrade in 2011, both MAGIC I and MAGIC II readout were substituted by Domino Ring Sampler version 4 (DRS4) analog memories (Sitarek et al., 2013). Besides uniforming the readout system in both telescopes, the DRS4 allows us to reduce the deadtime w.r.t. previous versions. Its functionality is based on the previous version 2, previously used in MII. The DRS4 analog memory chip worked as follow: the signal coming from the receiver boards enters in a 1024 capacitor

array. While the signal passes through a capacitor, the device is being charged, switching from one capacitor to the next one with an external clock. The charge in a capacitor is proportional to the time period of the clock. Once the cycle is finished, it starts over overwriting the first capacitor and so on. In case a trigger is reported, the procedure is stopped, and the capacitors of a defined Region of Interest (RoI) are written into disk. The position of this RoI is determined by the Zd and Az pointing, in order to cover the evolution of the arrival Cherenkov photons. The sampling frequency and the size of RoI can be optimized taking into account that, for very slow sampling velocities, the precision of the Cherenkov wave is lost, while very fast velocities reduces the available time to determine a trigger¹³. All the recorded events by DAQ have a time stamp proffered by a Rubidium clock. The Rubidium clock, with a precision of 3×10^{-11} per second, provides the absolute time. It is in turn synchronized with a Global Positioning System (GPS) with a precision of ns.

OTHER SUBSYSTEMS

Monitoring weather systems: At the MAGIC site, there is several instrumentation with the goal to monitor the weather conditions in order to evaluate if observations can be safely performed, and in that case, whether data weather corrections are required. Main safety weather conditions are evaluated through a weather station located in the roof of the CH (from where wind, humidity speed and direction can be read). Even in the case where safe conditions are accomplished, and the telescopes can operate, data quality is strongly dependent on the sky clearness. Shifters rely on three different instruments to judge whether data taking is worth it. The AllSky camera provide a wide FoV optical image where a qualitative estimation on clouds outside. A Pyrometer, installed in the center of the mirror dish and pointing to the same direction than the telescopes, measures the temperature of the sky¹⁴ and provides an atmospheric transparency estimation. Thus, an estimation of the *cloudiness* (c , higher cloudiness implies lower transparency) is given by:

$$c = \frac{T_{low} - T_m}{T_{low} - T_{up}}, \quad (3.2)$$

¹³ This is specially critical for pointing directions in which the expected Δt of the Cherenkov front-wave between the two telescopes is maximal

¹⁴It measures Infra-Red (IR) radiation that fits to a blackbody spectrum, obtaining this way the temperature. The measured temperature increases if the sky is cloudy, because it reflects radiation from the ground.

Transmission Range	AOD [%]
Perfect	$0.85 < t$
Good	$0.7 < t < 0.85$
Correctable	$0.55 < t < 0.7$

Table 3.1: Based on Laser Imaging Detection and Ranging (LIDAR) information taken during the data taking, data is divided into three transmission ranges where *Perfect*, *Good* and *Correctable* (that account for transmissions (t) above 85% , 70% and 55% of the standard AOD obtainable during clear nights). LIDAR correction can be applied to Good data and are mandatory to Correctable data. Data with with transmission ranges below 55% can not be recovered.

T_{low} and T_{up} correspond to the temperature of the sky at its worst and best conditions, respectively, which are set to $T_{low} = 250$ K and $T_{up} = 200$ K. T_m is the measured temperature by the pyrometer.

Finally and most important, a LIDAR measures the cloud density distribution along the line of sight (l.o.s.) of the telescope pointing. The LIDAR is located in an independent dome on the CH roof, and flashes a laser at a position shifted by 3° from the observing source (Fruck et al., 2014a). The pulsed light from the laser is backscattered by the clouds and aerosols on the sky. The transparency is measured as a function of the arrival time distribution of the backscattered photons. LIDAR observations (performed in parallel with MAGIC data taking) are very important. LIDAR can provide transmission estimation at different altitudes of 3, 6, 9 and 12 km. Typically, based on the LIDAR measurements, MAGIC data is classified into three Atmospheric Optical Depth (AOD) ranges (see Table 3.1). Data collected within an AOD higher than 85% of the AOD of a clear night, is considered to be perfect, and can be used to do science. Instead, if the AOD is measure do be between 75% and 85% of the one of a clear night, data is considered to be good. Physical parameters estimated are going to be correct, thus a small bias is going to be introduced due to the differences w.r.t to the MC simulations (where not clouds have been simulated). LIDAR corrections are required for data with AOD between 55% and 75%. In case LIDAR data is not available, data corrections cannot be applied, however, due to a very good correlation between the LIDAR AOD *above 9 km* and cloudiness (see Figure 3.14), data within the highest LIDAR AOD range ($c < \sim 40$) is still analyzed.



Figure 3.13: LIDAR picture, credit M. Will.

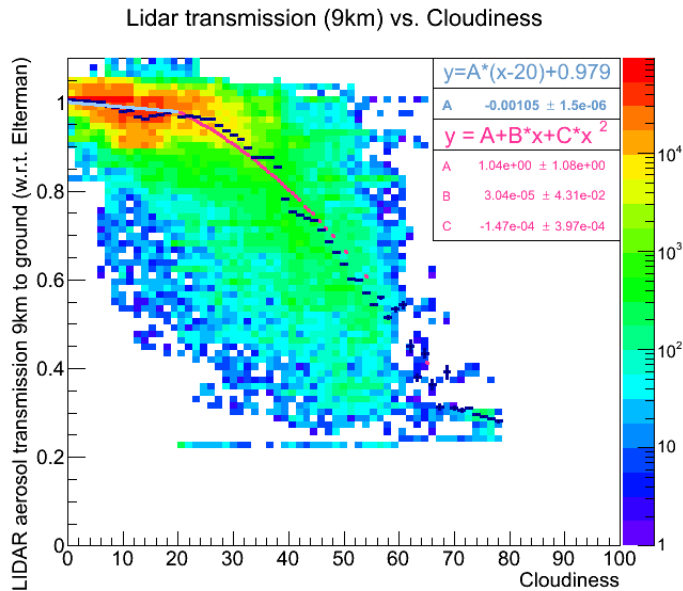


Figure 3.14: (**Figure by** Betorz, 2015) Correlation between LIDAR AOD above 9 km with cloudiness. In case LIDAR data is not available, we can rely on the Pyrometer to discriminate between good and bad data. In such case, only data with Perfect LIDAR AOD is analyzed.

3.2.2 DATA TAKING

All subsystems of MAGIC Telescopes are controlled and monitored from the Central Control (CC) program Zanin et al. (2009). The CC defines standards for all observational procedures, and this section briefly describes what observation modes can be used and what types of data can be taken with the

MAGIC Telescopes.

POINTING MODES

There are two standard observation modes in MAGIC: the *tracking* (*ON/OFF*) mode and the *wobble mode*.

In tracking mode telescopes are pointing directly to the source, in such a way that the nominal position of the target is located at the center of each camera. Data recorded in this configuration are called ON data. In order to properly estimate the residual background in the ON sample, additional, dedicated observations of so-called OFF region(s) are required. OFF data are recorded from areas where no significant gamma-ray emission is expected, under the same circumstances as the ON observations (e.g., same Zd range, NSB level, AOD, HVs).

Wobble, or the false source tracking mode (Fomin et al., 1994), consists of observations where telescopes are alternatively tracking (at least) two directions on the sky, located with a slight offset w.r.t. the nominal position of the source. For MAGIC, the standard¹⁵ offset is 0.4° , with wobble positions changing every 20 minutes to ensure uniform (*Az*) coverage of the sky and avoid possible bias. The main advantage of this technique is that it does not require any additional OFF data, since signal and the background control regions are “simultaneously” observed. At the same time, weather changes affect (almost) exactly the same way both regions. Background region, for every pointing, is defined in the respective pointing partners in the same direction within the FoV as the position of the source. Still, the wobble mode observations have two main drawbacks: loss in the gamma-ray efficiency, due to the smaller effective trigger area around the source, and a possible bias introduced by the off-center source position consequence of the camera inhomogeneities (specially critical if the distribution between the different wobbles is not properly balanced).

Furthermore for the case of the *two* MAGIC telescopes, stereo observations originate an uneven acceptance along the FoV, referred to as the “stereo blob”, caused by the broken azimuthal symmetry due to the relative orientations of the telescopes. The presence of the “blob” can be significantly irregular at the lowest energies.

¹⁵ This wobble distance has been optimized mainly for point-like analysis.

DATA TYPES

Independently on the observation mode, MAGIC data are classified according to the kind of events that are recorded. Three kinds of events are typically recorded during the standard observations:

- *Pedestal events*: randomly triggered events, digitized and recorded for measurement of the baseline value and evaluation of the effects the NSB light and the readout electronics noise have. The contribution of both components is further extracted, pixel-by-pixel, in the calibration of the data. The probability of recording an actual shower is negligible.
- *Calibration events*: triggered by the calibration system of each telescope (Figure 3.2.1), through generation of light pulses that mimic Cherenkov showers in terms of duration and wavelength. The calibration events are further applied in the calibration of the data (§3.3.1) – they are used to calculate the arrival time offsets as well as the conversion factor between the ADC counts and phe.
- *Data run*: events triggered by the trigger subsystem (Figure 3.2.1).

Each telescope data runs also include pedestal and calibration events, interleaved with the data run events. The interleaved events are further used to maintain the pedestal values and calibration constants updated during the sequential calibration of the data. Additionally, information from all complementary instruments operating at the site is also stored with the data in the form of reports to be used later during the analysis.

3.2.3 DATA ANALYSIS

Data analysis in MAGIC is performed with the standard MAGIC Analysis & Reconstruction Software (MARS) (Zanin, 2013). MARS is an object-oriented C++ software based on ROOT¹⁶ libraries and classes. MARS converts the raw ADC counts stored by DAQ into processed high-level data. The final goal of the analysis is to determine the characteristics of the incoming particle: incoming direction, energy and whether an event was generated by a γ ray or a CR (γ /hadron separation). However, along the procedure, data size is largely reduced, so that data storage and accessibility are easiest. In this section, I will briefly describe the main data types of MAGIC.

¹⁶<https://root.cern.ch/>

- *MC simulation*: IACTs measurements strongly rely on MC simulations. The reason for that being, that no calibrated (human made) γ ray source was ever placed outside the atmosphere shining towards the Earth, so no real calibration measurement has ever been made. MC simulations are used for ground based instruments to extract the Instrument Response Function (IRF), a mapping between the incoming photon flux and the detected events, normally described into three main quantities: the *migration matrix*, a mapping between true and reconstructed energy; the *effective area*, the efficiency of the instrument at detecting γ rays, typically represented by an *ideal* surface perpendicular to the photon incoming direction; and angular resolution (although angular resolution can also be obtained from real data). MC simulations reproduce the different steps real data should follow; the Monte-Carlo gamma ray is simulated through the atmosphere inducing an electromagnetic cascade, where all the secondary particles generated in the shower are traced back to ground level; second the associated Cherenkov light produced in the cascade is reflected in the mirrors towards the camera; and third, Cherenkov light reaching the camera is simulated through the electronics.
- *RAW data*: this is all the data generated each night after observation (as explained in Section 3.2.2). This is the most heavy data product (in terms of computer resources) since for each recorded event the ADC counts for each capacitor inside the RoI for both telescopes is written into disk. Data from all subsystems complementing MAGIC observations (LIDAR, weather station, starguider...) can also be considered as RAW data.
- *Calibration*: ADC counts as a function of time (from RAW data), are converted into phe. Calibration events are used in order to estimate the conversion factor.
- *Image cleaning and Hillas parameters calculation*: Image cleaning aims to keep only pixels in which Cherenkov photons from the shower produced signal, discarding those pixels that do not contain useful information of the shower image (Aliu et al., 2009; Lombardi, 2011). After the image cleaning, an ellipse is fit to the surviving pixels and the momenta of this fit (up to second order) are the so-called Hillas parameters¹⁷ used in the MAGIC analysis (shown in Figure 3.15). This process is performed for each telescope independently.
- *Stereo image parameters*: In case (as it is typically the case) of being

¹⁷ I recently learned that Micheal Hillas passed away. May he rest in peace.

observations performed in stereo mode, images from both instruments are merged into one single image (see 3.16). Events only contained in one of the telescopes (or whose parameters between both telescopes differ very much) are discarded.

- *Data Quality, γ /hadron separation and event determination:* data quality cuts are necessary to guarantee reliable results. Data quality of the events is disturbed by technical problems or bad weather conditions and can be estimated by using different indicators. Typically (and as the case of this thesis), standard data quality cuts are based on the transmission of the atmosphere at the time the event was recorded (Figure 3.2.1). Quality cuts can also be used in case of a failure or miss-fuction of any hardware/software element. Finally, every event surviving this selection is assigned an estimated energy, an estimated direction, and a parameter expressing the likeliness of the event coming from a primary gamma ray or a CR, called “hadronness” (h). This is done through a Random Forest (RF) boosted tree classification method (Albert et al., 2008b), which compares a sample of real events taken from a background control region with a MC simulated sample of gamma-ray events. As a by-product, the RF assigns each event a parameter that is a measure of the resemblance of an event to a gamma-ray induced shower ($h \rightarrow 0$) and to a hadron-induced shower ($h \rightarrow 1$). It is obvious that the MC samples need to describe genuinely the instrumental setup in order for the estimators to be accurate.
- *High level analysis:* Energy, arrival time and direction (typically ONLY) from γ ray events is used to perform studies on the VHE sky where the total exposure of the telescope for a particular FoV, is of course another important quantity. Standard byproducts in which γ -ray sources are studies are *skymaps*, *θ^2 -plots*, *flux* (or Spectral Energy Distributions (SEDs)) of *light-curve* in which the distribution of γ rays is shown as a function of the sky, angular distance w.r.t. the source center, event per unit of time and surface (or energy per unit of time and surface) and time (see Figure 3.17 for examples). In this work, for the matter of indirect DM searches, we focus on a dedicated analysis that exploits the spectral information of DM candidates, that no astrophysical counterpart could reproduce (Aleksić et al., 2012a) (explained in next section).

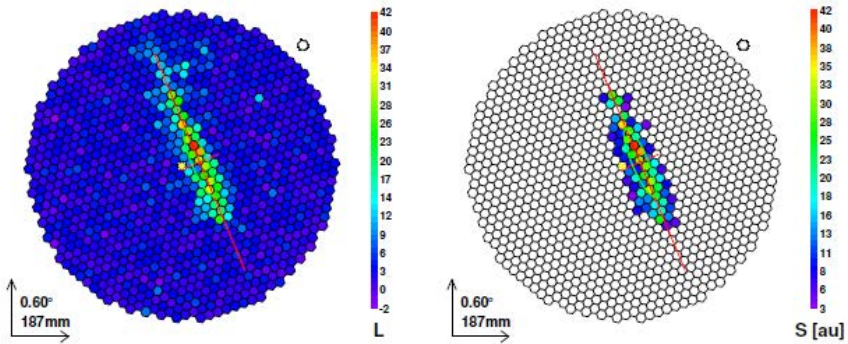


Figure 3.15: Schematic view of the Hillas parameters.

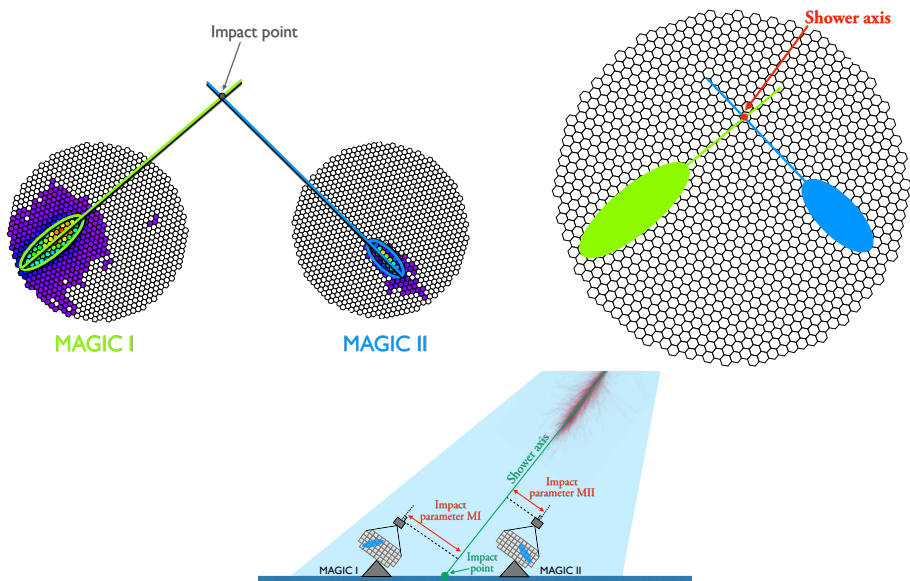


Figure 3.16: Schematic view of the Stereo parameters.

3.2.4 THE FULL LIKELIHOOD METHOD

The Full Likelihood (FL) method (FL, Aleksić et al., 2012a) is a dedicated analysis approach for indirect DM searches with IACTs. The FL analysis takes advantage of the distinct features expected in the γ -ray spectrum of DM origin, achieving better sensitivity w.r.t. the standard *ON/OFF* method. The method, used in Aleksić et al. (2014c), lead to the most stringent constraints to the annihilation cross-section of DM particles for masses above \sim TeV and was included as a reference value in the Particle Data Group (PDG) edition of

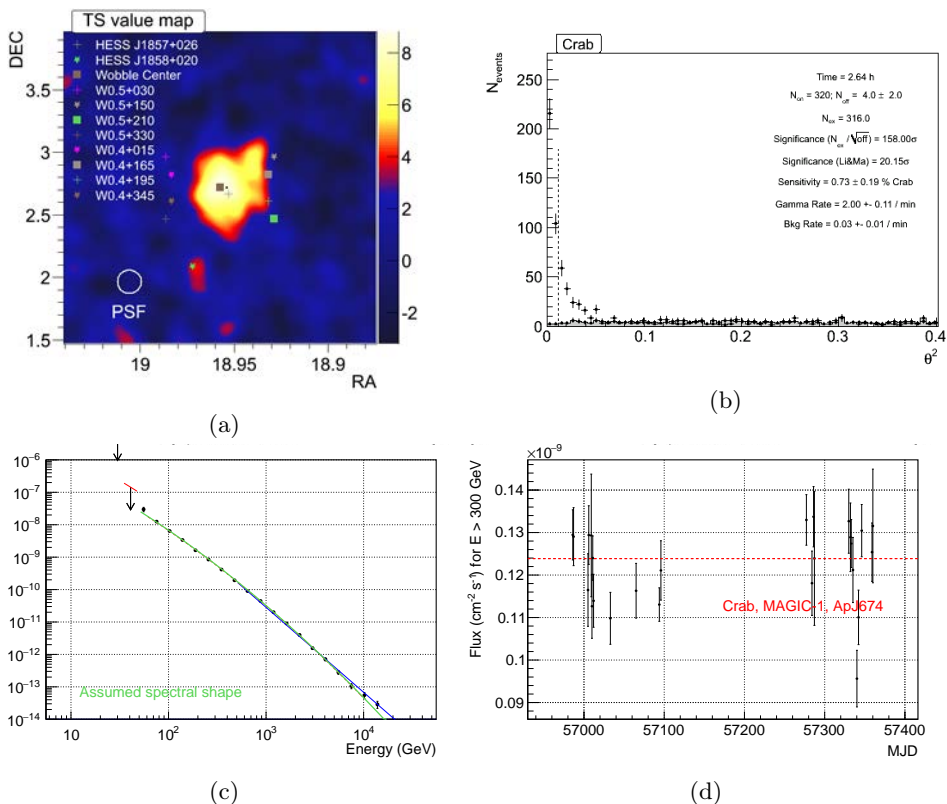


Figure 3.17: Standard analysis plot examples. (top left) shows a skyMap, the distribution of the arrival γ rays events within the observed FoV where the color-scale is associated with a test statistics of the probability of being the emission generated through background-only (the null hypothesis). (top right) shows a θ^2 -plot, the distribution of reconstructed distances of γ rays events, w.r.t. to the the position of the null hypothesis source, it is typically used to claim a discovery by integrating the number of signal events up to a certain angular region, and compare it with an only-background region. In case of a positive detection spectral (botom left) or light-curve (bottom right) analysis are performed to understand the energy and time evolution of the source.

2015. The method provides the framework for a global, sensitivity-optimized, indirect Dark Matter search, that allows the combination of the results of all Cherenkov observatories of the present generation (this also applies to data taken from the same instrument under different hardware configurations), and has been applied in the first joined analysis with Fermi-LAT (Ahnen et al., 2016b), providing the widest mass range ever explored by a single gamma-ray analysis, also included in PDG’s 2017 edition. More over, the inclusive analysis is completely generic, and can also be used to perform a global, search combining data from present and future gamma-ray and neutrino detectors.

Analytic formulas for the photon yield in these cases can be taken from (Cembranos et al., 2011). However, we preferred to computed the average γ -ray spectrum per annihilation process ($dNdE$) for a DM particles of masses between 100 GeV and 100 TeV decaying into the SM pairs previously mentioned. For each channel and mass, we average the γ -ray spectrum resulting from 10^7 decay events of a generic resonance with mass m_{DM} into the specified pairs. For each simulated event, we trace all the decay chains, including the muon radiative decay ($\mu^- \rightarrow e^- \bar{\nu}_e \nu_\mu \gamma$), not active in PYTHIA by default), down to stable particles (see Figure 2.19).

The likelihood method is used on the estimation of model parameters that can describe a set of independent data. The conventional likelihood explores the existence of an astrophysical source based on Poissonian variables, i.e. number of detected events in the ON region (n) and number of detected events in the background region(s) (m). Thus, one can obtain the number of gamma rays (g) and background events (b) in the ON region by maximizing the likelihood function (\mathcal{L}):

$$\mathcal{L}(g, b|n, m) = \frac{(g+b)^n}{n!} e^{-(g+b)} \times \frac{(\tau b)^m}{m!} e^{-\tau b} \quad (3.3)$$

where τ is the normalization between the ON and the background region (which in can be computed as the ratio of γ -like events recorded in ON/OFF within a region outside the region of interest, and equal instrument acceptance). The FL increases the sensitivity by assuming the spectral shape of the source beforehand:

$$\mathcal{L}(g, b|n, m) = \frac{(g+b)^n}{n!} e^{-(g+b)} \times \frac{(\tau b)^m}{m!} e^{-\tau b} \times \prod_{i=1}^{n+m} \mathcal{P}(E_i) \quad (3.4)$$

where \mathcal{P} is the Probability Density Function (PDF) of the event i with measured or estimated energy E_i .

The binned version of Equation 3.4 (for annihilating DM) can be written as:

$$\begin{aligned}
 & \mathcal{L}(\langle\sigma v\rangle; \boldsymbol{\nu} | \mathcal{D}) \\
 = & \mathcal{J}(J | J_{\text{obs}}, \sigma_J) \\
 & \times \prod_{i=1}^{N_{\text{samples}}} \mathcal{T}(\tau_i | \tau_{\text{obs},i}, \sigma_{\tau,i}) \\
 & \times \prod_{j=1}^{N_{\text{bins}}} \left[\frac{(g_{ij}(\langle\sigma v\rangle) + b_{ij})^{N_{\text{ON},ij}}}{N_{\text{ON},ij}!} e^{-(g_{ij}(\langle\sigma v\rangle) + b_{ij})} \times \frac{(\tau_i b_{ij})^{N_{\text{OFF},ij}}}{N_{\text{OFF},ij}!} e^{-(\tau_i b_{ij})} \right]
 \end{aligned}$$

where

$$\begin{aligned}
 \boldsymbol{\nu} &= \{b_{ij}\}_{i=1,\dots,N_{\text{samples}}; j=1,\dots,N_{\text{bins}}} \\
 \mathcal{D} &= \{N_{\text{ON},ij}, N_{\text{OFF},ij}\}_{i=1,\dots,N_{\text{samples}}; j=1,\dots,N_{\text{bins}}}
 \end{aligned} \tag{3.5}$$

where the index i refers to all independent sets of data, and j -th to the estimated energy bin. The nuisance parameters are collectively referred to by $\boldsymbol{\nu}$ and \mathcal{D} are the datasets; g_{ij} and b_{ij} are the estimated number of signal and background events respectively; $N_{\text{ON},ij}$ are the number of observed events in the ON region and $N_{\text{OFF},ij}$ is the number of observed events in the corresponding OFF bin; \mathcal{J} is the likelihood for the J -factor; \mathcal{T} is the likelihood function for τ_i (the OFF/ON acceptance ratio), parameterized by a Gaussian function with mean $\tau_{\text{obs},i}$ and variance $\sigma_{\tau,i}^2$, which includes statistical and systematic uncertainties. We consider a systematic uncertainty for to the parameter τ_i , $\sigma_{\tau}^{\text{sys}} = 0.015\tau_{\text{obs},i}$, added in quadrature to the statistical one. This value has been established on the base of a dedicated performance study (Aleksić et al., 2016a).

b_{ij} , J and τ_i are nuisance parameters, whereas g_{ij} depend on the free parameter $\langle\sigma v\rangle$ through:

$$g_{ij}(\langle\sigma v\rangle) = T_{\text{obs},i} \int_{E'_{\text{min},j}}^{E'_{\text{max},j}} dE' \int_0^{\infty} dE \frac{d\phi(\tau)}{dE} A_{\text{eff}}(E)_i G(E'|E)_i, \tag{3.6}$$

Where $T_{\text{obs},i}$ is the total observation time, E and E' , the true and estimated gamma-ray energy, respectively, and $E'_{\text{min},j}$ and $E'_{\text{max},j}$ the minimum and maximum energies, respectively, of the j -th energy bin. Finally, A_{eff} is the effective collection area and G the probability density function of the energy estimator, both computed from a MC simulated gamma-ray dataset (following the spatial distribution expected for DM-induced events, see Chapter 5).

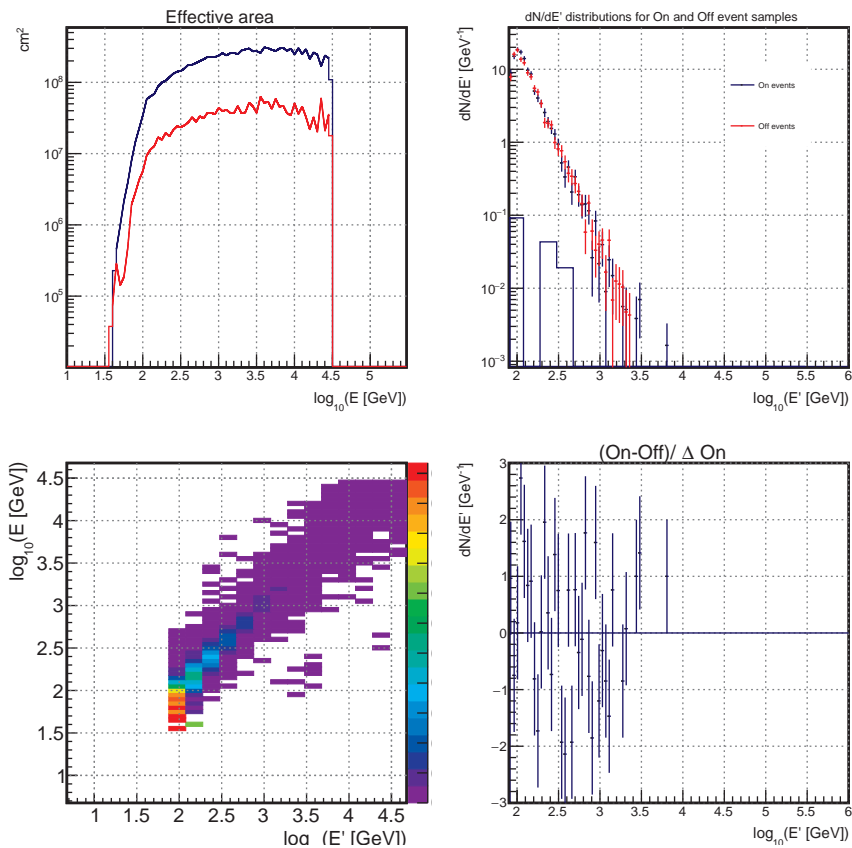


Figure 3.18: FL sample inputs: (top and bottom left) effective area (A_{eff}) for ON and OFF region (blue and red line respectively, in units of cm^2) and migration matrix (G) computed from MC events, (top and bottom right) dN/dE' and relative difference of events after cuts in ON and OFF regions. dN/dE' for foreground emission (if considered in the likelihood, solid line).

The data inputs for the likelihood are the number of events detected in the ON, and OFF regions for the different bins in estimated energy (after all analysis cuts), plus the IRF computed from the tailored MC for the specific observation period (see Figure 3.18). The null hypothesis as given by $g_{ij} = 0; \forall i, j$. The test hypotheses ($g_{ij} > 0$) are built considering the flux computed using Equation 2.8 *and* under the hypotheses of different pure DM decays. Following Ahnen et al. (2016b), we make a model independent search where using the PYTHIA simulation package version 8.205 (Sjöstrand et al., 2015), we model the gamma-ray DM emission. We compute the average gamma-ray spectrum per decay process (dN/dE) for a DM particles decaying into the SM pairs. For

each channel and mass, we average the gamma-ray spectrum resulting from 10^7 decay events of a generic resonance with mass m_{DM} into the specified pairs. For each simulated event, we trace all the decay chains, including the muon radiative decay ($\mu^- \rightarrow e^- \bar{\nu}_e \nu_\mu \gamma$), not active in PYTHIA by default), down to stable particles (see Figure 2.19).

From Equation 3.5 we define the profile likelihood ratio as,

$$\lambda_P(\langle\sigma v\rangle|\mathcal{D}) = \frac{\mathcal{L}(\langle\sigma v\rangle; \widehat{\nu}|\mathcal{D})}{\mathcal{L}(\widehat{\langle\sigma v\rangle}; \widehat{\nu}|\mathcal{D})}, \quad (3.7)$$

where $\widehat{\langle\sigma v\rangle}$ and $\widehat{\nu}$ are the values maximizing \mathcal{L} , and $\widehat{\nu}$ the value that maximizes $\mathcal{L}(\langle\sigma v\rangle; \widehat{\nu}|\mathcal{D})$. Upper limits in $\langle\sigma v\rangle$ at 95% Confidence Level (CL) ($\langle\sigma v\rangle^{UL}$) are given for:

$$-2 \ln \lambda_P(\langle\sigma v\rangle^{UL}|\mathcal{D}) = 2.71. \quad (3.8)$$

We compute $-2 \ln \lambda_P$ vs. $\langle\sigma v\rangle$ for the range of $\langle\sigma v\rangle$ fulfilling $-2 \ln \lambda_P(\langle\sigma v\rangle) \leq 2.71$. For each considered $\langle\sigma v\rangle$, the values of the nuisance parameters are found using the Migrad algorithm included in the ROOT package¹⁸.

Everything said in this Section is **also** valid for decaying DM if $\langle\sigma v\rangle \rightarrow 1/\tau_{DM}$, where τ_{DM} is the decay life-time of the DM particle (note that the likelihood goes linear with $1/\tau_{DM}$).

3.3 THE FUTURE CHERENKOV TELESCOPE ARRAY (CTA)



Figure 3.19: Animation of the CTA North array observatory at LP. Picture also show real images of the MAGIC telescopes. Picture taken from <https://www.cta-observatory.org>.

The Cherenkov Telescope Array (CTA) is the next generation ground-based observatory for γ -ray astronomy at VHE. With more than 100 telescopes located

¹⁸Available at <http://root.cern.ch>

in the northern and southern hemispheres, CTA will be the world's largest and most sensitive high-energy gamma-ray observatory (see Figure 3.19). CTA will improve the performance of the current IACTs abruptly: CTA is expected to reach an angular resolution of $< 0.1^\circ$ for most of the energies, with an energy resolution of 10–15%, a wide FoV of 8-10° and a ten times better sensitivity (see Figure 3.20). All these improvements, along with the huge energy range

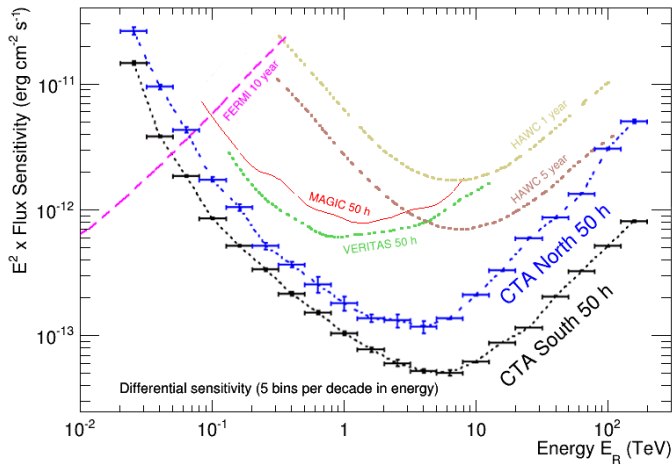


Figure 3.20: **(Figure taken from <https://www.cta-observatory.org>)** CTA sensitivity curves. Differential energy flux sensitivity of CTA compared to the existing gamma-ray instruments. The sensitivity curves for the Northern (blue points) and Southern (black points) hemisphere arrays are shown separately for 50 hours of observations.

covered, will allow CTA to expand the current knowledge on several scientific subjects (Acharya et al., 2017), which can be encompassed into three categories:

1. Study the origin of CRs: We aim to delve into how and where particles are accelerated and how they propagate within the Universe.
2. Explore extreme particle acceleration: CTA will allow us to probe extreme environments, to study in detail processes happening close to black holes, within relativistic jets or winds. Thus, we will understand better the mechanisms working behind different sources such as pulsars, plerions or microquasars.
3. Study the physics frontiers: with such low energy threshold, our goal is to shed light on the nature of DM and its distribution and get deeper into physics beyond the DM.

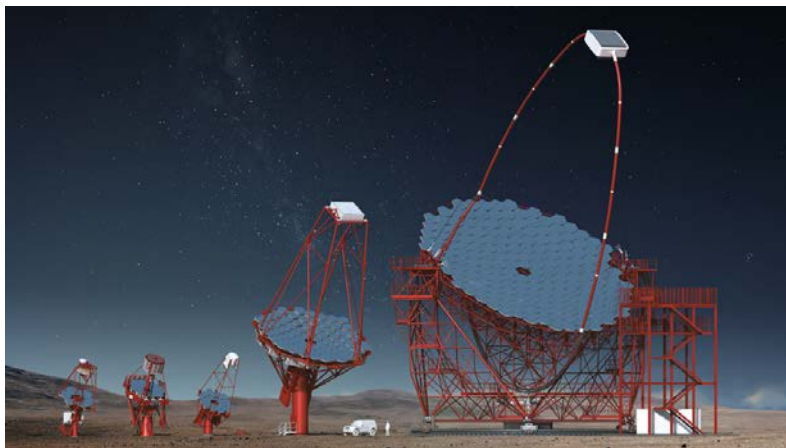


Figure 3.21: CTA prototypes designs. *From left to right:* Three different SST, MST and LST. Picture taken from <https://www.cta-observatory.org>.

CTA telescopes are expected to be distributed between two observatories, one on the Northern and one on the Southern hemispheres. The Northern array will be located in La Palma (LP), at El Roque de los Muchachos along with the MAGIC telescopes. The Southern one is expected to be placed in the Paranal Observatory (Chile). CTA will operate three different kind of IACTs, according their sizes they are commonly referred as, Large Size Telescope (LST), Medium Size Telescope (MST) and Small Size Telescope (SST) (see Figure 3.21).

Figure 3.22 shows the different telescope type contributions to the over-all differential sensitivity of CTA. LSTs govern the low energy range below 100 GeV. MSTs dominate in the CTA core energies, up to 5 TeV, where SSTs start to monopolize performance. We saw in Figure 2.19 how, photon spectra from WIMP particles with masses within GeV – TeV range, annihilating (or decaying) into SM particles is expected to peak around the \sim GeV range, or lower energies, thus the LST dominates the CTA sensitivity for *standard* WIMP searches.

3.3.1 LARGE SIZE TELESCOPE

The LST telescope (Collaboration, 2016) is designed to achieve the lowest energies, down to 20 GeV. The LST is collaborative effort of more than 100 scientist from eight countries (Brazil, France, Germany, India, Italy, Japan, Spain and Sweden). The planned baseline for CTA includes 4 LST in each hemisphere. Each LST has a parabolic reflector of 23 m diameter held by a tubular structure made of carbon fiber and steel tubes. The light-structure,

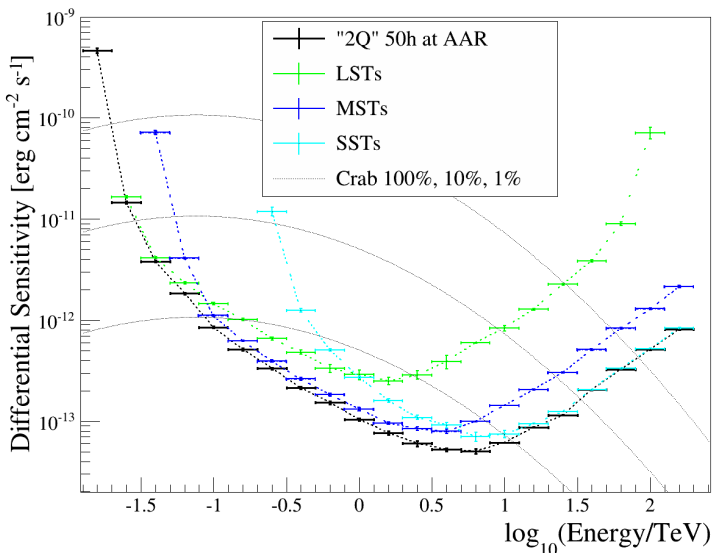


Figure 3.22: (figure by Hassan et al., 2016) Different telescope type contributions to the over-all differential sensitivity of CTA-S candidate layout “2Q”, simulated at the Namibian site (50 hours, north/south pointing average). LSTs govern the low energy range below 100 GeV. MSTs dominate in the CTA core energies, up to 5 TeV, where SSTs start to monopolize performance.

despite its 45 m height, allows the telescope to re-point within 20 s. The LST camera weight less than two tons and it is composed by 1855 0.1° FoV PMTs, grouped in 265 clusters, that provides a total FoV of 4.5° . In very *vague* words, the LST is the big brother of MAGIC where the design on structure, camera and readout have been based. The main difference relies on the trigger system where, as opposed to the MAGIC case, all the trigger subsystem has been integrated inside the camera¹⁹. This is a requirement of the CTA observatory, in order to operate in stereo mode with a large number of telescopes several hundred of meters away one from each other. The first LST prototype (LST1) is expected to be fully installed in LP by mid-2018 and constructions on the structure have already started (see Figure 3.23). Once the structure construction is finished the camera will be installed, a project that Institut de Física d’Àltes Energies (IFAE) has been involved.



Figure 3.23: Picture taken on 4th of December from LP by **Javier Herrera**. It was taken during the LST1 operation of lifted the mirror dish on top of the understructure.

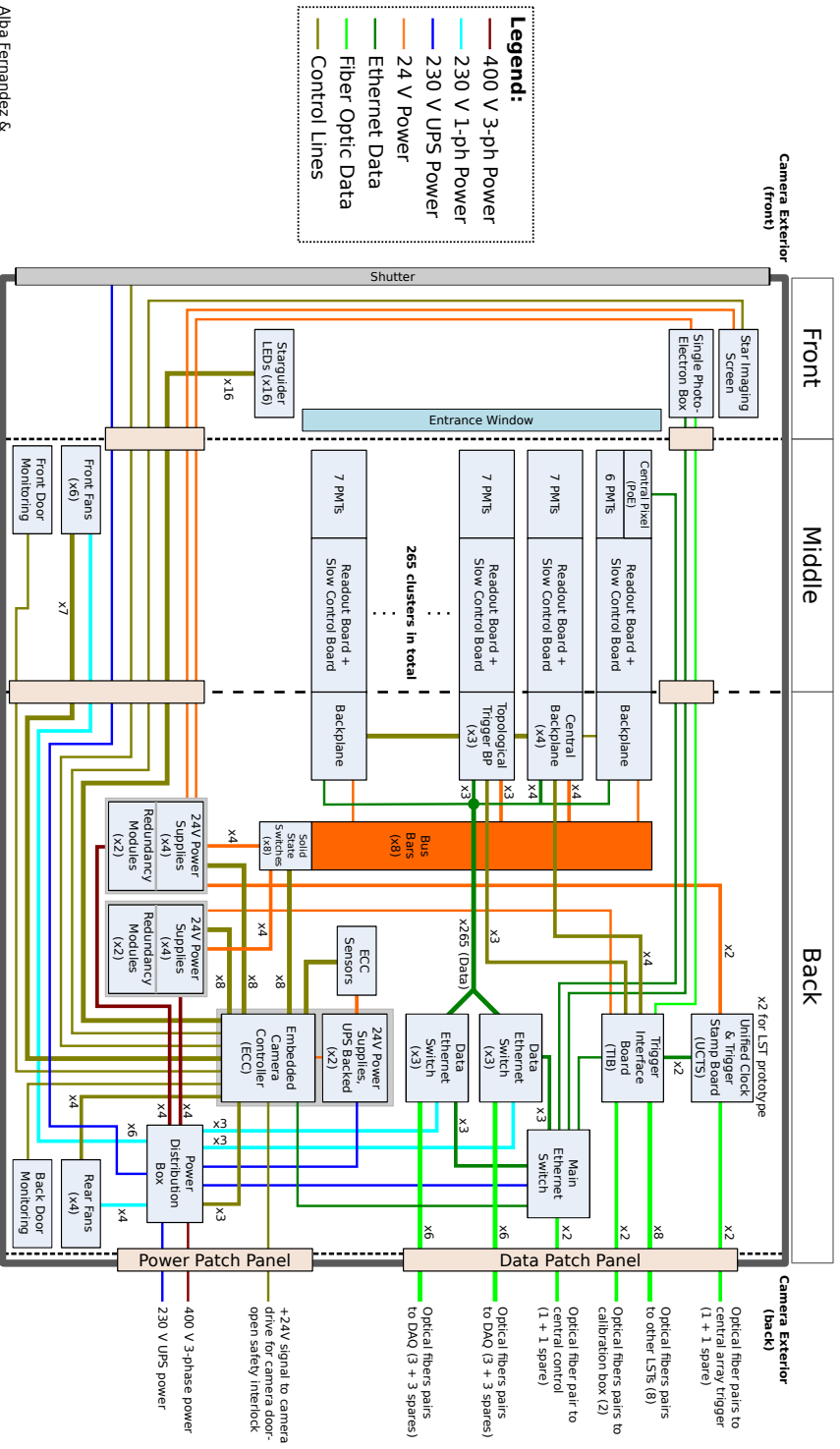
LST1 CAMERA

Figure 3.24 shows the electrical diagram of the LST camera. The different cabling needed to connect and power all subsystems is classified in seven types, labeled in the image (Fernández-Barral, 2017). The camera itself can be split into three sections: *front*, *middle* and *back*.

Front part of the LST camera This is the outer part of the camera, the one in contact with the environment. The most external component is the shutter or lid, which prevents light from entering in the camera, protecting this way the PMTs from the daylight. In addition, it provides protection against adverse environmental conditions, such as rain, during the day. The goal of the entrance window, placed after the shutter, is to protect the instrumentation from any aggression (rain, dust, e.g.) during observational time.

Middle part of the LST camera The *middle* part of the camera encompasses the 265 clusters, where the trigger and readout take place. Figure 3.25 shows a cluster, where all parts are identified. Each cluster is formed by 7 Hamamatsu PMTs, to which light guides are attached. The output signal of each PMT is preamplified with low noise by the Pre-Amplifier for the Cherenkov Telescope Array (PACTA), an Amplification-Specific Integrated Circuit (ASIC) designed by the ICC-UB group. Two differential paths form

¹⁹ Remember magic PMT signal is transported through optical fibers up to the CH, where the trigger logic is applied.



© Alba Fernandez & Scott Griffiths, IFAE 2016

Figure 3.24: (Figure by Fernández-Barral, 2017) Electrical diagram of the LST camera. The camera is divided into *front*, *middle* and *back* parts. The cabling used for different purposes is highlighted with different colors and its functionality is shown in the legend.

Last Revised: 2016/06/10

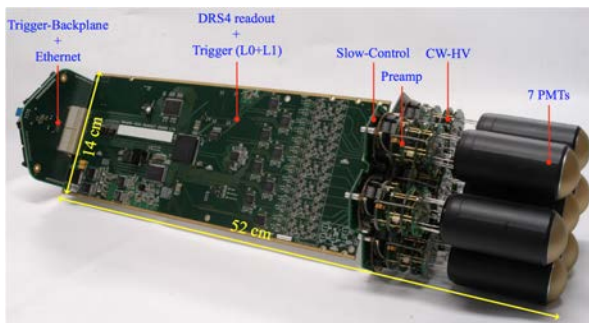


Figure 3.25: LST module with all components highlighted: 7 photodetectors, followed by the HV chip and the preamplifier (PACTA), the Slow Control board, *Dragon* board in which L0+L1 mezzanine is attached (the trigger board is connected to the opposite side of the board seen in the image) and finally the backplane where the Ethernet switches are placed.

the output of PACTA: the low-gain and the high-gain branch. The PMTs are connected to the readout board through the Slow Control Board (SCB). This device controls the HV of the detectors and monitors different parameters as the Direct Current (DC) current, temperature or humidity. Thus, the signal from the seven channels (one for each PMT) enters in the readout board, which in the case of the LST is called *Dragon*. Each signal is replicated to reach both readout and trigger subsystems. To the trigger board (L0+L1 mezzanine) only a copy of the high-gain paths are sent. The L0+L1 mezzanine is a unique Printed Circuit Board (PCB) board composed by the connectors and the corresponding L0 and L1 ASIC, on charge of the main functionality (as accommodate the signal and take the trigger decisions). Two trigger options are available: the sum trigger and the majority trigger.

In the sum trigger signals above a certain threshold are clipped to avoid using spurious signals, like After Pulses (APs). After clipping, signals from the seven channels are summed, which corresponds to the L0 output. On the other hand, the majority trigger discriminates the signals of each pixel according to a specific threshold. If the signal overpasses that threshold, a square signal is issued. The emitted signals for each channel are added and the result would constitute the output of the L0. The output of the L0 decision is sent to the L0 fan-out, placed in the backplane board (located already in the *back* part of the camera, see Figure 3.24). From there, the L0 output is sent to the six neighbouring clusters and, in turn, it receives the L0 signals from those clusters. Thus, these six signals along with the one of the own cluster is sent to the L1 part of the trigger mezzanine. At the L1 level, a selected

combination of L0 signals is compared to a threshold, if the sum of the signals overcomes the threshold, the L1 ASIC a signal is sent to the L1 distribution subsystem (also placed in the backplane). This signal is then transmitted to the Trigger Interface Board (TIB) where command is sent to the other backplanes to start the readout at the front-end electronics. The signal from each channel is saved in a buffer formed by four DRS4 chips (with 1024 capacitors each). The transmission of the data is then performed by Ethernet cables controlled by a Field Programable Gate Array (FPGA) situated in the *Dragon*. All the 265 modules are placed in a metallic structure prepared at Centro de Investigaciones Energeticas Medioambientales y Tecnologicas (CIEMAT).

Back part of the LST camera As seen before, the backplanes and the TIB are placed in this section of the camera. The backplanes are then the connection between the modules and the rest of the subsystems, a part from connecting all modules together: both the 24 V DC Power Supply Unit (PSU) and the Ethernet connection are provided through the backplanes.

Part II

Technical Work

Chapter 4

DATA MANAGEMENT AT PIC: *ToMaRe*

This project has been done in collaboration with P. Cumani and J. Delgado

4.1 INTRODUCTION

MAGIC RAW data taken from LP are processed into different higher level product data (Calibrated, Star, SuperStar, ...) which are lighter in terms of computer storage but meaningful in terms of physics, from where high-level analysis are produced. The processing of this RAW data takes place in computer facilities in La Palma, after each night of observations, and is handled by the On-Site Analysis (OSA) team. OSA processed data are transferred to Port d'Informació Científica (PIC) however, it can happen, due to for example a bug or a change in a process scheme, that data needs to be reprocessed afterwards. This reprocessings can affect large samples of data where, the Tool for Massive Reprocessing (ToMaRe) (Palacio et al., 2015, ¹) developed during my thesis, uses big data and parallel computing skills to deal with large datasets to deal with it. If required, the newly processed data are transferred to the MAGIC data base and made available to all MAGIC members, otherwise, data is downloaded only fore those interested members.

4.2 CODE USAGE

ToMaRe is composed by a complex structure of codes, and GRID accesses and permissions however, the execution of the reprocessing can be executed and monitored through very limited number and user friendly scripts. All the

¹Internal document from the MAGIC Collaboration

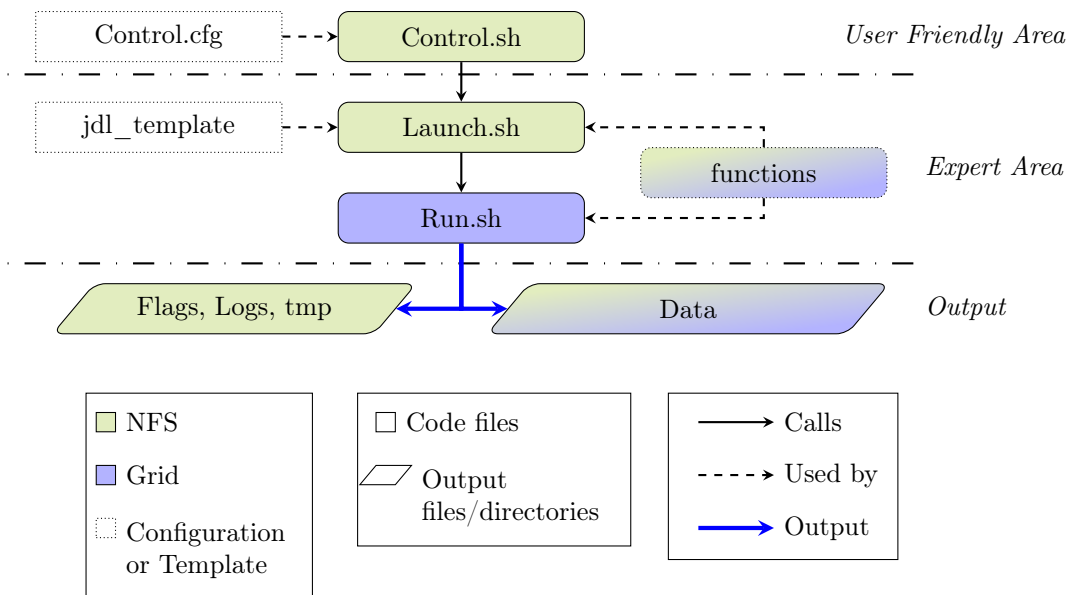


Figure 4.1: Flow diagram of the reprocessing code. The green boxes refer to processes run, or directory created, in NFS. The blue boxes refer to processes run, or directory created, in Grid. The *functions* box refers to the files *functions.sh* and *copy2dCache.sh*. The user friendly area refers to the file that are used directly by the user, while the expert area comprises all the other files used by tool. **Credit to P. Cumani.**

settings of the data to be processed can be determined through a configuration file (*Control.cfg* in Figure 4.1, where data periods, sources, telescopes or data products can be specified (as well as software versions). The processing is activated by calling *Control.sh* (in Figure 4.1), that will check that the user has the correct permissions, or to operate in GRID environment, and will split the data into small, individual, complete autonomic jobs, that will be send. Each job evolution is tracked through in two ways: 1) a *flag* file us automatically generated and updated “life” while the job is running where the job status is shown; 2) A detailed *Log* file is generated before the job is exit, useful mainly for debugging. Once all jobs are finished, data has been either transferred to the MAGIC database or copied into a local path. Some extra scripts, provided by ToMaRe can be used to monitor and centralize the outcome of each jobs into one single file, in order to verify the good processing of the whole data sample.

4.3 CODE STRUCTURE

The code is written to be modular and easy to expand. A flow diagram of the whole reprocessing code is shown in Figure 4.1. The *Control.sh* file:

- checks for observations in the indicated period of the possibly indicated sources.
- creates the *Logs* directory and the *Data* directory in local directory (the latter only in the case of *moveToGrid* equal 0) and the launcher log file,
- calls the appropriate launcher, depending on the choice of the process indicated in the configuration file.

The launcher:

- creates the *Flags* and *tmp* directories, as well as the sequence file, the flag file and the telescope/run specific log file,
- creates the proper *.jdl* file from the template, containing the executable (the *Run* file), and the sequence and functions files,
- launch one job per run number in Grid.

The *Run(process)* files are the ones actually executed in grid, where “process” is a MARS standard executable. The code starts by copying the input data files from Grid to the node in which the job will run. The *process* is then run on these files. The files created by the *process* (both the data and the summary ROOT file) are then copied either in the MAGIC data base or in a local storage (depending on the settings).

Most of the common functions between the two processes are collected in the *functions* (functions with different purposes) and *copy2dCache* (functions related to the copying processes) files. For this reason, the two files are also copied to Grid to be used by *Run(process)*.

Several checks are performed in all the parts of the process. If the check fails, it can result in a warning or an error, either fatal or not. In both cases a message is printed in the flag and the log file. In the case of a warning the process continues normally whereas in the case of a fatal error the process is stopped and the output up to the error is copied into the log and flags file before exiting the program.

Finally, a summary of the numbers of job run and the errors and warnings issued by the process can be accessed, where the code checks all the files present in the Logs and Flags directories. In the output directories there should be present only the log and flag files produced by the last call of *Control.sh* *Control.cfg*. If this is not the case, the number of jobs, warnings and errors will comprise also all the results of the previous calls of the program. If the total number of job ID in the launcher file is different from the number of flags file in the output directory (either because one of the file has been deleted or the code was run twice with two different configuration files) a warning is issued.

4.4 CONCLUSION

ToMaRe has already proven to be very helpful (almost a requirement) in order to address two major issues reported on the MAGIC data base during the last years. In a near future, once the MAGIC stops operation, ToMaRe's approach of accessing MAGIC data will become very relevant for two reasons: The first one being that sooner or later MAGIC analyzers will migrate to newer and more sensitive instruments (as CTA), and the number of people with knowledge on MAGIC analysis details could be largely reduced. ToMaRe can be used as a repository of knowledge on analysis details and software to be kept for the future; Secondly, and following in the same direction, the capability of reproducing MAGIC results in an automatic and fast procedure, allows to reproduce all current MAGIC results, reducing the current required data storage to maintain by the MAGIC collaboration. If required, MAGIC data could be re-analyzed in order to search for new signals undetected during MAGIC era. This feature is going to be very relevant for the future conversion of MAGIC data into the standard format of γ ray astronomy, typically known as Data Level 3 (DL3)².

²<http://gamma-astro-data-formats.readthedocs.io/en/latest/general/index.html>

Chapter 5

THE DONUT MC: POINT-LIKE VS EXTENDED MC SIMULATIONS

*This project has been done in collaboration with M. Vazquez-Acosta and J. Rico.
Special thanks to M. Vazquez-Acosta for having one of the main ideas behind the project.*

5.1 INTRODUCTION

IRFs of IACTs are usually evaluated by means of MC simulations (Majumdar et al., 2005; Carmona et al., 2007). For many practical purposes, it is enough to evaluate IRFs for point-like γ -ray sources. However, IRFs depend in general on the relative arrival direction of the γ ray with respect to the telescope pointing direction¹. This means that the evaluation of IRFs for extended sources of arbitrary shape would in principle need a simulation of a γ - ray sample with arrival directions distributed following the particular source morphology. This morphology is expected to be very different from source to source (e.g.: the diffuse emission of the Milky Way plane (Ackermann et al., 2017; Ahnen et al., 2017a), nearby supernova remnants (Flinders, 2016; Aliu et al., 2014) or the expected gamma emission from DM halos (Aleksić et al., 2014c; Palacio et al., 2016b)). In order to compute the IRF applicable to the study of these sources, while making an efficient use of the computing resources devoted to MC simulations, we have developed a method, which we dub *donut MC*, that is described and characterized in here.

¹ This is the case when observations are performed in *wobble mode*.

5.2 MAGIC MC PRODUCTIONS

MAGIC observations of point-like sources are typically carried out in wobble mode, i.e. with the telescope pointing successively at two or more directions at a certain distance w (the wobble distance, typically in MAGIC $w = 0.4^\circ$) away from the source position. The corresponding IRFs are computed using the so-called *point-like MC*, which consists of γ rays simulated with true directions uniformly distributed in a ring centered at the telescope pointing direction and a radius of w (see Figure 5.1, left) to cover for all possible orientations between the pointing direction and the source position. Figure 5.2 (left) shows the distribution of true directions for simulated events from the point-like MC, where $w = 0.4$ [deg]. For each event, we define d as being the angular distance between the true direction and the center of the FoV. We also define θ as reconstructed distance of the event, the angular distance between the true and reconstructed directions. For the point-like MC, $d = w$ by construction.

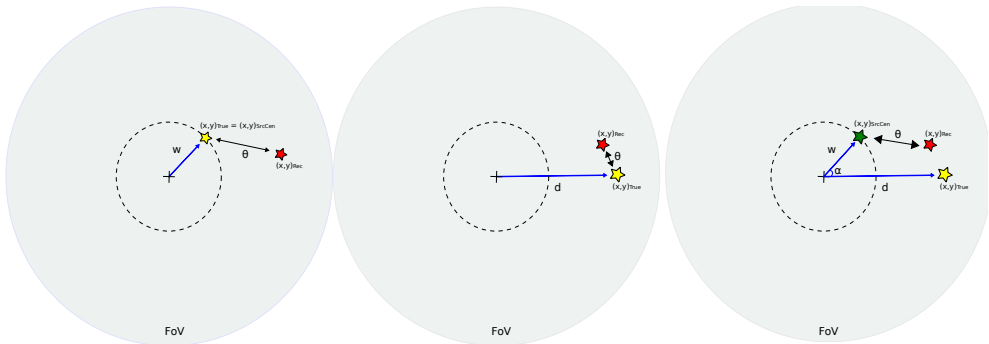


Figure 5.1: Definition of variables for point-like MC (left), diffuse MC (center) and Donut MC (right). For point-like, source center and true direction are the same, both being on top of a ring at a distance w w.r.t. the center of the FoV. For diffuse MC true direction can be anywhere within the FoV, while no source center is defined (could be anywhere since the extension of the source is not defined). For the donut MC, the distribution of true directions w.r.t the source center follows one of \mathcal{P} , where the source center is defined on top of the w -ring. See text for details.

Extended sources, on the other hand, do not have a well defined source position, however, the wobbling procedure is still applied by pointing the telescope w deg away from a certain direction that we call the *source center*. For evaluating the IRFs in this case, the natural procedure would be to simulate γ rays with true directions following the previously mentioned source morphology around the source center, and the source centers uniformly distributed in a ring centered at the telescope pointing direction and a radius of w . Such ded-

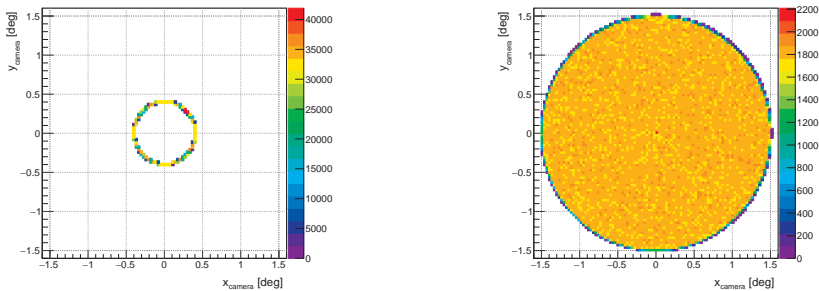


Figure 5.2: Distribution of true directions of simulated events in the point like (left) and diffuse (right) MAGIC MC productions, shown in camera coordinates. For the point-like case, this also corresponds to the distribution of the source centers.

icated MC production would demand at least as much computer resources as the point-like production, but would only be applicable for the study of a very specific morphology.

As an effective alternative, we have developed a method to select simulated events from a MC production consisting of γ rays with true directions uniformly distributed in a $\sim 1.5^\circ$ radius FoV (called *diffuse MC*, see Figure 5.2, right). We can also define, for events within this diffuse MC, the angular distance θ (see Figure 5.1, center), however this time there is no associated source center, since the extension of the source is not defined (this could be anywhere, even outside the telescope FoV). The donut selection procedure, only adds a negligible overhead to the computing-intensive process of the full diffuse MC production, which is common for all possible source morphologies, thus making an efficient use of the computing resources available to MC simulations.

We assume a circular symmetric morphology w.r.t. the source center, hereafter named the *surface brightness profile* of the source (\mathcal{P} , see Figure 5.3), were for the typical case of moderately-extended source, the distribution of true γ -ray directions resulting from our procedure has the shape resembling that of a tasty *donut* (see Figure 5.4, right), where the name of the method comes from. We describe here the procedure of donut MC selection and the consistency tests that show that our implementation actually produces the expected results.

5.3 DONUT METHOD PROCEDURE

The donut MC method is the procedure by which a new MC sample is generated, specific for the study of given \mathcal{P} , by selecting events from the diffuse MC

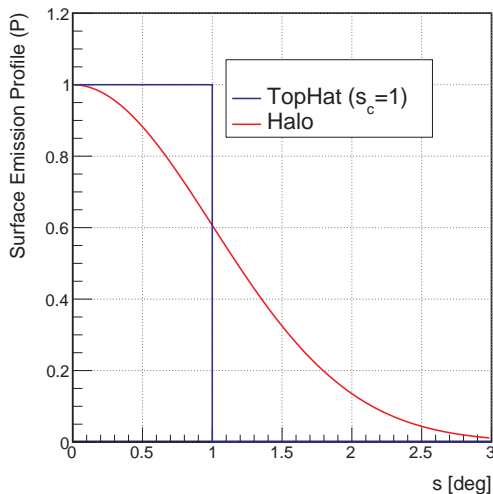


Figure 5.3: Circular symmetric relative surface brightness profile (\mathcal{P}) as a function of the angular distance w.r.t the source center (s), where the intensity of the source has been normalized to 1 at the center of the source. Two different \mathcal{P} s are shown: Halo, smoothly decreasing in intensity towards the edges of the source; and TopHat, with constant intensity up to a distance $s_c = 1$ [deg] (here named *TopHatXXX*, being $XXX \equiv X.XX$ [deg]

(see Figure 5.2 right). The method maximizes the number of selected events in the new MC sample, while keeping them statistically uncorrelated.

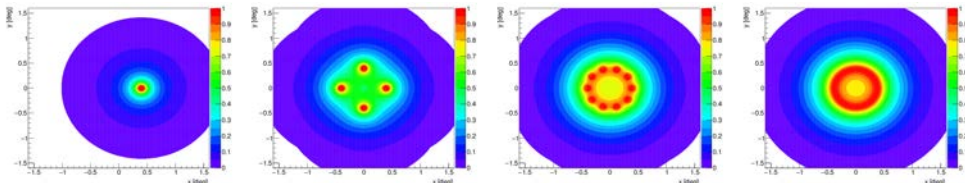


Figure 5.4: Expected distribution of γ – ray true directions for different number of source center/pointing direction orientations (from left to right: halo 1, halo 4, halo 10 and halo 100) realizations shown in camera coordinates, for a given typical radially symmetric source (\mathcal{P}). Image in the most right corresponds to the donut method joint PDF (\mathcal{D} , see main text for further explanations).

In order to understand the procedure, let us first consider a simplified version, here named *halo 1*. Starting from the diffuse MC (see Figure 5.2, right), we select events based on \mathcal{P} (halo, Figure 5.3) but only for one single, fixed, orientation between the pointing direction and the source center (see Figure 5.4, most left). If we use the *halo1* sample to compute the IRF corresponding to

the assumed \mathcal{P} , we would get the correct result, but with large statistical uncertainties, given the relative low statistics of the selected sample with respect to the original one, and only valid for one possible orientation between pointing direction and source center. We can generalize the halo 1 selection procedure for n halos (halo 4, halo 10 and halo 100 cases are shown in the right-most plots of Figure 5.4). If halo- n were constructed simply by repeating the selection procedure of halo 1, the probability of having an event, from the original diffuse DM, selected more than once, would be larger the larger the value of n .

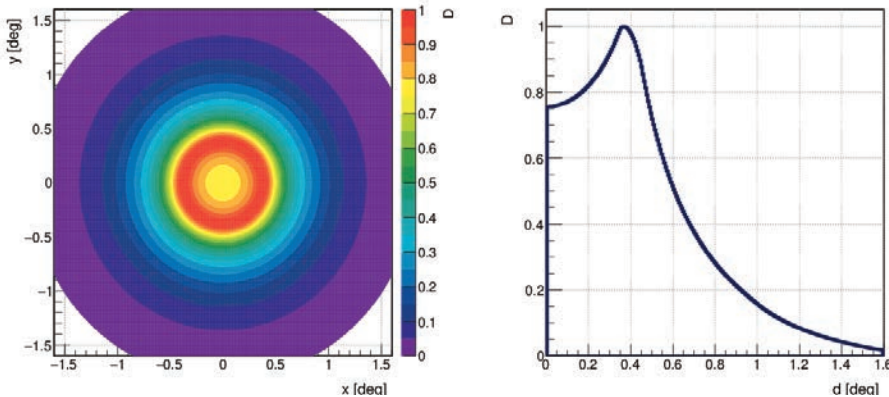


Figure 5.5: *Donut step 1* where left panel shows the distribution of true directions after of \mathcal{D} (considering \mathcal{P} and $w = 0.4$ [deg], covering all possible orientations between the pointing direction and the source center position) in cartesian coordinates (x, y) w.r.t. the FoV. Right panel shows a circular projection of \mathcal{D} as a function of the distance to the center of the FoV, where $d = 0$, corresponds to $(x, y) = (0, 0)$.

In the donut method, this problem is solved dividing the selection procedure into two steps. First, events (from the diffuse MC) are selected according to a joint probability density function (\mathcal{D}) from the convolution of all possible source center/pointing direction orientations (see Figure 5.5, left). \mathcal{D} , by construction, is circularly symmetric w.r.t. the center of the telescope FoV (see Figure 5.5, right). In a second step, selected events are associated with a source center randomly chosen from the expected w -ring such that, at the end of the selection process, all events with a common source center are spatially distributed according to \mathcal{P} (see Figure 5.6).

5.4 TESTING THE METHOD

To show that this procedure works as expected we have performed the following tests:

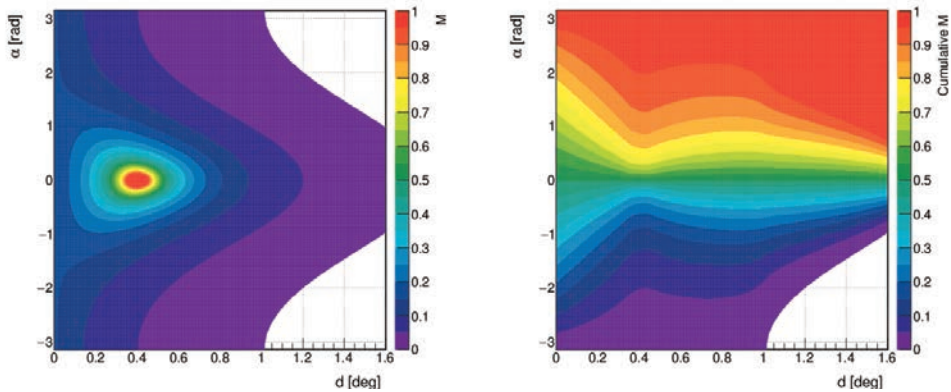


Figure 5.6: *Donut step 2* where left panel shows the joint PDF \mathcal{M} , \mathcal{P} is centered at $(w, \alpha)_{SorCen}$ and evaluated at $(d, 0)_{true}$, where $w = 0.4$ [deg]. Right panel shows the cumulative of \mathcal{M} for $\forall \alpha$. Selected γ – ray at d have a probability 1 of being assigned a source center at $(w, \alpha)_{SorCen}$, with $w = 0.4$ [deg] and $\alpha \in [-\pi, \pi]$.

- Check that the distributions of d and θ agree, within statistical uncertainty, for the halo- n and donut realizations (see Figure 5.7, right). The halo- n and donut distributions show very good agreement, and a reduction of statistical uncertainty with growing n .

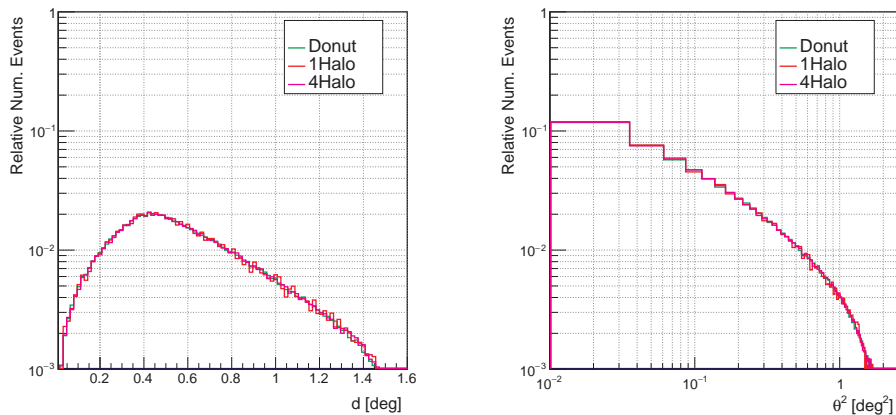


Figure 5.7: Comparison between halo 1 (red), halo 4 (pink) and donut MC (green), where left (right) plot shows the distribution of d (θ^2).

- Check that the Aeff as a function of the E agree, within statistical uncertainties, computed for halo- n and donut realizations (see Figure 5.8). The halo- n and donut distributions show very good agreement, and a reduction of statistical uncertainty with growing n .

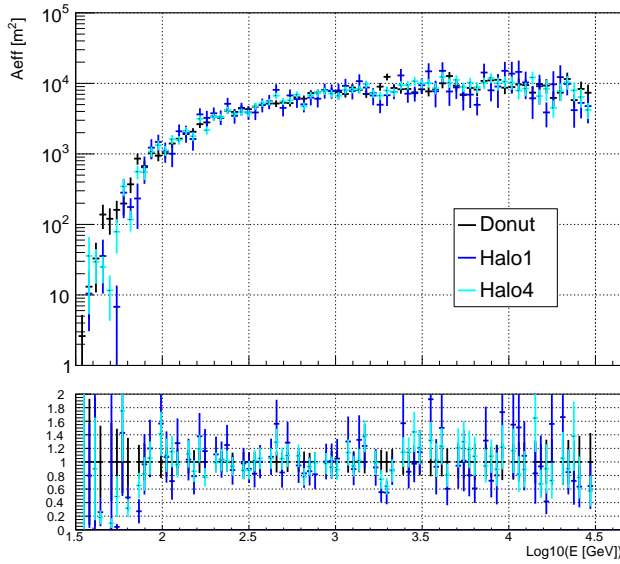


Figure 5.8: Comparison of A_{eff} vs E_{true} computed from halo 1, halo 2 and donut MC.

- We also expect the IRFs computed with the donut method to converge to those for a point like MC when we use a very narrow source morphology. In order to check this, we have produced four different donut realizations taking the expected distribution true directions morphology to be a top-hat function with radius 0.4, 0.2, 0.1 and 0.05 deg, respectively, placed at a wobble distance of 0.4 deg (TopHat in Figure 5.3). Figure 5.9 and Figure 5.10 shows the comparison of A_{eff} vs E_{true} between these four realizations compared to the A_{eff} vs E_{true} obtained from the point-like MC. Differences are smaller for smaller values of the radius, with almost perfect convergence between the 0.05 deg radius halo and the point-like MC.

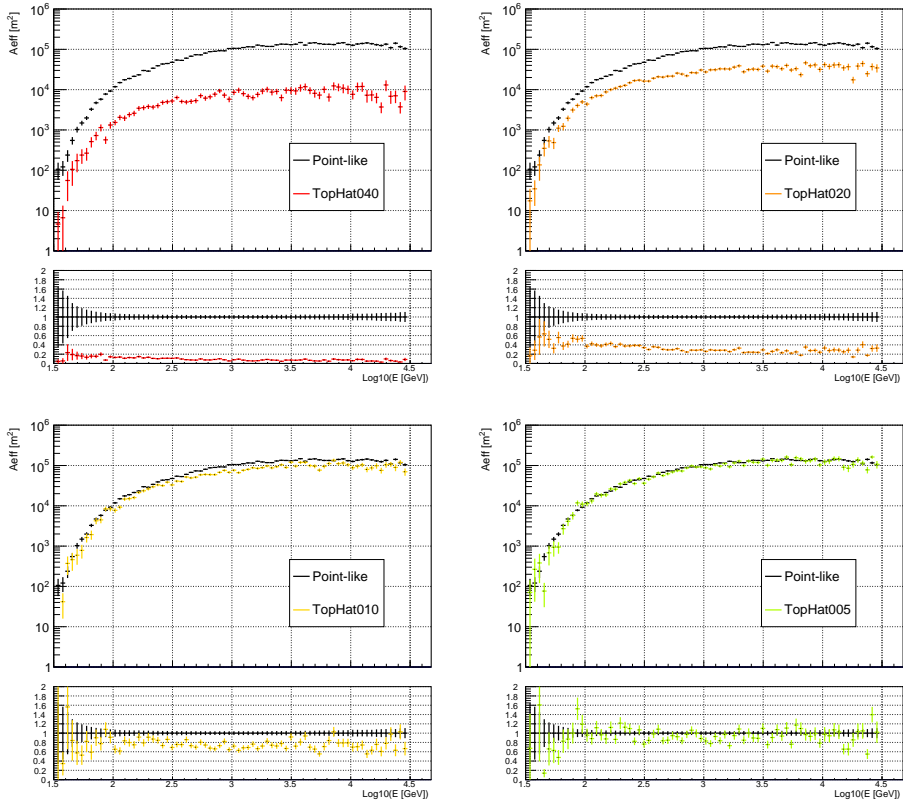


Figure 5.9: Comparison of A_{eff} vs E_{true} computed from donut realizations using top-hat profiles of 0.4, 0.2, 0.1 and 0.05 deg (from top bottom and left to right, respectively) and point-like MC.

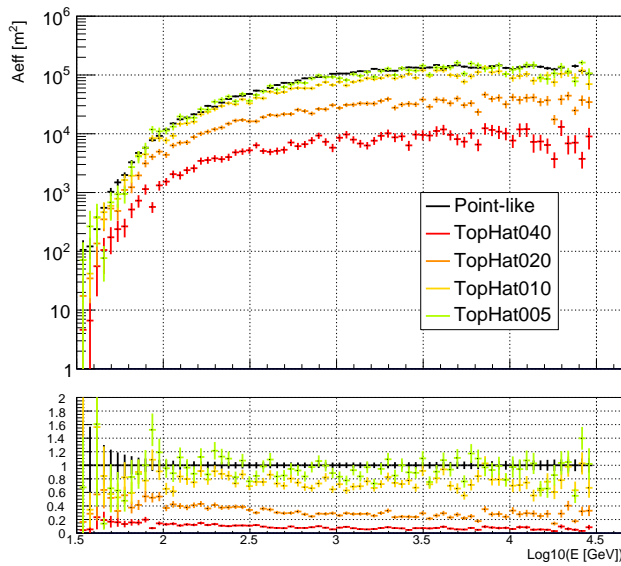


Figure 5.10: Ratio comparison of A_{eff} w.r.t. point-like vs E_{true} computed from donut realizations using top-hat profiles of 0.4, 0.2, 0.1 and 0.05 deg and point-like MC.

Chapter 6

POINTING OPTIMIZATION FOR IACTS

This project has been done in collaboration with D. Navarro-Girones and J. Rico.

We thank T. Hassan without whom this would not have been possible.

IACTs detect γ rays with energies from ~ 50 GeV to ~ 100 TeV. Their typical FoVs are of the order of the degree ($\sim 1-10^\circ$), with a decreasing off-axis performance (i.e. for increasing γ -ray arrival angles w.r.t. the pointing direction). They often operate in the so called *wobble mode*, in which the source under study is observed off-axis (by a certain *wobble* angular distance), in such a way that symmetric *signal* and *background control* regions can be derived simultaneously for a given observation.. We present a procedure to compute the optimal wobble distance and signal region for extended γ -ray sources, taking into account the off-axis instrument performance and the surface emission profile of the source. We take as study case indirect DM searches (where an a priori knowledge on the expected signal morphology can be assumed) and provide optimal pointing strategies for searches on DM from dSphs observed with current and future IACTs.

6.1 INTRODUCTION

IACTs are ground based instruments capable of detecting γ rays with energies from ~ 50 GeV to ~ 100 TeV. Observations are often performed in the so called *wobble mode*, in which the nominal pointing of the telescope has an offset w (the *wobble distance*) w.r.t the position of the source under observation (or, for moderate extended sources, w.r.t its center). Using such method, *signal* and *background control* regions (ON and OFF) within regions of equal size and instrument performance (because they are located symmetrically w.r.t the pointing direction) are observed at the same time. This makes an efficient use of the limited duty cycles of IACTs, while minimizing possible systematic differences in the acceptance for ON and OFF regions (due e.g. to atmospheric changes between ON and OFF on-axis observations). The value of w can be optimized if one takes into account that: for large wobble distances, ON and OFF are defined close to the edge of the FoV, where the acceptance decreases; while for short ones it may not be possible to define an appropriate signal free background control region. These effects become critical for moderate extended sources, as the case for instance of the expected signal coming from the DM halos of the milky way or from nearby dSph galaxies.

Here we present a procedure to optimize the wobble distance of IACTs observations taking into account the off-axis performance of the instrument and the expected spatial morphology of the source. As a study case, we focus on indirect DM searches with IACTs, where we compute the optimal values for w and the signal region size (θ_c), for a list of dSphs to be observed for current and future IACTs.

We have implemented the method in a tool that is valid to optimize the pointing strategy of a “general” IACT observing a “general” source. The tool is accessible from:

```
https://github.com/IndirectDarkMatterSearchesIFAE/
```

A release version (*V00_00*), from where the results presented here were computed, can be accessed by:

```
$ git clone https://github.com/IndirectDarkMatterSearchesIFAE/ObservationOptimization.git
$ git checkout V00_00
```

The downloaded package is provided together with tutorials in order to help acquiring the basic skills required to reproduce the results shown here. The

software is flexible and new sources (not necessary related to DM) and new instruments can be easily defined.

The rest of this chapter is structured as follows: in Section 6.2 we introduce the IACT technique and define a set of quantities that allow us to quantify the off-axis performance of an instrument; in Section 6.3 we introduce the quality factor that we use as figure of merit for the optimization of the pointing strategy; in Section 6.4 we apply the method for the case of indirect DM searches and present optimal values for w and θ_c for a set of dSphs to be observed with two different IACTs (MAGIC and CTA); finally, in Section 6.5 we briefly discuss the current status of the software, its applicability and current limitations.

6.2 OFF-AXIS PERFORMANCE

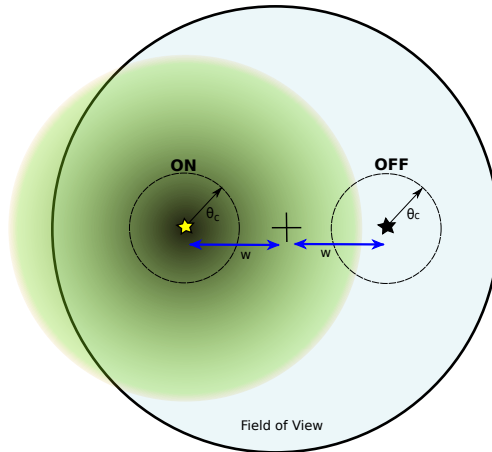


Figure 6.1: Schematic configuration of the FoV during *wobble* mode observations. The telescope pointing has an offset distance (w , w.r.t the center of the source under study (yellow star)). *Signal (ON)* is defined as a circular region around this position (with angular size θ_c). One *background control* region (circular region around OFF, black star) is defined with same angular size, symmetrically with respect to the signal region. Figure shows how, for very extended emissions (green area), signal events are also expected to be reconstructed inside OFF.

IACTs typical FoV is of the order of the degree ($\sim 1-10^\circ$). Under wobble mode operation, typically, a circular ON region is defined aligned with the center of the source under study, centered at a distance w w.r.t. the center of the FoV, with angular size θ_c w.r.t to the center of the source (see Figure 6.1). One or several OFF regions are defined within the same FoV, in such a way

that background statistical uncertainties are minimized and instrumental associated uncertainties are also kept low¹. For moderate extended sources, as the case we focus in here, only 1 OFF region is considered, with same θ_c as ON, placed symmetrically to each other w.r.t. the center of the FoV (circled ON and OFF in Figure 6.1).

Due to the optics of the instrument, IACTs have a decreasing performance at detecting γ rays reaching the edges of the FoV, w.r.t the center (the nominal pointing direction of the instrument). In order to characterize the off-axis performance of IACTs, we define the *relative acceptance* of an instrument (ϵ), as the percentage of degradation (the fraction of events that are missed) w.r.t. the performance at the center of the FoV (where it is expected to be the best). This acceptance, by construction, takes always values between 0 and 1, and can be defined as;

$$\epsilon(d) = \frac{\mathcal{R}_{\text{ON}}(d)}{\mathcal{R}_{\text{ON}}(d=0)}, \quad (6.1)$$

being \mathcal{R}_{ON} the rate of events passing all the analysis cuts (i.e. γ -ray candidates) inside the ON region, and d is the off-set distance w.r.t pointing direction (we assume ϵ to be circular symmetric w.r.t the center of the FoV). In Equation 6.1, we are implicitly assuming θ_c to be much smaller than the scale of the FoV ($\theta_c \ll 5^\circ$), otherwise, for large integration regions ($\theta_c \sim 5^\circ$), ϵ may vary from one point to another within the integration region. Identically, we could have defined \mathcal{R}_{OFF} as the rate of γ -ray candidates inside the OFF region, where Equation 6.1 would still be valid.

6.2.1 RELATIVE ACCEPTANCE (ϵ) FOR REAL IACTS

We compute now ϵ for two real instruments operating now, or in a near future: The Magic Telescopes and CTA.

THE MAGIC TELESCOPES

MAGIC is a system of two gamma-ray Cherenkov telescopes located at the Roque de los Muchachos Observatory in LP (Canary Islands, Spain), sensitive to cosmic gamma rays in the VHE domain, i.e. in the range between ~ 50 GeV and ~ 50 TeV (Aleksić et al., 2016a). MAGIC has been taking data since 2004 (with MAGIC-I), and latter on upgraded to a stereo system in 2009 (with the

¹ The response of the camera over the FoV is not perfectly homogeneous. Different wobble strategies try to minimize these effects.

construction of MAGIC-II). MAGIC core science is focused on the study of the CR origin in either galactic or extragalactic targets, but it is well-known that cosmic gamma rays constitute also a probe for several fundamental physics quests, including DM (see, e.g. Doro et al., 2013). Magic FoV is $\sim 3.5^\circ$ wide, where standard point-like observations are performed in *wobble mode*, being $(w, \theta_c)_{\text{MAGIC}} = (0.4^\circ, \sim 0.1^\circ)$.

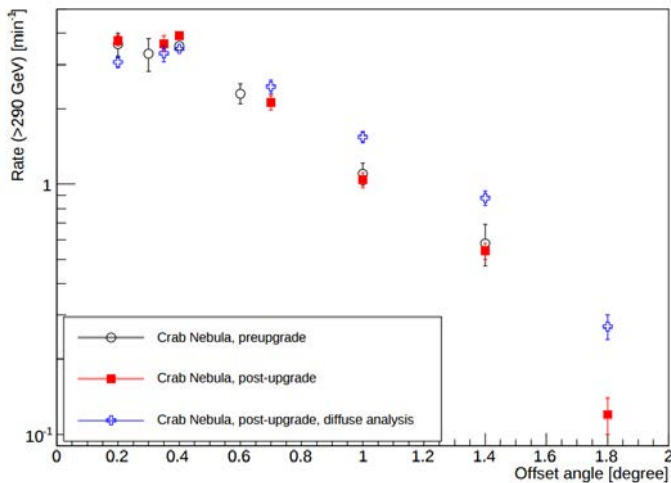


Figure 6.2: **(Figure taken from Aleksić et al., 2016a)** Crab-Nebula gamma-ray candidate rate as a function of the *Offset angle* (named after d in the text). Black empty circles: data from before the upgrade (Aleksić et al., 2012b), red filled squares: current data blue empty crosses: current data with “diffuse” analysis.

Figure 6.2 shows the rate of γ -ray candidate events detected from the direction of Crab-Nebula observed at different values of d , for three different hardware stable configurations of MAGIC. Note that each data point in Figure 6.2, corresponds to dedicated MAGIC observation on the Crab Nebula, taken in wobble mode in which $w = d$ and $\theta_c = \theta_{c,\text{MAGIC}}$. Following Equation 6.1, we compute the relative acceptance of MAGIC telescopes (ϵ_{MAGIC}) from the data from Figure 6.2 labelled as *Crab Nebula post-upgrade*, hereafter named *MAGIC Point-like*.

CTA

We also compute the acceptance for CTA (Acharya et al., 2017, CTA), the next generation ground-based observatory for γ -ray astronomy at VHE. With more than 100 telescopes located in the northern and southern hemispheres, CTA

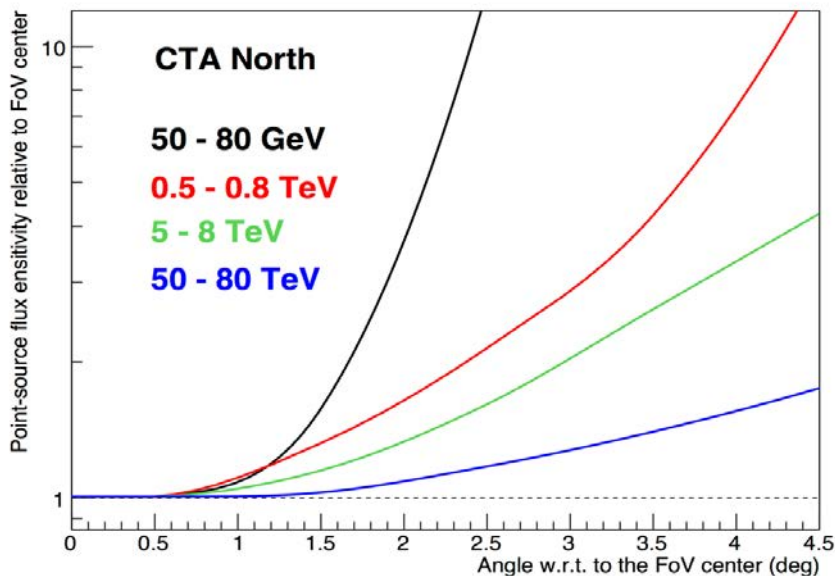


Figure 6.3: **(Figure taken from www.cta-observatory.org)**. Relative off-axis sensitivity (δ), as a function of the off-set distance (d) normalized to the one at the center of the FoV, for four different energy bins.

will be the world's largest and most sensitive high-energy γ -ray observatory. Figure 6.3 shows the relative off-axis sensitivity (δ) normalized to the center of the FoV for four different energy bins of CTA. In order to compute the relative acceptance of CTA (ϵ_{CTA})², we need to consider that δ can be written as

$$\delta(d) = \frac{\mathcal{S}(d)}{\mathcal{S}(d=0)}$$

where $\mathcal{S}(d) \propto \left(\frac{N_{\text{ON}}(d)}{\sqrt{N_{\text{OFF}}(d)}} \right)^{-1}$, (6.2)

being \mathcal{S} the sensitivity of the instrument. Based on Equation 6.2, Equation 6.1 can be re-written as:

$$\epsilon_{\text{CTA}}(d) = \frac{1}{\delta^2(d)}. \quad (6.3)$$

We focus here on the lower energy range (*CTA North 50-80 GeV*), the most relevant one for DM discovery, however the calculations are valid for all four different energy ranges.

² We are considering here ϵ of the full CTA array. In reality, CTA will be formed by IACTs of different kind, each telescope type with a possible different ϵ .

Figure 6.4 shows ϵ_{MAGIC} & ϵ_{CTA} as a function of d . We stress, based on ϵ , we cannot compare the absolute acceptances of the two instruments.

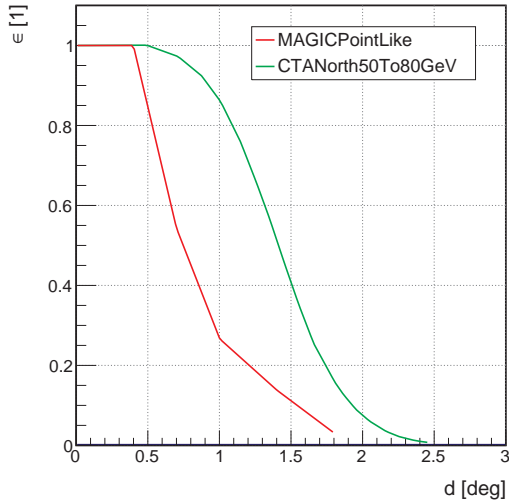


Figure 6.4: ϵ_{MAGIC} (red) and ϵ_{CTA} (green) as a function of d (see text for details).

6.3 QUALITY FACTOR (\mathcal{Q} -FACTOR)

We define a quality factor \mathcal{Q} (Q -factor) as, the number of γ rays candidates from the source under study integrated in ON divided by the square-root of the number γ rays candidates integrated in the same region coming from background. Assuming the main contribution of background to be flat along the FoV, \mathcal{Q} can be written as:

$$\mathcal{Q}(\theta_c) = \frac{\int_{\theta=0}^{\theta_c} \int_{\varphi=0}^{2\pi} \theta d\theta d\varphi \mathcal{P}(\theta)}{\sqrt{\int_{\theta=0}^{\theta_c} \int_{\varphi=0}^{2\pi} \theta d\theta d\varphi}} = \frac{\int_{\Delta\Omega_{\text{ON}}} d\Omega_{\text{ON}} \mathcal{P}(\theta)}{\sqrt{\int_{\Delta\Omega_{\text{ON}}} d\Omega_{\text{ON}}}}$$

where $d\Omega_{\text{ON}} = \theta d\theta d\varphi$, (6.4)

θ and φ are the circular coordinates w.r.t to the center of the ON region (see Figure 6.5a), \mathcal{P} is proportional to the number of γ rays from the source arriving from an infinitesimal small region ($\mathcal{P} = \mathcal{A} \cdot dN/d\Omega$ in Figure 6.6a), $\Delta\Omega_{\text{ON}}$ is the region defined by: θ between 0 and θ_c ; and φ between 0 and 2π . We fix the value of \mathcal{A} such that $\mathcal{Q}_{\text{max}} = 1$.

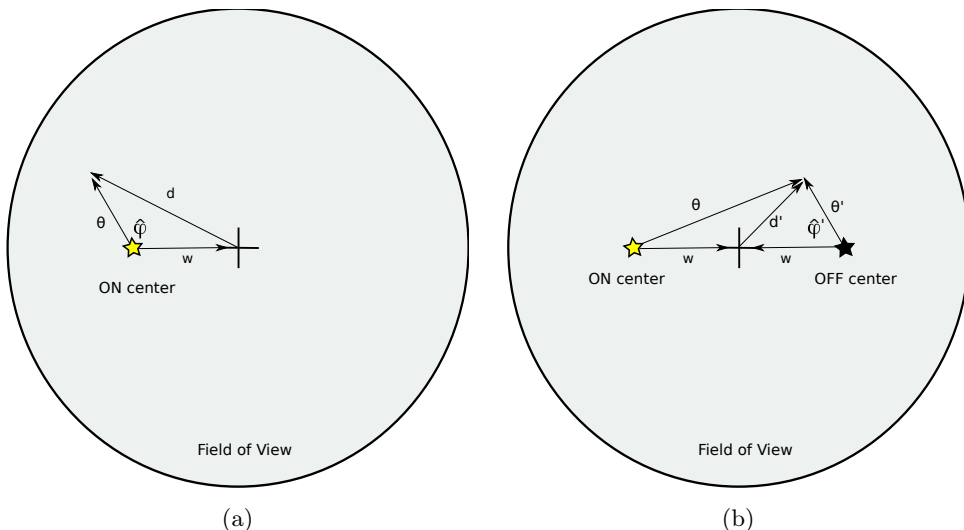


Figure 6.5: Definition of variables: (left) w is the distance between the center of a source (yellow star) and the center of the FoV. θ is the distance between the center of the source and any point of the FoV. And d is the distance of any point in the FoV and the center of the FoV. The three quantities are related by φ , the angle formed by the vectors $\vec{\theta}$ and \vec{w} . (right) as for the case of (a) but θ' , φ' and d are defined w.r.t. a mirror direction w.r.t. the source, which is located at the same w but at the opposite site of the FoV (black star). Note that $d(w, \theta, \varphi) = d'(w, \theta', \varphi')$.

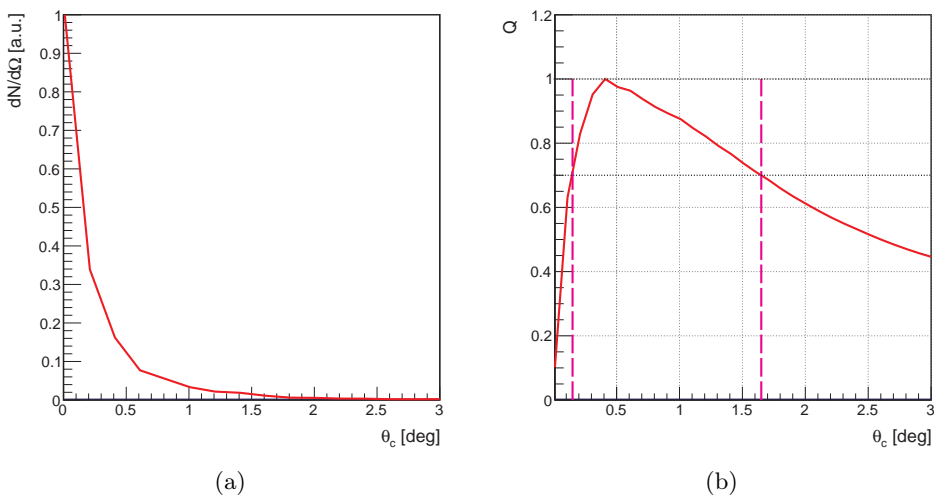


Figure 6.6: Left: $dN/d\Omega$ for the Coma dSph for annihilation DM taken as an example from (Bonnivard et al., 2015). See section Section 6.4 for more details. Right: Q -factor computed from $dN/d\Omega$ from Coma. θ_{opt} is defined as the value of θ_c that optimizes \mathcal{Q} ($\mathcal{Q} = 1$). An interval around θ_{opt} is defined where \mathcal{Q} is worsened by a 30% (magenta lines).

\mathcal{Q} is maximal when the signal dominates, the most, over the square-root of the amplitude of the background and, in general, given a \mathcal{P} , \mathcal{Q} will increase with larger values of θ_c up to a point where, for even larger values, only background events will be integrated and \mathcal{Q} will decrease (see Figure 6.6b). We define θ_{opt} as the value of θ_c that maximizes \mathcal{Q} ($\mathcal{Q}_{\text{max}} = 1$ by definition). An interval around θ_{opt} is defined where \mathcal{Q} is worsened by a 30% (marked with purple dashed lines in see Figure 6.6b).

6.3.1 $\mathcal{Q}_{\mathcal{A}}$: FINITE ACCEPTANCE

As introduced in Section 6.2, the off-axis performance of an instrument degrades towards the edges of the FoV. We should stress that, unlike θ_c which can always be modified during the analysis, w is fixed during the data taking (by fixing the position of the center of the source w.r.t to the center of the FoV) and can not be modified a posteriori. It is hence important to take into account ϵ in order to determine the optimal distance w when planing future observations. We define $\mathcal{Q}_{\mathcal{A}}$ as:

$$\mathcal{Q}_{\mathcal{A}}(w, \theta_c) = \frac{\int_{\Delta\Omega_{\text{ON}}} d\Omega_{\text{ON}} \mathcal{P}(\theta) \epsilon(d)}{\sqrt{\int_{\Delta\Omega_{\text{ON}}} d\Omega_{\text{ON}} \epsilon(d)}}; \quad (6.5)$$

$$\text{where } d = \sqrt{\theta^2 + w^2 - 2 \cdot \theta \cdot w \cdot \cos(\varphi)}$$

In Figure 6.7, we have computed $\mathcal{Q}_{\mathcal{A}}$ as a function of the observational variables w and θ_c using \mathcal{P} defined in Figure 6.6a and ϵ_{MAGIC} . For very large values of w and θ_c , ϵ is low, and $\mathcal{Q}_{\mathcal{A}}$ decreases. We define $\theta_{\text{opt}}(w_{\text{opt}})$ as the value of $\theta_c(w)$ that optimizes $\mathcal{Q}_{\mathcal{A}}$ ($\mathcal{Q}_{\mathcal{A}} = 1$). Again, an interval around both values is defined where $\mathcal{Q}_{\mathcal{A}}$ is worsened by a 30%.

6.3.2 $\mathcal{Q}_{\mathcal{L}}$: LEAKAGE EFFECT

Another effect to consider when planing observations at a given w , is that for low values of w , ON and OFF regions are close to each other, and according to \mathcal{P} , it may not be possible to define a *signal-free* OFF region. This *Leakage effect* is schematically shown in Figure 6.1, where γ ray events from \mathcal{P} (green circular area aligned with ON) are expected to be reconstructed inside OFF.

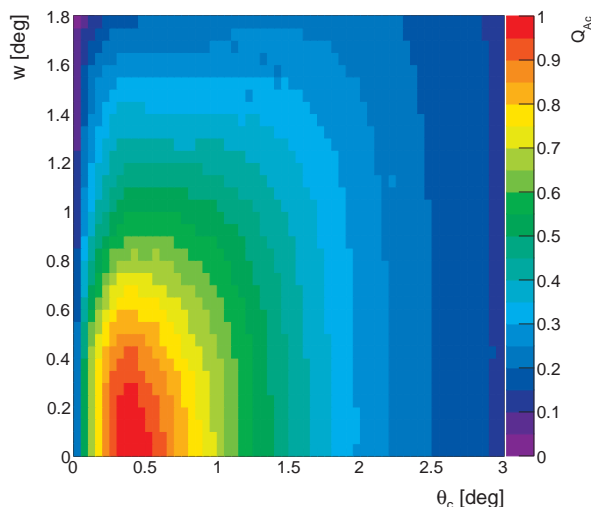


Figure 6.7: \mathcal{Q}_{sc} as a function of θ_c and w , computed from $dN/d\Omega$ in Figure 6.6a and ϵ_{MAGIC} .

We have approximated \mathcal{Q}_{sc} as;

$$\mathcal{Q}_{sc}(w, \theta_c) = \frac{\int_{\Delta\Omega_{\text{ON}}} d\Omega_{\text{ON}} \mathcal{P}(\theta) - \int_{\Delta\Omega_{\text{OFF}}} d\Omega_{\text{OFF}} \mathcal{P}(\theta)}{\sqrt{\int_{\Delta\Omega_{\text{ON}}} d\Omega_{\text{ON}}}}$$

$$\text{where } d\Omega_{\text{OFF}} = \theta' d\theta' d\varphi', \quad (6.6)$$

$$\theta = \sqrt{(2w)^2 + \theta'^2 + 2 \cdot (2w) \cdot \theta' \cdot \cos \varphi'}, \quad (6.7)$$

θ' and φ' are the circular coordinates w.r.t. the OFF center, and $\Delta\Omega_{\text{OFF}}$ is the region defined by: θ' between 0 and θ_c ; and φ' between 0 and 2π (see Figure 6.5b). Note that when integrating over $\Delta\Omega_{\text{OFF}}$, \mathcal{P} has to be evaluated w.r.t. the ON center (yellow star and θ in Figure 6.5b)

Figure 6.8 shows \mathcal{Q}_{sc} as a function of the observational variables w and θ_c . Large values of w are favoured since, the distance between ON and OFF regions gets larger with w and hence, the leakage between both regions smaller. w_{opt} , θ_{opt} and their contour regions are defined as above.

Alternatively , we could have defined \mathcal{Q}_{sc} as:

$$\mathcal{Q}_{sc}(w, \theta_c) = \frac{\int_{\Delta\Omega_{\text{ON}}} d\Omega_{\text{ON}} \mathcal{P}(\theta)}{\sqrt{\int_{\Delta\Omega_{\text{OFF}}} d\Omega_{\text{OFF}} (1 + \mathcal{P}(\theta))}} \quad (\text{NOT}) \quad (6.8)$$

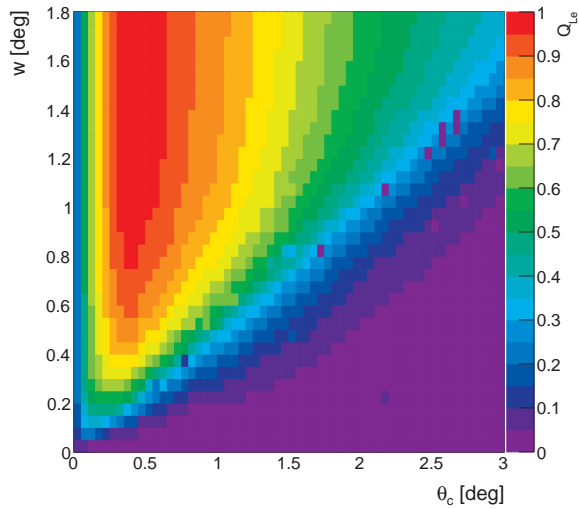


Figure 6.8: \mathcal{Q}_s as a function of θ_c and w , computed from $dN/d\Omega$ in Figure 6.6a.

however, in this case the determination of \mathcal{A} becomes much more difficult, if not impossible.

6.3.3 $\overline{\mathcal{Q}}$: “ACCEPTANCE + LEAKAGE” EFFECT

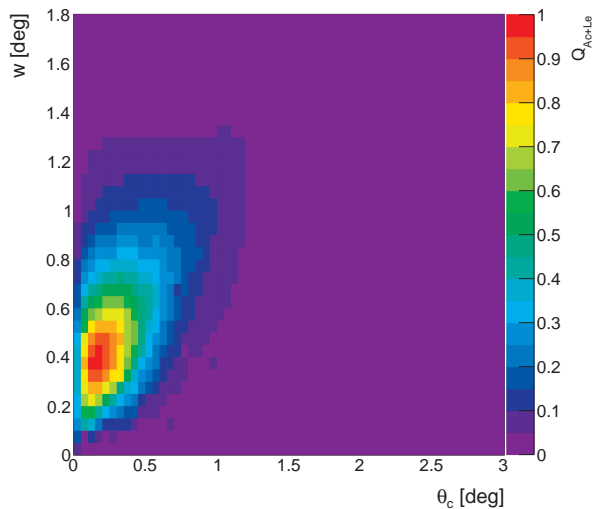


Figure 6.9: $\overline{\mathcal{Q}}$ as a function of θ_c and w , computed from $dN/d\Omega$ in Figure 6.6a and ϵ_{MAGIC} .

In general, we want to compute the optimal pointing strategy taking both

effects into account, the finite acceptance of the instrument and the leakage of signal between ON and OFF. For that, we define $\overline{\mathcal{Q}}$:

$$\begin{aligned} \overline{\mathcal{Q}}(w, \theta_c) &= \mathcal{Q}_{Ac+Le}(w, \theta_c) \\ &= \frac{\int_{\Delta\Omega_{\text{ON}}} d\Omega_{\text{ON}} \mathcal{P}(\theta) \epsilon(d) - \int_{\Delta\Omega_{\text{OFF}}} d\Omega_{\text{OFF}} \mathcal{P}(\theta) \epsilon(d')}{\sqrt{\int_{\Delta\Omega_{\text{ON}}} d\Omega_{\text{ON}} \epsilon(d)}}; \end{aligned} \quad (6.9)$$

$$\text{where} \quad (d =) d' = \sqrt{\theta'^2 + w^2 - 2 \cdot \theta' \cdot w \cdot \cos(\varphi')}$$

Figure 6.9 shows $\overline{\mathcal{Q}}$ as a function of the observational variables w and θ_c . The optimal range of w_{opt} and θ_{opt} is now much narrower.

6.4 w_{OPT} & θ_{OPT} FOR INDIRECT DM SEARCHES WITH DSPHS

We apply the method for the first time to optimize the pointing strategy of the MAGIC telescopes and the CTA array for indirect DM searches. Geringer-Sameth et al. (2015); Bonnivard et al. (2015) provide the JFactor for both, the annihilating and the decaying scenario (see k in Equation 2.9), for two different sets of DM halos hosting a dSph satellite of the Milky Way (MW), as a function θ_c . As introduced in Section 2.3.3, the expected morphology of signal of DM is determined by the JFactor. In the case of indirect DM searches, we take the $dJ/d\Omega$ ($dJ/d\Omega$ in Equation 2.10) as the source brightness profile of the source as:

$$\frac{dN}{d\Omega} = \frac{dJ}{d\Omega} \quad (6.10)$$

We provide optimize the pointing strategy of MAGIC and CTA considering all possible cases based on: all available sources from both authors Bonnivard et al. (2015); Geringer-Sameth et al. (2015); the two possible type of candidates in Equation 2.9 (*Annihilation* and *Decay*); and based on $\overline{\mathcal{Q}}$, taking into account the two effects introduced in Section 6.3, *Acceptance* and *Leakage*.

6.4.1 ANNIHILATING WIMP

Figure 6.10 show the J-factors for annihilation (J_{ann}) as a function of θ_c for all available dSphs in (Bonnivard et al., 2015, left) and (Geringer-Sameth et al., 2015, right). The values w_{opt} , θ_{opt} , and their ranges, for are shown in Table 6.1 and 6.2.

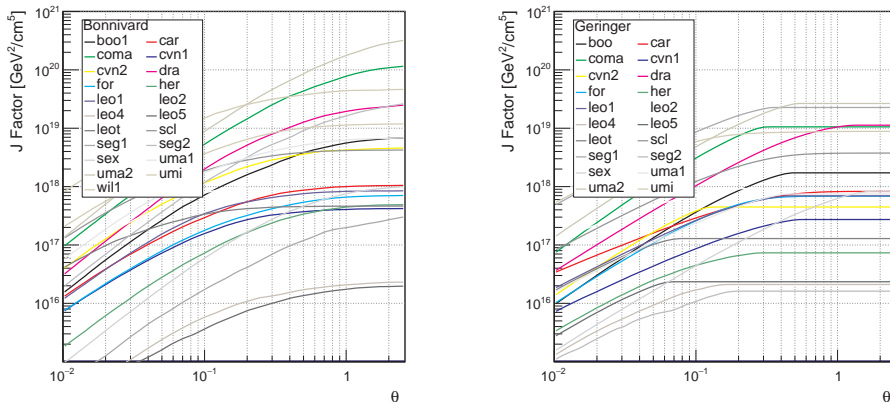


Figure 6.10: J_{ann} -factor (in units of $\text{GeV}^2\text{cm}^{-5}$) as a function of the integration angle θ (in units of deg) for a set of dSphs presented in (Bonnivard et al., 2015, left) and (Geringer-Sameth et al., 2015, right).

source	MAGICPointLike				CTANorth50To80GeV			
boo1	0.1	(0.05, 0.2)	0.30	(0.15, 0.50)	0.15	(0.05, 0.45)	0.60	(0.25, 1.06)
car	0.05	(0, 0.2)	0.30	(0.10, 0.45)	0.05	(0, 0.25)	0.45	(0.10, 1.01)
coma	0.15	(0.05, 0.3)	0.35	(0.25, 0.50)	0.3	(0.1, 0.45)	0.60	(0.40, 1.06)
cvn1	0.05	(0, 0.15)	0.30	(0.10, 0.45)	0.05	(0, 0.2)	0.45	(0.10, 1.01)
cvn2	0.1	(0.05, 0.2)	0.30	(0.15, 0.45)	0.1	(0.05, 0.25)	0.45	(0.20, 1.01)
dra	0.15	(0.05, 0.25)	0.35	(0.20, 0.50)	0.2	(0.1, 0.45)	0.65	(0.30, 1.06)
for	0.05	(0, 0.15)	0.30	(0.10, 0.45)	0.05	(0, 0.25)	0.45	(0.10, 1.01)
her	0.1	(0.05, 0.2)	0.35	(0.20, 0.50)	0.15	(0.05, 0.4)	0.55	(0.25, 1.01)
leo1	0.05	(0.05, 0.15)	0.30	(0.10, 0.45)	0.05	(0.05, 0.2)	0.45	(0.10, 1.01)
leo2	0.05	(0, 0.1)	0.30	(0.10, 0.45)	0.05	(0, 0.1)	0.40	(0.10, 1.01)
leo4	0.05	(0.05, 0.2)	0.30	(0.15, 0.45)	0.1	(0.05, 0.25)	0.50	(0.15, 1.01)
leo5	0.1	(0, 0.2)	0.30	(0.15, 0.50)	0.1	(0.05, 0.3)	0.50	(0.20, 1.01)
leot	0	(0, 0.05)	0.35	(0.05, 0.45)	0	(0, 0.05)	0.45	(0.05, 1.01)
scl	0.05	(0, 0.15)	0.30	(0.10, 0.45)	0.05	(0, 0.15)	0.45	(0.10, 1.01)
seg1	0.1	(0.05, 0.25)	0.35	(0.20, 0.50)	0.3	(0.05, 0.55)	0.70	(0.40, 1.06)
seg 2	0.15	(0.05, 0.25)	0.35	(0.20, 0.50)	0.25	(0.1, 0.55)	0.70	(0.35, 1.06)
sex	0.15	(0.05, 0.3)	0.35	(0.25, 0.50)	0.25	(0.1, 0.55)	0.70	(0.35, 1.06)
uma1	0.05	(0.05, 0.2)	0.30	(0.10, 0.45)	0.1	(0.05, 0.25)	0.45	(0.15, 1.01)
uma2	0.15	(0.05, 0.3)	0.35	(0.25, 0.50)	0.25	(0.1, 0.6)	0.75	(0.40, 1.11)
umi	0.05	(0, 0.15)	0.30	(0.10, 0.45)	0.05	(0, 0.2)	0.45	(0.10, 1.01)
will	0.05	(0, 0.15)	0.30	(0.10, 0.45)	0.05	(0, 0.2)	0.45	(0.10, 1.01)

Table 6.1: List of optimal pointing wobble distances (w_d) and signal sizes (θ) for annihilating WIMP based on Bonnivard et al. (2015).

For the case of MAGIC, comparing the optimal values (w_{opt} , θ_{opt}) with the ones currently used in MAGIC (w_M , θ_M), we see that for most of the cases the values are compatible. This means that most of those sources are seen by MAGIC as point-like sources; We want to note however a few things. There are however few cases in which the source appears as extended for MAGIC (i.e. *cvn1* from Geringer-Sameth et al., 2015)). We also note the disagreement between these and the optimal values for the same source considered in Bonnivard et al. (2015). The discrepancies between the authors make obvious the large uncertainties these DM profiles are affected, however, this matter is out of the

source	MAGICPointLike				CTANorth50To80GeV			
	w_d	θ	w_d	θ	w_d	θ	w_d	θ
boo	0.1	(0.05, 0.25)	0.35	(0.20, 0.50)	0.2	(0.05, 0.4)	0.60	(0.30, 1.01)
car	0	(0, 0.1)	0.35	(0.05, 0.45)	0	(0, 0.15)	0.45	(0.05, 1.01)
coma	0.15	(0.05, 0.25)	0.35	(0.20, 0.50)	0.2	(0.05, 0.3)	0.50	(0.25, 1.01)
cvn1	0.05	(0, 0.15)	0.30	(0.10, 0.45)	0.05	(0, 0.25)	0.50	(0.10, 1.01)
cvn2	0.05	(0.05, 0.1)	0.20	(0.10, 0.45)	0.05	(0.05, 0.1)	0.40	(0.10, 1.01)
dra	0.1	(0.05, 0.25)	0.35	(0.20, 0.50)	0.25	(0.05, 0.5)	0.65	(0.35, 1.06)
for	0.1	(0.05, 0.2)	0.30	(0.15, 0.45)	0.1	(0.05, 0.25)	0.45	(0.20, 1.01)
her	0.05	(0, 0.15)	0.30	(0.10, 0.45)	0.05	(0, 0.15)	0.40	(0.10, 1.01)
leo1	0.05	(0, 0.15)	0.35	(0.10, 0.45)	0.05	(0, 0.25)	0.45	(0.10, 1.01)
leo2	0	(0, 0.05)	0.25	(0.05, 0.45)	0	(0, 0.05)	0.45	(0.05, 1.01)
leo4	0.05	(0, 0.1)	0.20	(0.10, 0.45)	0.05	(0, 0.1)	0.40	(0.10, 1.01)
leo5	0	(0, 0.05)	0.10	(0.05, 0.45)	0	(0, 0.05)	0.45	(0.05, 1.01)
leot	0	(0, 0.05)	0.10	(0.05, 0.45)	0	(0, 0.05)	0.45	(0.05, 1.01)
scl	0.05	(0, 0.2)	0.30	(0.10, 0.45)	0.05	(0, 0.25)	0.45	(0.10, 1.01)
seg1	0.05	(0, 0.2)	0.35	(0.15, 0.45)	0.1	(0, 0.3)	0.45	(0.20, 1.01)
seg2	0	(0, 0.1)	0.25	(0.05, 0.45)	0	(0, 0.1)	0.45	(0.05, 1.01)
sex	0.1	(0.05, 0.25)	0.35	(0.20, 0.50)	0.2	(0.05, 0.55)	0.65	(0.30, 1.06)
uma1	0.05	(0, 0.2)	0.35	(0.10, 0.45)	0.05	(0, 0.3)	0.45	(0.15, 1.01)
uma2	0.15	(0.05, 0.25)	0.35	(0.20, 0.50)	0.2	(0.05, 0.45)	0.60	(0.30, 1.01)
umi	0	(0, 0.1)	0.35	(0.05, 0.45)	0	(0, 0.1)	0.45	(0.05, 1.01)

Table 6.2: List of optimal pointing wobble distances (w_d) and signal sizes (θ) for annihilating WIMP based on Geringer-Sameth et al. (2015).

scope of this work. We also note how for some sources (i.e: for Bonnivard car, cvn1, leo1, leot; and for Geringer car, leo2, leo4, leot, seg1), θ_{opt} appears to be smaller than the typically used in MAGIC. This is an unphysical result since we did not take into account the instrument PSF. It should also be said that the method does not take into account systematic effects that may affect the real analysis. The systematic error on the background events integrated in the ON region, is going to be proportional (a fix percentage) to the statistics of the number of events integrated in OFF. This means that for two different configurations (two different w and θ_c pairs) that give similar \mathcal{Q} , we should give priority to the one with lower θ_c (lower statistics). Once systematic effects taken into account, the sensitivity is going to be better.

For the case of CTA, such values can be taken as reference values in order to schedule future observations however two things should be noted: 1) CTA will be composed of two observatories, one operating on the North (*CTAN*) hemisphere and one on the south (*CTAS*) however, we treated all dSphs with the same instrument acceptance regardless of their position in the sky; 2) Each CTA site (CTAN and CTAS) will be integrated by, up to, three different type of telescopes and hence, once CTA analysis scheme is defined, a proper optimization could be performed for the pointing of each Telescope.

6.4.2 DECAYING WIMP

Figure 6.11 show the J-factors for decay (D-factors, in GeVcm^{-2}) as a function of the integration angle θ (in *deg*) for all available dSphs in (Bonnivard et al., 2015, left) and (Geringer-Sameth et al., 2015, right). In Tables 6.3 and 6.4,

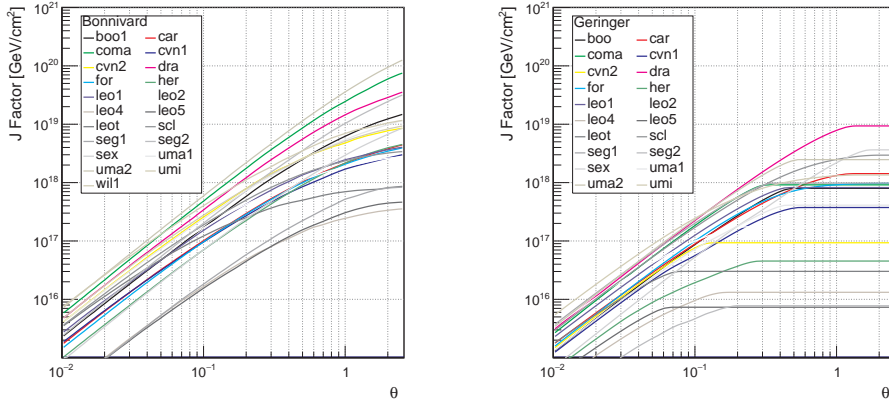


Figure 6.11: J-factor for decay (or D-factor, in units of GeVcm^{-2}) as a function of the integration angle θ (in units of deg) for a set of dSph presented in (Bonnivard et al., 2015, left) and (Geringer-Sameth et al., 2015, right).

source	MAGICPointLike				CTANorth50To80GeV			
	w_d	(w_d, θ)	w_d	(w_d, θ)	w_d	(w_d, θ)	w_d	(w_d, θ)
boo1	0.25	(0.1, 0.4)	0.4	(0.3, 0.6)	0.35	(0.15, 0.7)	0.8	(0.45, 1.2)
car	0.15	(0.05, 0.3)	0.35	(0.25, 0.55)	0.3	(0.1, 0.6)	0.7	(0.45, 1.1)
coma	0.3	(0.15, 0.5)	0.5	(0.35, 0.65)	0.45	(0.2, 0.8)	0.85	(0.55, 1.2)
cvn1	0.15	(0.05, 0.3)	0.35	(0.25, 0.5)	0.3	(0.1, 0.6)	0.75	(0.4, 1.1)
cvn2	0.2	(0.05, 0.3)	0.35	(0.25, 0.55)	0.3	(0.15, 0.55)	0.7	(0.4, 1.1)
dra	0.2	(0.1, 0.4)	0.4	(0.3, 0.6)	0.45	(0.2, 0.8)	0.85	(0.55, 1.2)
for	0.15	(0.05, 0.3)	0.35	(0.25, 0.55)	0.3	(0.1, 0.6)	0.75	(0.45, 1.1)
her	0.2	(0.05, 0.35)	0.4	(0.25, 0.6)	0.35	(0.15, 0.7)	0.8	(0.5, 1.2)
leo1	0.15	(0.05, 0.3)	0.35	(0.25, 0.55)	0.3	(0.1, 0.55)	0.7	(0.4, 1.1)
leo2	0.15	(0.05, 0.3)	0.35	(0.2, 0.5)	0.2	(0.05, 0.5)	0.65	(0.3, 1.1)
leo4	0.15	(0.05, 0.3)	0.35	(0.25, 0.5)	0.25	(0.1, 0.55)	0.7	(0.4, 1.1)
leo5	0.2	(0.05, 0.35)	0.4	(0.25, 0.55)	0.35	(0.1, 0.65)	0.8	(0.45, 1.1)
leot	0.1	(0.05, 0.2)	0.35	(0.15, 0.5)	0.1	(0.05, 0.35)	0.5	(0.2, 1)
scl	0.15	(0.05, 0.25)	0.35	(0.2, 0.5)	0.25	(0.1, 0.5)	0.65	(0.35, 1.1)
seg1	0.2	(0.05, 0.3)	0.35	(0.25, 0.55)	0.35	(0.15, 0.7)	0.8	(0.45, 1.2)
seg2	0.25	(0.1, 0.4)	0.45	(0.25, 0.6)	0.45	(0.2, 0.85)	0.85	(0.6, 1.2)
sex	0.2	(0.1, 0.4)	0.4	(0.25, 0.6)	0.4	(0.15, 0.75)	0.85	(0.5, 1.2)
uma1	0.15	(0.05, 0.3)	0.35	(0.25, 0.55)	0.3	(0.1, 0.6)	0.7	(0.4, 1.1)
uma2	0.3	(0.15, 0.45)	0.5	(0.35, 0.65)	0.5	(0.2, 0.9)	0.96	(0.6, 1.2)
umi	0.15	(0.05, 0.3)	0.35	(0.25, 0.55)	0.3	(0.1, 0.55)	0.7	(0.4, 1.1)
wil1	0.15	(0.05, 0.25)	0.35	(0.2, 0.5)	0.3	(0.1, 0.6)	0.7	(0.4, 1.1)

Table 6.3: List of optimal pointing wobble distances (w_d) and signal sizes (θ) for decaying WIMP based on Bonnivard et al. (2015).

the optimal values (w_{opt} , θ_{opt}) for these dSphs are given for the MAGIC and CTA.

In this case, for the case of MAGIC most of these sources are considered to be rather extended (this is expected taking into account the dependence on ρ in Equation 2.9). However, w_{opt} is still compatible with the MAGIC standard one in most of the cases.

The previous CTA discussion (for Annihilating WIMPs) is also valid in here.

source	MAGICPointLike				CTANorth50To80GeV			
	w_d	θ	w_d	θ	w_d	θ	w_d	θ
boo	0.2	(0.1, 0.4)	0.40	(0.25, 0.55)	0.35	(0.15, 0.5)	0.70	(0.40, 1.01)
car	0.15	(0.05, 0.3)	0.35	(0.25, 0.55)	0.3	(0.1, 0.6)	0.75	(0.40, 1.11)
coma	0.2	(0.1, 0.3)	0.35	(0.25, 0.50)	0.25	(0.1, 0.35)	0.50	(0.30, 0.96)
cvn1	0.15	(0.05, 0.35)	0.35	(0.25, 0.55)	0.25	(0.1, 0.45)	0.65	(0.35, 1.01)
cvn2	0.1	(0.05, 0.1)	0.20	(0.15, 0.45)	0.1	(0.05, 0.15)	0.35	(0.15, 1.01)
dra	0.2	(0.1, 0.4)	0.40	(0.30, 0.60)	0.55	(0.2, 0.8)	0.91	(0.60, 1.16)
for	0.15	(0.05, 0.3)	0.35	(0.25, 0.50)	0.25	(0.1, 0.5)	0.65	(0.35, 1.06)
her	0.05	(0.05, 0.2)	0.30	(0.15, 0.45)	0.1	(0.05, 0.25)	0.40	(0.20, 1.01)
leo1	0.2	(0.05, 0.35)	0.40	(0.25, 0.55)	0.25	(0.1, 0.45)	0.65	(0.35, 1.01)
leo2	0.1	(0.05, 0.15)	0.30	(0.15, 0.45)	0.1	(0.05, 0.2)	0.35	(0.15, 1.01)
leo4	0.05	(0.05, 0.1)	0.20	(0.10, 0.45)	0.05	(0.05, 0.15)	0.40	(0.10, 1.01)
leo5	0.05	(0, 0.05)	0.10	(0.10, 0.45)	0.05	(0, 0.05)	0.40	(0.10, 1.01)
leot	0.05	(0, 0.05)	0.15	(0.10, 0.45)	0.05	(0, 0.05)	0.40	(0.10, 1.01)
scl	0.15	(0.05, 0.3)	0.35	(0.25, 0.55)	0.3	(0.1, 0.55)	0.70	(0.40, 1.06)
seg1	0.15	(0.05, 0.3)	0.35	(0.25, 0.50)	0.25	(0.1, 0.35)	0.55	(0.35, 1.01)
seg2	0.05	(0.05, 0.15)	0.25	(0.10, 0.45)	0.05	(0.05, 0.2)	0.40	(0.10, 1.01)
sex	0.15	(0.1, 0.3)	0.35	(0.20, 0.55)	0.45	(0.15, 0.85)	0.85	(0.55, 1.21)
uma1	0.15	(0.05, 0.3)	0.35	(0.25, 0.55)	0.25	(0.1, 0.45)	0.60	(0.35, 1.01)
uma2	0.25	(0.1, 0.45)	0.45	(0.30, 0.60)	0.35	(0.15, 0.55)	0.70	(0.45, 1.06)
umi	0.1	(0.05, 0.25)	0.35	(0.20, 0.50)	0.15	(0.05, 0.35)	0.55	(0.25, 1.01)

Table 6.4: List of optimal pointing wobble distances (w_d) and signal sizes (θ) for decaying WIMP based on Geringer-Sameth et al. (2015).

6.5 CONCLUSIONS AND REMARKS

In this work, we propose a method to optimize the wobble pointing strategy for IACTs. The method provides the optimal wobble offset and signal integration region distances taking into account the off-axis performance of the instrument and the surface brightness profile of the source under observation (that needs to be assumed). We characterize the off-axis performance of two IACTs currently working or plant for the near future: the MAGIC telescopes and CTA. The method, has been designed for observations on moderate extended sources within IACTs where ON and OFF regions are defined with the same size, symmetrically distributed w.r.t. the center of the FoV. We focus on the case of indirect DM searches, the use-case for which the method was initially developed, and apply the method for the first time and provide with the optimal values for a set of published DM distributions on nearby dSphs.

The method is general enough to optimize the pointing strategy of any IACT observing any source of γ rays (no need to be from DM). The method has been implemented into a software tool that is freely distributed through the open-software package *githup*. A released version has been released from where the results presented in here have been reproduced. This released version also provides with tutorials and explanations on the main features of the package. Extending the current software to include other instruments (not considered in here) or new source profiles, is rather straight-forward.

We consider this method to be a power-fool tool in order to plan current and future observations within the IACT community in a very simple and fast

procedure, as the case for example, of the expected extended emission of the *Geminga pulsar*, one of the brightest gamma-ray sources, a promising candidate for emission of VHE pulsed γ rays Abdo et al. (2010b); Ahnen et al. (2016c); Abeysekara et al. (2017). The tool will become extremely useful during the starting phase of CTA, where observations with the new instruments are going to be planned. We leave as a future work the extension of the method in two directions. From one side, including in the method, the angular resolution response of the instrument, would extend the applicability of the method the very point-like limit of sources without adding a heavy overhead of calculations. We did not take it into account so far, since initially, since for moderate extended sources (the case that initially interested and that we focus in here) these effects are rather irrelevant. On the second side, following up with the next CTA operation, pointing strategies within CTA should be optimized telescope-wise (the relative acceptance of the different kind of telescopes forming CTA can differ considerably from one to another), for what the details of the CTA analysis line would be required (which by the time of this work, were still not available).

Chapter 7

LST CAMERA NOISE TESTS

*This project has been done in collaboration with O. Blanch, S. Griffiths and
A. Fernandez-Barral
Special thanks to C. Delgado, C. Díaz and G. Martínez for all the support and
infrastructure during our stay at CIEMAT.*

7.1 INTRODUCTION

In September 2016, a mechanical and electronic characterization of the first LST prototype camera is performed at CIEMAT, Madrid. We searched for noise (conducted and radiated) induced after the integration of the LST modules to the camera, operating under conditions as the ones expected after being installed at the telescope. Previous measurements performed on single LST module (Fernandez and Griffiths, 2016), show that two components of noise are expected: from the switching-mode PSU used to power the camera; and due to the short distance between neighbouring working modules. In order to test this two hypothesis, we run a series of standard measurements (such as DRS4 capacitors charge measurements and L0 and L1 rate scans) under several different cluster configurations, that allow us to isolate each different noise components. Similar tests along with characterization and quality control are scheduled January 2018 at IFAE (Barcelona) with a larger number of modules, in order to cover the entire camera. The conclusions of this tests have been used to plan the IFAE tests that will give green light to ship the camera pieces to LP for the final assembly on the first LST.

This Chapter is organized as follows: In Section 7.2, we introduce the hardware components involved in the tests; in Section 7.3 the analysis performed is explained along with the noise estimators defined, in Section 7.4, the main results

obtained are presented; Finally in Section 7.6 we conclude the outcome of the tests. A detailed documentation on the tests procedure and the outcome of the analysis has been documented in Palacio et al. (2016a, 2017)¹ respectively.

7.2 TESTS CIEMAT

The main goal of the tests is to evaluate the level of noise present through the trigger path of the modules, and estimate the noise induced due to the switching mode PSU (w.r.t. a low noise linear PSUs) and due to the proximity of the neighbouring modules in the final camera integration. Each module is composed by 7 PMTs, followed by the HV chip and PACTA, the Slow Control board, *Dragon* board in which L0+L1 mezzanine is attached and finally the back-plane where the Ethernet switches are placed (see Figure 3.25). Each channel is provided with a pulse generator that can induce electrical currents at a given frequency into PACTA, simulating the PMT output signal.



Figure 7.1: Switching mode PSU and redundancy module used in the LST camera.

The characterization is carried out with only 35 Modules (35Ms) of the LST camera. Two switched-mode PSUs, a linear PSU and a redundancy module unit YR80.241 are also used (see Figure 7.1). The power is distributed module through a bus bar distribution the modules through the Cluster Holder Frame (CHF) (a picture of the CHF is shown in Figure 7.2) from where power cabling reaches each module.

¹ Internal documentation of the LST collaboration

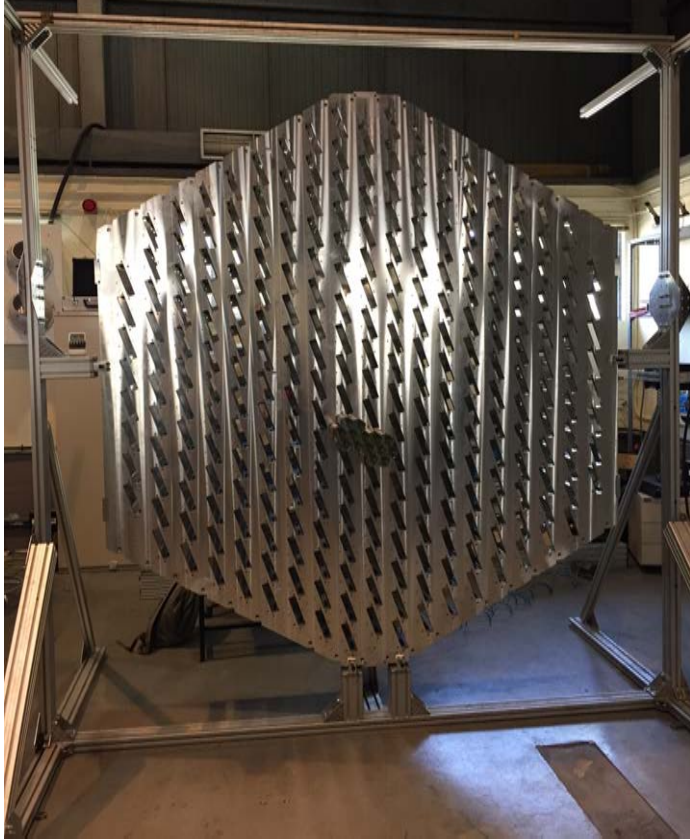


Figure 7.2: CHF metallic structure for the LST modules during tests at CIEMAT. Each module is introduced to one of the holes through the front part of the CHF and is fixed with the back-plane board, through the back of the CHF.

The main body of the tests consists in running several *Rate Scans*, a procedure in which we measure the number of triggered events as a function of the DT. We repeated these rate scans for different trigger settings, cluster distribution along the CHF (see Figure 7.3), and two different type of PSUs (linear and switching mode). The tests were performed in an ambient light exposed environment, where HVs had to remain OFF through all the tests. More information on the set-up, power distribution and parallel measurements during the tests can be found in Delgado and Mangano (2016); Delgado (2016); Griffiths (2016)².

In order to achieve our goals while coordinating with other tests going on in parallel during the same dates minimizing the overall time needed, 4 different

² Internal documentation of the LST collaboration

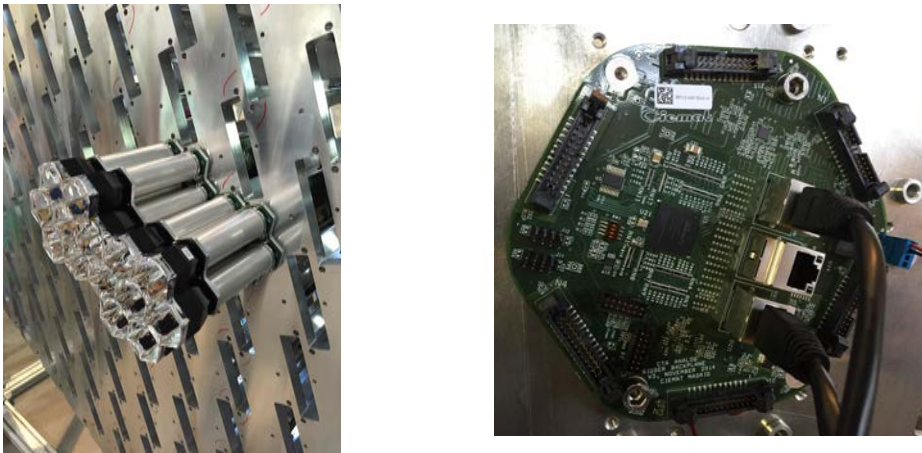


Figure 7.3: Front (left) and back (right) view of the modules after being assembled into the CHF.

distributions of the modules through the CHF have been elected for the tests: *Module15*, *Vertical*, *Diagonal* and *Cheese* (see Figure 7.4). All configurations but *Module15* are powered with the switching-mode PSU, whereas *Module15* uses a low noise linear PSU. These configurations (whose names are motivated with the apparent shape of the modules over the CHF after the integration), allow us to isolate the two different noise components introduced before.

7.3 DATA ANALYSIS

We show in this section the different rate scans we performed, and the noise estimators we defined for each case.

7.3.1 L0 RATE PEDESTAL SCAN

We measure the rate of L0 triggered events, per channel per module, as a function of the applied DT for the 4 different configurations. Note that the DT is indeed, a *differential* DT, where only wave pulses (from the DRS4, see Section 3.3.1) crossing the DT are triggered. The scanned range of DTs goes from ~ 400 to ~ 850 Digital-to-Analog Converter (DAC), where the effective zero is located ~ 550 DAC. Since no external source is present, only ambient noise around the effective zero threshold, should be triggered. We define *sigma threshold* (σ_{thresh}) as the width of the saturated rate interval of DTs, as an estimator of the amplitude of the noise. Figure 7.5 shows, as an example, the L0 rate pedestal scan result for channel zero of module 192.168.1.10, σ_{thresh}

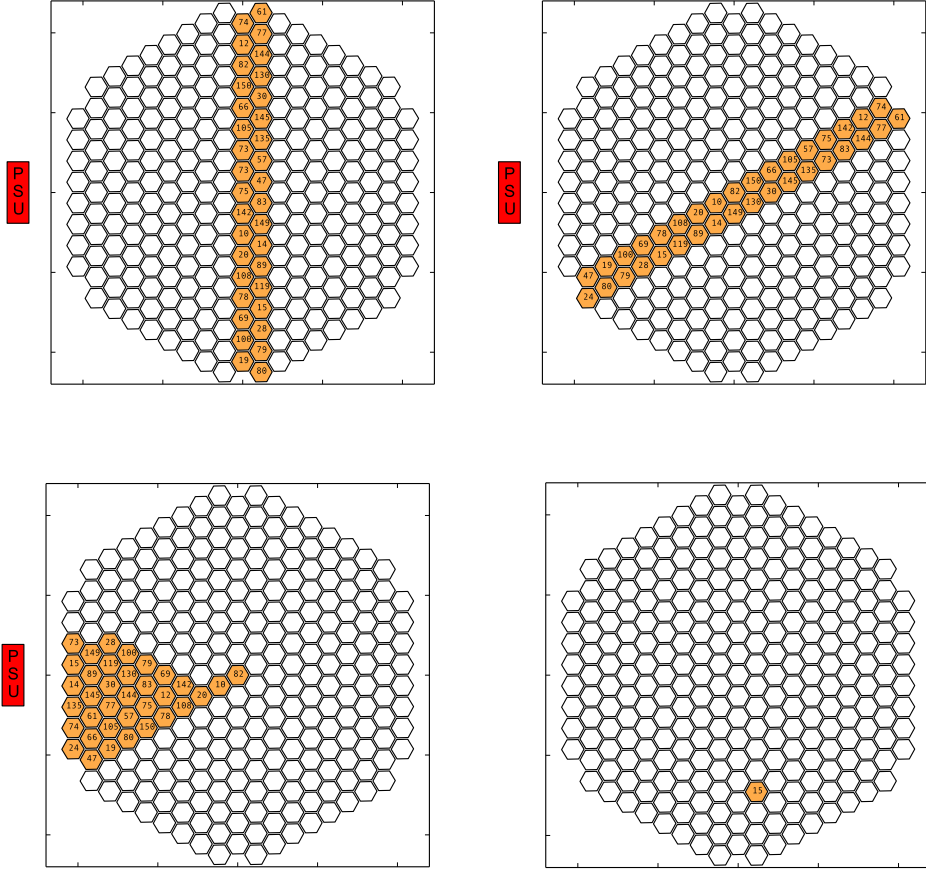


Figure 7.4: LST modules distributed through the CHF structure in four different configurations: Vertical (top left), Diagonal (top right), Cheese (bottom left) and Module15 (bottom right). All cluster configurations, but linear, where powered with the switching mode PSU.

is indicated through the pink arrows.

7.3.2 L0 RATE SCAN WITH PULSE INJECTION

We measure the rate of L0 triggered events, per channel per module, as a function of the applied DT for the 4 configurations. In this case, pulse injection is ON, and pulse induced events are also expected to trigger. The DT range scanned is divided into two different regions dominated by the two different effects. For values of the discriminator around the effective zero, ambient noise and pulse induced events are expected to trigger, whereas for larger values, only

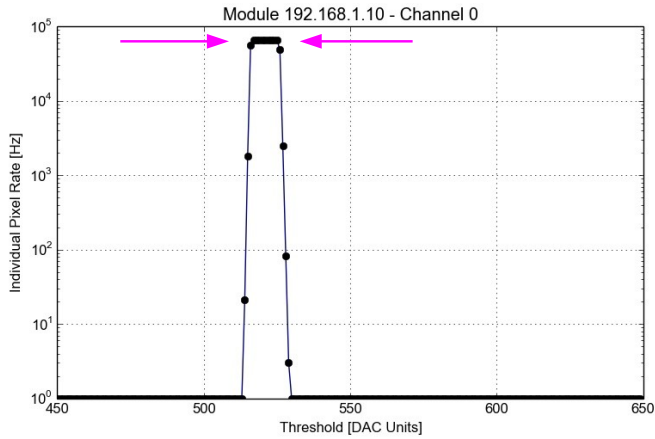


Figure 7.5: L0 rate pedestal scan example. The figure shows the individual L0 rate of channel 0 of module 192.168.1.10 as a function of the discriminator threshold (in DAC units). Sigma threshold (σ_{thresh}) is defined as the width of the saturated points (pink arrows).

pulse induced events will be triggered. Figure 7.6 shows, as an example, the

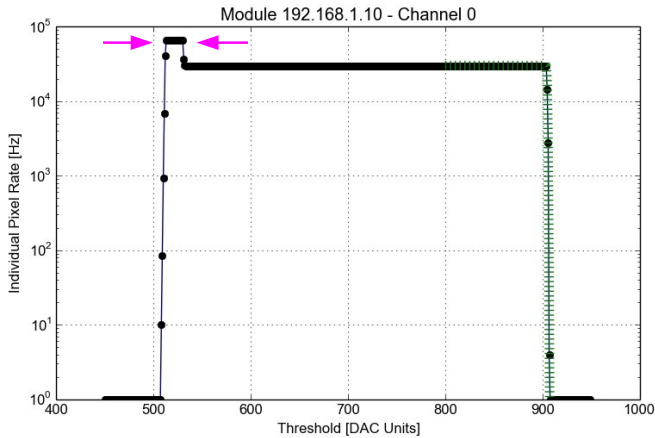


Figure 7.6: L0 rate scan with pulse injection example. Figure shows the individual L0 rate of channel 0 of module 192.168.1.10 (chosen arbitrarily) as a function of the discriminator threshold (in DAC units). Sigma threshold (σ_{thresh}) is defined as the width of the saturated points around the ambient noise (pink arrows) and sigma pulse (σ_{pulse}) is defined as the sigma value of the best fitting ErF to the region where the pulse stops getting triggered (green dashed line).

L0 rate scan with pulse injection for channel zero of module 192.168.1.10. As before, we define sigma threshold (σ_{thresh}) as the width of the saturated rate values in Figure 7.6 (as indicated through the pink arrows) as an estimator of the amplitude of the ambient noise. We also define sigma pulse (σ_{pulse}) as the best-fitting value of of an Error Function (ErF) (as in Equation 7.1,

$$erf(x) = \mathcal{A} \frac{2}{\sqrt{\pi}} \int_{DT_{min}}^x e^{-\left(\frac{x-\rho}{\sigma_{pulse}}\right)^2} dx, \quad (7.1)$$

where the amplitude \mathcal{A} has been fixed to the pulse injection frequency and only ρ and σ_{pulse} are free parameters. The fit region is fixed to be for $DT > 800$ DAC (see green dashed line).

7.3.3 L1 RATE PEDESTAL SCAN

We measure the rate of L1 triggered events, per module (all L0s are unified into one L1 trigger), as a function of the DT for the 4 configurations. Only ambient noise events should trigger. Note that the scanned interval of the L1-DT is, $DT > 0$, the L1-DT is unipolar. This means that modules having an effective zero threshold baseline on the negative side of the discriminator are not likely to trigger any ambient noise events. Figure 7.7 shows, as an

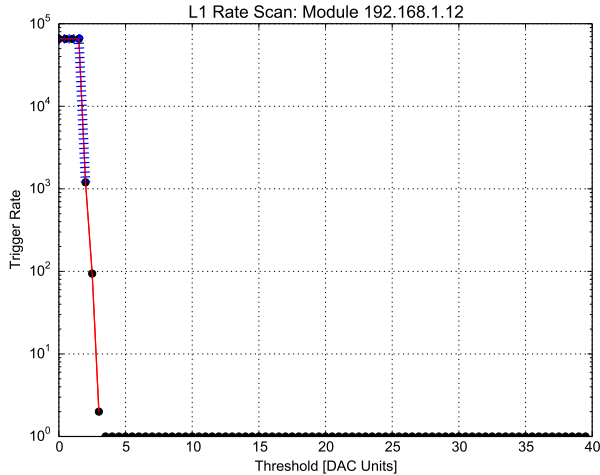


Figure 7.7: L1 rate pedestal scan example. Figure shows the individual L1 pedestal rate of module 192.168.1.12 (chosen arbitrarily) as a function of the discriminator threshold. Scanned regions with measured rates equal to zero are shown to be 1 in the plot only for plotting purposes. Sigma threshold (σ_{thresh}) is defined as the sigma value of the best fitting ErF around the ambient noise events region (blue dashed line).

example, the local L1 rate pedestal scan for module 192.168.1.12. We define sigma threshold (σ_{thresh}) as the best fitting value of ErF (see Equation 7.1), where again, the amplitude has been fixed to the pulse generator frequency and only ρ and σ_{thresh} are free parameters.

7.3.4 L1 RATE SCAN WITH PULSE INJECTION

We measure the rate of L1 triggered events, per module, as a function of the discriminator threshold for all configurations. Pulse injection is on, and the scanned region of the discriminator is again be divided into two different regions of interest (see section 7.3.2). Modules having the zero threshold on the negative side of the discriminator are not going to trigger on ambient noise events, and hence, the noise (baseline) peak will not be visible in these measurements. Figure 7.8 shows, as an example, the local L1 rate scan with pulse

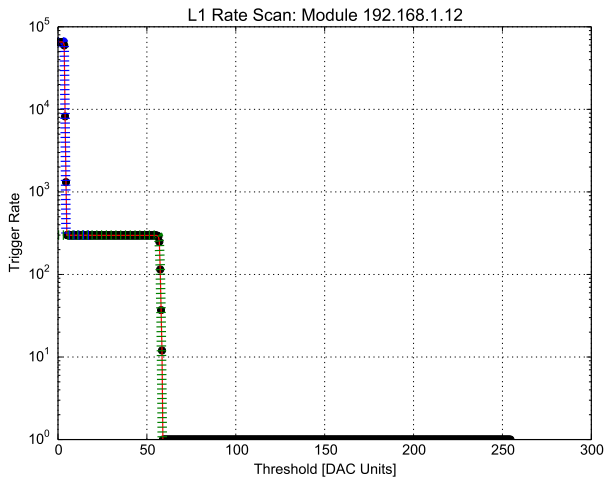


Figure 7.8: L1 rate scan with pulse injection example. Figure shows the individual L1 rate scan with pulse injection of module 192.168.1.12 as a function of the discriminator threshold. Sigma threshold (σ_{thresh}) and sigma pulse (σ_{pulse}) are defined as the sigma value of the best fitting ErF around the ambient noise (blue dashed line) and the pulse events (green dashed line) regions respectively.

injection for module 192.168.1.12. We define sigma threshold and sigma pulse (σ_{thresh} and σ_{pulse}) as the best fitting values of two ErFs (see Equation 7.1), the first one around the region with ambient noise (blue dashed line), and the second one around the pulse triggered events (green dashed line). In both cases, the amplitude of the function in both fits has been fixed, to the saturated amplitude value in the first case and to the pulse generator frequency in

the second, and only ρ and $\sigma_{thresh,pulse}$ are free parameters for the fit.

7.4 RESULTS

In this section we present the results obtained for each of the for tests presented, for the four configurations.

7.4.1 L0 RATE PEDESTAL SCAN

SIGMA THRESHOLD

Results are synthesized in Figure 7.9 where σ_{thresh} for all configurations is shown as a function of the distance to the power supply unit (left) and as a function of the configuration (right), where the values of each configuration are labelled with the same color. The sizes of the markers in Figure 7.9 right are proportional to the number of modules. From figure 7.9 we see that all

Sigma Threshold - L0Scan Pedestal

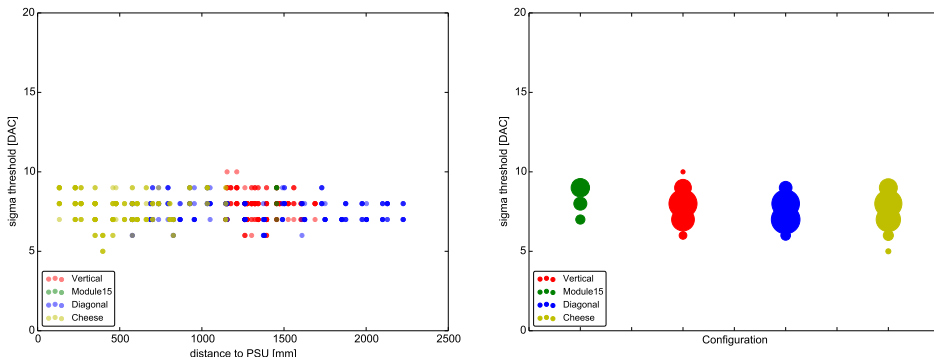


Figure 7.9: Results for σ_{thresh} for L0 pedestal rate scan. The figure shows σ_{thresh} for all PMTs of all modules as a function of the distance to the PSU (left) and module configuration (right). Size of the points (right) is proportional to the number of events.

measured σ_{thresh} are between 5 and 10 DAC units. The absolute scale of these values is not well defined, however, the relative differences between different modules and configurations can tell us about the noise present. Looking at figure 7.9, one can tell that the dependence of the noise on the distance to the PSU and on the configuration is rather small. In order to quantify such dependence, we fit with a straight line the distribution of σ_{thresh} shown in figure 7.9 (left), for all modules and distributions together. We bin the data in bins of 50 mm, from 0 to 2500 mm. The fitted distribution of points and the

outcome of the fit can be seen in figure 7.10. The best fitting values for a straight line are 8.0 and $-2.7 \cdot 10^{-4}$, for B_0 and B_1 respectively. According to these values, the largest difference between the closest and the farthest modules to the PSU, at distances of 0 and 2500 mm, would be smaller than 10%.

Sigma Threshold Fit - L0Scan Pedestal

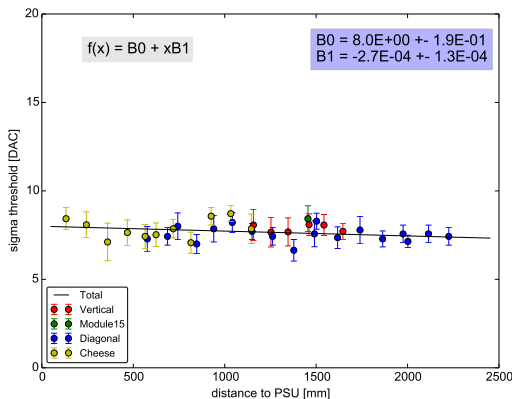


Figure 7.10: Distribution of σ_{thresh} versus the distance to the PSU for all modules and distributions. X axis shows the distance to the PSU, in bins of 50 mm. Each entry on the image represents the mean value and the standard deviation of the measurements contained in that bin for a given configuration. A fit of a straight line to all distributions is also shown (black line) together with the best fitting parameters.

7.4.2 L0 RATE SCAN WITH PULSE INJECTION

SIGMA THRESHOLD

We focus first on the results obtained for σ_{thresh} for the L0 rate scan with pulse injection. Figure 7.11 shows the results for σ_{thresh} for the L0 rate scan with pulse injection for all channels of all available modules for the 4 configurations. The figures show σ_{thresh} as a function of the distance to the power supply unit (left) and as a function of the configuration (right), where the values of each configuration have been labelled with the same color. From figure 7.11 we see that all measured σ_{thresh} are between 10 and 20 DAC units. The values for σ_{thresh} are now larger compared to the ones obtained in the pedestal scan in Section 7.4.1. In order to quantify the dependence of the noise, we fit with a straight line to the distribution of σ_{thresh} shown in figure 7.11, (left) for all modules and distributions together. We bin the data in bins of 50 mm, from 0 to 2500 mm. The fitted distribution of points and the outcome of the fit can be

Sigma Threshold - L0Scan Pulse

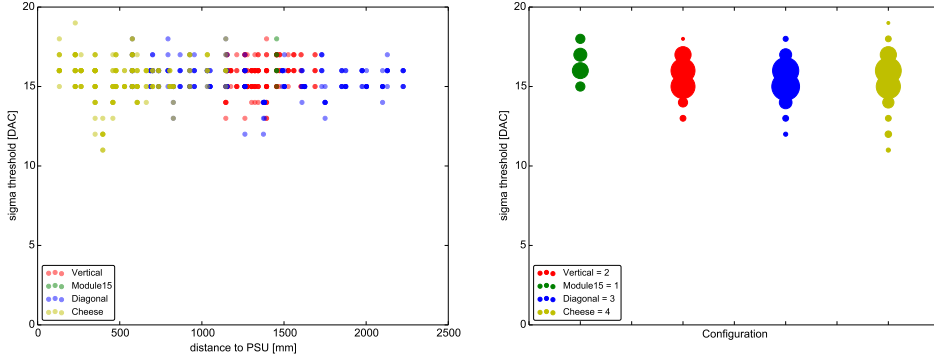


Figure 7.11: Results for σ_{thresh} for L0 rate scan with pulse injection. The figure shows σ_{thresh} for all channels of all modules as a function of the distance to the PSU (left) and module configuration (right). The sizes of the points (right) are proportional to the number of events.

seen in figure 7.12.

The best fitting values for a straight line are $1.6 \cdot 10^1$ and $-2.3 \cdot 10^{-4}$, for B_0 and B_1 respectively. According to these values, the highest difference between the closest and the farthest modules to the PSU, at a distances of 0 and 2500 mm, would be smaller than 5%.

SIGMA PULSE

We focus here on the results obtained for σ_{pulse} for the L0 rate scan with pulse injection. Figure 7.13 shows the results for σ_{pulse} for the L0 rate scan with pulse injection. The figures show σ_{pulse} as a function of the distance to the power supply unit (left) and as a function of the configuration (right), where the values of each configuration have been labelled with the same color. From figure 7.13 we see that all measured σ_{pulse} are between 0 and 1 DAC units. Values for σ_{pulse} are smaller than both values measured previously for σ_{thresh} (for L0Pedestal & L0Pulse). This does not mean that the noise measured here is smaller than before, but that we defined a new estimator to quantify it. However this time, σ_{pulse} is defined in a way that its value has a meaning in distribution theory. We can understand σ_{pulse} as the standard deviation of a Gaussian distribution, and hence, conclude that the measured noise in this test is below one unit of DAC. In order to quantify the dependence of the noise, we fit with a straight line to the distribution of σ_{pulse} versus the distance to

Sigma Threshold Fit - L0Scan Pulse

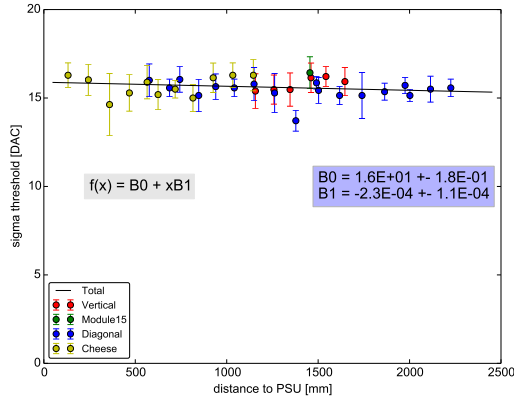


Figure 7.12: Distribution of σ_{thresh} versus the distance to the PSU for all modules and distributions. The x-axis shows the distance to the PSU, in bins of 50 mm. Each entry in the plot represents the mean value and the standard deviation of the measurements contained in that bin for a given configuration. A fit of a straight line to all distributions is also shown (black line) together with the best fitting parameters.

Sigma Pulse - L0Scan Pulse

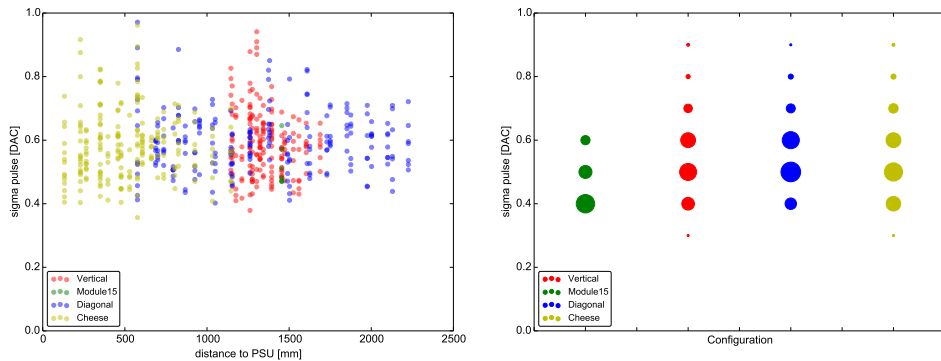


Figure 7.13: Results on σ_{pulse} for L0 rate scan with pulse injection. Figure shows σ_{pulse} for all channels of all modules as a function of the distance to the PSU (left) and module configuration (right). Size of the points (right) is proportional to the number of events.

the PSU shown in figure 7.13 (left), for all modules and distributions. We bin the data in bins of 50 mm, from 0 to 2500 mm. The fitted distribution of points and the outcome of the fit can be seen in figure 7.14. The best fitting values for a straight line are $5.7 \cdot 10^{-1}$ and $1.3 \cdot 10^{-5}$, for B_0 and B_1 respectively. According to these values, the largest difference between the closest and the

farthest modules to the PSU, at distances of 0 and 2500 mm, would be smaller than 6%.

Sigma Pulse Fit - L0Scan Pulse

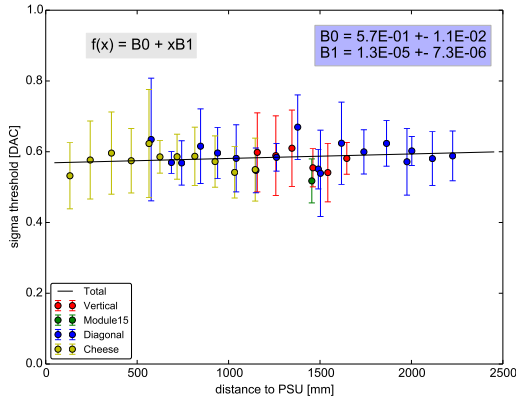


Figure 7.14: Distribution of σ_{thresh} versus the distance to the PSU for all modules and distributions. The x-axis shows the distance to the PSU, in bins of 50 mm. Each entry in the plot represents the mean value and the standard deviation of the measurements contained in that bin for a given distribution. A fit of a straight line to all distributions is also shown (black line) together with the best fitting parameters.

7.4.3 L1 RATE PEDESTAL SCAN

SIGMA THRESHOLD

Figure 7.15 shows the results for σ_{thresh} for the L1 rate pedestal scan. The figures show σ_{thresh} as a function of the distance to the power supply unit (left) and as a function of the configuration (right), where the values of each configuration have been labelled with the same color. From figure 7.15 we see that all measured σ_{thresh} are between 0 and 1 DAC units. By examining the general behaviour we see that the noise measured in this test doesn't depend much on the distance to the PSU nor on the configuration tested. In order to quantify the dependence of the noise, we fit with a straight line the distribution of σ_{thresh} shown in figure 7.15 (left), for all modules and distributions. We bin the data in bins of 500 mm, from 0 to 2500 mm. The fitted distribution of points and the outcome of the fit can be seen in figure 7.16. The best fitting values for a straight line are $1.1 \cdot 10^{-1}$ and -1.2×10^{-5} , for B_0 and B_1 respectively. According to these values, and taking into account the associated error bars, the largest difference between the closest and the farthest modules to the PSU, at distances of 0 and 2500 mm, is compatible with zero.

Sigma Threshold - L1Scan Pedestal

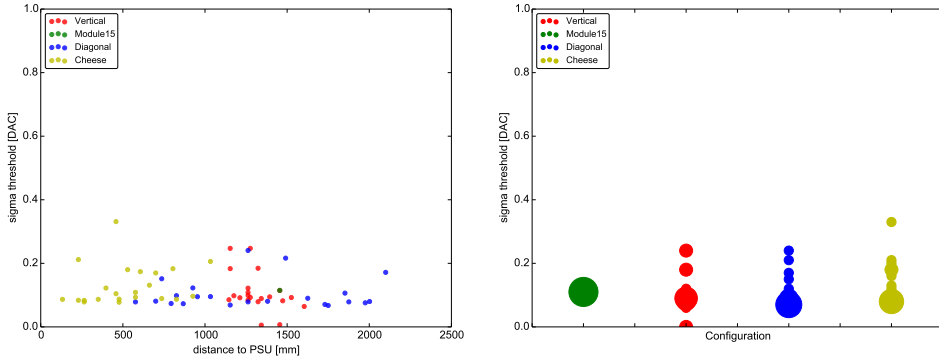


Figure 7.15: σ_{thresh} for L1 pedestal rate scan. The figure shows σ_{thresh} for all modules as a function of the distance to the PSU (left) and module configuration (right). The sizes of the points (right) are proportional to the number of events.

Sigma Threshold Fit - L1Scan Pedestal

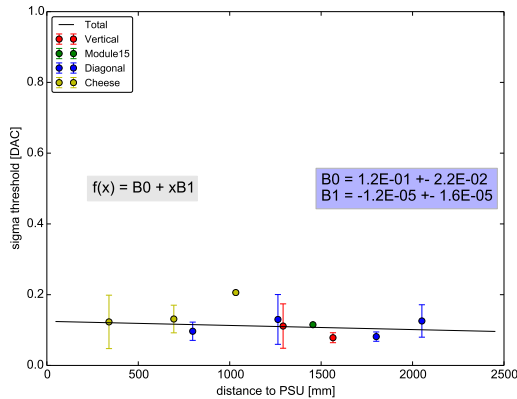


Figure 7.16: Distribution of σ_{thresh} versus the distance to the PSU for all modules and distributions. The x-axis shows the distance to the PSU from 0 to 2500 mm, in bins of 500 mm. Each entry on the image represents the mean value and the standard deviation of the measurements contained in that bin for a given configuration. A fit of a straight line to all distributions is also shown (black line) together with the best fitting parameters.

7.4.4 L1 RATE SCAN WITH PULSE INJECTION

SIGMA THRESHOLD

We focus first on the results obtained for σ_{thresh} for the L1 rate scan with pulse injection. Figure 7.17 shows the results for σ_{thresh} for the L1 rate scan with

pulse injection. The figures show σ_{thresh} as a function of the distance to the power supply unit (left) and as a function of the configuration (right), where the values of each configuration have been labelled with the same color. From

Sigma Threshold - L1Scan Pulse

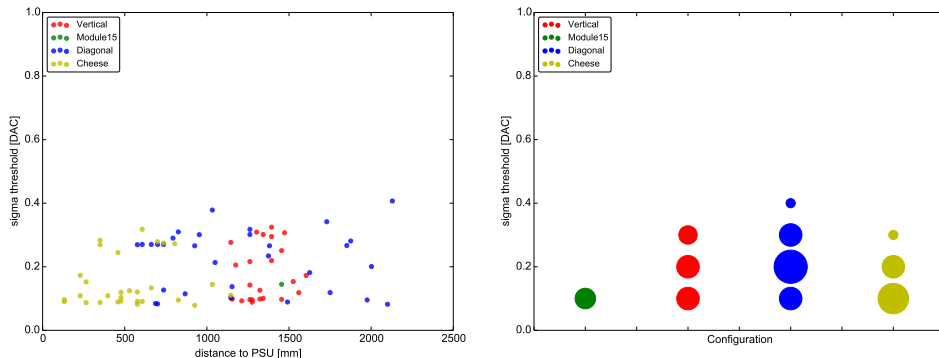


Figure 7.17: σ_{thresh} for L1 rate scan with pulse injection. The figure shows σ_{thresh} for all modules as a function of the distance to the PSU (left) and module configuration (right). The sizes of the points (right) are proportional to the number of events.

figure 7.17, we see that all measured σ_{thresh} are between 0 and 1 DAC units. The noise measured in this test is smaller than one unit of DAC. By inspecting the general behaviour we see that the noise measured in this test doesn't depend much on the distance to the PSU nor on the configuration tested. In order to quantify the dependence of the noise, we fit with a straight line the distribution of σ_{thresh} shown in figure 7.17 (left), for all modules and distributions. We bin the data in bins of 500 mm, from 0 to 2500 mm. The fitted distribution of points and the outcome of the fit can be seen in figure 7.18. The best fitting values for a straight line are $2.1 \cdot 10^{-1}$ and $-2.1 \cdot 10^{-6}$, for B_0 and B_1 respectively. According to these values, and taking into account the associated errors bars, the largest difference between the closest and the farthest modules to the PSU, at a distances of 0 and 2500 mm, is compatible with zero.

SIGMA PULSE

We will focus now on the results obtained for σ_{pulse} for the L1 rate scan with pulse injection. Figure 7.19 shows the results for σ_{pulse} for the L1 rate scan with pulse injection. The figures show σ_{pulse} as a function of the distance to the power supply unit (left) and as a function of the configuration (right), where the values of each configuration have been labelled with the same color. In this case, due to technical reasons explained in section Palacio et al. (2017), only

Sigma Threshold Fit - L1Scan Pulse

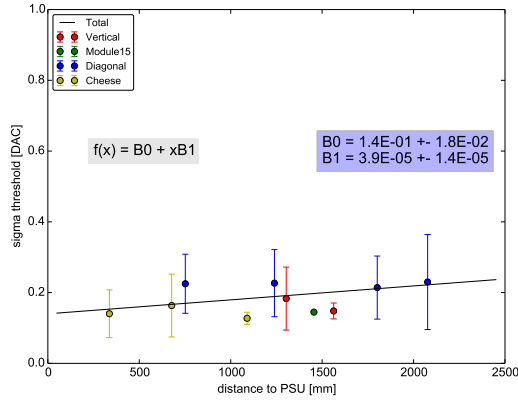


Figure 7.18: Distribution of σ_{thresh} versus the distance to the PSU for all modules and distributions. The x-axis shows the distance to the PSU, in bins of 500 mm. Each entry in the plot represents the mean value and the standard deviation of the measurements contained in that bin. Measurements from different configurations are shown in different colors. A fit of a straight line to all distributions is also shown (black line) together with the best fitting parameters.

two configurations are shown, Diagonal and Cheese. From figure 7.19 we see

Sigma Pulse - L1Scan Pulse

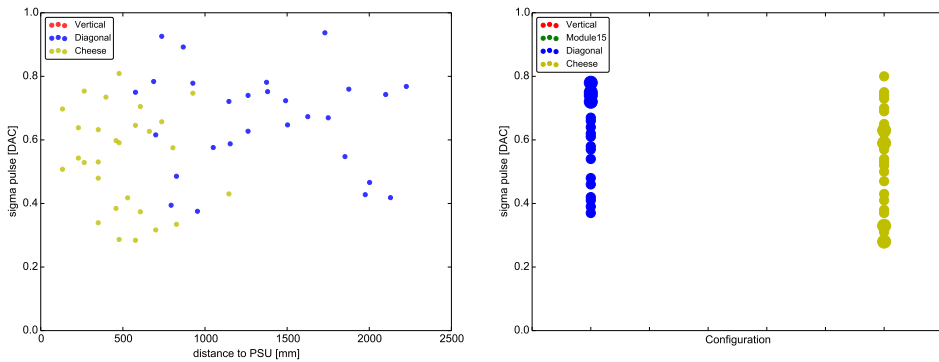


Figure 7.19: σ_{pulse} for L1 rate scan with pulse injection. The figure shows σ_{pulse} for all modules as a function of the distance to the PSU (left) and module configuration (right). The sizes of the points (right) are proportional to the number of events.

that all measured σ_{pulse} are between 0 and 1 DAC units. The noise measured in this test is smaller than one unit of DAC. By inspecting the general behaviour we see that the noise measured in this test doesn't depend much on the distance to

the PSU nor on the configuration tested. In order to quantify the dependence of the noise, we fit with a straight line to the distribution of σ_{pulse} versus the distance to the PSU shown in figure 7.19 for all modules and distributions. We bin the data in bins of 50 mm, from 0 to 2500 mm. The fitted distribution of points and the outcome of the fit can be seen in figure 7.20. The best fitting values for a straight line are $5.8 \cdot 10^{-1}$ and $3.5 \cdot 10^{-5}$, for B_0 and B_1 respectively. According to these values, and taking into account the associated errors bars, the largest difference between the closest and the farthest modules to the PSU, at distances of 0 and 2500 mm, is compatible with zero.

Sigma Pulse Fit - L1Scan Pulse

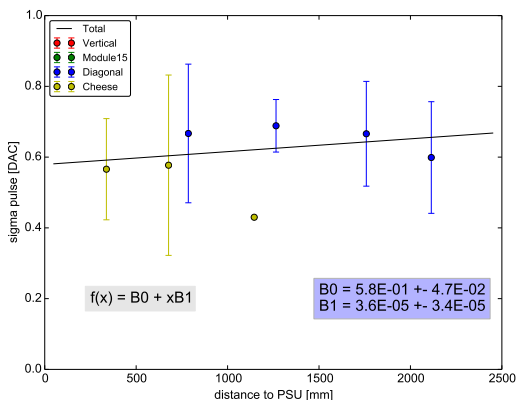


Figure 7.20: Distribution of σ_{pulse} versus the distance to the PSU for all modules and distributions. The x-axis shows the distance to the PSU, in bins of 50 mm. Each entry in the plot represents the mean value and the standard deviation of the measurements contained in that bin. Measurements from different configurations are shown in different colors. A fit of a straight line to all distributions is also shown (black line) together with the best fitting parameters.

7.5 COMPARISON WITH A LINEAR POWER SUPPLY

From Section 7.4 we conclude that the dependence of the noise on the distance to the PSU or the configuration of the modules is small. We will use this information to measure the extra noise due to using switching mode PSU. We took data with module 192.168.1.15 for each of the 4 configurations. Three of the configurations (Vertical, Diagonal and Cheese) used the switching mode PSUs as a source of power, whereas Module15 uses the low noise linear PSU. The linear power supply could only power a single module, since they take ~ 1 Amp each. Differences between those two measurements will tell us about the

extra noise induced by the switching mode PSU.

7.5.1 L0 RATE SCAN FOR MODULE 15

Figures 7.21 (7.22) shows a distribution of the values of σ_{thresh} (σ_{thresh} left and σ_{pulse} right) per each channel of Module 192.168.1.15 (since module 15 was the only module tested being powered by the linear PSU), for the L0 rate scans in the configurations Vertical, Diagonal and Cheese, divided by the value for the same channels for the configuration Module15. The figures also show the mean and the standard deviation values for these distributions. Having 3 configurations powered with the switching mode PSU and 7 channels in Module 15, the mean values and the standard deviation values are calculated with an statistics of 21 points. In all three examples, the distribution values are compatible with 1. Therefore, we did not measure any excess noise induced by the PSU unit.

Switching vs Linear PSU - L0Scan Pedestal

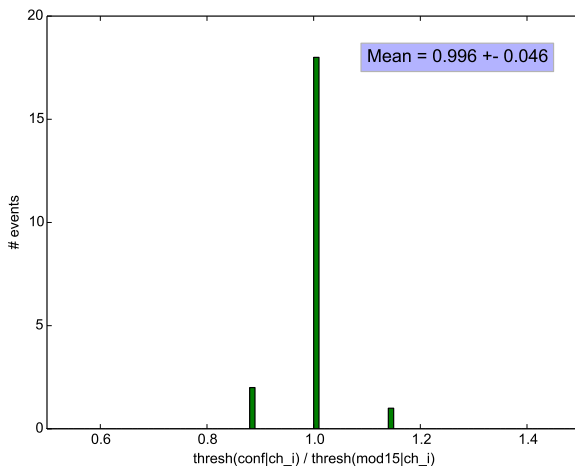


Figure 7.21: σ_{thresh} values for each channel of module 192.168.1.15 for L0 rate scan pedestal for configurations Vertical, Diagonal, and Cheese divided by the value of the same channel for configuration Module15.

7.5.2 L1 RATE SCAN FOR MODULE 15

We also check that measurements were compatible with a hypothesis of no extra noise for the L1 rate scans. Although the data seems to confirm such hypothesis, the statistics this time comes from only 3 data points, one per

Switching vs Linear PSU - L0Scan Pedestal with PI

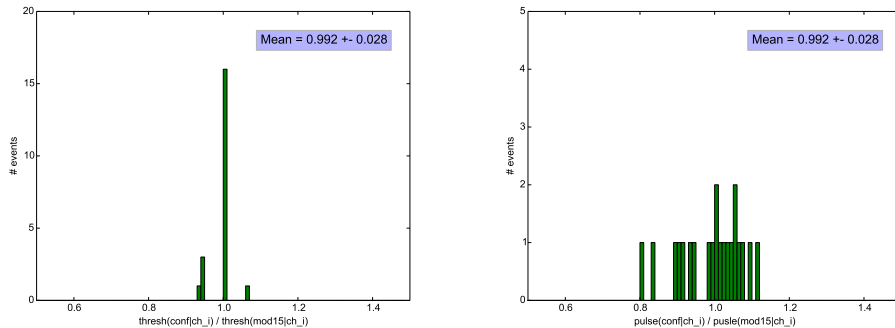


Figure 7.22: σ_{thresh} (left) and σ_{pulse} (right) values for each channel of module 192.168.1.15 for L0 rate scan with pulse injection for configurations Vertical, Diagonal, and Cheese divided by the value of the same channel for configuration Module15.

each configuration (vertical, diagonal and cheese). Any quantification of such compatibility would be meaningless although it may be worth to stress that based on the previous measurements, L1 seems to be less sensitive to noise.

7.6 CONCLUSIONS OF THE TESTS

In September 2016 we tested for noise in the trigger lines of 35M of the first LST prototype using the final configuration of the cluster holder. These tests took place at CIEMAT, where we searched mainly for two different contributions of noise: noise induced due to the use of a switching mode PSU and noise induced by the proximity of neighbouring modules in the final camera configuration. We measure absolute differences in the noise of different modules through the camera below 1 dac unit and relative differences below the 10% level. Although data seem to favour a small correlation between the noise and the distance of the module to the PSU, taking into account their associated uncertainty, this correlation is compatible with zero. We did not measure any significant difference between the noise of the different configurations tested due to the proximity of the neighbouring operating modules. Under the assumption that no noise correlation is present with the configuration of the modules, we also measured the extra noise induced by the switched mode PSU with respect to a low noise linear PSU. No significance extra noise induced by the switched mode PSU was measured. The general conclusion is that, with the current data, we were able to answer the questions we wanted to, but the associated statistics to each measurement, and hence it's associated error bars,

could have been reduced by repeating each measurement shown in here several times, what would have relatively easy to do while running the tests. It is also worth to stress that data also seems to show that L0 scans are more sensitive to noise than what L1 are.

In March 2018, the complete LST camera will be located at IFAE, and hence the opportunity for repeating these same measurements with larger statistics. Since IFAE has available a dark room, similar tests will be performed while having HVs On for the first time with the full camera. We consider this possibility an opportunity to also improve the current measurements, although the numbers we quantify in this document are enough to conclude that the noise induced by the switched mode PSU used for the first LST prototype and the distribution of the clusters on the camera holder are acceptable for operation and compatible with what was expected. On the other side, due to the difficulties we experienced during the data taking in CIEMAT we consider the opportunity to repeat the tests at IFAE, before the final integration in LP, as an opportunity to improve our performance running the tests and hence minimize the possibility of unexpected problems in LP, where the working conditions are going to be much harder. In this direction, a discussion regarding the optimal parameter settings and the best estimators to quantify the noise should happen before the camera arrives to IFAE, in order to improve, if needed, the current situation. Finally, and coming back to the previous statement regarding the associated uncertainties of the measurements presented in here, we would suggest to increase the number of scans taken per configuration (repeat the same measurement more than once), which would require very little extra man power (only requires the extra time to run the tests), during the data taking of the tests but provide much better statistical uncertainty determination.

Part III

Indirect Dark Matter Searches with MAGIC

Chapter 8

TRIANGULUM II

*This project has been done in collaboration with J. Rico and M. Doro.
I also thank F. Saturni for his contribution with CLUMPY computations.*

Using the MAGIC gamma-ray telescopes, we searched for signals produced by DM annihilation in the recently discovered dwarf spheroidal satellite galaxy Triangulum II (Tri II). Based on Tri II first data, the inferred distance and large amount and concentration of DM, predict gamma-ray fluxes from Tri II's to be similar to those from the vicinity of the Galactic Center, making Tri II a prime target for indirect DM searches. With 62 hours of observations, we have not detected any gamma-ray signal from Tri II, and we have consequently set upper limits to the thermally-averaged annihilation cross section. Based on Tri II initial paradigm, we reach 0.4×10^{-24} (0.8×10^{-25}) $\text{cm}^3 \text{s}^{-1}$ for pure $b\bar{b}$ ($\tau^+\tau^-$) annihilation channels. The interpretation of these results however, has been challenged by recent optical data on Tri II star population, that disprove this scenario being Tri II's DM concentration compatible with zero.

8.1 INTRODUCTION

DSphs provide excellent opportunities for studying a multitude of aspects of galaxy formation and cosmology. First, dSphs are especially sensitive to stellar feedback. They have shallow gravitational potentials because they have little mass. As a result, supernovae and even winds from low-mass stars can redistribute the metals in the galaxy’s gas (Larson, 1974) and even expel metals from the galaxy (Dekel and Woo, 2003). Second, and most important in this work, dSphs contain a great deal of DM, exhibiting Mass to Light (M/L) ratios of tens to thousands in solar units (Simon and Geha, 2007; Simon et al., 2015). The overwhelming dominance of DM relative to the luminous matter makes dSphs the ideal targets for examining DM density profiles (Walker et al., 2006) and searching for self-annihilation of the DM particle in gamma-rays (Drlica-Wagner et al., 2015).

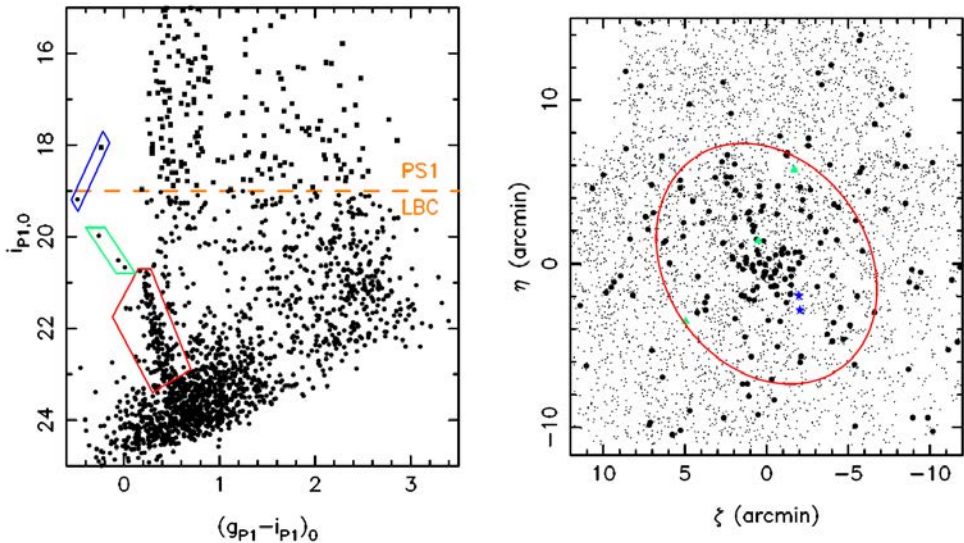


Figure 8.1: **(Figure by Laevens et al., 2015)** *Left*: The combined PS1-Large Binocular Camera (LBC) Color-Magnitude Diagram (CMD) of all sources within the central $2 r_h$ region of Tri II. *Right*: Spatial distribution of all sources corresponding to the CMD on the left. Large dots correspond to the stars falling within the red CMD box in the left panel and show a clear overdensity.

Hierarchical structure formation leads to a clumpy distribution of DM in the MW (Hütten et al., 2016). These clumps are possible targets to search for DM annihilation with present and future γ -ray instruments. Many uncertainties exist on the clump distribution, leading to disputed conclusions about

the expected number of detectable clumps and the ensuing limits that can be obtained from non-detection. During the last years, thanks to observational projects such as SDSS (York et al., 2000), the DES (The Dark Energy Survey Collaboration, 2005) and Pan-STARRS-I (PSI) (Kaiser et al., 2002), dSphs and more DM-dominated systems have been discovered. The association of these faint objects is sometimes unclear (Willman and Strader, 2012): a candidate can be considered a dSph if it shows evidence for DM, including a velocity dispersion in excess of what would be expected from stellar mass alone, or a dispersion in stellar metallicity, which indicates chemical self-enrichment (the present mass of stars alone would not have been enough to retain supernova ejecta); It is considered to be a Globular Cluster (GC) otherwise, normally showing higher luminosity and being more extended. It is becoming apparent however, that previously clear distinction between the compact GCs and dSphs, blurs out for faint systems (Laevens et al., 2015). GCs are among the oldest stellar systems in the Universe (Krauss and Chaboyer, 2003). They have witnessed the earliest stages of star formation and were also present during later epochs of structure formation. Apart from resolved stellar population studies of galaxies, which are restricted primarily to the Local Group, extragalactic GC systems provide one of the best probes to investigate the formation and assembly histories of galaxies (Harris, 1991; Peng et al., 2002; Georgiev et al., 2010), processes that are expected to be dominated by DM, where particle interactions between DM and baryons are the dominant uncertainty to determine the evolution of the system (Ricotti et al., 2016; Conroy et al., 2011; Ibata et al., 2013).

Our target of interest is the recently discovered dSph Tri II (also dubbed Laevens II/Lae II), located at 36 kpc, at RA 02h13m17.4s, Dec: $+36^{\circ}10'42.4''$. Tri-II was discovered (Laevens et al., 2015) in 2015 with the PSI photometric survey, where an overdensity of stars at a given sky direction was detected. These observations were followed up with the LBC (reaching more than 2 magnitudes deeper than PSI). Figure 8.1 (left, taken from Laevens et al., 2015) shows the combined PSI-LBC CMD of all sources within the central 2 half-light radii ($2 r_h$) region of Tri II. The red box highlights the main sequence of the stellar system. Right panel in Figure 8.1 shows the spatial distribution of all sources corresponding to the CMD on the left, where large dots correspond to the stars falling within the red CMD box in the left panel and show a clear overdensity. Tri II's luminosity ($450 M_{\odot}$) and $2 r_h$ (34 pc) are comparable to Segue 1, the faintest galaxy known (see Figure 8.2).

In order to properly assess the problem of the nature of Tri II, spectroscopic

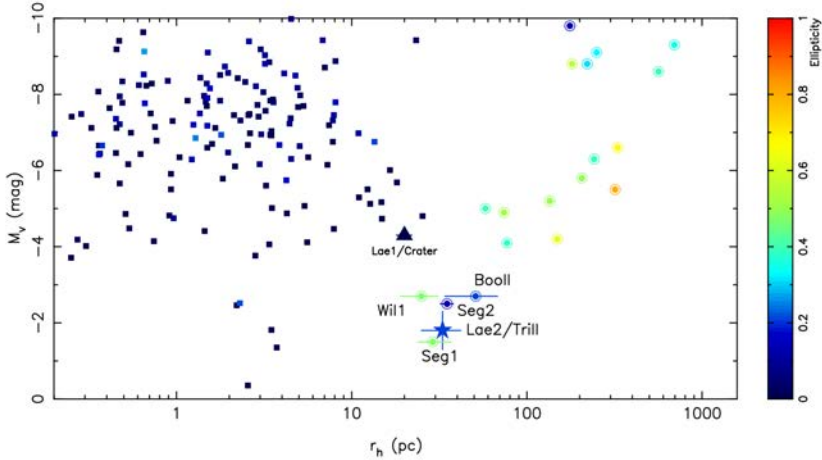


Figure 8.2: **(Figure by Laevens et al., 2015)** The distribution of MW satellites in size–magnitude space. GICs are shown as squares, dSphs are shown as circles and Tri II is represented by the large star symbol. The color scale indicates the ellipticity of the various satellites. Tri II’s ellipticity and half-mass radius show very similar values to those of the four satellites: Seg1, Seg2, BoöII and Wil1.

observations are carried on 6 (Kirby et al., 2015) and 13 (Martin et al., 2016) star members of Tri II respectively. Tri II satisfies the definition of a dSph, it’s velocity dispersion (σ_v) is much too large to be explained by stars alone and has among the lowest measured mean metallicity of any galaxy. A large dispersion in metallicity is found, evidence for chemical self-enrichment, making evidence of a large amount of DM. Even in the assumption that all observed stars are members of Tri II, some of them might still be binaries, where the orbital velocity of the binary would artificially inflate our measurement of σ_v . In order to correct for this effect, Kirby et al. (2015) recalculated σ_v for each of the six subsets of member stars formed by removing one star where still, all $\sigma_{v,i}$ are well separated from zero. More over, Tri II mean radial velocity is measured to be very negative. Hence, it is unclear whether Tri-II is in dynamical equilibrium but, if so, Tri-II would be the most DM-dominated galaxy known, and it would be an excellent candidate for the indirect DM annihilation.

Based on these studies two independent computations on the DM distribution of Tri II were performed (Hayashi et al., 2016; Genina and Fairbairn, 2016). Typically, in order to investigate DM distributions (and their uncertainties) in the dSphs, the dynamical mass model based on *Jeans equation* need to be constructed and applied to the line-of-sight velocity data of dSphs member stars. In fitting dynamical mass models to kinematic data, it is usually assumed that

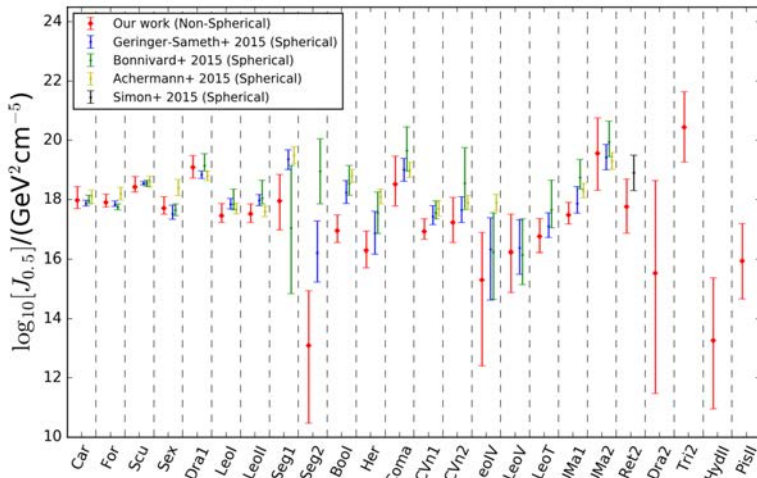


Figure 8.3: **(Figure by Hayashi et al., 2016)** Comparison of $J_{0.5}$. The red symbols denote the results of Hayashi et al. (2016). The blue, green, yellow and black ones are estimated by Geringer-Sameth et al. (2015), Bonnivard et al. (2015), Ackermann et al. (2015) and Simon et al. (2015), respectively.

both, the star members and DM, are spherically distributed (Charbonnier et al., 2012; Geringer-Sameth et al., 2015; Bonnivard et al., 2015). In Hayashi et al. (2016) instead, the astrophysical factor is evaluated using generalized axisymmetric¹ mass models based on *axisymmetric Jeans equation*. Based on the photometric data in Laevens et al. (2015) and the spectroscopic data in Martin et al. (2016); Kirby et al. (2015), Tri II is found to be among the most promising but large uncertain targets for DM annihilation (see Figure 8.3). Due to the limited kinematic sample size (6 and 13 stars), 1σ uncertainties in Tri II values (and in general for these ultra-faint dSphs) are much larger than those of classical dSphs.

Tri II is optimally observed from La Palma, where it culminates at $\sim 7^\circ$ zenith angle, which allows low-energy threshold observations. Based on the exceptionally good prospects of DM detection published by that date, Tri II was observed with the MAGIC telescopes between August 2016 and January 2017 for ~ 60 hours in dark, good weather and stable hardware conditions. The source was observed off-axis, alternating two opposed pointing directions 0.4° away from Tri II. For each of the pointing directions, the residual cosmic ray (CR) background in the signal (ON) region around Tri II was estimated by counting the number of events detected in a symmetric “OFF” region placed

¹ Assuming a non-spherical mass models for dSphs.

at the same relative location with respect to the pointing direction, but during the observations at the complementary pointing direction. The directions of Tri II and of the two pointing positions lie in an axis inclined 140° with respect to the line of constant declination at the Tri II position, which prevents the relatively bright nearby star *Tri Beta-4* ($M = 3.02$) from illuminating the trigger area of the MAGIC cameras (Aleksić et al., 2016b).

In 2017, new spectroscopic data on Tri II were published (Kirby et al., 2017), where additional data were taken for all stars listed in Kirby et al. (2015); Martin et al. (2016). A binary star system was identified among the Tri II star members (previously taken into account when computing σ_v). All updated velocities (but one) are consistent with a single radial velocity within their 1σ error bars, in other words, the velocity dispersion of Tri II can not be resolved. This revision to the velocity dispersion removes the most direct evidence for DM in Tri II. Future optical data on Tri II should confirm or disprove these results, establishing unambiguously its nature, and DM content. We focus here on the data collected by MAGIC during Aug 2017 and Jan 2017 and base our analysis on spectroscopic data on Trig II previous that Kirby et al. (2017).

The rest of this Chapter is structured as follows. In Section 8.2, we discuss more in detail the modelization of DM annihilation in Tri II. In Section 8.3 we describe the strategy for MAGIC observations and data reconstruction, tailored to the DM expectations. In Section 8.4 we provide lower limits for the DM particle annihilation cross-section for several channels, which are later on put into context with the current knowledge we have on Tri II in Section 8.5.

8.2 DARK MATTER CONTENT

In Genina and Fairbairn (2016), evolution of the JFactor vs the integration angle (θ) is shown for Trig-II for the first time (see Figure 8.4, blue). The JFactor is computed based on photometric data from Laevens et al. (2015) and spectroscopic data in Martin et al. (2016), solving the Jeans equation with the public code CLUMPY (Charbonnier et al., 2012), assuming Zhao-Hernquist profile (see Equation 2.11, ZH). We cross-checked these results with CLUMPY (Saturni, private communication), and following the prescription of Bonnivard et al. (2016). We also assumed the JFactor profile from a ZH DM density profile, and obtained the JFactor by running a CLUMPY executable (jeansMCMC) that performs an Markov Chain Monte Carlo (MCMC) Jeans analysis over real data of a dSph (surface brightness Laevens et al. (2015) + stellar kinematics Martin

et al. (2016)). In this way, the parameters for a ZH DM density profile (scale density, scale radius, exponents) of Tri II were estimated. We also removed stars with membership estimate < 0.95 from Martin et al. (2016), selecting a final sample of 14 stars similarly to Genina and Fairbairn (2016). Figure 8.4 (red, Zhao Hern MCMC, ZHMC) shows the computed average properties of the posterior distribution (median + 1sigma confidence interval) after 80.000 repetitions. Such JFactor matches well that of Genina and Fairbairn (2016) and extends until 2° , however, seems to be unphysical since keeps growing for very large values of θ . We also computed the best-fit parameters (maximal likelihood) for the profile from the posterior distribution (black, Zhao Hern Best Fit, ZHBF), from what we obtain $\alpha = 1.2$, $\beta = 5.2$, $\gamma = 0.058$; And the median scale parameters $r_s = 0.17$ kpc and scale density $\rho_s = 2.1 \times 10^{10} [\text{M}_\odot \text{kpc}^{-3}]$. The ZHBF profile, reproduces a finite size of Tri II and leads to total JFactors for the DM annihilation of $J_{\text{ann}}(< 0.5^\circ) = 10^{21} \text{ GeV}^2 \text{cm}^{-5}$. This is almost 2 orders of magnitude higher than Segue 1 (Hayashi et al., 2016), considered to be among the most promising regions in the sky to study DM, where MAGIC has already been observing (Aleksić et al., 2011, 2014c). Finally, we propagated the uncertainties from ZHMC to ZHBF (we assume ZHBF to have the same uncertainties than ZHMC).

DONUT MONTECARLO

In case of DM annihilating with the above ZHBF parameterization, the expected signal extension is ~ 0.3 deg, which means that the optimal angular cut (θ_c) to search for DM is of the order of the telescope point spread function (about 0.1 deg). In order to take into account the extension of the source into the analysis, following the explanation in Chapter 5, we generated the corresponding *Donut MC* for annihilating DM in Tri II. As introduced in Section 2.3, the expected surface brightness profile of γ rays from DM can be obtained from the $dJ/d\Omega$ ($dJ/d\Omega$ in Equation 2.10), from which the Donut procedure generated. Fig Figure 8.5 shows the Tri II DM density integrated on the line of sight (in $\text{GeV}^2 \text{cm}^{-5} \text{sr}^{-1}$), as a function of the offset angle w.r.t. the center of the cluster (in deg). This profile (properly normalized) is taken as the expected brightness profile of the Tri II signal (see Chapter 5).

8.3 OBSERVATION, DATA RECONSTRUCTION AND ANALYSIS

MAGIC observations on Tri II started in August 2016 and lastet until January 2017 (while Tri II is observable from LP), where ~ 60 h were taken. Some

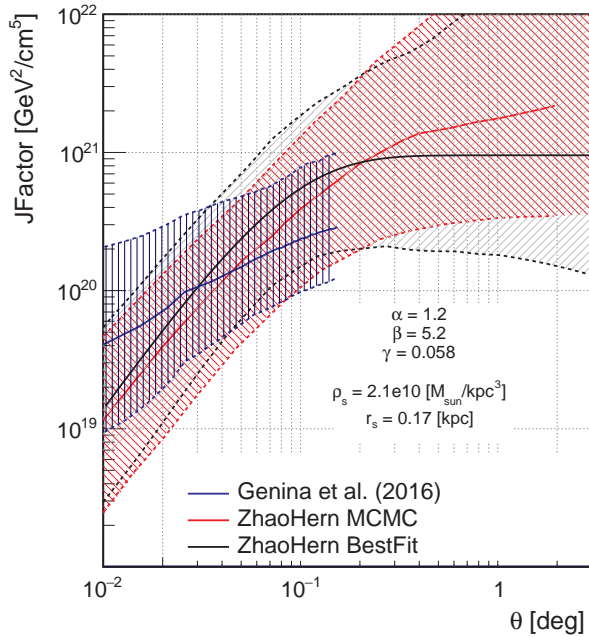


Figure 8.4: JFactor for annihilation as a function of θ (the integration angle) for Triangulum II computed (by Genina and Fairbairn, 2016, (blue)), from ZHM (red), and for ZHBF (with $\alpha = 1.2$, $\beta = 5.2$, $\gamma = 0.058$, $\rho_s = 2.1 \times 10^{10} [M_\odot \text{ kpc}^{-3}]$, $r_s = 0.17$ [kpc]), see text for details. Color bands represent the 1 sigma uncertainty (typically parametrized as a Gaussian function defined in $\text{Log}_{10}(J)$), where uncertainties for *ZH Best Fit* have been obtained from *ZH MCMC*.

IRF	Period	All data [h]	Selected [h]
ST.03.07	2016.04.29-current	63.7	60.2

Table 8.1: MAGIC data collected from Triangulum II between August 2016 and January 2017. All data were taken during the same Hardware Stable Period (HSP) (defined by a unique set of IRFs: *ST.03.07*). Data were taken between 5-35 deg in zenith. *Selected* is data surviving quality cuts on atmosphere transmission.

general characteristics of the available dataset is reported in Table 8.1. The data were taken in wobble mode (Fomin et al., 1994), where both signal (ON) and background control region (OFF) are observed within the same FoV. For both wobble pointing directions, *Tri Beta-4* is inside the FoV (clearly seen as a blob in the DC and L0-trigger distinctions, see Figure 8.6), however, the performance of the instrument is not affected while data taking since the star is out of the trigger region (see Figure 3.2.1). Wobbles are grouped in pairs, in which background estimation for a given wobble direction is measured on

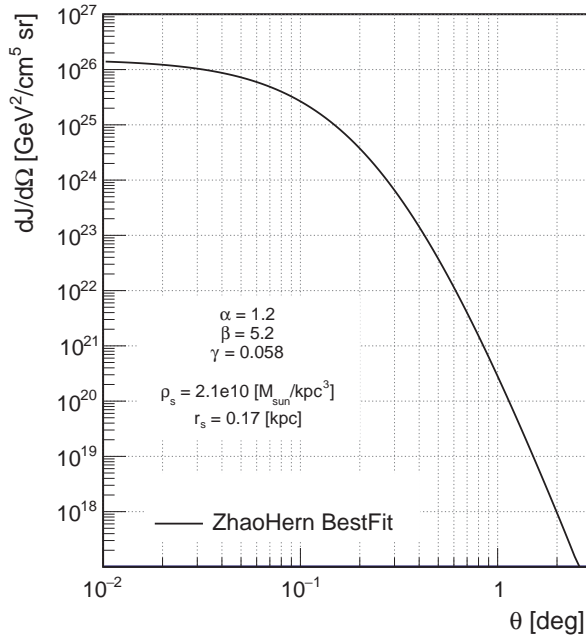


Figure 8.5: Tri II DM density integrated on the line of sight (in $\text{GeV}^2\text{cm}^{-5}\text{sr}^{-1}$), as a function of the offset angle w.r.t. the center of the cluster. This emission profile is used as a seed to generate the *Donut Monte Carlo*, tailored for the case of annihilating DM in Tri II.

the corresponding partner². All Tri II data were taken under the same HSP, labeled as *ST.03.07* (see Table 8.1). Each HSP is analyzed using its specific instrumental response functions (IRFs: comprised of effective area for signal and background, energy migration matrix, energy and angular resolution, energy bias).

QUALITY CUTS

In order to ensure a good observational campaign, and to ensure a comparable azimuth distribution for both wobble pointing positions (which in turns guarantee a low systematic uncertainty in background estimation Aleksić et al., 2014c), observations were followed closely, on a daily basis, where interaction with the crew at the site (operating the telescopes during the data taking) took place each night before observations started. Figure 8.7 shows the distribution of reconstructed events as a function of the azimuth pointing of the telescope, for both wobble directions (left) and the relative difference between the two

² Such method of background estimation keeps the systematic uncertainties in the estimation of the residual background as low as possible (particularly for low energies).

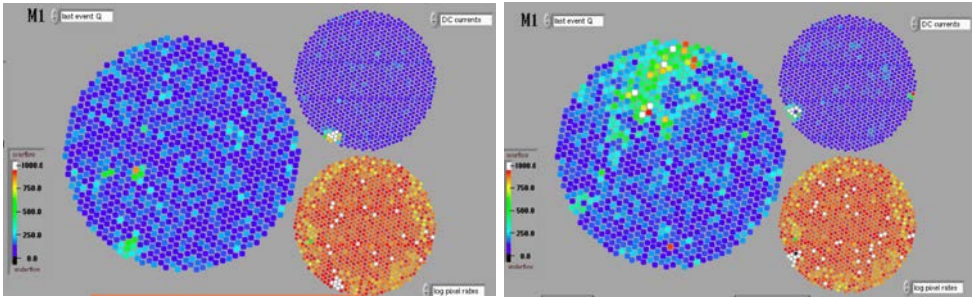


Figure 8.6: Screen-shot taken during the data taking of Tri II data from LP. The wobble pointing was optimized to keep *Tri Beta-4* ($M = 3.02$), as far as possible from both wobble pointing directions. Left panel shows the *collected charge* (Q , big circle left), the DC current (upper-right) and the individual L0-trigger rate (lower-right) for each pixel in MAGIC-I for wobble pointing 1. Right panel shows same information for pointing 2. The position of the *Tri Beta-4* can be clearly seen in both pointing directions, as a blob in the lower left border of the DC and L0-trigger distinctions. The performance of the instrument is not affected since the star is out of the trigger region (see Figure 3.2.1).

Begin	End	LIDAR Transmission		Selected [h]
		Range	AOD [%]	
2016-08-29	2016-11-29	Perfect	$0.85 < t$	60.20
		Good	$0.7 < t < 0.85$	1.05
		Correctable	$0.55 < t < 0.7$	0.38

Table 8.2: Based on LIDAR information taken during the data taking, data was divided into three transmission ranges. *Perfect*, *Good* and *Correctable* (that account for above 85% , 70% and 55% of the standard AOD obtainable during clear nights).

distributions (right).

After each night of observation we also run over the data some standard executables of the standard MARS (Zanin, 2013), so that the correctness of the data was verified) where we also measured the point-like significance of the γ -ray signal at the position of Tri II. By doing this, we did not introduce any significant bias in the analysis since the basic scheme of the analysis was decided beforehand.

As explained in Section 3.2.3, the basic data reconstruction of the data sample for each pointing is performed separately (Aleksić et al., 2012b). Data between 5° and 35° zenith range were selected, based on the NSB light level, allowing data with average median DC current not larger than three times the NSB of a standard moonless night. It was shown by Ahnen et al. (2017c), that this choice does not affect measurably the performance in terms of sensitivity,

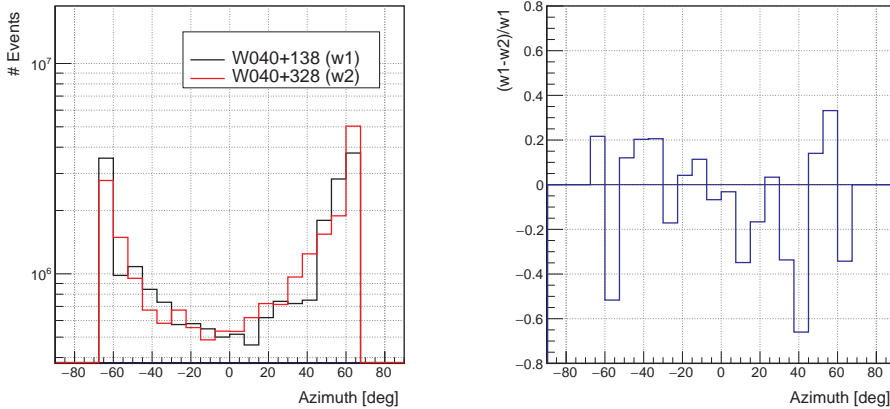


Figure 8.7: Distribution of reconstructed events as a function of the azimuth pointing of the telescope, for both wobble directions (left) and the relative difference between both wobble directions (right).

energy threshold and energy resolution. We further performed a data quality selection based on the atmospheric transmission at the time of observation, as measured by the MAGIC elastic LIDAR (Fruck et al., 2014b). We divided the data into three AOD transmission ranges: *Perfect*, *Good* and *Correctable* (that account for above 85%, 70% and 55%, respectively, of the standard AOD obtainable during clear nights). For several nights during the campaign, the LIDAR telescope could not operate, and hence, no AOD measurement was available. For those nights, we selected only data within the good range of transmission, based on the *Pyrometer*, a second instrument also operating from LP during observations monitoring the weather conditions. As it has been shown (Figure 3.14), both instruments provide compatible measurements for AOD above 85% (note that no transmission correction could be applied based on Pyrometer data only). A summary on the data quality can be found in Table 8.2, where a large fraction of the recorded data has been classified into the Good transmission range. We only focus in here in the analysis of the 60.2 h of such AOD.

Finally, every event surviving this selection is assigned an estimated energy, an estimated arrival direction, and a value of the test statistic for signal/background discrimination, called “hadronness” (h), computed by a Random Forest (RF) boosted tree classification method (Albert et al., 2008b).

DEFINITION OF THE REGION OF INTEREST

In order to search for signal of annihilating DM we define a *circular* signal-search around the source defined by θ_c . Typically in MAGIC, the precise values of h_c and θ_c are optimized using a sample of Crab Nebula observations, in order not to bias the selection. In our case, the Crab Nebula is no longer a good probe, mainly because its emission profile does not follow the one expected for DM annihilation (but point-like instead). In order to optimize the analysis cuts we compute, using fast MC simulations, the expected results in case of no DM signal is present, and select the values of h_c and θ_c optimizing our result for the best sensitivity (the lowest result in the measured thermally averaged cross-section). This procedure has already been applied in other DM searches in MAGIC (Ahnen et al., 2017b)³. We scanned the parameter space of:

$$\begin{aligned} h_c \in (0, 1) \quad \text{or} \quad h_c(E') \in (0, 1) \quad ; \\ 0.1 < \theta_c < 0.2 \quad [\text{deg}] \quad . \end{aligned} \quad (8.1)$$

h_c was selected either energy independent, or in estimated energy bins fixing and energy-independent γ -ray selection efficiency ($h(E')$, computed from the % of MC events that survive). Figure 8.8 shows the relative inverse sensitivity to thermally averaged annihilation cross-section for DM masses of 100 GeV (black), 1TeV (red), 10 TeV (green) and 100 TeV (blue) annihilating into $b\bar{b}$ channel, as a function of θ_c for a fixed Hadronness cut ($h_c = 0.2$). The best sensitivity is obtained for values of $\theta_c = 0.13$ [deg]. Figure 8.9 also shows the relative inverse sensitivity to the thermally averaged annihilation cross-section, this time as a function of h_c (left) and for $h_c(E')$ (right), for a $\theta_c = 0.13$ [deg]. The best sensitivity is obtained for values of $h = 0.2$ (left) or $h_c(E') = 80$ %.

Finally, in Figure 8.10 the sensitivity to thermally averaged annihilation cross-section for DM masses between 100 GeV and 100 TeV annihilating into a $b\bar{b}$ pair, as a function of different combinations of θ_c , h_c and $h_c(E')$. The best sensitivity for most of the DM mass range scanned is obtained for values of $\theta_c = 0.13$ and $h_c(E') = 80$ %, and as a result, these values we use in the analysis.

BINNED LIKELIHOOD ANALYSIS

A first analysis on the whole data sample shows no evidence of γ -ray emission from Tri II position. Figure 8.11 shows the distribution of θ^2 for events in ON

³J. Palacio is a corresponding author of this publication.

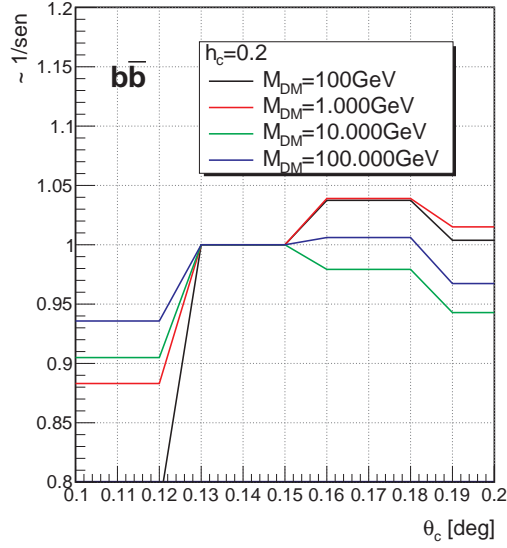


Figure 8.8: Inverse of the sensitivity to the thermally averaged annihilation cross-section relative to its value for $\theta_c = 0.15$ [deg] (computed following the prescriptions explained in the text) for DM masses of 100 GeV (black), 1 TeV (red), 10 TeV (green) and 100 TeV (blue) annihilating into a $b\bar{b}$ pair, as a function of θ_c for a fixed Hadronness cut ($h_c = 0.2$).

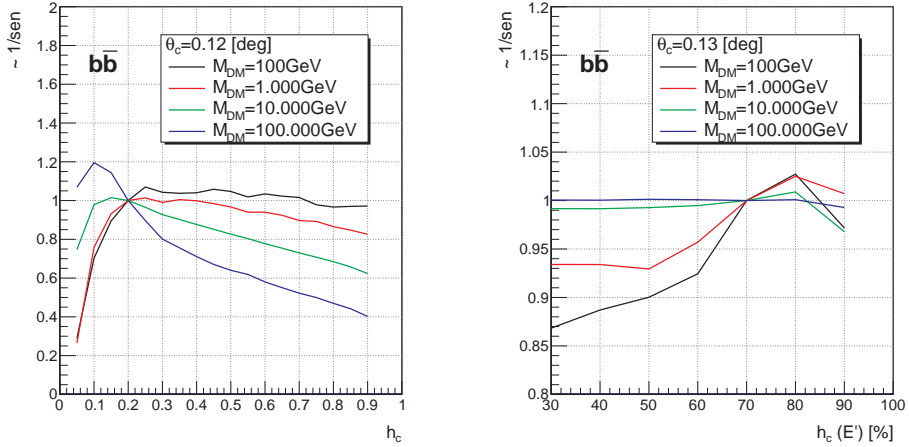


Figure 8.9: Relative inverse sensitivity to the thermally averaged annihilation cross-section (computed following the prescriptions explained in the text) for DM masses of 100 GeV (black), 1 TeV (red), 10 TeV (green) and 100 TeV (blue) annihilating into a $b\bar{b}$ pair, as a function of h_c (left) and $h_c(E')$ (right), for $\theta_c = 0.13$.

(red) and OFF (grey) regions, where 13.769 (~ 14.055) γ -ray candidates were reconstructed inside a circular region of θ_c^2 [deg²] around the ON (OFF) region,

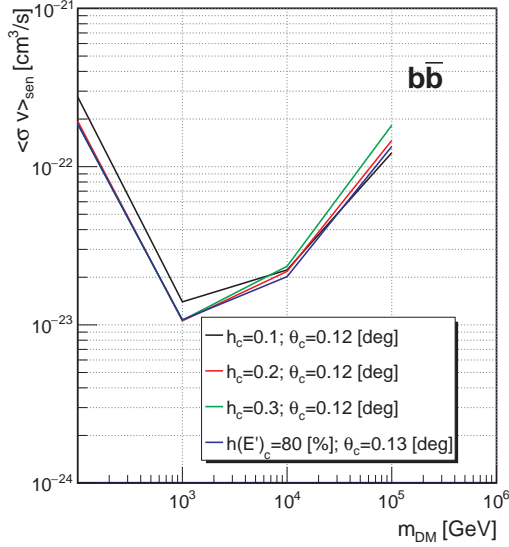


Figure 8.10: $\langle\sigma v\rangle_{eff}$ (computed following the prescriptions explained in the text) for DM masses between 100 GeV and 100 TeV annihilating into a $b\bar{b}$ pair, as a function of different combinations of θ_c , h_c and $h_c(E')$.

and ~ -286 γ -ray candidates are the number of excesses (taking into account the difference in exposure between both regions). Figure 8.11 shows the sky-map centered in the target sky position. Also in this case, no significant γ -ray excess over the background in the sky region of Tri II (yellow dashed circle) is seen.

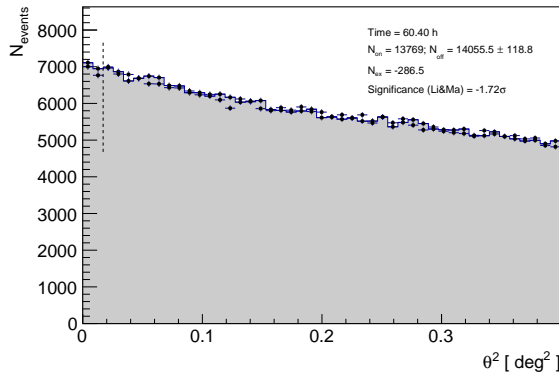


Figure 8.11: θ^2 distributions of ON (blue) and OFF (grey) regions resulting from 60.4 hours of MAGIC stereoscopic observations of Tri II taken between August 2016 and January 2017. The region between zero and the vertical dashed line (at $\theta_c^2 = 0.132$ [deg 2]) represents the ON and OFF integration regions.

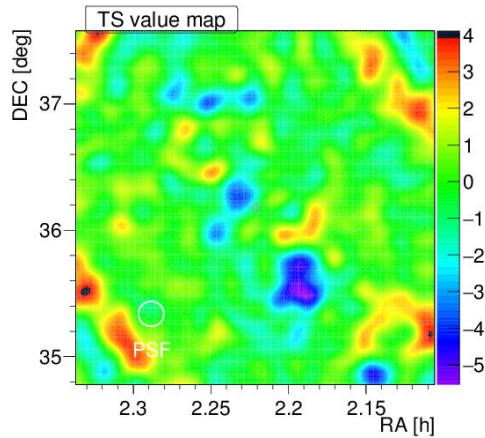


Figure 8.12: Significance sky-map centered at the Tri II sky position from 60.4 hours of MAGIC stereoscopic observations taken between August 2016 and January 2017. Tri II center position is marked with an empty white cross. The color scale represents the test statistic value distribution. The dashed yellow circle represents the region defined by $\theta_c = 0.13$ [deg]. The MAGIC PSF (for the given analysis cuts) of 0.11° is also shown (white circle).

We follow here the full likelihood method FL introduced in Section 3.2.4 We computed the average γ -ray spectrum per annihilation process (dN/dE) for a DM particles of masses between 100 GeV and 100 TeV decaying into the SM pairs $b\bar{b}$, $\tau^+\tau^-$, $\mu^+\mu^-$ and W^+W^- . The joint likelihood entering λ_P (see Equation 3.7) is the product of two likelihood functions, one per considered pointing direction (i), each of which can be written as: with $\log_{10}(J_{\text{obs}}/\text{GeV}^2\text{cm}^{-5}) = 20.98 \pm 0.55^4$ (see Figure 8.4); As previously mentioned, we parametrize the uncertainty in the background estimation as a systematic uncertainty in the parameter τ_i , $\sigma_\tau^{\text{sys}} = 1.5\%$, added in quadrature to the statistical one. This value has been established on the base of a dedicated performance study (Aleksić et al., 2016a).

Finally, A_{eff} is the effective collection area (after all analysis cuts) and G the probability density function of the energy estimator, both computed from a MC simulated γ -ray dataset following the spatial distribution expected for DM-induced signals from Tri II (see Chapter 5).

⁴ σ_J is evaluated at $\theta_c = 0.13$ [deg], the signal integration angle.

We define independent likelihood functions for each HSP, *Zd range* and *wobble pointing* (see Table 8.3). Each likelihood term, based on independent data samples and IRFs, is linked to the rest through the common DM parameter, $\langle\sigma v\rangle$ (as can be seen in Equation 3.5). In our case, 2 independent likelihood

HSP	ST.03.07
Zenith angle	5 – 35
Wobble pointing	W0.4 (+148, +328)

Table 8.3: List of the different bins for which independent likelihoods are defined. According to the classification presented in the table, binned in *hardware stable period*, *Zd range* and *wobble pointing* (see Table 8.3), 2 independent samples have been generated.

terms (one for each wobble pointing).

8.4 RESULTS: CONSTRAINTS TO THE CROSS SECTION

In this section we present results on thermal averaged cross-section ($\langle\sigma v\rangle$) for DM particles annihilating into different SM particle pairs, achieved with ~ 60 hours of good quality data from the Tri II dSph. The search is performed for DM particles of masses between 100 GeV and 100 TeV for annihilating scenarios into $b\bar{b}$, W^+W^- , $\tau^+\tau^-$ and $\mu^+\mu^-$, annihilating modes representative for most of typical annihilating DM models. When minimizing the likelihood, we restricted the value of the cross-section to the physical range ($\langle\sigma v\rangle \geq 0$).

Figure 9.12 shows the one-sided 95% C.L. upper limit on $\langle\sigma v\rangle$ for DM particles annihilating into a $b\bar{b}$ (top-left), W^+W^- (top-right), $\tau^+\tau^-$ (bottom-left) and $\mu^+\mu^-$ (bottom-right) pair, achieved with the Perseus cluster data sample, obtained with a binned likelihood analysis (from $E'_{\min} = 80$ to $E'_{\max} = 10^6$ GeVs divided in $N_{\text{bins}} = 10$ bins equidistant in $\log E'^5$). In addition, the two-sided 68% and 95% containment bands for the distribution of limits under the null hypothesis are also reported. The containment bands were computed from the distribution of the values of $\langle\sigma v\rangle^{UL}$ obtained from the analysis of 300 realizations of the null hypothesis ($\langle\sigma v\rangle = 0$), consisting of toy MC simulations (for both signal and background regions), assuming the same exposures as for the real data, and with the factors τ_i treated as nuisance parameters in the likelihood function (as for the data). It also shows the thermal relic cross-section ($\langle\sigma v\rangle_{th} = 3 \times 10^{-26} \text{ cm}^3 \text{ s}^{-1}$) typically considered a reference value for WIMP

⁵ Empty bins were allowed to re-adjust and merge with neighboring ones.

8.4 RESULTS: CONSTRAINTS TO THE CROSS SECTION

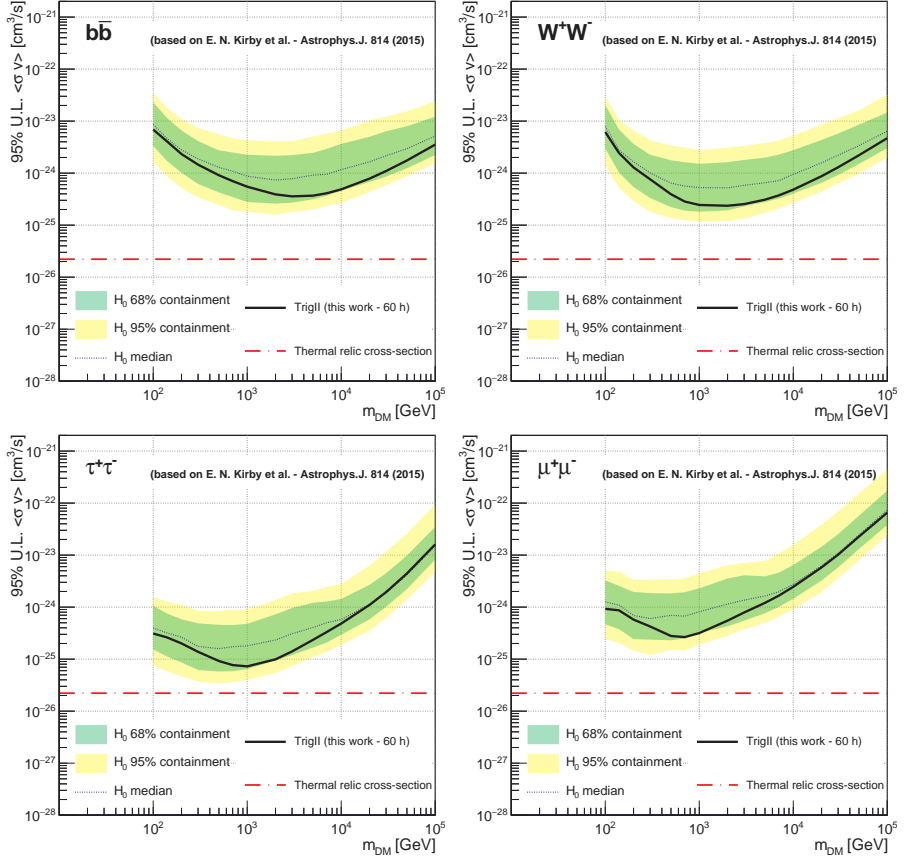


Figure 8.13: One-sided 95% CL upper limits on the thermally-averaged cross-section of DM particles annihilating, into $b\bar{b}$ (top left), W^+W^- (top right), $\tau^+\tau^-$ (bottom left) and $\mu^+\mu^-$ (bottom right) from 60 h of good quality data from the Tri-II dSph. Green (yellow) band corresponds to the 1- (2)- σ distribution of same estimator computed from 300 simulations of the null hypothesis (no DM signal) of the same data sample. $\langle\sigma v\rangle_{th}$ is also shown in the plot as a reference value. No evidence of DM annihilation is found in either channels.

searches.

We see that our result is within the 2-sigma band of the null hypothesis, for the full range of DM masses explored, and so we cannot claim any evidence of DM in Tri II annihilating into neither channel: $b\bar{b}$, W^+W^- , $\tau^+\tau^-$ nor $\mu^+\mu^-$. We reach sensitivities of $2 \times 10^{-25} \text{ cm}^3 \text{ s}^{-1}$ in all channels, and only factor 10 above $\langle\sigma v\rangle_{th}$. We will put our results in context, w.r.t. previous MAGIC and NON MAGIC results, in the next section.

8.5 CONCLUSIONS AND REMARKS

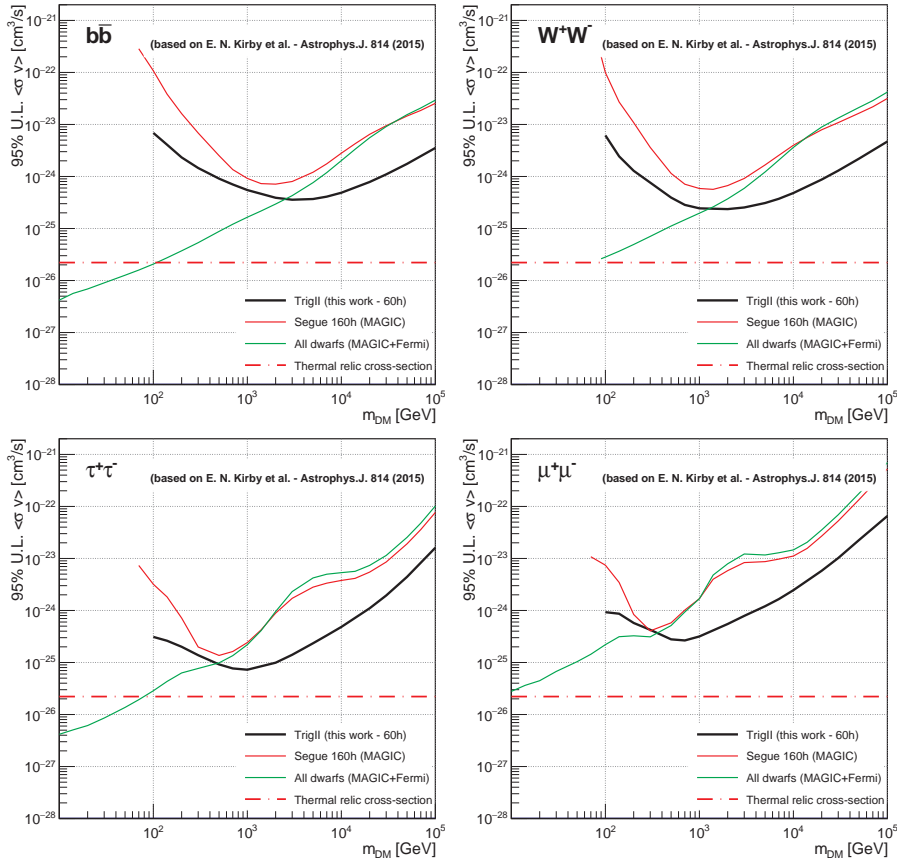


Figure 8.14: 95% CL upper limits on the thermally-averaged cross-section of DM particles annihilating, into $b\bar{b}$ (top left), W^+W^- (top right), $\tau^+\tau^-$ (bottom left) and $\mu^+\mu^-$ (bottom right) from 60 h of good quality data from the Triangulum dwarf spheroidal galaxy (black, this work), compared with previous MAGIC results on Segue I (Aleksić et al., 2014c) and with Fermi-MAGIC combined search on dwarfs (Ahnen et al., 2016b). The red-dashed-dotted line shows the thermal relic cross-section from Ref. Steigman et al. (2012). Trigg II results, reaching sensitivities of 0.2×10^{-24} $\text{cm}^3 \text{s}^{-1}$ in all channels, are almost one order of magnitude that previous MAGIC results, and the most constraining results for DM masses above ~ 2 TeV. Note that Trigg II results are based on Kirby et al. (2015), where the interpretation of DM on Trigg II has been later challenged in Kirby et al. (2017).

Figure 8.14 shows the comparison of our results (obtained with 60 h on Trigg II) with those from MAGIC on 158 hours on Segue 1 (Aleksić et al., 2014c), *Fermi*-MAGIC combined analysis of data on 15 DGs (Ahnen et al., 2016b). Galactic Center halo with HESS (Abdallah et al., 2016). MAGIC results can be directly comparable between them, although there has been differences in the

treatment on the nuisance parameters between both analysis ($\sigma_{\tau}^{sys} = 0$ was assumed for Segue analysis). More recent *Fermi*-LAT results include Tri II among the analyzed targets (Albert et al., 2017b) however, in order to compare both results one must consider important caveats, given how they assume a much lower JFactor obtained from a purely empirical formula (roughly two orders of magnitude lower than what we considered), which would make the comparison artificially desfavourable for *Fermi*-LAT.

Our new result represents an improvement of a factor ~ 10 with respect to those from the previous best dSph, Segue 1, and as such is the most constraining experimental limits to $\langle\sigma v\rangle$, obtained from dSphs, of WIMPs in the mass range above 2 TeV. However, the latest spectroscopic data on Tri II Kirby et al. (2017) removes the most direct evidence for DM in Tri II, challenging previous interpretations on Tri II DM content Kirby et al. (2015); Martin et al. (2016). The authors revise their estimate in σ_v , based on the new data and taking into account the newly discovered binarity member and claim that all but one updated velocities of the 13 (1 from Kirby et al. (2015), 7 from Martin et al. (2016) and 5 from both) member stars of their work are consistent with a single radial velocity within their $1\text{-}\sigma$ error bars so that they cannot resolve the velocity dispersion of Tri II. This is in small tension with a previous statement in Kirby et al. (2015) where they removed the same star on the calculation. We also stress that, Albert et al. (2017b) empirical approach, that assumes the recently discovered stellar systems to occupy similar DM halos to the population of known dSphs scaling inverse square of their distances, gives also inconsistent results with Kirby et al. (2015); Martin et al. (2016); Kirby et al. (2017).

Future optical data on Tri II should confirm or disprove these results, establishing unambiguously its nature, and DM content. Let us repeat once more, to avoid confusion, the Tri II results presented are based on Kirby et al. (2015); Martin et al. (2016), Tri II's first spectroscopic data.

Chapter 9

THE PERSEUS GALAXY CLUSTER

*This project has been done in collaboration with J. Rico, M. Doro. and M. Vazquez-Acosta.
I also thank M. A. Sanchez-Conde and F. Zandanel for their time and discussion.*

CGs are the largest known gravitationally bound structures in the Universe, with masses around $10^{15} M_{\odot}$, a large fraction of it in the form of DM. The ground-based IACT MAGIC made a deep survey of the Perseus CG with almost 400 h between 2009 and 2017. This is the deepest ground based observational campaign on any CG performed so far in the VHE regime. We search for γ ray signals from DM particles decaying into standard model pairs in the mass range between ~ 200 GeV and ~ 200 TeV. We apply a likelihood analysis optimized for the spectral and morphological features expected from DM decay and find no evidence of decaying DM achieving sensitivities of $\sim 10^{26}$ s in all channels considered. Our results are better than previous MAGIC results, and the most constraining results for DM masses above ~ 20 TeV.

9.1 INTRODUCTION

CGs are the largest and most massive gravitationally bound systems in the Universe, with radii of few Mpc and total masses $M \sim (10^{14} - 10^{15}) M_{\odot}$, of which galaxies, gas, and DM contribute roughly for 5%, 15% and 80%, respectively (see Sarazin, 1986; Dai et al., 2007, for a general overview). CGs are powerful cosmological tools for testing the evolution of the Universe (see Voit, 2005). While no CG has been firmly detected as a γ -ray source so far (Reimer et al., 2003; Perkins et al., 2006; Aharonian, 2009a,b; Domainko et al., 2009; Galante, 2009; Kiuchi et al., 2009; Acciari et al., 2009), they are expected to be γ -ray emitters on the following general grounds: (1) CGs are actively evolving objects and being assembled today, in the latest and most energetic phase of hierarchical structure formation; (2) CGs serve as cosmic energy reservoirs for powerful sources such as radio galaxies and supernova-driven galactic winds; (3) Finally, CGs contain large amounts of gas with embedded magnetic fields, often showing direct evidence for shocks and turbulence as well as relativistic particles. Reviews on non-thermal processes in CGs as well as numerical simulations are found in Kushnir et al. (2009); Dolag et al. (2008).

In the cosmological hierarchic clustering model, large-scale structure grow hierarchically through merging and accretion of smaller systems into larger ones, and CGs are the latest and most massive objects to form (see Peebles, 1994). For our purpose, it is worth noting that CGs now a days, present very large M/L ratios and considerable overdensities, which are crucial for indirect DM searches. Despite the fact that they are not as near as other potential DM candidates, as the dSph (Acciari et al., 2010), the large DM masses of CG makes them ideal laboratories for the search of a DM γ -ray signal (Jeltema et al., 2009; Pinzke et al., 2009). This is specially true for exploring the parameter space of decaying DM candidates, where the fluxes of DM coming from CG are expected to be larger than the ones from other dSphs, typically considered optimal sources for indirect DM searches. Figure 9.1 shows how, in general, the JFactor for annihilation, J_{ann} , (decay, J_{dec}) of the dSphs is higher (lower) than the one from the Perseus CG.

The Perseus CG has been largely considered among the most promising targets for the detection of γ rays coming from neutral pion decay resulting from hadronic CR interactions with the ICM (Aleksić et al., 2010a; Pinzke and Pfrommer, 2010; Pinzke et al., 2011). The Perseus CG is a cool-core cluster, the brightest in X-rays, and the dynamics of its galaxies hints that about 80% of the total matter content is in the form of DM, thus amounting for

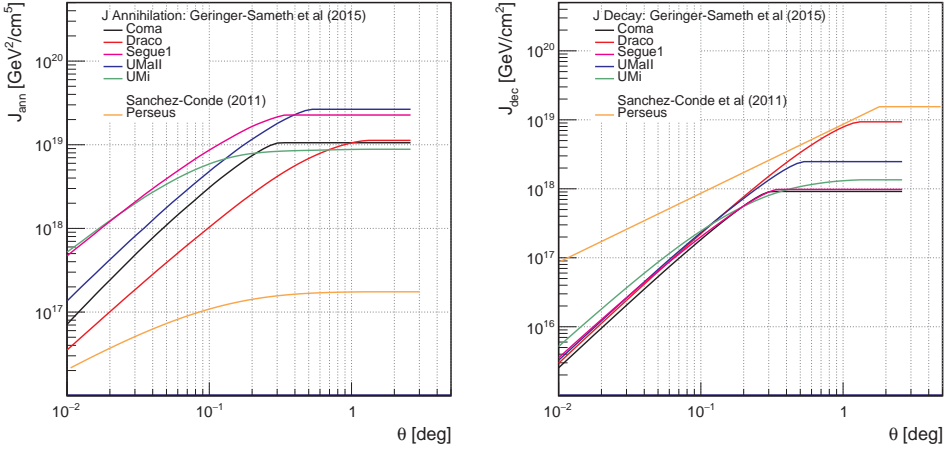


Figure 9.1: Comparison of the JFactor for the annihilation (J_{ann} , left) and the decay (J_{dec} , right) scenario, in units of $\text{GeV}^2\text{cm}^{-5}$ and GeVcm^{-2} respectively, as a function of the integration angle (θ), for Perseus CG (Sanchez-Conde et al., 2011) and for a set dSphs (Coma, Draco, Segue 1, UMa I and UMa II from Geringer-Sameth et al., 2015), typically considered for indirect DM searches.

about $10^{14} M_{\odot}$. The Perseus CG also hosts three bright radio galaxies (Ryle and Windram, 1968): NGC 1275, the central dominant galaxy of the cluster, NGC 1265, archetype of a head-tail radio galaxy, in which the jets are bent by their interaction with the ICM, and IC 310, a peculiar object that shows properties of different classifications and which could be an intermediate state between a BL Lac and a radio galaxy. The AGNs of both NGC 1275 and IC 310 show a bright and variable γ -ray emission in the energy ranges the *Fermi*-Large-Area Telescope (*Fermi*-LAT, Neronov and Vovk, 2010; *Fermi* LAT Collaboration, 2010).

MAGIC has been observing the Perseus CG since 2009, in several distinct campaigns in which different scientific cases were investigated using a common dataset, what favoured the dedication at which MAGIC has been monitoring the Perseus CG region. Note that, in general, IACTs suffer from limited duty cycles (in terms of limited hours of *clean-dark* conditions at the sites where observations are performed); and limited FoV (of the order of the degree) what forces the community to devote dedicated observations for nearly each individual source of interest (making recyclability of data very unlikely). These MAGIC campaigns however, proved very fruitful: produced the strongest limits on CR acceleration in the core of the cluster and the cosmic ray to thermal

pressure (Aleksić et al., 2010a, 2012c), the Active Galactic Nuclei (AGN)¹, NGC 1275 at the center of the cluster was clearly detected and modeled (Aleksić et al., 2012d, 2014b), as well as the detection and interesting results came from the peculiar radio-galaxy IC 310 located at 0.6° from the Perseus CG center, providing interesting clue in the mechanism of acceleration of cosmic rays close to black holes (Aleksić et al., 2010b, 2014a,d).

Here we focus on the search of signatures of DM decays from the Perseus CG. The Perseus CG was carefully chosen over other nearby CGs after considering the expected γ -ray emission from decaying DM and, of course, taking into account the large data sample MAGIC had accumulated during the last years. We search a data sample of 200 hours of clean-dark data of the Perseus CG for signals of decaying DM particles in the mass range from 200 GeV to 200 TeV decaying into $b\bar{b}$, $\tau^+\tau^-$, $\mu^+\mu^-$ and W^+W^- pairs, representative for most of typical decaying DM models, in the extended region of the DM halo surrounding the center of the Perseus CG (using some assumptions on the DM content in the Perseus CG). We take into account the astrophysical γ -ray emission of the central radio-galaxy NGC 1275 during these campaigns, in order not to be miss-interpreted as DM. We compute the 95% CL lower-limit decay-lifetime and find no evidence of DM. Our results are better than previous results on decaying DM obtained with MAGIC on Segue 1 (Aleksić et al., 2014c), and the most constraining results for DM masses above 2×10^4 GeV, and the most constraining from ground based experiments for all DM masses. Moreover, these are the first results on decaying DM within the VHE community based on CGs data.

The rest of the Chapter is structured as follows. In Section 9.2, we discuss more in detail the decaying DM scenario in Perseus, our knowledge on the DM distribution in the cluster, and the DM decay flux expected at the Earth. In Section 9.3 we describe the strategy for MAGIC observations and data reconstruction, tailored on the DM expectations. In Section 9.4 we provide lower limits for the DM particle lifetime for several decay channels, which are later on put into context in Section 9.5.

¹ A compact region at the center of a galaxy that has a much higher luminosity over at least some portion of the electromagnetic spectrum than normal.

9.2 DARK MATTER CONTENT

In Sanchez-Conde et al. (2011) a comparison of indirect DM searches between dSph and CG is presented, in order to elucidate which object class is the best target for indirect searches with γ rays. The authors build a mixed sample containing some of the most promising nearby dSphs and local CGs, and compute their DM annihilation and decay flux by making use of the latest modeling of their DM density profiles. For the decay case, the authors claim that among CGs, *Virgo* represents the one with the highest flux, however, its large spatial extension can be a serious handicap for IACT's observations and subsequent data analysis, and they consider the Perseus CG, to be a good alternative due to its more moderate emission region size.

Following Sanchez-Conde et al. (2011) we parametrize the distribution of dark matter in the Perseus CG region with a Navarro-Frenk-White (NFW) profile (Zhao-Hern (ZH), Equation 2.11, where $\alpha = 1$, $\beta = 2$ and $\gamma = 1$, Navarro et al. (1996)),

$$\rho(r) = \frac{\rho_s}{r/r_s (1+r/r_s)^2}$$

with

$$r_s = 0.477 \text{ Mpc};$$

$$\rho_s = 7.25 \times 10^{14} \text{M}_\odot \text{Mpc}^{-3}. \quad (9.1)$$

The Perseus CG is located at 77.7 Mpc ($z=0.0183$) distance, and is expected to host around 10^{14} M_\odot of DM. In comparison, one of the most promising dSphs to search for DM, Segue 1 (already introduced in Chapter 8) is at a distance of 23 kpc ($23 \cdot 10^{-3} \text{ Mpc}$) with a total mass of about $0.6 \cdot 10^6 \text{ M}_\odot$. In other words, the Perseus CG is 10^3 times farther away, and contains 10^6 times more DM, than Segue I. Figure 9.1 (remember the dependence on ρ^n in Equation 2.9) shows the JFactor of the Perseus CG and Segue I, where the the JFactor for annihilation, J_{ann} (decay, J_{dec}) of Segue 1 is higher (lower) than the one from the Perseus CG. This is in general true, for most of CGs and dSphs typically considered for indirect DM searches. For the case of decaying DM in the Perseus CG, this results in a *total* J_{dec} of $1.5 \times 10^{19} \text{ GeV cm}^{-2}$, among the highest JFactors computed, making the Perseus CG one of the most suitable regions of the sky to study the parameter space of decaying DM. Note however that, in Sanchez-Conde et al. (2011), no uncertainties in neither of the two parameters defining the profile (r_s , ρ_s) are given. Table 9.1 shows the current available measurements on the Virial mass of Perseus. Based on Table 9.1, and being conservative, an educated guess for the uncertainties on the Perseus mass estimation can be $\sim 60\%$, that should propagated linearly

	M_{200} [$10^{14} M_{\odot}$]	M_{500} [$10^{14} M_{\odot}$]
Reiprich and Boehringer (2000)	$10.80^{+0.46+30\%}_{-0.41-30\%} h_{50}^{-1}$	$6.84^{+0.29+30\%}_{-0.26-30\%} h_{50}^{-1}$
Chen et al. (2007)	-	$6.08^{+1.55}_{-2.85}$

Table 9.1: Summary of measurements of the Virial mass of the Perseus CG, M_X , is the mass enclosed at a radius R_X , the distance at which the mass density, reaches X times the critical density of the universe. h_{50} is the *Hubble constant* (H_0) divided by 50 and is ≈ 1.4 .

to JFactor (for the decay case only). One of the reasons for the lack of measurements on the mass of the Perseus CG, is that Perseus is very extended in the sky ($\sim 6^\circ$ diameter, see Figure 9.1), so more modern satellites with better resolution but typically smaller field-of-view have problems in dealing with it. These mass measurements however, only provide an estimation on the precision with which the total matter density in Perseus is measured. They do not provide information on how well the distribution of DM in Perseus is known. A correct determination on the associated uncertainties in r_s and ρ_s , and hence on the JFactor as a function of the integration angle θ , is rather complex and was considered to be out of the scope of this work. In order to do that, one would need to take into account both, data on the cluster mass (i.e: through the gas density Reiprich and Boehringer (2000); Chen et al. (2007), galaxy distribution among the cluster, and optical data on weak or strong lensing) and simulations on the cluster formation Klypin et al. (2016) in order to generate the matter density profiles. Moreover, for very rich baryon environments (as the case of clusters) one should even consider implications on the interaction between DM and baryons (Duffy et al., 2010). Some works on this direction have been performed for other clusters, as the case of Coma (Colafrancesco et al., 2006) or Fornax (Ando and Nagai, 2012), but is still lacking for Perseus. Taking into account the current available information on Perseus and, in order to proceed with the analysis, and benefit from the large data sample we present in here (and also, not to bias the analysis in direction), we considered no uncertainties (a perfect knowledge) on the astrophysical factor of Perseus. We stress however, that typical associated uncertainties for decay DM for cluster of galaxies are (in relative units) substantially lower than the associated uncertainties typically considered for annihilating DM in dwarfs, basically for two different reasons: The first one related to the different dependence in ρ^n for the two cases in Equation 2.9, as explained before; The second one due to the statistics associated to the measurements to determine the DM content of the object. From the current available studies, we estimate that a conservative estimate of the total JFactor uncertainty amounts to 60%, which would change

the DM decay upper limits by a factor 2. More detailed studies are needed on the decay JFactor uncertainties for CGs in the future.

DONUT MONTECARLO

According to the above NFW parameterization of the DM density profile, the virial radius is seen under an angle of $\sim 1.5^\circ$ (Matsushita et al., 2013), much larger than the telescope angular resolution (PSF $\sim 0.1^\circ$). In order to take into account the extension of the source in the analysis, following the explanation in Chapter 5, we generated the corresponding *Donut MC* sample for decaying DM in the Perseus CG. The expected emission profile of the signal can be obtained from $dJ/d\Omega$ ($dJ/d\Omega$ in Equation 2.10), and is used as an input from where the Donut MC is generated. Fig Figure 9.2 shows the Perseus CG $dJ/d\Omega$, as

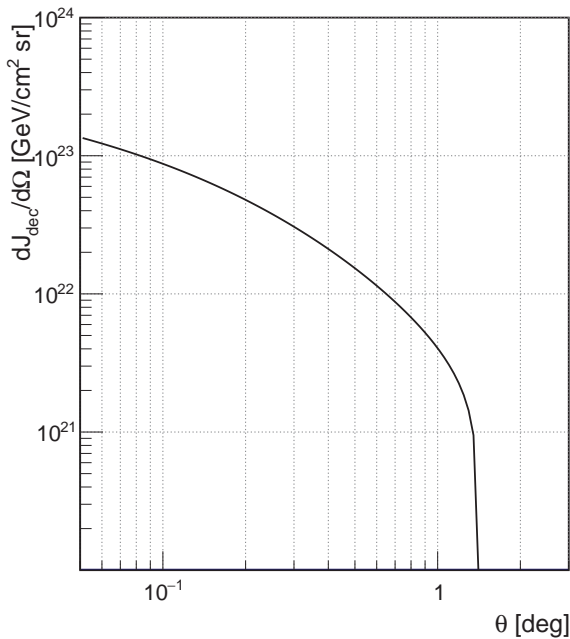


Figure 9.2: The Perseus CG dark matter density integrated on the line of sight (in $\text{GeVcm}^{-2}\text{sr}^{-1}$), as a function of the offset angle w.r.t. the center of the cluster (in deg). This emission profile is taken as a reference to generate the *Donut MonteCarlo*, tailored for the case of decaying DM in the Perseus CG.

a function of the offset angle w.r.t. the center of the cluster.

9.3 OBSERVATION, DATA RECONSTRUCTION AND ANALYSIS

		Telescope Pointing					
Period	Dates	\mathcal{A}			\mathcal{B}		
		All data [h]	Event Cleaning		All data [h]	Event Cleaning	
			quality [h]	specific [h]		quality [h]	specific [h]
$\mathcal{P}1$	2009.11.01-2009.06.01	94.7	56.4	45.4	-	-	-
$\mathcal{P}2$	2012.09.01-2013.01.17	9.2	9.1	9.1	59.4	40.2	36.8
$\mathcal{P}3$	2013.07.27-2014.08.05	17.5	16.7	14.8	55	30.2	28.9
$\mathcal{P}4$	2014.08.31-2014.11.22	16.6	10.4	10.1	21.7	21.7	7.5
$\mathcal{P}5$	2014.11.24-2016.04.28	6.8	3.9	3.9	29.3	22.32	21.9
$\mathcal{P}6$	2016.04.29-2017.08.02	44.1	41.9	12.2	20.5	16.02	11.1
TOTAL		185.9	138.4	106.1	188.9	119.2	96.2

Global sample selected 202.2 h

Table 9.2: Observations of the Perseus cluster with the MAGIC telescopes for two different telescope pointings \mathcal{A} and \mathcal{B} for different observational periods. The number of hours taken for each period and after event cleaning: *quality* cuts are based on NSB+AOD, *specific* cuts are based on the night-wise significance of *NGC1275*, *NGC1265* or *IC310*. See text for details.

MAGIC has been taking data at the Perseus CG since 2009, in one of the deepest campaign on a single sky region the instrument ever took. The campaign took place over several consecutive years, and now comprises almost 400 h. The main features of the full available dataset are reported in Table 9.2 (where two different observational projects have been using observations of from the Perseus CG). Data were taken in wobble mode (Fomin et al., 1994), where both signal (ON) and background control regions (OFF) are observed within the same FoV. The radio-galaxy *NGC 1275* is located at the baricenter of the cluster and, four symmetric wobble positions are taken around this point (labelled \mathcal{A} in Figure 9.6) at 0.4° wobble distance. Additionally, two pointing positions at the same wobble distance where taken around an intermediate point between NGC 1275 and a second radio-galaxy in the cluster (labeled \mathcal{B} in Figure 9.6), also a TeV emitter called *IC 310*. The performance of the analysis on NGC 1275 (or IC 310) is typically worse in the \mathcal{B} -pointing, because of the incomplete symmetry around the target of interest, this increases the background systematics, but it was chosen as a compromise to monitor at the same time this two potential γ -ray emitters, both very variable sources. The third object is shown Figure 9.6, the galaxy NGC 1265, clearly detected in X-rays (Sun et al., 2005), but never seen active in the MAGIC sensitivity regime. Wobbles are grouped in pairs (see Figures 9.6 and 9.7) in which the residual background for a given wobble ON region is estimated for the OFF region of the corresponding wobble partner².

² Such method of background estimation keeps the possible systematics due to inhomogeneities in the response of the camera field as low as possible.

9.3 OBSERVATION, DATA RECONSTRUCTION AND ANALYSIS

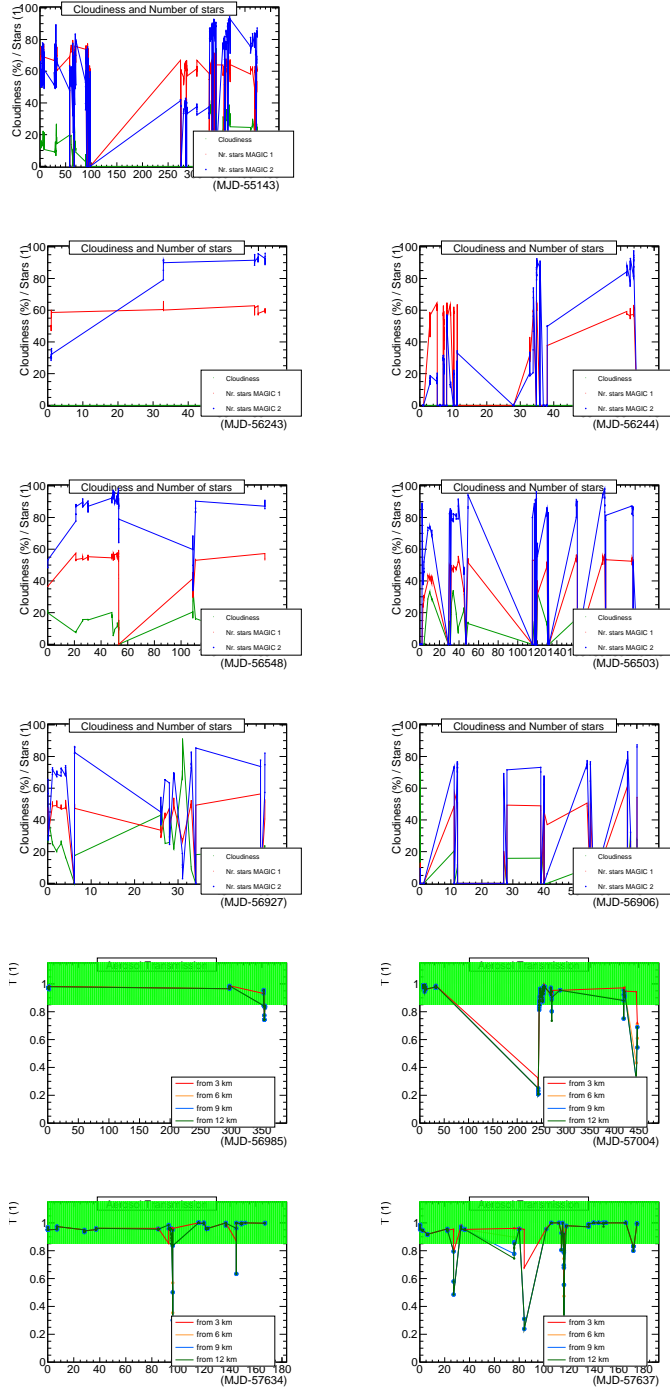


Figure 9.3: Atmospheric transmission during the Perseus observations. Left (right) column corresponds to pointing \mathcal{A} (\mathcal{B}). From top to bottom, rows correspond to HSPs: ST.01.02, ST.03.01, ST.03.03, ST.03.05, ST.03.06 and ST.03.07. When available, LIDAR transmission at 9km is used, *cloudiness* instead.

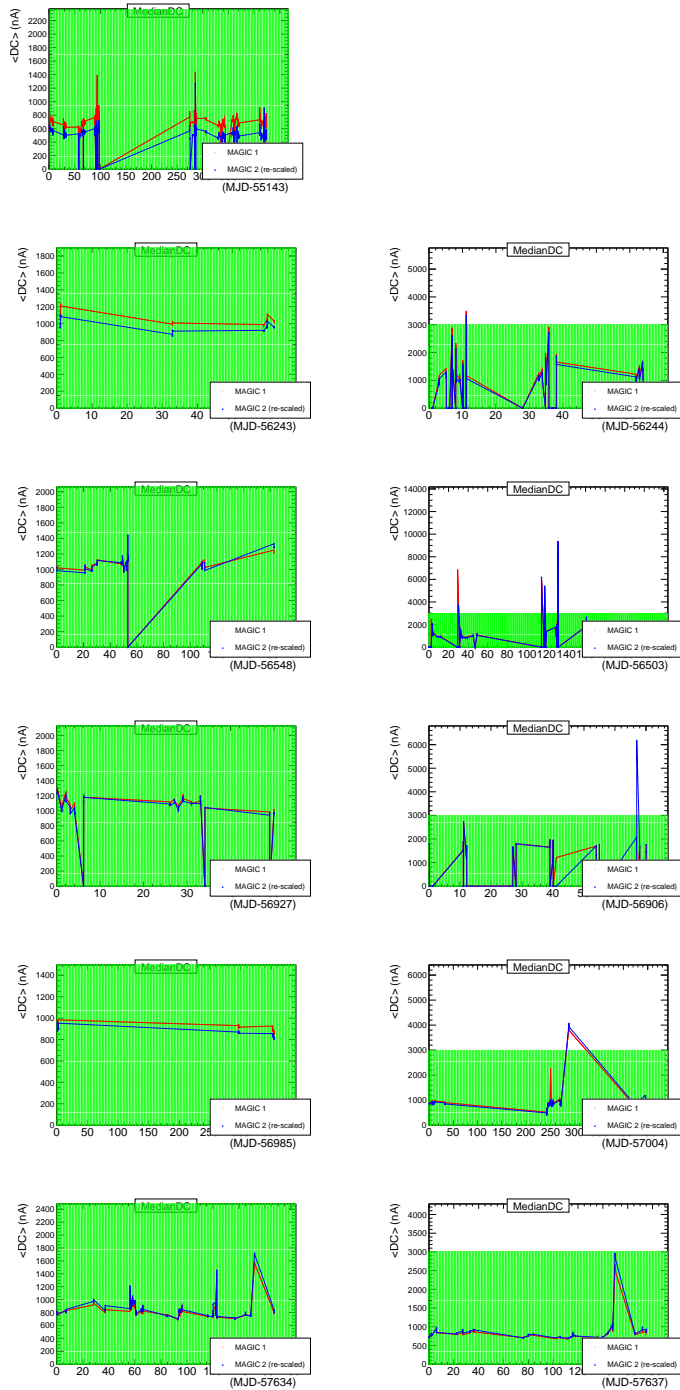


Figure 9.4: Mean DC current during the Perseus Observations. Left (right) column corresponds to pointing \mathcal{A} (\mathcal{B}). From top to bottom, rows correspond to HSPs: ST.01.02, ST.03.01, ST.03.03, ST.03.05, ST.03.06 and ST.03.07. Green Area (not always visible) is data surviving the cuts

source	RA [<i>hh:mm:ss</i>]	Dec [<i>dd:mm:ss</i>]
NGC 1275	03:19:48.1	41:30:42.0
NGC 1265	03:18:15.7	41:51:27.4
IC 310	03:16:43.0	41:19:29.0

Table 9.3: Sky coordinate in *Right Ascension* (RA) and *Declination* (Dec) of three astrophysical sources in the FoV of Perseus. *NGC 1275* and *IC 310* have already been detected with MAGIC. *NGC 1265* is expected to be a gamma-ray emitter but has never been detected within the MAGIC sensitivity band.

In addition, during the Perseus campaigns, MAGIC has gone through several hardware upgrades (Aleksić et al., 2016b,a), that required a dedicated MC simulations. The HSP are labeled as $\mathcal{P}i$ where differences between periods may arise from substantial instrument changes (e.q. the change of the camera or read-out of the system) or minor changes (mirror substitution, mirror alignment, etc). All different subsamples are analyzed using specific IRFs.

Separately, for each data sample, we performed the basic data reconstruction (Aleksić et al., 2012b) that allows to estimate energy and direction of the recorded events. Data between 5° and 50° zenith range were selected, according to both quality and specific cuts. For the quality cuts, the selection was based on the atmospheric transparency at the time of observation based on data from the MAGIC elastic LIDAR (Fruck et al., 2014b). We selected data with total AOD larger than 85% of that of a clear night, which guarantees the highest performance and smallest systematics. We also impose a cut on the size of the event (the amount of collected Cherenkov light) of 80 Photoelectrons (PHE), discarding low signal events. We further selected data based on the NSB light level, allowing data with average illumination not larger than three times that of a standard moonless night (as suggested in Ahnen et al., 2017c, to guarantee maximum performance). Moreover, as specific cuts, we also removed entire nights in which the significance of any of the astrophysical sources NGC 1275, NGC 1265 and IC 310 (see Table 9.3 for locations) was measured to be higher than 3σ (see Figure 9.8 for night-wise variability and Table 9.2 for details on the data surviving each cut). Excluding periods of data with very strong significances minimises the possible systematic effect introduced, while no bias in the search for DM is introduced since the evaluation of the significance of NGC 1275, NGC 1265 and IC 310 are performed out of the signal region where we later search for DM (as it will be introduced later). Events surviving all the above selection cuts are assigned an estimated energy, an estimated direction, and a parameter expressing the likeliness of the event coming from a primary gamma ray or a cosmic ray, called “hadronness” (h).

This is done through a RF boosted tree classification method (Albert et al., 2008b). The classification is based on a tailored MC production that takes into account the exact spatial distribution of decay DM expected signal, and reweights events according to a specific DM profile. The result is a donut-shaped MC that accurately provide IRFs. This procedure was firstly applied to the case of the Ursa Major II dwarf spheroidal galaxy (Ahnen et al., 2017b) and has been extensively discussed in Chapter 5.

DEFINITION OF THE REGION OF INTEREST AND SIGNAL CONTAMINATION

In order to search for an extended signal of decaying DM, and also taking into account the presence of astrophysical gamma-ray emitters in the FoV (in particular of NGC 1275, located at the center of the Cluster), we define a *ring-shaped* signal-search region by two angular cuts ($\mathcal{R}2$, defined in Figures 9.6 and 9.7, by $(\theta_{min}, \theta_{max})$) w.r.t the center of the cluster, excluding in this way from the search $\mathcal{R}1$ (the circular region θ_{min} , centered on NGC 1275), the central region of the cluster where NGC 1275 emission is expected to dominate.

Due to the finite angular resolution of the instrument, γ ray events from astrophysical origin in NGC 1275 are expected to be reconstructed within $\mathcal{R}2$. This contamination, if not properly modelled, could be miss-interpret as a DM evidence. In order to model NGC 1275's activity, we measure the number of NGC 1275 excess events inside $\mathcal{R}1$. Assuming NGC 1275 to be a point-like source (taking into account the nature of the source, and the distance to the Perseus CG, this is a safe assumption), the ratio of events reconstructed inside $\mathcal{R}1$ and $\mathcal{R}2$ is determined by the instrument angular PSF. We compute this ratio from a point-like MC, chosen to be representative for each of the two observational projects, each HSP and *zenith range*, and weighted to reproduce NGC1275's spectra (measured in Ahnen et al., 2016a). Since IACTs PSF strongly dependent on the energy range of the events, we compute this ratio as a function of the estimate energy (E'). We define the scaling factors C as,

$$C(E') = \frac{N_{\mathcal{R}2}(E')}{N_{\mathcal{R}1}(E')}; \quad (9.2)$$

where $N_{\mathcal{R}1}$ ($N_{\mathcal{R}2}$) is the number of point-like MC events reconstructed inside $\mathcal{R}1$ ($\mathcal{R}2$), see Figure 9.9, and E' is expressed in the same intervals than the rest of the IRFs. The number of expected NGC 1275 events inside $\mathcal{R}2$ ($f_{\mathcal{R}2}$) is then, estimated to be:

$$f_{\mathcal{R}2} = C f_{\mathcal{R}1}, \quad (9.3)$$

(where $f_{\mathcal{R}2}$ is f in Equation 9.5). Figure 9.10 shows the computed values C for both observational periods, all HSP MC samples and both zenith ranges. We emphasize that only 1 point-like MC is produced for a given HSP/zenith range in, however, the two observational projects \mathcal{A} and \mathcal{B} , have different observational zenith distributions, and hence C has been computed specifically for each. Figure 9.10 also shows (solid line) the corresponding C -factors computed from the MAGIC PSF presented in Aleksić et al. (2016a), taking into account statistical uncertainties the agreement is pretty good.

Figure 9.11 shows the measured γ -ray event rate from NGC 1275 (dN/dE') in the region $\mathcal{R}1$. A final remark should be made regarding the number of expected NGC 1275's events ($f_{\mathcal{R}2}$). These have been computed from the number of excess events $f_{\mathcal{R}1}$ (measured inside $\mathcal{R}1$, see Figure 9.11), and hence, $f_{\mathcal{R}2}$ is a random variable that can have negative values. We only considered $f_{\mathcal{R}2}$ different from zero for those samples in which the total number of NGC 1275's excess events was positive ($\sum_{j=0}^{N_{\text{bins}}} f_{\mathcal{R}1,j} > 0$), otherwise, $f_{\mathcal{R}2}$ for that sample (see later Equation 9.5).

CUTS OPTIMIZATION

Typically in MAGIC, the precise values of h and θ (for this particular case h , θ_{min} and θ_{max}) are optimized, in order not to bias the selection, using a sample of the well-measured Crab Nebula observations. In our case, the Crab Nebula is no longer a good probe, mainly because its emission profile does not follow the one expected from decaying DM (but point-like instead). In order to optimize the cuts defining $\mathcal{R}2$, we select θ_{min} and θ_{max} as those values minimizing the width of the $-2 \ln \lambda_{\mathcal{P}}$ (Equation 3.7) function around its minimum, without checking the position of the minimum (to avoid biases), and fixing the value of the nuisance parameters to their mean values. This procedure has already been applied in other DM searches in MAGIC (Ahnen et al., 2017b)³. We scanned the grid parameter space of:

$$\begin{aligned} h(E') &\in (0, 1) \\ 0 < \theta_{min} < \theta_{max} < 0.35 & \quad [\text{deg}]. \end{aligned} \quad (9.4)$$

The former efficiency cut for $h(E')$ are energy dependent cuts, based on the fraction of MC events that survive. θ_{min} was constrained to be lower than θ_{max} for obvious reasons. Finally, we also constrained θ_{max} to be lower than 0.35° . The normalization between ON/OFF regions (τ) is computed from the ratio

³ J. Palacio is a corresponding author of this publication.

between the number of events inside a region adjacent to each region. The maximum θ_{max} value, ensures a decent statistical reliable computation on τ . As a result of the optimization, we obtained $h=80\%$, $\theta_{min} = 0.10^\circ$ and $\theta_{max} = 0.33^\circ$. These are important numbers for the analysis: this is a highly non standard signal region in MAGIC; the extension of the optimal signal region (θ_{max}) is by far larger than for a typical point-like analysis; Moreover, according to these values, the contamination fraction of decay DM events accounts up to $\sim 10\%$ ($\sim 50\%$) for pointing strategy \mathcal{A} (\mathcal{B}).

BINNED LIKELIHOOD ANALYSIS

We construct a binned likelihood, following Section 3.2.4, for decaying DM as:

$$\begin{aligned}
 & \mathcal{L}(1/\tau_{\text{DM}}; \boldsymbol{\nu} | \mathcal{D}) \\
 = & \mathcal{J}(J|J_{\text{obs}}) \\
 & \times \prod_{i=1}^{N_{\text{samples}}} \mathcal{T}(\tau_i | \tau_{\text{obs},i}, \sigma_{\tau,i}) \\
 & \times \prod_{j=1}^{N_{\text{bins}}} \left[\frac{(g_{ij}(1/\tau_{\text{DM}}) + b_{ij} + f_{ij})^{N_{\text{ON},ij}}}{N_{\text{ON},ij}!} e^{-(g_{ij}(1/\tau_{\text{DM}}) + b_{ij} + f_{ij})} \right. \\
 & \left. \times \frac{(\tau_i b_{ij} + g_{ij}^{\text{OFF}}(1/\tau_{\text{DM}}))^{N_{\text{OFF},ij}}}{N_{\text{OFF},ij}!} e^{-(\tau_i b_{ij} + g_{ij}^{\text{OFF}}(1/\tau_{\text{DM}}))} \right] \quad (9.5)
 \end{aligned}$$

where

$$\begin{aligned}
 \boldsymbol{\nu} &= \{b_{ij}\}_{i=1, \dots, N_{\text{samples}}; j=1, \dots, N_{\text{bins}}} \\
 \mathcal{D} &= \{N_{\text{ON},ij}, N_{\text{OFF},ij}\}_{i=1, \dots, N_{\text{samples}}; j=1, \dots, N_{\text{bins}}}
 \end{aligned}$$

where, apart from the terms introduced in Equation 3.5, now g_{ij} and g_{ij}^{OFF} are the estimated number of signal events for the ON and OFF regions respectively; f_{ij} is the expected number of foreground events from NGC 1275; and we considered $\mathcal{J} = \delta(J_{\text{obs}} - J_{\text{obs}})$. Again, we consider a systematic uncertainty for to the parameter τ_i , $\sigma_{\tau}^{\text{sys}} = 0.015\tau_{\text{obs},i}$, added in quadrature to the statistical one. This value has been established on the base of a dedicated performance study Aleksić et al. (2016a).

As previously mentioned, A_{eff} and G are computed from a MC simulated

\mathcal{A}	
HSP	$\mathcal{P}1, \mathcal{P}2, \mathcal{P}3, \mathcal{P}4, \mathcal{P}5, \mathcal{P}6$
Zenith angle	$5 - 35$
Wobble pointing	$W0.4 (+058, +157, +238, +337)$

\mathcal{B}	
HSP	$\mathcal{P}2, \mathcal{P}3, \mathcal{P}4, \mathcal{P}5, \mathcal{P}6$
Zenith angle	$5 - 35, 35 - 50$
Wobble pointing	$W0.26 (+108, +288)$

Table 9.4: List of the different bins for which independent IRFs (and hence, independent likelihoods) are defined. According to the classification presented in the table, binned in *observational project*, *hardware stable period*, *Zd range* and *wobble pointing* (see Table 9.4), 42 independent MC samples have been generated.

gamma-ray dataset (following the spatial distribution expected for decay DM-induced events from Perseus, see Chapter 5). Moreover, the effective area for the γ rays of DM reconstructed within the OFF region ($A_{\text{eff,OFF}}$, black solid line in top left panel in Figure 3.18) and the dN/dE of NGC 1275's foreground events (black solid line in top right panel in Figure 3.18) are also inputs of each likelihood sample.

The null hypothesis is the case where $1/\tau_{\text{DM}} = 0$, while the test hypotheses are built considering the flux computed using Equation 2.9, under the hypothesis of different DM particles with masses from 200 GeV to 200 TeV for pure decays ($b\bar{b}$, $\tau^+\tau^-$, $\mu^+\mu^-$ and W^+W^-) as a representative set of the type of spectra models often reproduce.

We define independent likelihoods for each *bin* in *observational project*, *HSP*, *Zd bin* and *wobble pointing* (see Table 9.4). Each likelihood term, based on an independent sample, is combined with the rest through the same parameter, $1/\tau_{\text{DM}}$ shown in Equation 9.5, for a total of $N_{\text{samples}} = 42$.

Using Equation 9.5 (following Equation 3.5) we define the profile likelihood ratio as,

$$\lambda_P(1/\tau_{\text{DM}} | \mathcal{D}) = \frac{\mathcal{L}(1/\tau_{\text{DM}}; \widehat{\nu} | \mathcal{D})}{\mathcal{L}(\widehat{1/\tau_{\text{DM}}}; \widehat{\nu} | \mathcal{D})}, \quad (9.6)$$

where $\widehat{1/\tau_{\text{DM}}}$ and $\widehat{\nu}$ are the values maximizing \mathcal{L} , and $\widehat{\nu}$ the value that maximizes \mathcal{L} for a given τ_{DM} (note that the likelihood goes linear with $1/\tau_{\text{DM}}$). Lower

limits in τ_{DM} at 95% confidence level (CL, τ_{DM}^{LL}) are given for:

$$-2 \ln \lambda_P (1/\tau_{\text{DM}}^{LL} | D) = 2.71. \quad (9.7)$$

9.4 RESULTS: CONSTRAINTS TO THE DECAY LIFE TIME

In this section we present the results on the lifetime (τ_{DM}) of DM particles decaying into different SM particle pairs achieved with data from 202 hours of good quality observations of the Perseus CG. The search is performed for DM particles of masses between 200 GeV and 200 TeV for decaying scenarios into $b\bar{b}$, $\tau^+\tau^-$, $\mu^+\mu^-$ and W^+W^- , decay modes representative for most of typical decaying DM models. When running the minimization we restricted the value of the lifetime to the physical range ($1/\tau_{\text{DM}} \geq 0$).

Figure 9.12 shows the 95% C.L. lower limit on the decay lifetime for DM particles (τ_{DM}^{LL}) obtained with a binned likelihood analysis (from $E'_{\text{min}} = 80$ to $E'_{\text{max}} = 10^6$ GeV divided in $N_{\text{bins}} = 10$ bins equidistant in $\log E'^4$). In addition, the two-sided 68% and 95% containment bands for the distribution of limits under the null hypothesis are also reported. The containment bands were computed from the distribution of the lower limits obtained from the analysis of 300 realizations of the null hypothesis ($1/\tau_{\text{DM}} = 0$), consisting of toy MC simulations (for both signal and background regions) generated from pure background PDFs, assuming similar exposures as for the real data, and τ assumed a nuisance parameter in the likelihood function.

We see that our result, is within the 2-sigma band of the expectation for null hypothesis, for the full range of DM masses explored, for what we can claim that we detect no evidence in the Perseus CG data sample of DM decaying into neither channel: $b\bar{b}$, W^+W^- , $\tau^+\tau^-$ nor $\mu^+\mu^-$. We reach sensitivities over 0.3×10^{25} s in all channels.

9.5 CONCLUSIONS AND REMARKS

Figure 9.13 shows the comparison of our results with those from MAGIC on 158 hours on Segue 1 (Aleksić et al., 2014c). We also show in the plot results from other instruments namely: limits from 48 h on Segue 1 from VERITAS (Aliu et al., 2012) and results on a Fermi search on the Galactic Center (Ackermann

⁴ Empty bins were allowed to re-adjust and merge with neighboring ones.

et al., 2012). MAGIC results can be directly comparable between them, although there have been differences in the treatment on the nuisance parameters between both analysis. Fermi results are more constraining (in the low DM mass range) and, they should be understood as independent measurements, affected by different systematics (Galactic Center studies are heavily affected on how to model the astrophysical diffuse emission of it, see Ackermann et al., 2012, for deeper discussion). Perseus results reach sensitivities over 0.3×10^{25} s in all channels, are better than previous MAGIC results, and the most constraining results for DM masses above ~ 20 TeV for all channels. In the most conservative approach, taking into possible uncertainties in the estimation of the Perseus CG in the JFactor our limits get a factor of 2 worse.

Decaying DM scenarios are currently investigated with several classes of instruments, and on different mass ranges. In the GeV-TeV mass range, there is a wide literature with constraints on decaying DM. The majority of limits make use of the Fermi-LAT instrument, sensitive in the MeV-GeV range, in two ways: either combining results from observations of galaxy clusters (Dugger et al., 2010; Ke et al., 2011; Zimmer et al., 2011; Huang et al., 2012; Charles et al., 2016) or making use of the integrated cosmological decaying DM contribution to the extragalactic diffuse light (see, e.g., Cirelli et al., 2012; Cohen et al., 2017), made up of prompt and secondary emission. It must be underlined that these results are not official results from the Fermi-LAT collaboration and that, in some cases, these limits depend on the model-dependent secondary components. At the TeV, where searches for diffuse emission are harder because of the limited field of view of ground based IACTs, the decaying DM case was discussed by Cirelli et al. (2012) showing lower limits on the decay DM lifetime with H.E.S.S. data on the Fornax galaxy cluster. At higher energies, the most stringent constraints on certain channels can be obtained with neutrinos in Icecube (Cohen et al., 2017) or ultra-high-energy cosmic-rays with the Pierre Auger Observatory (PAO), KASCADE and CASA-MIA (Aab, 2015; Kang et al., 2015; Chantell et al., 1997).

A final comment should be made in order to properly address the comparison between Perseus and Segue 1 MAGIC results. Taking into account the difference in exposure and astrophysical factor between the two sources, one would expect larger differences between the results obtained by each measurement. In order to understand the actual difference between both, we need to consider the systematic treatment between both analysis is substantially different. In Perseus we considered a binned likelihood (instead of unbinned) where no background model was provided. We also increased the number of nuisance

parameters by including τ (also affected by a systematic uncertainty). On the other hand, we showed how due to the pointing, DM events were expected to be reconstructed in our background control region (the “Leakage” effect). The Perseus pointing strategy (for indirect DM searches) could also be optimized following Chapter 6. The current Perseus pointing strategy, which proved to be very profitable in terms of VHE astronomy (Aleksić et al., 2010a, 2012c,d, 2014b, 2010b, 2014a,d), has an effect of $\sim 10\%$ and $\sim 50\%$ in the final sensitivity for indirect DM searches for pointings \mathcal{A} and \mathcal{B} respectively.

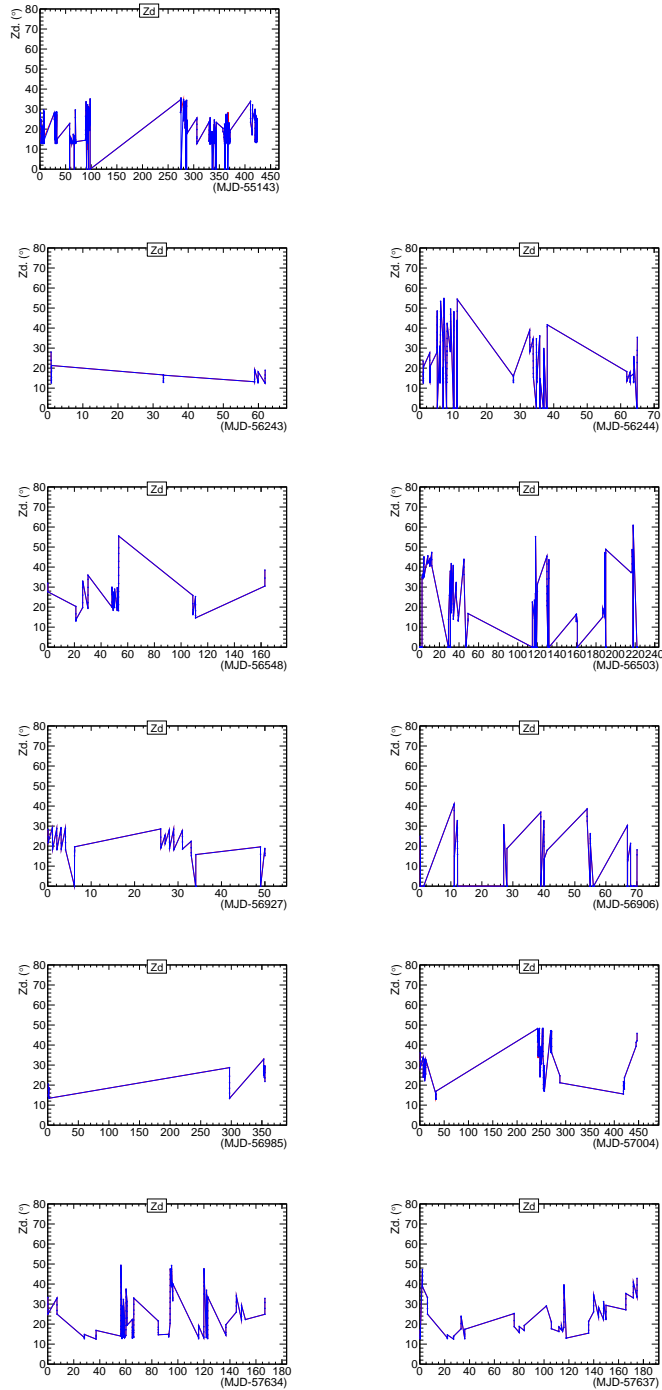


Figure 9.5: Zenith distribution during the Perseus Observations. Left (right) column corresponds to pointing \mathcal{A} (\mathcal{B}). From top to bottom, rows correspond to HSPs: ST.01.02, ST.03.01, ST.03.03, ST.03.05, ST.03.06 and ST.03.07. Data between 5 and 50 in zenith was selected.

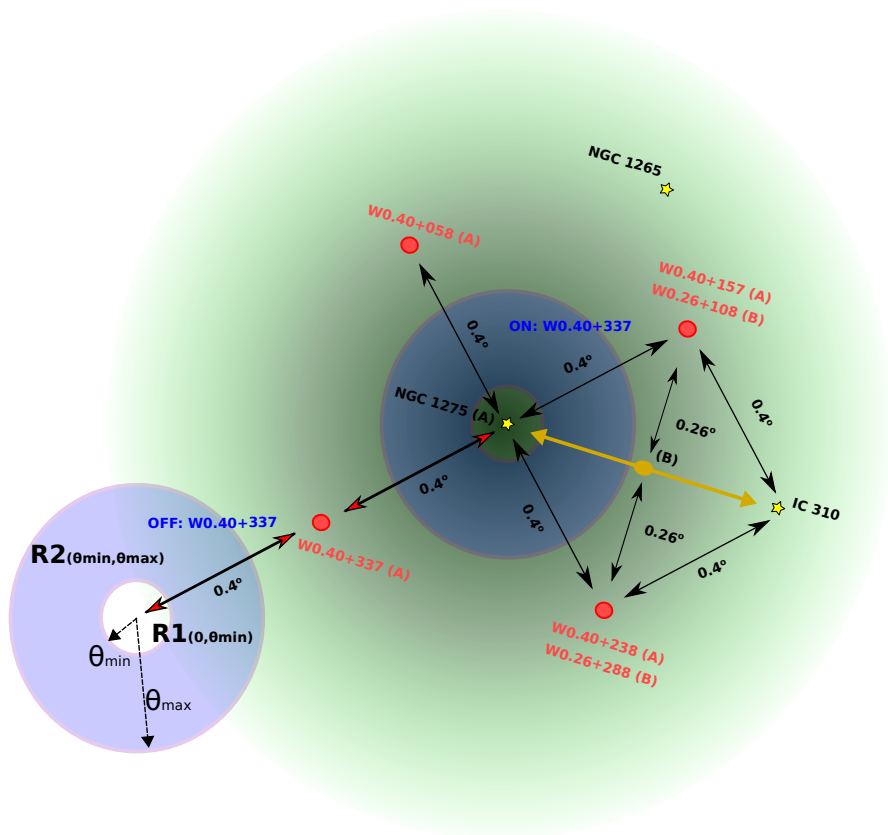


Figure 9.6: Schematic view of the Perseus Cluster FoV. The location of three radio galaxies members of the Perseus cluster (IC 310, NGC 1275 and NGC 1265) are shown with yellow stars. The green area around the position of NGC 1275 represents the distribution of inferred from Sanchez-Conde et al. (2011). The MAGIC telescopes have taken data using 4 different pointing positions (red circles), wobbling around 2 directions, \mathcal{A} and \mathcal{B} . Signal (*ON*) and background (*OFF*) regions are shown for pointing $W0.40+337$ of project \mathcal{A} . $\mathcal{R}1$ and $\mathcal{R}2$ are two different regions defined by the angular cuts θ_{min} and θ_{max} (shown for the *OFF* region and defined for the similarly for the *ON* region). The image illustrates the expected contamination" (leakage) of the *OFF* region with DM signal.

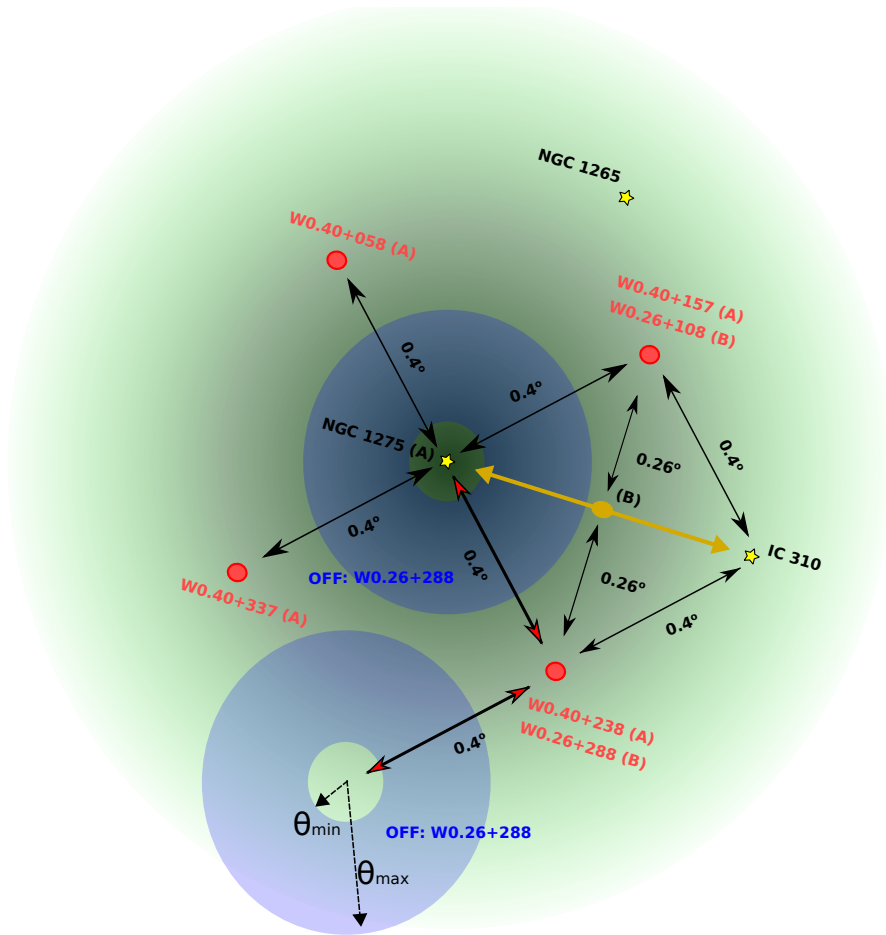


Figure 9.7: Same as Figure 9.6 but for pointing $W0.40+337$ of project B .

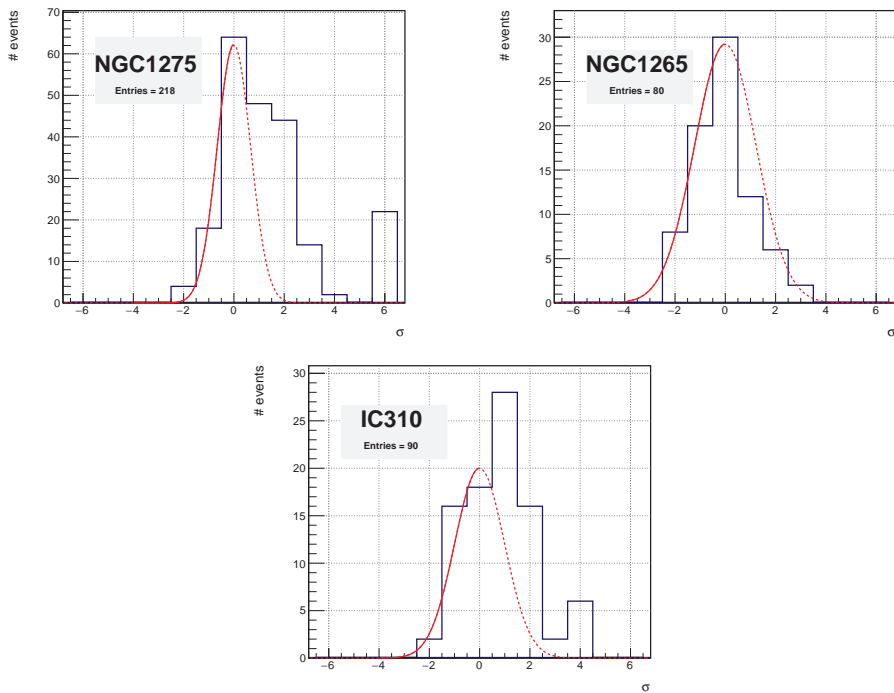


Figure 9.8: Distribution of night-wise significance at of NGC 1275 (top left), NGC 1265 (top right) and IC 310 (bottom). All entries above (below) 5 sigmas have been merged into the last (first) bin. A *Gaussian* function was fitted in the negative range of the distribution, and plotted for the positive range as well. The asymmetry on the distribution hints the existence night-wise variability for NGC 1275 and IC 310.

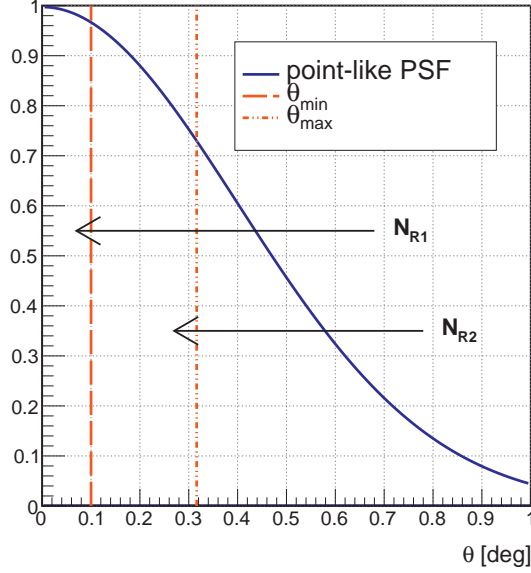


Figure 9.9: Point-like PSF (blue) as a function of θ . Figure also shows θ_{\min} and θ_{\max} (vertical dashed), where the number N_{R1} and N_{R2} are integrated.

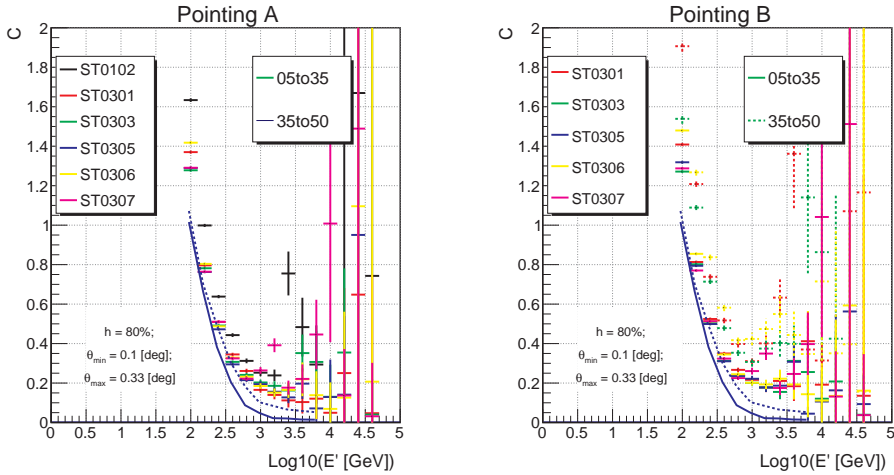


Figure 9.10: C -factors as a function of the estimated energy (E'), computed from *point-like* MC, for each of the considered HSP for NGC 1275's spectral energy and zenith observation distribution for pointing \mathcal{A} (left) and \mathcal{B} (right). Optimized values of $h_c, \theta_{\min,c}$ and $\theta_{\max,c}$ have been used (see text for details). Blue solid (dashed) line represents the same C -factors computed from MC (Crab Nebula data) in Figure 14 from Aleksić et al. (2016a).

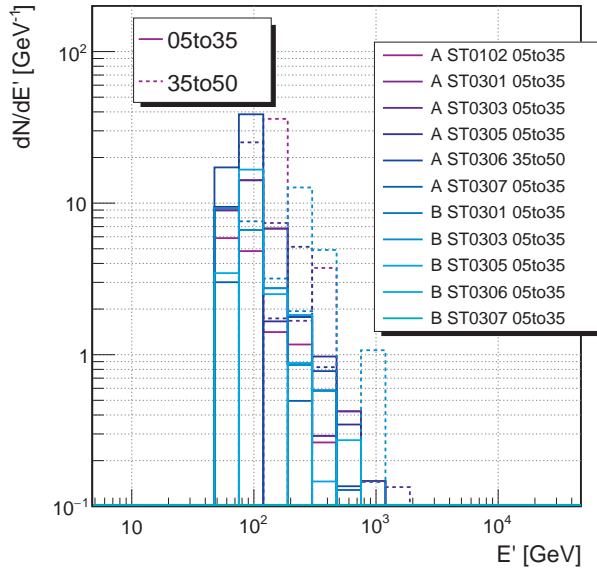


Figure 9.11: NGC 1275’s measured event rate (dN/dE' , being E' the reconstructed energy) in the region $\mathcal{R}1$, for both observational projects (\mathcal{A} and \mathcal{B}), for all HSP (ST.01.02, ST.03.01, ST.03.03, ST.03.05, ST.03.06, ST.03.07) and both zenith ranges ($05to35$ to $35to50$). Each data sample has been normalized to 250 h, so that comparisons between them can be performed.

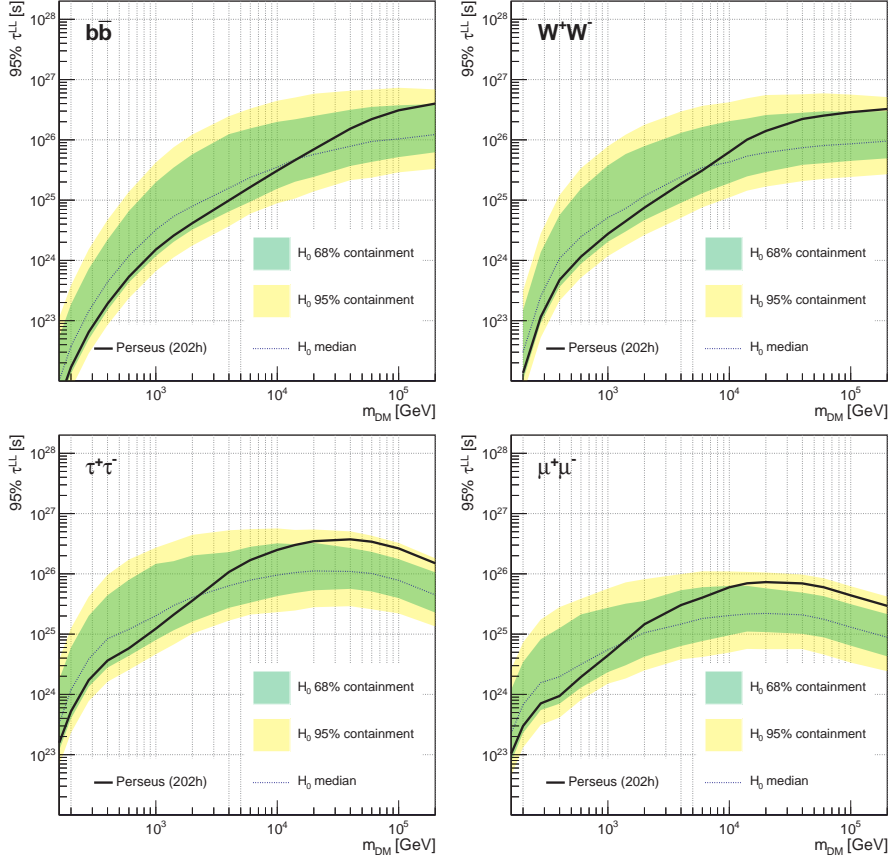


Figure 9.12: Black line shows the 95% CL lower limit to the life-time of DM particles decaying into $b\bar{b}$ (top-left), $\tau^+\tau^-$ (top-right), W^+W^- (bottom-left) and $\mu^+\mu^-$ (bottom-right) for DM masses from 200 GeV to 200 TeV obtained from 202 h of good quality observations of the Perseus CG. Green (yellow) band corresponds to the 68% and 95% containment bands of the distribution of same estimator computed from 300 simulations of the null hypothesis ($1/\tau_{DM}=0$) mimicking conditions of the data sample.

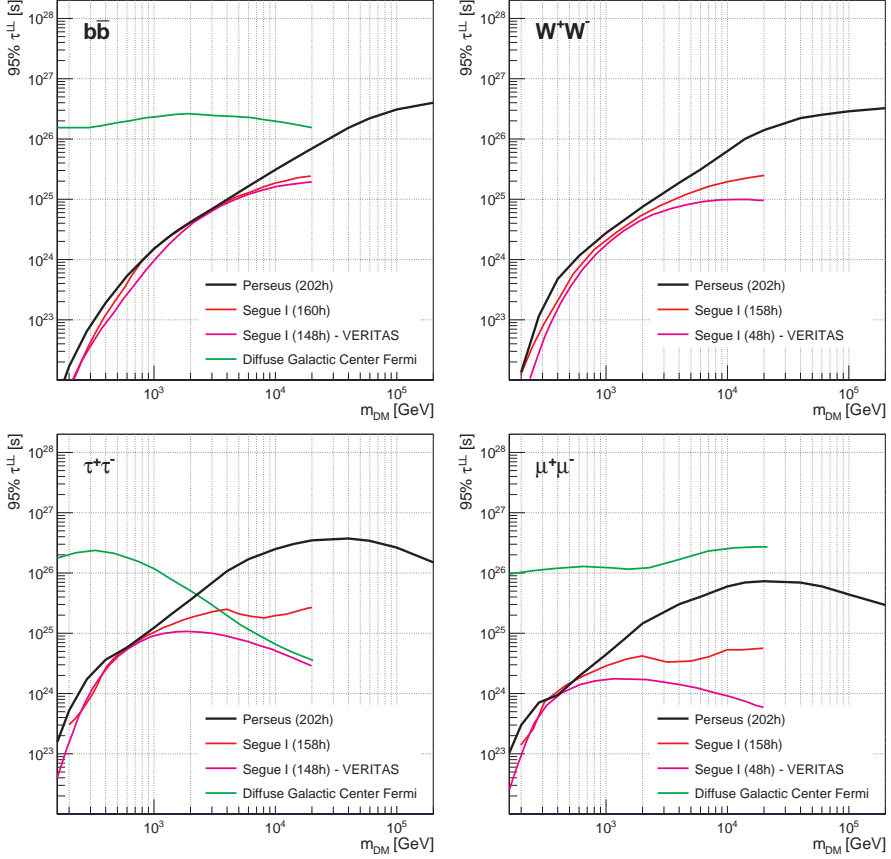


Figure 9.13: Black solid line shows the 95% CL lower limit on decay life-time for DM decaying into $b\bar{b}$ (top-left), W^+W^- (top-right), $\tau^+\tau^-$ (bottom-left) and $\mu^+\mu^-$ (bottom-right) for DM masses from 200 GeV to 200 TeV from 202 h of good quality data from the Perseus cluster of galaxy where JFactor is a fixed parameter, compared with previous MAGIC results on 158 h on Segue 1 (Aleksić et al., 2014c). We also show in the plot results from other collaborations: limits on 48 h on Segue 1 from VERITAS (Aliu et al., 2012) and results from the Fermi search in the Galactic Center (Ackermann et al., 2012). Perseus results reach sensitivities over 0.3×10^{25} s in all channels, are better than previous MAGIC results, and the most constraining results for DM masses above ~ 20 TeV for all channels.

Chapter 10

SUMMARY, CONCLUSIONS AND REMARKS

The nature of DM and DE are among the most fundamental scientific questions humans face today and its determination will constitute a major breakthrough not only contributing to the general view we have of the Cosmos and its history, but also opening a new era in the understanding of its smallest constituents and the forces driving their interactions. During the last decades, efforts to try to understand the nature of DM have been carried by a large variety of research institutes from countries all over the world, both in the theory and the experimental sides, so far with no clear evidence of success. In this thesis, I have focused on indirect DM searches, i.e. the search of SM products reaching the Earth with IACTs. We search for γ rays with GeV-TeV energies due to the annihilation or decay of a putative WIMP particle. Such particle, not considered within the SM particle zoo, is postulated to populate the most DM dominated environments (i.e., those showing a gravitational unbalance between the force inferred from the motion of nearby constituents and the total mass supposedly exerting this field).

I showed how current ground based astronomy (and generally, all high energy experimental physics) is developing large data samples whose storage, maintenance and processing becomes a real challenge for ongoing and future plant experiments. In this thesis, I developed a tool that helps MAGIC to overcome this problem, by automatizing the conversion between the heavy-raw products generated by the telescope to lighter high-level analysis products to be performed within the GRID network environment. The developed tool is also going to be useful in order to transform the current MAGIC database into the currently proposed standard data format for γ -ray astronomy.

Focusing on γ -ray astronomy dedicated to indirect DM searches I argued how,

the expected morphology of the γ ray signal can be moderately extended w.r.t. standard point-like γ -ray emitters. This can be a real challenge for pointing-mode instruments, as IACTs. In this respect, two improvements have been proposed and developed within the work presented in this thesis. First, at an analysis level, a new method for the correct computation of IRFs for moderate extended sources has been proposed, developed and characterized. Starting from a general MC for extended sources (with γ rays simulated covering all the telescope FoV) and assuming a definite surface brightness profile of the source (in the case of indirect DM searches, this is proportional with $dJ/d\Omega$), MC γ rays are selected following the expected spatial distribution of events, from where the IRF is computed. The IRFs inferred are only valid for the assumed morphology, and hence dedicated computation is required for each different source, however the method adds a negligible computer overload compared to the general MC generation. The method considers observations to be performed in wobble mode, alternating the pointing of the instrument at different offset positions w.r.t. to the source center, however on-site observations are also taken into account (in the limit case which the wobble distance is zero).

Secondly, I also proposed a method to optimize the wobble pointing strategy of IACTs. I have used the surface brightness profile of the source, and taken into account the off-axis performance of the instrument, to provide the optimal wobble distance and angular signal integration region at which the source should be observed and analyzed. It has been emphasized how, while the angular signal region can always be modified at analysis level, the wobble distance is fixed during the data taking, and hence, the final sensitivity of the analysis strongly depends on this choice. The method has therefore, a potential applicability for scheduling observations for ongoing and future experiments. The idea was initially motivated for indirect DM searches, where it has been implemented for the first time to optimize the pointing strategy of MAGIC for indirect DM searches on dSphs, but the method is completely general for γ ray astronomy, and can be applied to any source and IACT telescopes. We have implemented the method into an open source environment that is freely distributed among all the γ -ray community, where the implementation of new sources and/or instruments is straightforward.

I have also contributed to the construction of the first LST prototype (which will probably become the first CTA telescope). The LST is the largest telescope type to opera within CTA, and hence will dominate the sensitivity in the lowest energy range. As it has been shown, γ -ray WIMP induced signal (either annihilation or decay) is expected to peak in this energy regime, mak-

ing the LST the most promising telescope for DM discovery once CTA starts operation. IFAE is leading the camera project of the LST, where I participated in the first assembly of the final camera modules to the cluster holder, that took place in August 2016 at CIEMAT lab infrastructures. We tested the trigger path noise levels of the modules while operating at conditions similar to the experimental ones. I estimated the noise level to be within the LST requirements and found no evidence for noise correlation w.r.t. neither the PSU nor the neighboring modules distance. Similar tests are taking place at IFAE during March 2018 with the full camera modules, before sending the camera to LP for the final assembly.

I have also shown the constraints imposed to the WIMP thermally averaged cross-section and/or decay life-time with observations of the MAGIC telescopes to one of the most DM dominated known dSphs and one of the most promising CG for indirect DM searches. After the unexpected discovery of Tri II, and its DM modelization, MAGIC performed an observational campaign where ~ 60 hours of good-dark quality data were recorded. A fast analysis was performed where no DM evidence was found, providing the most stringent limits on the thermally annihilation cross section of WIMP DM particles annihilating into SM pairs $b\bar{b}$, W^+W^- , $\tau^+\tau^-$ and $\mu^+\mu^-$. While the results of this analysis were being drafted for a publication, newer optical data on Tri II challenged significantly the interpretation of DM in Tri II, making it compatible with zero. Newer data on Tri II is required in order to clarify its DM content. The Perseus CG campaign instead, has been a long standing project of the MAGIC Collaboration, reaching at 2017 over 400 hours of recorded data. I analyze the data and searched for hints of decaying DM using a highly non-standard analysis (w.r.t. the MAGIC standards): I consider the spill-over effect of the nearest γ -ray emitters from the RoI in order not to be miss-interpret as DM; due to the pointing strategy and the expected large signal extension, the contamination of DM induced events into the background control region is taken into account, what reduces the final sensitivity reached. I find no evidence of decaying DM with lifetimes shorter than $\sim 10^{26}$ s in all considered decaying channels. Our results are the best obtained with MAGIC, and the most constraining results for DM masses above ~ 20 TeV.

LIST OF FIGURES

2.1	Star rotational curves in Galaxies	8
2.2	Schematic view of strong lensing	10
2.3	Strong lensing observations from Abell 2218	10
2.4	The Bullet cluster to cluster collision	11
2.5	Schematic view of the Universe's history	12
2.6	CMB radiation	14
2.7	CMB power spectrum	15
2.8	The baryon acoustic peak	17
2.9	Λ CDM constraints from DES year1	18
2.10	The Millennium Simulation Project	19
2.11	The 2dF redshift survey	20
2.12	Preferred region in the $\Omega_m - \Omega_\Lambda$ plane	20
2.13	WIMP miracle thermal relic density.	24
2.14	Representation of well-motivated DM candidates	30
2.15	WIMP interaction diagram	34
2.16	ATLAS mSUGRA/cMSSM exclusion limits	35
2.17	Spin-independent WIMP-nucleon cross section limits	37
2.18	The positron fraction in high-energy cosmic rays.	40
2.19	DM γ -ray spectra	44
3.1	Atmosphere's impenetrability	47
3.2	Cherenkov radiation emission	49
3.3	Cherenkov radiation lightpool.	50
3.4	EAS sketch.	51
3.5	MC simulation of EM and hadronic cascades.	53
3.6	Sketch of the imaging atmospheric Cherenkov technique.	54
3.7	IACT stereo reconstruction	55
3.8	Picture of the MAGIC telescopes.	56
3.9	MAGIC and subsystems.	57
3.10	Moving degrees of the MAGIC telescope	57

LIST OF FIGURES

3.11	Moon filter installation in LP, October 2014.	59
3.12	Macrocells in the current MAGIC camera version.	62
3.13	LIDAR image	65
3.14	LIDAR vs Pyrometer	65
3.15	Hillas parameters scheme.	70
3.16	Stereo parameters scheme.	70
3.17	Standard analysis plot examples	71
3.18	Full likelihood sample example.	74
3.19	CTA North array at LP	75
3.20	CTA sensitivity curves	76
3.21	CTA prototypes designs.	77
3.22	CTA telescope sensitivity	78
3.23	LST dish mounting	79
3.24	Electrical diagram of the LST camera.	80
3.25	LST module components.	81
4.1	ToMaRe flow diagram	86
5.1	MC variables	90
5.2	MC true direction	91
5.3	Donut surface brightness profile	92
5.4	Donut γ ray distribution	92
5.5	Donut method: step 1	93
5.6	Donut methos: step 2	94
5.7	Donut comparison plots	94
5.8	Donut Aeff comparison	95
5.9	Tophat Aeff comparison	96
5.10	Tophat Aeff ratio comparison	97
6.1	Wobble mode variables	102
6.2	MAGIC gamma-ray rate vs offset angle	104
6.3	CTA relative off-axis sensitivity	105
6.4	MAGIC & CTA relative acceptance	106
6.5	Wobble mode variables	107
6.6	$dN/d\Omega$ and Q -factor for annihilation from Coma	107
6.7	$\mathcal{Q}_{\mathcal{A}}$ vs θ_c and w	109
6.8	$\mathcal{Q}_{\mathcal{F}}$ vs θ_c and w	110
6.9	$\overline{\mathcal{Q}}$ vs θ_c and w	110
6.10	J_{ann} -factor for a set of dSph	112
6.11	J_{dec} -factor for a set of dSph	114

7.1	LST PSU and redundancy module	118
7.2	CHF metallic structure for the LST modules	119
7.3	LST cluster assembled into the CHF	120
7.4	CIEMAT cluster distributions	121
7.5	L0 rate pedestal scan	122
7.6	L0 rate scan with pulse injection	122
7.7	L1 rate pedestal scan	123
7.8	L1 rate scan with pulse injection	124
7.9	σ_{thresh} L0 pedestal	125
7.10	σ_{thresh} L0 pedestal vs distance to the PSU	126
7.11	σ_{thresh} L0 with pulse injection	127
7.12	σ_{thresh} L0 with pulse injection vs distance to the PSU	128
7.13	σ_{pulse} L0 with pulse injection	128
7.14	σ_{pulse} L0 with pulse injection vs distance to the PSU	129
7.15	σ_{thresh} L1 pedestal	130
7.16	σ_{thresh} L1 pedestal vs distance to the PSU	130
7.17	σ_{thresh} L1 with pulse injection	131
7.18	σ_{thresh} L1 with pulse injection vs distance to the PSU	132
7.19	σ_{pulse} L1 with pulse injection	132
7.20	σ_{pulse} L1 with pulse injection vs distance to the PSU	133
7.21	σ_{thresh} L0 pedestal for linear PSU	134
7.22	σ_{thresh} and σ_{pulse} L0 with pulse injection for linear PSU	135
8.1	PSI-LBC Tri II optical data	140
8.2	MW satellites in size–magnitude space	142
8.3	Tri II’s $J_{0.5}$ comparison	143
8.4	Tri II’s JFactor vs θ	146
8.5	Tri II’s $dJ/d\Omega$	147
8.6	Presence of <i>Tri Beta-4</i> during Tri II data taking	148
8.7	Tri II’s data Zd distribution	149
8.8	$\sim 1/sen$ vs θ_c	151
8.9	$\sim 1/sen$ vs h_c and $h_c(E')$	151
8.10	$\langle\sigma v\rangle_{eff}$ vs m_{DM}	152
8.11	Tri II θ^2 plot	152
8.12	Tri II’s skymap	153
8.13	Tri II $\langle\sigma v\rangle$ limits	155
8.14	Tri II $\langle\sigma v\rangle$ comparison	156
9.1	JFactor comparison: CG vs dSph	161
9.2	Perseus CG dark matter density	165

LIST OF FIGURES

9.3	Perseus atmospheric transmission	167
9.4	Perseus mean DC	168
9.5	Perseus Zd distribution	177
9.6	Perseus FoV: Pointing \mathcal{B}	178
9.7	Perseus FoV: Pointing \mathcal{B}	179
9.8	NGC 1275, NGC 1265 and IC 310 night-wise significances	180
9.9	Point-like PSF and scaling factors	181
9.10	C -factors as a function of the estimated energy	181
9.11	NGC 1275's measured event rate	182
9.12	Perseus sensitivity to decay lifetime	183
9.13	Perseus decay lifetime limits comparison	184

LIST OF TABLES

2.1	SM particles and their superpartners in the MSSM model . . .	25
3.1	LIDAR transmission ranges	64
6.1	Optimal θ_c and w for annihilation in Bonnivard	112
6.2	Optimal θ_c and w for annihilation in Geringer	113
6.3	Optimal θ_c and w for decay in Bonnivard	114
6.4	Optimal θ_c and w for decay in Geringer	115
8.1	Tri II data resume	146
8.2	Tri II data transmission	148
8.3	Tri II data bins	154
9.1	Perseus virial mass	164
9.2	Observations of the Perseus cluster with the MAGIC telescopes for two different telescope pointings \mathcal{A} and \mathcal{B} for different observational periods. The number of hours taken for each period and after event cleaning: <i>quality</i> cuts are based on NSB+AOD, <i>specific</i> cuts are based on the night-wise significance of <i>NGC1275</i> , <i>NGC1265</i> or <i>IC310</i> . See text for details.	166
9.3	Gamma-ray emitter coordinates	169
9.4	Perseus data bins	173

BIBLIOGRAPHY

Search for squarks and gluinos using final states with jets and missing transverse momentum with the ATLAS detector in $\sqrt{s} = 7$ TeV proton-proton collisions. 2012.

The Pierre Auger Observatory: Contributions to the 34th International Cosmic Ray Conference (ICRC 2015), 2015. URL <http://inspirehep.net/record/1393211/files/arXiv:1509.03732.pdf>.

Georges Aad et al. Observation of a new particle in the search for the Standard Model Higgs boson with the ATLAS detector at the LHC. *Phys. Lett.*, B716: 1–29, 2012. doi: 10.1016/j.physletb.2012.08.020.

Georges Aad et al. Search for supersymmetry at $\sqrt{s} = 13$ TeV in final states with jets and two same-sign leptons or three leptons with the ATLAS detector. *Eur. Phys. J.*, C76(5):259, 2016. doi: 10.1140/epjc/s10052-016-4095-8.

R Aaij et al. First Evidence for the Decay $B_s^0 \rightarrow \mu^+ \mu^-$. *Phys. Rev. Lett.*, 110(2):021801, 2013. doi: 10.1103/PhysRevLett.110.021801.

J. Aalbers et al. DARWIN: towards the ultimate dark matter detector. *JCAP*, 1611:017, 2016. doi: 10.1088/1475-7516/2016/11/017.

C. E. Aalseth et al. Search for An Annual Modulation in Three Years of CoGeNT Dark Matter Detector Data. 2014.

C. E. Aalseth et al. DarkSide-20k: A 20 Tonne Two-Phase LAr TPC for Direct Dark Matter Detection at LNGS. 2017.

M. G. Aartsen et al. Search for annihilating dark matter in the Sun with 3 years of IceCube data. *Eur. Phys. J.*, C77(3):146, 2017. doi: 10.1140/epjc/s10052-017-4689-9.

BIBLIOGRAPHY

- R. Abbasi et al. Search for Neutrinos from Annihilating Dark Matter in the Direction of the Galactic Center with the 40-String IceCube Neutrino Observatory. 2012.
- B. P. Abbott et al. Observation of Gravitational Waves from a Binary Black Hole Merger. *Phys. Rev. Lett.*, 116(6):061102, 2016a. doi: 10.1103/PhysRevLett.116.061102.
- B. P. Abbott et al. Astrophysical Implications of the Binary Black-Hole Merger GW150914. *Astrophys. J.*, 818(2):L22, 2016b. doi: 10.3847/2041-8205/818/2/L22.
- T. M. C. Abbott et al. Dark Energy Survey Year 1 Results: Cosmological Constraints from Galaxy Clustering and Weak Lensing. 2017.
- H. Abdallah et al. Search for dark matter annihilations towards the inner Galactic halo from 10 years of observations with H.E.S.S. *Phys. Rev. Lett.*, 117(11):111301, 2016. doi: 10.1103/PhysRevLett.117.111301.
- A. A. Abdo et al. Fermi Large Area Telescope Observations of the Crab Pulsar and Nebula. *Astrophys. J.*, 708:1254–1267, 2010a. doi: 10.1088/0004-637X/708/2/1254.
- A. A. Abdo et al. Fermi LAT observations of the Geminga pulsar. *Astrophys. J.*, 720:272, 2010b. doi: 10.1088/0004-637X/720/1/272.
- Aous A. Abdo et al. Measurement of the Cosmic Ray e^+ plus e^- spectrum from 20 GeV to 1 TeV with the Fermi Large Area Telescope. *Phys. Rev. Lett.*, 102:181101, 2009. doi: 10.1103/PhysRevLett.102.181101.
- S. Abdollahi et al. Cosmic-ray electron-positron spectrum from 7 GeV to 2 TeV with the Fermi Large Area Telescope. *Phys. Rev.*, D95(8):082007, 2017. doi: 10.1103/PhysRevD.95.082007.
- A. U. Abeysekara et al. Extended gamma-ray sources around pulsars constrain the origin of the positron flux at Earth. 2017. doi: 10.1126/science.aan4880.
- V. A. Acciari et al. VERITAS Upper Limit on the VHE Emission from the Radio Galaxy NGC 1275. *Astrophys. J.*, 706:L275–L280, 2009. doi: 10.1088/0004-637X/706/2/L275.
- V. A. Acciari et al. VERITAS Search for VHE Gamma-ray Emission from Dwarf Spheroidal Galaxies. *Astrophys. J.*, 720:1174–1180, 2010. doi: 10.1088/0004-637X/720/2/1174.

-
- M. Acciarri et al. Measurement of energetic single photon production at LEP. *Phys. Lett.*, B346:190–198, 1995. doi: 10.1016/0370-2693(95)00023-E.
- B. S. Acharya et al. Science with the Cherenkov Telescope Array. 2017.
- M. Ackermann et al. Constraints on the Galactic Halo Dark Matter from Fermi-LAT Diffuse Measurements. *Astrophys. J.*, 761:91, 2012. doi: 10.1088/0004-637X/761/2/91.
- M. Ackermann et al. Searching for Dark Matter Annihilation from Milky Way Dwarf Spheroidal Galaxies with Six Years of Fermi Large Area Telescope Data. *Phys. Rev. Lett.*, 115(23):231301, 2015. doi: 10.1103/PhysRevLett.115.231301.
- M. Ackermann et al. Search for extended sources in the Galactic Plane using 6 years of Fermi-Large Area Telescope Pass 8 data above 10 GeV. 2017.
- M. Actis et al. Design concepts for the Cherenkov Telescope Array CTA: An advanced facility for ground-based high-energy gamma-ray astronomy. *Exper. Astron.*, 32:193–316, 2011. doi: 10.1007/s10686-011-9247-0.
- P. A. R. Ade et al. Planck 2013 results. XVI. Cosmological parameters. *Astron. Astrophys.*, 571:A16, 2014. doi: 10.1051/0004-6361/201321591.
- P. A. R. Ade et al. Planck 2015 results. XIII. Cosmological parameters. *Astron. Astrophys.*, 594:A13, 2016. doi: 10.1051/0004-6361/201525830.
- S. Adrian-Martinez et al. Search of Dark Matter Annihilation in the Galactic Centre using the ANTARES Neutrino Telescope. *JCAP*, 1510(10):068, 2015. doi: 10.1088/1475-7516/2015/10/068.
- Oscar Adriani et al. An anomalous positron abundance in cosmic rays with energies 1.5-100 GeV. *Nature*, 458:607–609, 2009. doi: 10.1038/nature07942.
- Kaustubh Agashe and Geraldine Servant. Warped unification, proton stability and dark matter. *Phys. Rev. Lett.*, 93:231805, 2004. doi: 10.1103/PhysRevLett.93.231805.
- M. Aguilar, G. Alberti, B. Alpat, A. Alvino, G. Ambrosi, K. Andeen, H. Anderhub, L. Arruda, P. Azzarello, A. Bachlechner, F. Barao, B. Baret, A. Barrau, L. Barrin, A. Bartoloni, L. Basara, A. Basili, L. Batalha, J. Bates, R. Battiston, J. Bazo, R. Becker, U. Becker, M. Behlmann, B. Beischer, J. Berdugo, P. Berges, B. Bertucci, G. Bigongiari, A. Biland, V. Bindi, S. Bizzaglia, G. Boella, W. de Boer, K. Bollweg, J. Bolmont, B. Borgia, S. Borsini,

M. J. Boschini, G. Boudoul, M. Bourquin, P. Brun, M. Buénerd, J. Burger, W. Burger, F. Cadoux, X. D. Cai, M. Capell, D. Casadei, J. Casaus, V. Cascioli, G. Castellini, I. Cernuda, F. Cervelli, M. J. Chae, Y. H. Chang, A. I. Chen, C. R. Chen, H. Chen, G. M. Cheng, H. S. Chen, L. Cheng, N. Chernoplyokov, A. Chikanian, E. Choumilov, V. Choutko, C. H. Chung, C. Clark, R. Clavero, G. Coignet, V. Commichau, C. Consolandi, A. Contin, C. Corti, M. T. Costado Dios, B. Coste, D. Crespo, Z. Cui, M. Dai, C. Delgado, S. Della Torre, B. Demirköz, P. Dennett, L. Derome, S. Di Falco, X. H. Diao, A. Diago, L. Djambazov, C. Díaz, P. von Doetinchem, W. J. Du, J. M. Dubois, R. Duperay, M. Duranti, D. D'Urso, A. Egorov, A. Eline, F. J. Epling, T. Eronen, J. van Es, H. Esser, A. Falvard, E. Fiandrini, A. Fiasson, E. Finch, P. Fisher, K. Flood, R. Foglio, M. Fohey, S. Fopp, N. Fouque, Y. Galaktionov, M. Gallilee, L. Gallin-Martel, G. Gallucci, B. García, J. García, R. García-López, L. García-Tabares, C. Gargiulo, H. Gast, I. Gebauer, S. Gentile, M. Gervasi, W. Gillard, F. Giovacchini, L. Girard, P. Goglov, J. Gong, C. Goy-Henningsen, D. Grandi, M. Graziani, A. Grechko, A. Gross, I. Guerri, C. de la Guía, K. H. Guo, M. Habiby, S. Haino, F. Hauler, Z. H. He, M. Heil, J. Heilig, R. Hermel, H. Hofer, Z. C. Huang, W. Hungerford, M. Incagli, M. Ionica, A. Jacholkowska, W. Y. Jang, H. Jinchi, M. Jongmanns, L. Journet, L. Jungermann, W. Karpinski, G. N. Kim, K. S. Kim, Th. Kirn, R. Kossakowski, A. Koulemzine, O. Kounina, A. Kounine, V. Koutsenko, M. S. Krafczyk, E. Laudi, G. Laurenti, C. Lauritzen, A. Lebedev, M. W. Lee, S. C. Lee, C. Leluc, H. León Vargas, V. Lepareur, J. Q. Li, Q. Li, T. X. Li, W. Li, Z. H. Li, P. Lipari, C. H. Lin, D. Liu, H. Liu, T. Lomtadze, Y. S. Lu, S. Lucidi, K. Lübelmeyer, J. Z. Luo, W. Lustermann, S. Lv, J. Madsen, R. Majka, A. Malinin, C. Mañá, J. Marín, T. Martin, G. Martínez, F. Masciocchi, N. Masi, D. Maurin, A. McInturff, P. McIntyre, A. Menchaca-Rocha, Q. Meng, M. Menichelli, I. Mereu, M. Millinger, D. C. Mo, M. Molina, P. Mott, A. Mujunen, S. Natale, P. Nemeth, J. Q. Ni, N. Nikonov, F. Nozzoli, P. Nunes, A. Obermeier, S. Oh, A. Oliva, F. Palmonari, C. Palomares, M. Paniccia, A. Papi, W. H. Park, M. Pauluzzi, F. Pauss, A. Pauw, E. Pedreschi, S. Pensotti, R. Pereira, E. Perin, G. Pessina, G. Pierschel, F. Pilo, A. Piluso, C. Pizzolotto, V. Plyaskin, J. Pochon, M. Pohl, V. Poireau, S. Porter, J. Poux, A. Putze, L. Quadrani, X. N. Qi, P. G. Rancoita, D. Rapin, Z. L. Ren, J. S. Ricol, E. Riihonen, I. Rodríguez, U. Roeser, S. Rosier-Lees, L. Rossi, A. Rozhkov, D. Rozza, A. Sabellek, R. Sagdeev, J. Sandweiss, B. Santos, P. Saouter, M. Sarchioni, S. Schael, D. Schinzel, M. Schmanau, G. Schwering, A. Schulz von Dratzig, G. Scolieri, E. S. Seo, B. S. Shan, J. Y. Shi, Y. M. Shi, T. Siedenburger, R. Siedling, D. Son, F. Spada, F. Spinella, M. Steuer, K. Stiff, W. Sun, W. H.

- Sun, X. H. Sun, M. Tacconi, C. P. Tang, X. W. Tang, Z. C. Tang, L. Tao, J. Tassan-Viol, Samuel C. C. Ting, S. M. Ting, C. Titus, N. Tomassetti, F. Toral, J. Torsti, J. R. Tsai, J. C. Tutt, J. Ulbricht, T. Urban, V. Vagelli, E. Valente, C. Vannini, E. Valtonen, M. Vargas Trevino, S. Vaurynovich, M. Vecchi, M. Vergain, B. Verlaet, C. Vescovi, J. P. Vialle, G. Viertel, G. Volpini, D. Wang, N. H. Wang, Q. L. Wang, R. S. Wang, X. Wang, Z. X. Wang, W. Wallraff, Z. L. Weng, M. Willenbrock, M. Wloch, H. Wu, K. Y. Wu, Z. S. Wu, W. J. Xiao, S. Xie, R. Q. Xiong, G. M. Xin, N. S. Xu, W. Xu, Q. Yan, J. Yang, M. Yang, Q. H. Ye, H. Yi, Y. J. Yu, Z. Q. Yu, S. Zeissler, J. G. Zhang, Z. Zhang, M. M. Zhang, Z. M. Zheng, H. L. Zhuang, V. Zhukov, A. Zichichi, P. Zuccon, and C. Zurbach. First result from the alpha magnetic spectrometer on the international space station: Precision measurement of the positron fraction in primary cosmic rays of 0.5–350 gev. *Phys. Rev. Lett.*, 110:141102, Apr 2013. doi: 10.1103/PhysRevLett.110.141102. URL <https://link.aps.org/doi/10.1103/PhysRevLett.110.141102>.
- M. Aguilar, L. Ali Cavazonza, B. Alpat, G. Ambrosi, L. Arruda, N. Attig, S. Aupetit, P. Azzarello, A. Bachlechner, F. Barao, A. Barrau, L. Barrin, A. Bartoloni, L. Basara, S. Başeğmez-du Pree, M. Battarbee, R. Battiston, J. Bazo, U. Becker, M. Behlmann, B. Beischer, J. Berdugo, B. Bertucci, V. Bindi, G. Boella, W. de Boer, K. Bollweg, V. Bonnivard, B. Borgia, M. J. Boschini, M. Bourquin, E. F. Bueno, J. Burger, F. Cadoux, X. D. Cai, M. Capell, S. Caroff, J. Casaus, G. Castellini, I. Cernuda, F. Cervelli, M. J. Chae, Y. H. Chang, A. I. Chen, G. M. Chen, H. S. Chen, L. Cheng, H. Y. Chou, E. Choumilov, V. Choutko, C. H. Chung, C. Clark, R. Clavero, G. Coignet, C. Consolandi, A. Contin, C. Corti, B. Coste, W. Creus, M. Crispoltoni, Z. Cui, Y. M. Dai, C. Delgado, S. Della Torre, M. B. Demirköz, L. Derome, S. Di Falco, F. Dimiccoli, C. Díaz, P. von Doetinchem, F. Dong, F. Donnini, M. Duranti, D. D’Urso, A. Egorov, A. Eline, T. Eronen, J. Feng, E. Fiandrini, E. Finch, P. Fisher, V. Formato, Y. Galaktionov, G. Gallucci, B. García, R. J. García-López, C. Gargiulo, H. Gast, I. Gebauer, M. Gervasi, A. Ghelfi, F. Giovacchini, P. Goglov, D. M. Gómez-Coral, J. Gong, C. Goy, V. Grabski, D. Grandi, M. Graziani, I. Guerri, K. H. Guo, M. Habiby, S. Haino, K. C. Han, Z. H. He, M. Heil, J. Hoffman, T. H. Hsieh, H. Huang, Z. C. Huang, C. Huh, M. Incagli, M. Ionica, W. Y. Jang, H. Jinchi, S. C. Kang, K. Kanishev, G. N. Kim, K. S. Kim, Th. Kirn, C. Konak, O. Kounina, A. Kounine, V. Koutsenko, M. S. Krafczyk, G. La Vacca, E. Laudi, G. Laurenti, I. Lazzizzera, A. Lebedev, H. T. Lee, S. C. Lee, C. Leluc, H. S. Li, J. Q. Li, J. Q. Li, Q. Li, T. X. Li, W. Li, Z. H. Li, Z. Y. Li, S. Lim, C. H. Lin, P. Lipari, T. Lippert, D. Liu,

- Hu Liu, S. Q. Lu, Y. S. Lu, K. Luebelsmeyer, F. Luo, J. Z. Luo, S. S. Lv, R. Majka, C. Mañá, J. Marín, T. Martin, G. Martínez, N. Masi, D. Maurin, A. Menchaca-Rocha, Q. Meng, D. C. Mo, L. Morescalchi, P. Mott, T. Nelson, J. Q. Ni, N. Nikonov, F. Nozzoli, P. Nunes, A. Oliva, M. Orcinha, F. Palmonari, C. Palomares, M. Paniccia, M. Pauluzzi, S. Pensotti, R. Pereira, N. Picot-Clemente, F. Pilo, C. Pizzolotto, V. Plyaskin, M. Pohl, V. Poireau, A. Putze, L. Quadrani, X. M. Qi, X. Qin, Z. Y. Qu, T. Rähkä, P. G. Rancoita, D. Rapin, J. S. Ricol, I. Rodríguez, S. Rosier-Lees, A. Rozhkov, D. Rozza, R. Sagdeev, J. Sandweiss, P. Saouter, S. Schael, S. M. Schmidt, A. Schulz von Dratzig, G. Schwing, E. S. Seo, B. S. Shan, J. Y. Shi, T. Siedenbueg, D. Son, J. W. Song, W. H. Sun, M. Tacconi, X. W. Tang, Z. C. Tang, L. Tao, D. Tescaro, Samuel C. C. Ting, S. M. Ting, N. Tomasetti, J. Torsti, C. Türkoğlu, T. Urban, V. Vagelli, E. Valente, C. Vannini, E. Valtonen, M. Vázquez Acosta, M. Vecchi, M. Velasco, J. P. Vialle, V. Vitale, S. Vitillo, L. Q. Wang, N. H. Wang, Q. L. Wang, X. Wang, X. Q. Wang, Z. X. Wang, C. C. Wei, Z. L. Weng, K. Whitman, J. Wienkenhöver, M. Willenbrock, H. Wu, X. Wu, X. Xia, R. Q. Xiong, W. Xu, Q. Yan, J. Yang, M. Yang, Y. Yang, H. Yi, Y. J. Yu, Z. Q. Yu, S. Zeissler, C. Zhang, J. Zhang, J. H. Zhang, S. D. Zhang, S. W. Zhang, Z. Zhang, Z. M. Zheng, Z. Q. Zhu, H. L. Zhuang, V. Zhukov, A. Zichichi, N. Zimmermann, and P. Zuccon. Antiproton flux, antiproton-to-proton flux ratio, and properties of elementary particle fluxes in primary cosmic rays measured with the alpha magnetic spectrometer on the international space station. *Phys. Rev. Lett.*, 117:091103, Aug 2016. doi: 10.1103/PhysRevLett.117.091103. URL <https://link.aps.org/doi/10.1103/PhysRevLett.117.091103>.
- F. Aharonian. Very high energy gamma-ray observations of the galaxy clusters Abell 496 and Abell 85 with H.E.S.S. *Astron. Astrophys.*, 495:27, 2009a. doi: 10.1051/0004-6361:200811372.
- F. Aharonian et al. Observations of the Crab Nebula with H.E.S.S. *Astron. Astrophys.*, 457:899–915, 2006. doi: 10.1051/0004-6361:20065351.
- F. Aharonian et al. The energy spectrum of cosmic-ray electrons at TeV energies. *Phys. Rev. Lett.*, 101:261104, 2008. doi: 10.1103/PhysRevLett.101.261104.
- F. A. Aharonian. Constraints on the multi-TeV particle population in the Coma Galaxy Cluster with H.E.S.S. observations. *Astron. Astrophys.*, 502:437, 2009b. doi: 10.1051/0004-6361/200912086.
- M. L. Ahnen et al. Deep observation of the NGC 1275 region with MAGIC:

- search of diffuse γ -ray emission from cosmic rays in the Perseus cluster. *Astron. Astrophys.*, 589:A33, 2016a. doi: 10.1051/0004-6361/201527846.
- M. L. Ahnen et al. Limits to dark matter annihilation cross-section from a combined analysis of MAGIC and Fermi-LAT observations of dwarf satellite galaxies. *JCAP*, 1602(02):039, 2016b. doi: 10.1088/1475-7516/2016/02/039.
- M. L. Ahnen et al. Search for VHE gamma-ray emission from Geminga pulsar and nebula with the MAGIC telescopes. *Astron. Astrophys.*, 591:A138, 2016c. doi: 10.1051/0004-6361/201527722.
- M. L. Ahnen et al. Observations of Sagittarius A* during the pericenter passage of the G2 object with MAGIC. *Astron. Astrophys.*, 601:A33, 2017a. doi: 10.1051/0004-6361/201629355.
- M. L. Ahnen et al. Indirect dark matter searches in the dwarf satellite galaxy Ursa Major II with the MAGIC Telescopes. 2017b.
- M. L. Ahnen et al. Performance of the MAGIC telescopes under moonlight. *Astropart. Phys.*, 94:29–41, 2017c. doi: 10.1016/j.astropartphys.2017.08.001.
- D. S. Akerib et al. Results from a search for dark matter in the complete LUX exposure. *Phys. Rev. Lett.*, 118(2):021303, 2017a. doi: 10.1103/PhysRevLett.118.021303.
- D. S. Akerib et al. Limits on spin-dependent WIMP-nucleon cross section obtained from the complete LUX exposure. *Phys. Rev. Lett.*, 118(25):251302, 2017b. doi: 10.1103/PhysRevLett.118.251302.
- A. Albert, M. André, M. Anghinolfi, G. Anton, M. Ardid, J.-J. Aubert, T. Avgitas, B. Baret, J. Barrios-Martí, S. Basa, V. Bertin, S. Biagi, R. Bormuth, S. Bourret, M.C. Bouwhuis, R. Bruijn, J. Brunner, J. Busto, A. Capone, L. Caramete, J. Carr, S. Celli, T. Chiarusi, M. Circella, J.A.B. Coelho, A. Coleiro, R. Coniglione, H. Costantini, P. Coyle, A. Creusot, A. Deschamps, G. De Bonis, C. Distefano, I. Di Palma, C. Donzaud, D. Doric, D. Drouhin, T. Eberl, I. El Bojaddaini, D. Elsässer, A. Enzenhöfer, I. Felis, L.A. Fusco, S. Galatà, P. Gay, S. Geißelsöder, K. Geyer, V. Giordano, A. Gleixner, H. Glotin, T. Grégoire, R. Gracia Ruiz, K. Graf, S. Hallmann, H. van Haren, A.J. Heijboer, Y. Hello, J.J. Hernández-Rey, J. Hößl, J. Hofestädt, C. Hugon, G. Illuminati, C.W. James, M. de Jong, M. Jongen, M. Kadler, O. Kalekin, U. Katz, D. Kießling, A. Kouchner, M. Kreter, I. Kreykenbohm, V. Kulikovskiy, C. Lachaud, R. Lahmann, D. Lefèvre, E. Leonora, M. Lotze, S. Loucatos, M. Marcelin, A. Margiotta, A. Marinelli,

BIBLIOGRAPHY

- J.A. Martínez-Mora, A. Mathieu, R. Mele, K. Melis, T. Michael, P. Migliozzi, A. Moussa, C. Mueller, E. Nezri, G.E. Pāvālaš, C. Pellegrino, C. Perrina, P. Piattelli, V. Popa, T. Pradier, L. Quinn, C. Racca, G. Riccobene, K. Roensch, A. Sánchez-Losa, M. Saldaña, I. Salvadori, D.F.E. Samtleben, M. Sanguineti, P. Sapienza, J. Schnabel, F. Schüssler, T. Seitz, C. Sieger, M. Spurio, Th. Stolarczyk, M. Taiuti, Y. Tayalati, A. Trovato, M. Tselengidou, D. Turpin, C. Tönnis, B. Vallage, C. Vallée, V. Van Elewyck, D. Vivolo, A. Vizzoca, S. Wagner, J. Wilms, J.D. Zornoza, and J. Zúñiga. Search for dark matter annihilation in the earth using the antares neutrino telescope. *Physics of the Dark Universe*, 16(Supplement C):41 – 48, 2017a. ISSN 2212-6864. doi: <https://doi.org/10.1016/j.dark.2017.04.005>. URL <http://www.sciencedirect.com/science/article/pii/S2212686417300225>.
- A. Albert et al. Searching for Dark Matter Annihilation in Recently Discovered Milky Way Satellites with Fermi-LAT. *Astrophys. J.*, 834(2):110, 2017b. doi: 10.3847/1538-4357/834/2/110.
- J. Albert et al. VHE Gamma-Ray Observation of the Crab Nebula and Pulsar with MAGIC. *Astrophys. J.*, 674:1037–1055, 2008a. doi: 10.1086/525270.
- J. Albert et al. Implementation of the Random Forest Method for the Imaging Atmospheric Cherenkov Telescope MAGIC. *Nucl. Instrum. Meth.*, A588: 424–432, 2008b. doi: 10.1016/j.nima.2007.11.068.
- J. Aleksić, J. Rico, and M. Martinez. Optimized analysis method for indirect dark matter searches with Imaging Air Cherenkov Telescopes. *JCAP*, 1210: 032, 2012a. doi: 10.1088/1475-7516/2012/10/032.
- J. Aleksić et al. MAGIC Gamma-Ray Telescope Observation of the Perseus Cluster of Galaxies: Implications for Cosmic Rays, Dark Matter and NGC 1275. *Astrophys. J.*, 710:634–647, 2010a. doi: 10.1088/0004-637X/710/1/634.
- J. Aleksić et al. Detection of very high energy gamma-ray emission from the Perseus cluster head-tail galaxy IC 310 by the MAGIC telescopes. *Astrophys. J.*, 723:L207, 2010b. doi: 10.1088/2041-8205/723/2/L207.
- J. Aleksić et al. Searches for Dark Matter annihilation signatures in the Segue 1 satellite galaxy with the MAGIC-I telescope. *JCAP*, 1106:035, 2011. doi: 10.1088/1475-7516/2011/06/035.
- J. Aleksić et al. Performance of the MAGIC stereo system obtained with Crab Nebula data. *Astropart. Phys.*, 35:435–448, 2012b. doi: 10.1016/j.astropartphys.2011.11.007.

- J. Aleksić et al. Constraining Cosmic Rays and Magnetic Fields in the Perseus Galaxy Cluster with TeV observations by the MAGIC telescopes. *Astron. Astrophys.*, 541:A99, 2012c. doi: 10.1051/0004-6361/201118502.
- J. Aleksić et al. Detection of very high energy gamma-ray emission from NGC 1275 by the MAGIC telescopes. *Astron. Astrophys.*, 539:L2, 2012d. doi: 10.1051/0004-6361/201118668.
- J. Aleksić et al. Rapid and multiband variability of the TeV bright active nucleus of the galaxy IC 310. *Astron. Astrophys.*, 563:A91, 2014a. doi: 10.1051/0004-6361/201321938.
- J. Aleksić et al. Contemporaneous observations of the radio galaxy NGC 1275 from radio to very high energy γ -rays. *Astron. Astrophys.*, 564:A5, 2014b. doi: 10.1051/0004-6361/201322951.
- J. Aleksić et al. Optimized dark matter searches in deep observations of Segue 1 with MAGIC. *JCAP*, 1402:008, 2014c. doi: 10.1088/1475-7516/2014/02/008.
- J. Aleksić et al. Black hole lightning due to particle acceleration at subhorizon scales. *Science*, 346:1080–1084, 2014d. doi: 10.1126/science.1256183.
- J. Aleksić et al. The major upgrade of the MAGIC telescopes, Part II: A performance study using observations of the Crab Nebula. *Astropart. Phys.*, 72:76–94, 2016a. doi: 10.1016/j.astropartphys.2015.02.005.
- J. Aleksić et al. The major upgrade of the MAGIC telescopes, Part I: The hardware improvements and the commissioning of the system. *Astropart. Phys.*, 72:61–75, 2016b. doi: 10.1016/j.astropartphys.2015.04.004.
- E. Aliu et al. Improving the performance of the single-dish Cherenkov telescope MAGIC through the use of signal timing. *Astropart. Phys.*, 30:293–305, 2009. doi: 10.1016/j.astropartphys.2008.10.003.
- E. Aliu et al. VERITAS Deep Observations of the Dwarf Spheroidal Galaxy Segue 1. *Phys. Rev.*, D85:062001, 2012. doi: 10.1103/PhysRevD.85.062001,10.1103/PhysRevD.91.129903. [Erratum: *Phys. Rev.D*91,no.12,129903(2015)].
- E. Aliu et al. Spatially Resolving the Very High Energy emission from MGRO J2019+37 with VERITAS. *Astrophys. J.*, 788:78, 2014. doi: 10.1088/0004-637X/788/1/78.

BIBLIOGRAPHY

G. Ambrosi et al. Direct detection of a break in the teraelectronvolt cosmic-ray spectrum of electrons and positrons. *Nature*, 552:63–66, 2017. doi: 10.1038/nature24475.

AMS-02.

Shin'ichiro Ando and Koji Ishiwata. Constraints on decaying dark matter from the extragalactic gamma-ray background. *JCAP*, 1505(05):024, 2015. doi: 10.1088/1475-7516/2015/05/024.

Shinichiro Ando and Daisuke Nagai. Fermi-LAT constraints on dark matter annihilation cross section from observations of the Fornax cluster. *JCAP*, 1207:017, 2012. doi: 10.1088/1475-7516/2012/07/017.

ANTARES.

Thomas Appelquist, Hsin-Chia Cheng, and Bogdan A. Dobrescu. Bounds on universal extra dimensions. *Phys. Rev.*, D64:035002, 2001. doi: 10.1103/PhysRevD.64.035002.

E. Aprile et al. XENON100 Dark Matter Results from a Combination of 477 Live Days. *Phys. Rev.*, D94(12):122001, 2016. doi: 10.1103/PhysRevD.94.122001.

E. Aprile et al. First Dark Matter Search Results from the XENON1T Experiment. *Phys. Rev. Lett.*, 119(18):181301, 2017. doi: 10.1103/PhysRevLett.119.181301.

T. Asaka, J. Hashiba, M. Kawasaki, and T. Yanagida. Spectrum of background x-rays from moduli dark matter. *Phys. Rev. D*, 58:023507, Jun 1998. doi: 10.1103/PhysRevD.58.023507. URL <https://link.aps.org/doi/10.1103/PhysRevD.58.023507>.

Takehiko Asaka and Mikhail Shaposhnikov. The nuMSM, dark matter and baryon asymmetry of the universe. *Phys. Lett.*, B620:17–26, 2005. doi: 10.1016/j.physletb.2005.06.020.

ATLAS.

Vladimir Avila-Reese. Understanding Galaxy Formation and Evolution. pages 115–165, 2006. doi: 10.1007/978-1-4020-5575-1_4. [Astrophys. Space Sci. Proc.2,115(2007)].

- Howard Baer, Ki-Young Choi, Jihn E. Kim, and Leszek Roszkowski. Dark matter production in the early Universe: beyond the thermal WIMP paradigm. *Phys. Rept.*, 555:1–60, 2015. doi: 10.1016/j.physrep.2014.10.002.
- Gabriela Barenboim, Christoph Andreas Ternes, and Mariam Tórtola. Neutrinos, DUNE and the world best bound on CPT violation. 2017.
- A. Barrau et al. The CAT imaging telescope for very high-energy gamma-ray astronomy. *Nucl. Instrum. Meth.*, A416:278–292, 1998. doi: 10.1016/S0168-9002(98)00749-9.
- Bruce A. Bassett and Renee Hlozek. Baryon Acoustic Oscillations. 2009.
- K. G. Begeman, A. H. Broeils, and R. H. Sanders. Extended rotation curves of spiral galaxies: Dark haloes and modified dynamics. *Mon. Not. Roy. Astron. Soc.*, 249:523, 1991.
- Jacob D. Bekenstein. Relativistic gravitation theory for the MOND paradigm. *Phys. Rev.*, D70:083509, 2004. doi: 10.1103/PhysRevD.70.083509,10.1103/PhysRevD.71.069901. [Erratum: *Phys. Rev.* D71,069901(2005)].
- V. Berezhinsky and J. W. F. Valle. The KeV majoron as a dark matter particle. *Phys. Lett.*, B318:360–366, 1993. doi: 10.1016/0370-2693(93)90140-D.
- Carola F. Berger, James S. Gainer, JoAnne L. Hewett, and Thomas G. Rizzo. Supersymmetry Without Prejudice. *JHEP*, 02:023, 2009. doi: 10.1088/1126-6708/2009/02/023.
- Rita Bernabei et al. Further results on the WIMP annual modulation signature by DAMA/NaI. *PoS*, AHEP2003:063, 2003.
- Rita Bernabei et al. The Annual Modulation Signature for Dark Matter: DAMA/LIBRA-Phase1 Results and Perspectives. *Adv. High Energy Phys.*, 2014:605659, 2014. doi: 10.1155/2014/605659.
- Gianfranco Bertone, Dan Hooper, and Joseph Silk. Particle dark matter: Evidence, candidates and constraints. *Phys. Rept.*, 405:279–390, 2005. doi: 10.1016/j.physrep.2004.08.031.
- J. Betorz. Search for correlations of atmospheric transmission obtained from the magic lidar and the pyrometer and characterization of asics for the cta. Master’s thesis, Bachelor Thesis - Universitat Autònoma de Barcelona, The address of the publisher, 2015.

BIBLIOGRAPHY

- Xiao-Jun Bi, Ming-zhe Li, and Xin-min Zhang. fermionic partner of the quintessence field as a candidate for dark matter. *Phys. Rev.*, D69:123521, 2004. doi: 10.1103/PhysRevD.69.123521.
- P. M. S. Blackett. A possible contribution to the night sky from the Cerenkov radiation emitted by cosmic rays. In *The Emission Spectra of the Night Sky and Aurorae*, page 34, 1948.
- N. W. Boggess et al. The COBE mission - Its design and performance two years after launch. *Astrophys. J.*, 397:420–429, 1992. doi: 10.1086/171797.
- V. Bonnivard, C. Combet, D. Maurin, M. G. Walker, and A. Geringer-Sameth. Dark matter annihilation factors in the Milky Way’s dwarf spheroidal galaxies. *J. Phys. Conf. Ser.*, 718(4):042005, 2016. doi: 10.1088/1742-6596/718/4/042005.
- V. Bonnivard et al. Dark matter annihilation and decay in dwarf spheroidal galaxies: The classical and ultrafaint dSphs. *Mon. Not. Roy. Astron. Soc.*, 453(1):849–867, 2015. doi: 10.1093/mnras/stv1601.
- Timothy D. Brandt. Constraints on MACHO Dark Matter from Compact Stellar Systems in Ultra-Faint Dwarf Galaxies. *Astrophys. J.*, 824(2):L31, 2016. doi: 10.3847/2041-8205/824/2/L31.
- Torsten Bringmann, Lars Bergstrom, and Joakim Edsjo. New Gamma-Ray Contributions to Supersymmetric Dark Matter Annihilation. *JHEP*, 01:049, 2008. doi: 10.1088/1126-6708/2008/01/049.
- Wilfried Buchmuller, Laura Covi, Koichi Hamaguchi, Alejandro Ibarra, and Tsutomu Yanagida. Gravitino Dark Matter in R-Parity Breaking Vacua. *JHEP*, 03:037, 2007. doi: 10.1088/1126-6708/2007/03/037.
- N. Cabibbo, G. R. Farrar, and L. Maiani. Massive photinos: Unstable and interesting. *Physics Letters B*, 105:155–158, October 1981. doi: 10.1016/0370-2693(81)91010-8.
- John E. Carlstrom, Gilbert P. Holder, and Erik D. Reese. Cosmology with the Sunyaev-Zel’dovich effect. *Ann. Rev. Astron. Astrophys.*, 40:643–680, 2002. doi: 10.1146/annurev.astro.40.060401.093803.
- E. Carmona, J. Sitarek, P. Colin, M. Doert, S. Klepser, S. Lombardi, M. Lopez, A. Moralejo, S. Pardo, V. Scalzotto, R. Zanin, and for the Magic Collaboration. Performance of the MAGIC Stereo System. *ArXiv e-prints*, October 2011.

- E. Carmona et al. Monte Carlo Simulation for the MAGIC-II System. In *Proceedings, 30th International Cosmic Ray Conference (ICRC 2007): Merida, Yucatan, Mexico, July 3-11, 2007*, volume 3, pages 1373–1376, 2007. URL <http://indico.nucleares.unam.mx/contributionDisplay.py?contribId=588&confId=4>. [3,1373(2007)].
- Oscar Catà, Alejandro Ibarra, and Sebastian Inghütt. Dark matter decays from nonminimal coupling to gravity. *Phys. Rev. Lett.*, 117(2):021302, 2016. doi: 10.1103/PhysRevLett.117.021302.
- Oscar Catà, Alejandro Ibarra, and Sebastian Inghütt. Dark matter decay through gravity portals. *Phys. Rev.*, D95(3):035011, 2017. doi: 10.1103/PhysRevD.95.035011.
- J. A. R. Cembranos, A. Dobado, and Antonio Lopez Maroto. Brane world dark matter. *Phys. Rev. Lett.*, 90:241301, 2003. doi: 10.1103/PhysRevLett.90.241301.
- J. A. R. Cembranos, A. de la Cruz-Dombriz, A. Dobado, R. A. Lineros, and A. L. Maroto. Photon spectra from WIMP annihilation. *Phys. Rev.*, D83:083507, 2011. doi: 10.1103/PhysRevD.83.083507.
- CERN.
- Ali H. Chamseddine, Richard L. Arnowitt, and Pran Nath. Locally Supersymmetric Grand Unification. *Phys. Rev. Lett.*, 49:970, 1982. doi: 10.1103/PhysRevLett.49.970.
- M. C. Chantell et al. Limits on the isotropic diffuse flux of ultrahigh-energy gamma radiation. *Phys. Rev. Lett.*, 79:1805–1808, 1997. doi: 10.1103/PhysRevLett.79.1805.
- A. Charbonnier, C. Combet, and D. Maurin. CLUMPY: a code for gamma-ray signals from dark matter structures. *Comput. Phys. Commun.*, 183:656–668, 2012. doi: 10.1016/j.cpc.2011.10.017.
- E. Charles et al. Sensitivity Projections for Dark Matter Searches with the Fermi Large Area Telescope. *Phys. Rept.*, 636:1–46, 2016. doi: 10.1016/j.physrep.2016.05.001.
- Serguei Chatrchyan et al. Observation of a new boson at a mass of 125 GeV with the CMS experiment at the LHC. *Phys. Lett.*, B716:30–61, 2012. doi: 10.1016/j.physletb.2012.08.021.

BIBLIOGRAPHY

- Xue-Lei Chen and Marc Kamionkowski. Particle decays during the cosmic dark ages. *Phys. Rev.*, D70:043502, 2004. doi: 10.1103/PhysRevD.70.043502.
- Yong Chen, T. H. Reiprich, H. Bohringer, Y. Ikebe, and Y. Y. Zhang. Statistics of X-ray observables for the cooling-core and non-cooling core galaxy clusters. *Astron. Astrophys.*, 2007. doi: 10.1051/0004-6361:20066471. [Astron. Astrophys.466,805(2007)].
- P. A. Cherenkov. Visible emission of clean liquids by action of gamma radiation. *Doklady Akademii Nauk SSSR*, 2:451, 1934. doi: citeulike:8699791.
- Daniel J. H. Chung, Edward W. Kolb, and Antonio Riotto. Superheavy dark matter. *Phys. Rev. D*, 59:023501, Nov 1998. doi: 10.1103/PhysRevD.59.023501. URL <https://link.aps.org/doi/10.1103/PhysRevD.59.023501>.
- Marco Cirelli. Dark Matter Indirect searches: phenomenological and theoretical aspects. *J. Phys. Conf. Ser.*, 447:012006, 2013. doi: 10.1088/1742-6596/447/1/012006.
- Marco Cirelli, Mario Kadastik, Martti Raidal, and Alessandro Strumia. Model-independent implications of the e^\pm , anti-proton cosmic ray spectra on properties of Dark Matter. *Nucl. Phys.*, B813:1–21, 2009. doi: 10.1016/j.nuclphysb.2013.05.002,10.1016/j.nuclphysb.2008.11.031. [Addendum: Nucl. Phys.B873,530(2013)].
- Marco Cirelli, Gennaro Corcella, Andi Hektor, Gert Hutsi, Mario Kadastik, Paolo Panci, Martti Raidal, Filippo Sala, and Alessandro Strumia. PPPC 4 DM ID: A Poor Particle Physicist Cookbook for Dark Matter Indirect Detection. *JCAP*, 1103:051, 2011. doi: 10.1088/1475-7516/2012/10/E01, 10.1088/1475-7516/2011/03/051. [Erratum: JCAP1210,E01(2012)].
- Marco Cirelli, Emmanuel Moulin, Paolo Panci, Pasquale D. Serpico, and Aion Viana. Gamma ray constraints on Decaying Dark Matter. *Phys. Rev.*, D86:083506, 2012. doi: 10.1103/PhysRevD.86.083506,10.1103/PhysRevD.86.109901.
- CMS.
- Timothy Cohen, Kohta Murase, Nicholas L. Rodd, Benjamin R. Safdi, and Yotam Soreq. γ -ray Constraints on Decaying Dark Matter and Implications for IceCube. *Phys. Rev. Lett.*, 119(2):021102, 2017. doi: 10.1103/PhysRevLett.119.021102.

- Sergio Colafrancesco, S. Profumo, and P. Ullio. Multi-frequency analysis of neutralino dark matter annihilations in the Coma cluster. *Astron. Astrophys.*, 455:21, 2006. doi: 10.1051/0004-6361:20053887.
- Shaun Cole et al. The 2dF Galaxy Redshift Survey: Power-spectrum analysis of the final dataset and cosmological implications. *Mon. Not. Roy. Astron. Soc.*, 362:505–534, 2005. doi: 10.1111/j.1365-2966.2005.09318.x.
- P. Colin. Probing the CR positron/electron ratio at few hundreds GeV through Moon shadow observation with the MAGIC telescopes. *Proc. of the 32nd ICRC, Beijing*, 6:194, 2011a. doi: 10.7529/ICRC2011/V06/1114.
- P. Colin. Probing the CR positron/electron ratio at few hundreds GeV through Moon shadow observation with the MAGIC telescopes. *Proc. of the 32nd ICRC, Beijing*, 6:194, 2011b. doi: 10.7529/ICRC2011/V06/1114.
- LST Collaboration. Large Size Telescope Technical Design Report. 2016.
- Charlie Conroy, Abraham Loeb, and David Spergel. Evidence Against Dark Matter Halos Surrounding the Globular Clusters MGC1 and NGC 2419. *Astrophys. J.*, 741:72, 2011. doi: 10.1088/0004-637X/741/2/72.
- Xin-Yu Dai, Christopher S. Kochanek, and Nicholas D. Morgan. The X-ray Properties of Optically-Selected Galaxy Clusters. *Astrophys. J.*, 658:917–928, 2007. doi: 10.1086/509651.
- DAMPE.
- A. Daum et al. First results on the performance of the HEGRA IACT array. *Astropart. Phys.*, 8:1–11, 1997. doi: 10.1016/S0927-6505(97)00031-5.
- Mathieu de Naurois and Daniel Mazin. Ground-based detectors in very-high-energy gamma-ray astronomy. *Comptes Rendus Physique*, 16:610–627, 2015. doi: 10.1016/j.crhy.2015.08.011.
- A. Dekel and J. Woo. Feedback and the fundamental line of low-luminosity low-surface-brightness/dwarf galaxies. *MNRAS*, 344:1131–1144, 2003. doi: 10.1046/j.1365-8711.2003.06923.x.
- C. Delgado. *C35 connectivity test*. LST Collaboration, CIEMAT, 2 2016. **LST INTERNAL DOCUMENT**.
- C. Delgado and S. Mangano. *C35 modules verification*. LST Collaboration, CIEMAT, 2 2016. **LST INTERNAL DOCUMENT**.

BIBLIOGRAPHY

- Mattia Di Mauro and Andrea Vittino. AMS-02 electrons and positrons: astrophysical interpretation and Dark Matter constraints. *PoS, ICRC2015:1177*, 2016.
- K. Dolag, A. M. Bykov, and A. Diaferio. Non-thermal processes in cosmological simulations. *Space Sci. Rev.*, 134:311, 2008. doi: 10.1007/s11214-008-9319-2.
- A. D. Dolgov and S. H. Hansen. Massive sterile neutrinos as warm dark matter. *Astropart. Phys.*, 16:339–344, 2002. doi: 10.1016/S0927-6505(01)00115-3.
- W. Domainko, D. Nedbal, J. A. Hinton, and O. Martineau-Huynh. New Results from H.E.S.S. Observations of Galaxy Clusters. *International Journal of Modern Physics D*, 18:1627–1631, 2009. doi: 10.1142/S021827180901545X.
- M. Doro et al. Dark Matter and Fundamental Physics with the Cherenkov Telescope Array. *Astropart. Phys.*, 43:189–214, 2013. doi: 10.1016/j.astropartphys.2012.08.002.
- A. G. Doroshkevich and P. D. Naselsky. Ionization history of the universe as a test for superheavy dark matter particles. *Phys. Rev. D*, 65:123517, Jun 2002. doi: 10.1103/PhysRevD.65.123517. URL <https://link.aps.org/doi/10.1103/PhysRevD.65.123517>.
- A. Drlica-Wagner et al. Eight Ultra-faint Galaxy Candidates Discovered in Year Two of the Dark Energy Survey. *Astrophys. J.*, 813(2):109, 2015. doi: 10.1088/0004-637X/813/2/109.
- A. R. Duffy, J. Schaye, S. T. Kay, C. Dalla Vecchia, R. A. Battye, and C. M. Booth. Impact of baryon physics on dark matter structures: a detailed simulation study of halo density profiles. *MNRAS*, 405:2161–2178, 2010. doi: 10.1111/j.1365-2966.2010.16613.x.
- Leanna Dugger, Tesla E. Jeltema, and Stefano Profumo. Constraints on Decaying Dark Matter from Fermi Observations of Nearby Galaxies and Clusters. *JCAP*, 1012:015, 2010. doi: 10.1088/1475-7516/2010/12/015.
- A. Einstein. Die Grundlage der allgemeinen Relativitätstheorie. *Annalen der Physik*, 354:769, 1916. doi: 10.1002/andp.19163540702.
- Daniel J. Eisenstein et al. Detection of the Baryon Acoustic Peak in the Large-Scale Correlation Function of SDSS Luminous Red Galaxies. *Astrophys. J.*, 633:560–574, 2005. doi: 10.1086/466512.

- John R. Ellis, J. S. Hagelin, Dimitri V. Nanopoulos, Keith A. Olive, and M. Srednicki. Supersymmetric Relics from the Big Bang. *Nucl. Phys.*, B238: 453–476, 1984. doi: 10.1016/0550-3213(84)90461-9.
- John R. Ellis, Jorge L. Lopez, and Dimitri V. Nanopoulos. Confinement of fractional charges yields integer charged relics in string models. *Phys. Lett.*, B247:257–264, 1990. doi: 10.1016/0370-2693(90)90893-B.
- John R. Ellis, S. Kelley, and Dimitri V. Nanopoulos. Constraints from gauge coupling unification on the scale of supersymmetry breaking. *Phys. Lett.*, B287:95–100, 1992. doi: 10.1016/0370-2693(92)91882-A.
- John R. Ellis, Toby Falk, Keith A. Olive, and Yudi Santoso. Exploration of the MSSM with nonuniversal Higgs masses. *Nucl. Phys.*, B652:259–347, 2003. doi: 10.1016/S0550-3213(02)01144-6.
- P. Fayet. Supersymmetry and weak, electromagnetic and strong interactions. *Physics Letters B*, 64(2):159 – 162, 1976. ISSN 0370-2693. doi: [https://doi.org/10.1016/0370-2693\(76\)90319-1](https://doi.org/10.1016/0370-2693(76)90319-1). URL <http://www.sciencedirect.com/science/article/pii/0370269376903191>.
- Pierre Fayet and S. Ferrara. Supersymmetry. *Phys. Rept.*, 32:249–334, 1977. doi: 10.1016/0370-1573(77)90066-7.
- Jonathan L. Feng. Dark Matter Candidates from Particle Physics and Methods of Detection. *Ann. Rev. Astron. Astrophys.*, 48:495–545, 2010. doi: 10.1146/annurev-astro-082708-101659.
- Jonathan L. Feng and Jason Kumar. The WIMPless Miracle: Dark-Matter Particles without Weak-Scale Masses or Weak Interactions. *Phys. Rev. Lett.*, 101:231301, 2008. doi: 10.1103/PhysRevLett.101.231301.
- Jonathan L. Feng, Arvind Rajaraman, and Fumihiro Takayama. Superweakly interacting massive particles. *Phys. Rev. Lett.*, 91:011302, Jul 2003a. doi: 10.1103/PhysRevLett.91.011302. URL <https://link.aps.org/doi/10.1103/PhysRevLett.91.011302>.
- Jonathan L. Feng, Arvind Rajaraman, and Fumihiro Takayama. SuperWIMP dark matter signals from the early universe. *Phys. Rev.*, D68:063504, 2003b. doi: 10.1103/PhysRevD.68.063504.
- Fermi LAT Collaboration. γ -RAY SPECTRAL EVOLUTION OF NGC 1275 OBSERVED WITH FERMI LARGE AREA TELESCOPE. *The Astrophysical Journal*, 715:1, 2010. doi: <https://doi.org/10.1088/0004-637X/715/1/554>.

BIBLIOGRAPHY

- A. Fernandez and S. Griffiths. *Power Supply Noise Tests*. LST Collaboration, IFAE, 2 2016. **LST INTERNAL DOCUMENT**.
- Alba Fernández-Barral. *Extreme particle acceleration in microquasar jets and pulsar wind nebulae with the MAGIC telescopes*. PhD thesis, IFAE and UAB Barcelona, 2017. URL https://www.dropbox.com/s/j1js8o2pooq1vcc/AlbaFdezBarral_PhDThesis.pdf?dl=0.
- D. J. Fixsen. The Temperature of the Cosmic Microwave Background. *ApJ*, 707:916–920, December 2009. doi: 10.1088/0004-637X/707/2/916.
- Andy Flinders. VERITAS Observations of the Geminga Supernova Remnant. *PoS*, ICRC2015:795, 2016.
- V. P. Fomin, A. A. Stepanian, R. C. Lamb, D. A. Lewis, M. Punch, and T. C. Weekes. New methods of atmospheric Cherenkov imaging for gamma-ray astronomy. 1: The False source method. *Astropart. Phys.*, 2:137–150, 1994. doi: 10.1016/0927-6505(94)90036-1.
- Urbano França, Roberto A. Lineros, Joaquim Palacio, and Sergio Pastor. Probing interactions within the dark matter sector via extra radiation contributions. *Phys. Rev.*, D87(12):123521, 2013. doi: 10.1103/PhysRevD.87.123521.
- Katherine Freese. Review of Observational Evidence for Dark Matter in the Universe and in upcoming searches for Dark Stars. *EAS Publ. Ser.*, 36: 113–126, 2009. doi: 10.1051/eas/0936016.
- Katherine Freese, Brian Fields, and David Graff. What are MACHOs? Limits on stellar objects as the dark matter of our halo. In *Proceedings, 2nd International Heidelberg Conference on Dark matter in astrophysics and particle physics (DARK 1998): Heidelberg, Germany, July 20-25, 1998*, pages 397–417, 1998.
- Christian Fruck, Markus Gaug, and Daniel Garrido Razmik Mirzoyan Lluís Font for the MAGIC Collaboration Roberta Zanin, Daniela Dorner. A novel LIDAR-based Atmospheric Calibration Method for Improving the Data Analysis of MAGIC. 2014a.
- Christian Fruck, Markus Gaug, Roberta Zanin, Daniela Dorner, Daniel Garrido, Razmik Mirzoyan, and Lluís Font. A novel LIDAR-based Atmospheric Calibration Method for Improving the Data Analysis of MAGIC. In *Proceedings, 33rd International Cosmic Ray Conference (ICRC2013): Rio de Janeiro, Brazil, July 2-9, 2013*, page 1054, 2014b. URL <http://inspirehep.net/record/1285998/files/arXiv:1403.3591.pdf>.

- Nicola Galante. Observation of Radio Galaxies and Clusters of Galaxies with VERITAS. 2009.
- Juan García-Bellido. Massive Primordial Black Holes as Dark Matter and their detection with Gravitational Waves. *J. Phys. Conf. Ser.*, 840(1):012032, 2017. doi: 10.1088/1742-6596/840/1/012032.
- Graciela Gelmini and Paolo Gondolo. DM Production Mechanisms. 2010.
- Anna Genina and Malcolm Fairbairn. The Potential of the Dwarf Galaxy Triangulum II for Dark Matter Indirect Detection. *Mon. Not. Roy. Astron. Soc.*, 463(4):3630–3636, 2016. doi: 10.1093/mnras/stw2284.
- Iskren Y. Georgiev, Thomas H. Puzia, Paul Goudfrooij, and Michael Hilker. Globular Cluster Systems in Nearby Dwarf Galaxies: III. Formation Efficiencies of Old Globular Clusters. *Mon. Not. Roy. Astron. Soc.*, 406:1967, 2010. doi: 10.1111/j.1365-2966.2010.16802.x.
- Alex Geringer-Sameth, Savvas M. Koushiappas, and Matthew Walker. Dwarf galaxy annihilation and decay emission profiles for dark matter experiments. *Astrophys. J.*, 801(2):74, 2015. doi: 10.1088/0004-637X/801/2/74.
- Gian F. Giudice, Markus A. Luty, Hitoshi Murayama, and Riccardo Rattazzi. Gaugino mass without singlets. *JHEP*, 12:027, 1998. doi: 10.1088/1126-6708/1998/12/027.
- Martin Goetz and Jesper Sommer-Larsen. Galaxy formation: warm dark matter, missing satellites, and the angular momentum problem. *Astrophys. Space Sci.*, 284:341–344, 2003. doi: 10.1023/A:1024073909753.
- S. Griffiths. *CIEMAT 35-module Test Power Procedure*. LST Collaboration, IFAE, 2 2016. **LST INTERNAL DOCUMENT**.
- Alan H. Guth, David I. Kaiser, and Yasunori Nomura. Inflationary paradigm after Planck 2013. *Phys. Lett.*, B733:112–119, 2014. doi: 10.1016/j.physletb.2014.03.020.
- W. E. Harris. Globular cluster systems in galaxies beyond the Local Group. *ARA&A*, 29:543–579, 1991. doi: 10.1146/annurev.aa.29.090191.002551.
- Tarek Hassan, Luisa Arrabito, Konrad Bernlör, Johan Bregeon, James Hinton, Tobias Jogler, Gernot Maier, Abelardo Moralejo, Federico Di Pierro, and Matthew Wood. Second large-scale Monte Carlo study for the Cherenkov Telescope Array. *PoS, ICRC2015:971*, 2016.

BIBLIOGRAPHY

- Kohei Hayashi, Koji Ichikawa, Shigeki Matsumoto, Masahiro Ibe, Miho N. Ishigaki, and Hajime Sugai. Dark matter annihilation and decay from non-spherical dark halos in galactic dwarf satellites. *Mon. Not. Roy. Astron. Soc.*, 461(3):2914–2928, 2016. doi: 10.1093/mnras/stw1457.
- Lars Hernquist. An Analytical Model for Spherical Galaxies and Bulges. *Astrophys. J.*, 356:359, 1990. doi: 10.1086/168845.
- M. Hirsch, R. A. Lineros, S. Morisi, J. Palacio, N. Rojas, and J. W. F. Valle. WIMP dark matter as radiative neutrino mass messenger. *JHEP*, 10:149, 2013. doi: 10.1007/JHEP10(2013)149.
- J. Holder et al. Status of the VERITAS Observatory. *AIP Conf. Proc.*, 1085: 657–660, 2009. doi: 10.1063/1.3076760.
- Dan Hooper, Pasquale Blasi, and Pasquale Dario Serpico. Pulsars as the Sources of High Energy Cosmic Ray Positrons. *JCAP*, 0901:025, 2009. doi: 10.1088/1475-7516/2009/01/025.
- Xiaoyuan Huang, Gilles Vertongen, and Christoph Weniger. Probing Dark Matter Decay and Annihilation with Fermi LAT Observations of Nearby Galaxy Clusters. *JCAP*, 1201:042, 2012. doi: 10.1088/1475-7516/2012/01/042.
- Edwin Hubble and Milton L. Humason. The Velocity-Distance Relation among Extra-Galactic Nebulae. *Astrophys. J.*, 74:43–80, 1931. doi: 10.1086/143323.
- P. Hut. Limits on masses and number of neutral weakly interacting particles. *Physics Letters B*, 69(1):85 – 88, 1977. ISSN 0370-2693. doi: [https://doi.org/10.1016/0370-2693\(77\)90139-3](https://doi.org/10.1016/0370-2693(77)90139-3). URL <http://www.sciencedirect.com/science/article/pii/0370269377901393>.
- M. Hütten, C. Combet, G. Maier, and D. Maurin. Dark matter substructure modelling and sensitivity of the Cherenkov Telescope Array to Galactic dark halos. *JCAP*, 1609(09):047, 2016. doi: 10.1088/1475-7516/2016/09/047.
- Alejandro Ibarra, David Tran, and Christoph Weniger. Decaying Dark Matter in Light of the PAMELA and Fermi LAT Data. *JCAP*, 1001:009, 2010. doi: 10.1088/1475-7516/2010/01/009.
- Rodrigo Ibata, Carlo Nipoti, Antonio Sollima, Michele Bellazzini, Scott Chapman, and Emanuele Dalessandro. Do globular clusters possess Dark Matter halos? A case study in NGC 2419. *Mon. Not. Roy. Astron. Soc.*, 428:3648, 2013. doi: 10.1093/mnras/sts302.

ICECUBE.

IceCube Collaboration, M. G. Aartsen, M. Ackermann, J. Adams, J. A. Aguilar, M. Ahlers, M. Ahrens, I. A. Samarai, D. Altmann, K. Andeen, and et al. Search for Neutrinos from Dark Matter Self-Annihilations in the center of the Milky Way with 3 years of IceCube/DeepCore. *ArXiv e-prints*, May 2017.

Koji Ishiwata. Axino Dark Matter in Moduli-induced Baryogenesis. *JHEP*, 09:122, 2014. doi: 10.1007/JHEP09(2014)122.

J. V. Jelley and N. A. Porter. Cerenkov Radiation from the Night Sky. *QJRAS*, 4:275, March 1963.

Tesla E. Jeltema, John Kehayias, and Stefano Profumo. Gamma Rays from Clusters and Groups of Galaxies: Cosmic Rays versus Dark Matter. *Phys. Rev.*, D80:023005, 2009. doi: 10.1103/PhysRevD.80.023005.

N. Kaiser, H. Aussel, B. E. Burke, H. Boesgaard, K. Chambers, M. R. Chun, J. N. Heasley, K.-W. Hodapp, B. Hunt, R. Jedicke, D. Jewitt, R. Kudritzki, G. A. Luppino, M. Maberry, E. Magnier, D. G. Monet, P. M. Onaka, A. J. Pickles, P. H. H. Rhoads, T. Simon, A. Szalay, I. Szapudi, D. J. Tholen, J. L. Tonry, M. Waterson, and J. Wick. Pan-STARRS: A Large Synoptic Survey Telescope Array. *SPIE*, 4836:154–164, 2002. doi: 10.1117/12.457365.

T. Kajita. Discovery of neutrino oscillations. *Rept. Prog. Phys.*, 69:1607–1635, 2006. doi: 10.1088/0034-4885/69/6/R01.

Theodor Kaluza. On the Problem of Unity in Physics. *Sitzungsber. Preuss. Akad. Wiss. Berlin (Math. Phys.)*, 1921:966–972, 1921.

D. Kang et al. A limit on the diffuse gamma-rays measured with KASCADE-Grande. *J. Phys. Conf. Ser.*, 632(1):012013, 2015. doi: 10.1088/1742-6596/632/1/012013.

Jiwei Ke, Mingxing Luo, Liucheng Wang, and Guohuai Zhu. Gamma-rays from Nearby Clusters: Constraints on Selected Decaying Dark Matter Models. *Phys. Lett.*, B698:44–51, 2011. doi: 10.1016/j.physletb.2011.02.055.

E. N. Kirby, J. G. Cohen, J. D. Simon, P. Guhathakurta, A. O. Thygesen, and G. E. Duggan. Triangulum II. Not Especially Dense After All. *ApJ*, 838:83, 2017. doi: 10.3847/1538-4357/aa6570.

BIBLIOGRAPHY

- Evan N. Kirby, Judith G. Cohen, Joshua D. Simon, and Puragra Guhathakurta. Triangulum II: Possibly a Very Dense Ultra-faint Dwarf Galaxy. *Astrophys. J.*, 814(1):L7, 2015. doi: 10.1088/2041-8205/814/1/L7.
- R. Kiuchi et al. CANGAROO-III search for TeV Gamma-rays from two clusters of galaxies. *Astrophys. J.*, 704:240–246, 2009. doi: 10.1088/0004-637X/704/1/240.
- Oskar Klein. Quantum Theory and Five-Dimensional Theory of Relativity. (In German and English). *Z. Phys.*, 37:895–906, 1926. doi: 10.1007/BF01397481. [Surveys High Energ. Phys.5,241(1986)].
- Anatoly Klypin, Gustavo Yepes, Stefan Gottlober, Francisco Prada, and Steffen Hess. MultiDark simulations: the story of dark matter halo concentrations and density profiles. *Mon. Not. Roy. Astron. Soc.*, 457(4):4340–4359, 2016. doi: 10.1093/mnras/stw248.
- M. Kowalski et al. Improved Cosmological Constraints from New, Old and Combined Supernova Datasets. *Astrophys. J.*, 686:749–778, 2008. doi: 10.1086/589937.
- H. Kraus and F. A. Danevich, editors. *Proceedings, 1st International Workshop 'Radiopure Scintillators for EURECA' (RPScint'2008)*, Kiev, 2009. INR, INR. URL <https://inspirehep.net/record/815016/files/arXiv:0903.1539.pdf>.
- Lawrence M. Krauss and Brian Chaboyer. Age Estimates of Globular Clusters in the Milky Way: Constraints on Cosmology. *Science*, 299:65–70, 2003. doi: 10.1126/science.1075631.
- Michael Kuhlen, Mark Vogelsberger, and Raul Angulo. Numerical Simulations of the Dark Universe: State of the Art and the Next Decade. *Phys. Dark Univ.*, 1:50–93, 2012. doi: 10.1016/j.dark.2012.10.002.
- D. Kushnir, B. Katz, and E. Waxman. Magnetic fields and cosmic rays in clusters of galaxies. *JCAP*, 9:024, 2009. doi: 10.1088/1475-7516/2009/09/024.
- Benjamin P. M. Laevens et al. A New Faint Milky Way Satellite Discovered in the Pan-STARRS1 3 pi Survey. *Astrophys. J.*, 802:L18, 2015. doi: 10.1088/2041-8205/802/2/L18.
- R. B. Larson. Effects of Supernovae on the Early Evolution of Galaxies. *Monthly Notices of the Royal Astronomical Society*, 169:229–245, 1974. doi: <https://doi.org/10.1093/mnras/169.2.229>.

- T. Lasserre. Not enough stellar mass machos in the galactic halo. *Astron. Astrophys.*, 355:L39–L42, 2000.
- Julien Lesgourgues and Sergio Pastor. Neutrino mass from Cosmology. *Adv. High Energy Phys.*, 2012:608515, 2012. doi: 10.1155/2012/608515.
- Andrei Linde. Inflationary Cosmology after Planck 2013. In *Proceedings, 100th Les Houches Summer School: Post-Planck Cosmology: Les Houches, France, July 8 - August 2, 2013*, pages 231–316, 2015. doi: 10.1093/acprof:oso/9780198728856.003.0006. URL <https://inspirehep.net/record/1280019/files/arXiv:1402.0526.pdf>.
- S. Lombardi. Advanced stereoscopic gamma-ray shower analysis with the MAGIC telescopes. *International Cosmic Ray Conference*, 3:266, 2011. doi: 10.7529/ICRC2011/V03/1150.
- C Longair. *High Energy Astrophysics. Vol. 1. Particles, Photons and their Detection.*, volume 1. Cambridge University Press, 1992.
- Rubén López-Coto. *Very-high-energy gamma-ray observations of pulsar wind nebulae and cataclysmic variable stars with MAGIC and development of trigger systems for IACTs*. PhD thesis, IFAE and UAB Barcelona, 2015. URL https://www.mpi-hd.mpg.de/personalhomes/rlopez/Theses/PhD_thesis.pdf.
- P. Majumdar, A. Moralejo, C. Bigongiari, O. Blanch, D. Sobczynska, and on behalf of the MAGIC collaboration. Monte Carlo simulation for the MAGIC telescope. In *Proceedings, 29th International Cosmic Ray Conference (ICRC 2005): Pune, India, 2005*, 2005. URL <https://cds.cern.ch/record/963471/files/15203-ger-majumdar-P-abs1-og27-oral.pdf>.
- N. F. Martin, R. A. Ibata, M. L. M. Collins, R. M. Rich, E. F. Bell, A. M. N. Ferguson, B. P. M. Laevens, H.-W. Rix, S. C. Chapman, and A. Koch. Triangulum II: A Very Metal-poor and Dynamically Hot Stellar System. *ApJ*, 818:40, 2016. doi: 10.3847/0004-637X/818/1/40.
- John C. Mather et al. Measurement of the Cosmic Microwave Background spectrum by the COBE FIRAS instrument. *Astrophys. J.*, 420:439–444, 1994. doi: 10.1086/173574.
- K. Matsushita, E. Sakuma, T. Sasaki, K. Sato, and A. Simionescu. Metal-mass-to-light ratios of the Perseus cluster out to the virial radius. *Astrophys. J.*, 764:147, 2013. doi: 10.1088/0004-637X/764/2/147.

BIBLIOGRAPHY

- S. S. McGaugh. The Baryonic Tully-Fisher Relation of Gas-rich Galaxies as a Test of Λ CDM and MOND. *AJ*, 143:40, February 2012. doi: 10.1088/0004-6256/143/2/40.
- M. Milgrom. A Modification of the Newtonian dynamics as a possible alternative to the hidden mass hypothesis. *Astrophys. J.*, 270:365–370, 1983. doi: 10.1086/161130.
- Abelardo Moralejo. *Búsqueda de fuentes cósmicas de radiación gamma de muy alta energía con el detector AIROBICC*. PhD thesis, 2002.
- I. V. Moskalenko and A. W. Strong. Production and propagation of cosmic ray positrons and electrons. *Astrophys. J.*, 493:694–707, 1998. doi: 10.1086/305152.
- Julio F. Navarro, Carlos S. Frenk, and Simon D. M. White. The Structure of cold dark matter halos. *Astrophys. J.*, 462:563–575, 1996. doi: 10.1086/177173.
- A. Neronov and I. Vovk. Evidence for strong extragalactic magnetic fields from Fermi observations of TeV blazars. *Science*, 328:73–75, 2010. doi: 10.1126/science.1184192.
- Hans Peter Nilles. Supersymmetry, Supergravity and Particle Physics. *Phys. Rept.*, 110:1–162, 1984. doi: 10.1016/0370-1573(84)90008-5.
- R. A. Ong et al. The GAPS Experiment to Search for Dark Matter using Low-energy Antimatter. 2017. URL <https://inspirehep.net/record/1628059/files/arXiv:1710.00452.pdf>.
- J. H. Oort. The force exerted by the stellar system in the direction perpendicular to the galactic plane and some related problems. *Bull. Astron. Inst. Netherlands*, 6:249, August 1932.
- E. Öpik. An estimate of the distance of the Andromeda Nebula. *ApJ*, 55, June 1922. doi: 10.1086/142680.
- E. W. Otten and C. Weinheimer. Neutrino mass limit from tritium beta decay. *Rept. Prog. Phys.*, 71:086201, 2008. doi: 10.1088/0034-4885/71/8/086201.
- J. Palacio, J. Cumani, and J. Delgado. ToMaRe: TOol for MAssive REprocessing. (*internal document*), 2015.

- J. Palacio, O. Blanch, S. Griffiths, and A. Fernandez. *35 Cluster Noise Test CIEMAT - Procedure Documentation*. LST Collaboration, 2 2016a. **LST INTERNAL DOCUMENT**.
- J. Palacio, O. Blanch, S. Griffiths, and A. Fernandez. *35 Cluster Noise Test CIEMAT - Results*. LST Collaboration, IFAE, 2 2017. **LST INTERNAL DOCUMENT**.
- Joaquim Palacio, M. Doro, M. Vazquez Acosta, P. Colin, C. Maggio, J. Rico, and F. Zandanel. Constraining the Dark Matter decay lifetime with very deep observations of the Perseus cluster with the MAGIC telescopes. *PoS, ICRC2015:1204*, 2016b.
- PAMELA.
- R.D. Peccei and Helen R. Quinn. $\{CP\}$ conservation in the presence of pseudoparticles*. In L. WOLFENSTEIN, editor, *$\{CP\}$ Violation*, pages 328 – 331. Elsevier, Amsterdam, 1989. ISBN 978-0-444-88114-4. doi: <https://doi.org/10.1016/B978-0-444-88081-9.50043-6>. URL <https://www.sciencedirect.com/science/article/pii/B9780444880819500436>.
- P. J. E. Peebles. *Principles of physical cosmology*. 1994.
- Eric W. Peng, Holland C. Ford, Kenneth C. Freeman, and Richard L. White. A Young blue tidal stream in NGC 5128. *Astron. J.*, 124:3144, 2002. doi: 10.1086/344308.
- Arno A. Penzias and Robert Woodrow Wilson. A Measurement of excess antenna temperature at 4080-Mc/s. *Astrophys. J.*, 142:419–421, 1965. doi: 10.1086/148307.
- Will J. Percival et al. The 2dF Galaxy Redshift Survey: The Power spectrum and the matter content of the Universe. *Mon. Not. Roy. Astron. Soc.*, 327: 1297, 2001. doi: 10.1046/j.1365-8711.2001.04827.x.
- Jeremey S. Perkins et al. TeV gamma-ray observations of the perseus and abell 2029 galaxy clusters. *Astrophys. J.*, 644:148–154, 2006. doi: 10.1086/503321.
- Anders Pinzke and Christoph Pfrommer. Simulating the gamma-ray emission from galaxy clusters: a universal cosmic ray spectrum and spatial distribution. *Mon. Not. Roy. Astron. Soc.*, 409:449, 2010. doi: 10.1111/j.1365-2966.2010.17328.x.

BIBLIOGRAPHY

- Anders Pinzke, Christoph Pfrommer, and Lars Bergstrom. Gamma-rays from dark matter annihilations strongly constrain the substructure in halos. *Phys. Rev. Lett.*, 103:181302, 2009. doi: 10.1103/PhysRevLett.103.181302.
- Anders Pinzke, Christoph Pfrommer, and Lars Bergstrom. Prospects of detecting gamma-ray emission from galaxy clusters: cosmic rays and dark matter annihilations. *Phys. Rev.*, D84:123509, 2011. doi: 10.1103/PhysRevD.84.123509.
- Lisa Randall and Raman Sundrum. Out of this world supersymmetry breaking. *Nucl. Phys.*, B557:79–118, 1999. doi: 10.1016/S0550-3213(99)00359-4.
- O. Reimer, M. Pohl, P. Sreekumar, and J. R. Mattox. Egret upper limits on the high-energy gamma-ray emission of galaxy clusters. *Astrophys. J.*, 588:155–164, 2003. doi: 10.1086/374046.
- Thomas H. Reiprich and Hans Boehringer. The mass function of an x-ray flux-limited sample of galaxy clusters. *Nucl. Phys. Proc. Suppl.*, 80:0917, 2000.
- Massimo Ricotti, Owen H. Parry, and Nickolay Y. Gnedin. A Common Origin for Globular Clusters and Ultra-faint Dwarfs in Simulations of the First Galaxies. *Astrophys. J.*, 831(2):204, 2016. doi: 10.3847/0004-637X/831/2/204.
- M. Ryle and M. D. Windram. The Radio Emission from Galaxies in the Perseus Cluster. *Monthly Notices of the Royal Astronomical Society*, 138:1–21, 1968. doi: 10.1093/mnras/138.1.1.
- P. Salati, F. Donato, and N. Fornengo. *Indirect dark matter detection with cosmic antimatter*, page 521. Cambridge University Press, 2010.
- Miguel A. Sanchez-Conde, Mirco Cannoni, Fabio Zandanel, Mario E. Gomez, and Francisco Prada. Dark matter searches with Cherenkov telescopes: nearby dwarf galaxies or local galaxy clusters? *JCAP*, 1112:011, 2011. doi: 10.1088/1475-7516/2011/12/011.
- C. L. Sarazin. X-ray emission from clusters of galaxies. *Reviews of Modern Physics*, 58:1–115, 1986.
- F. G. Saturni. .
- Martin Schmaltz and David Tucker-Smith. Little Higgs review. *Ann. Rev. Nucl. Part. Sci.*, 55:229–270, 2005. doi: 10.1146/annurev.nucl.55.090704.151502.

- J. D. Simon et al. Stellar Kinematics and Metallicities in the Ultra-Faint Dwarf Galaxy Reticulum II. *Astrophys. J.*, 808(1):95, 2015. doi: 10.1088/0004-637X/808/1/95.
- Joshua D. Simon and Marla Geha. The Kinematics of the Ultra-Faint Milky Way Satellites: Solving the Missing Satellite Problem. *Astrophys. J.*, 670: 313–331, 2007. doi: 10.1086/521816.
- Julian Sitarek, Markus Gaug, Daniel Mazin, Riccardo Paoletti, and Diego Tescaro. Analysis techniques and performance of the Domino Ring Sampler version 4 based readout for the MAGIC telescopes. *Nucl. Instrum. Meth.*, A723:109–120, 2013. doi: 10.1016/j.nima.2013.05.014.
- Torbjörn Sjöstrand, Stefan Ask, Jesper R. Christiansen, Richard Corke, Nishita Desai, Philip Ilten, Stephen Mrenna, Stefan Prestel, Christine O. Rasmussen, and Peter Z. Skands. An Introduction to PYTHIA 8.2. *Comput. Phys. Commun.*, 191:159–177, 2015. doi: 10.1016/j.cpc.2015.01.024.
- S. Smith. The Mass of the Virgo Cluster. *ApJ*, 83:23, January 1936. doi: 10.1086/143697.
- George F. Smoot et al. Structure in the COBE differential microwave radiometer first year maps. *Astrophys. J.*, 396:L1–L5, 1992. doi: 10.1086/186504.
- D. N. Spergel et al. First year Wilkinson Microwave Anisotropy Probe (WMAP) observations: Determination of cosmological parameters. *Astrophys. J. Suppl.*, 148:175–194, 2003. doi: 10.1086/377226.
- Gary Steigman, Basudeb Dasgupta, and John F. Beacom. Precise Relic WIMP Abundance and its Impact on Searches for Dark Matter Annihilation. *Phys. Rev.*, D86:023506, 2012. doi: 10.1103/PhysRevD.86.023506.
- Ming Sun, D. Jerius, and C. Jones. A Small x-ray corona of the narrow-angle tail radio galaxy NGC 1265 soaring through the Perseus cluster. *Astrophys. J.*, 633:165–173, 2005. doi: 10.1086/452620.
- R. A. Sunyaev and Ya. B. Zeldovich. Small scale fluctuations of relic radiation. *Astrophys. Space Sci.*, 7:3–19, 1970.
- R. A. Sunyaev and Ya. B. Zeldovich. The Observations of relic radiation as a test of the nature of X-Ray radiation from the clusters of galaxies. *Comments Astrophys. Space Phys.*, 4:173–178, 1972.

BIBLIOGRAPHY

- R. A. Sunyaev and Ya. B. Zeldovich. Microwave background radiation as a probe of the contemporary structure and history of the universe. *Ann. Rev. Astron. Astrophys.*, 18:537–560, 1980. doi: 10.1146/annurev.aa.18.090180.002541.
- Andi Tan et al. Dark Matter Results from First 98.7 Days of Data from the PandaX-II Experiment. *Phys. Rev. Lett.*, 117(12):121303, 2016. doi: 10.1103/PhysRevLett.117.121303.
- The Dark Energy Survey Collaboration. The Dark Energy Survey. *ArXiv Astrophysics e-prints*, October 2005.
- G. Mark Voit. Tracing cosmic evolution with clusters of galaxies. *Rev. Mod. Phys.*, 77:207–258, 2005. doi: 10.1103/RevModPhys.77.207.
- R Wagner. *Measurement of VHE γ -ray emission from four blazars using the MAGIC telescope and a comparative blazar study*. PhD thesis, 2006.
- Matthew G. Walker, Mario Mateo, Edward W. Olszewski, Rebecca A. Bernstein, Xiao Wang, and Michael Woodroffe. Internal kinematics of the fornax dwarf spheroidal galaxy. *Astron. J.*, 131:2114–2139, 2006. doi: 10.1086/500193,10.1086/505303. [Erratum: *Astron. J.*132,968(2006)].
- T. C. Weekes et al. Observation of TeV gamma rays from the Crab nebula using the atmospheric Cerenkov imaging technique. *Astrophys. J.*, 342:379–395, 1989. doi: 10.1086/167599.
- J. Wess and J. Bagger. *Supersymmetry and supergravity*. Princeton, NJ (United States); Princeton Univ. Press, Jan 1992.
- Beth Willman and Jay Strader. 'Galaxy,' Defined. *Astron. J.*, 144:76, 2012. doi: 10.1088/0004-6256/144/3/76.
- Edward Witten. Mass hierarchies in supersymmetric theories. *Physics Letters B*, 105(4):267 – 271, 1981. ISSN 0370-2693. doi: [https://doi.org/10.1016/0370-2693\(81\)90885-6](https://doi.org/10.1016/0370-2693(81)90885-6). URL <http://www.sciencedirect.com/science/article/pii/0370269381908856>.
- XENONT1T.
- W. M. Yao et al. Review of Particle Physics. *J. Phys.*, G33:1–1232, 2006. doi: 10.1088/0954-3899/33/1/001.
- Donald G. York et al. The Sloan Digital Sky Survey: Technical Summary. *Astron. J.*, 120:1579–1587, 2000. doi: 10.1086/301513.

- R. Zanin, J. Cortina, and for the MAGIC Collaboration. The Central Control of the MAGIC telescopes. 2009.
- Roberta Zanin. MARS, The MAGIC analysis and reconstruction software. In *Proceedings, 33rd International Cosmic Ray Conference (ICRC2013): Rio de Janeiro, Brazil, July 2-9, 2013*, page 0773, 2013. URL <http://www.cbpf.br/%7Eicrc2013/papers/icrc2013-0773.pdf>.
- HongSheng Zhao. Analytical models for galactic nuclei. *Mon. Not. Roy. Astron. Soc.*, 278:488–496, 1996. doi: 10.1093/mnras/278.2.488.
- Stephan Zimmer, Jan Conrad, and Anders Pinzke. A Combined Analysis of Clusters of Galaxies - Gamma Ray Emission from Cosmic Rays and Dark Matter. 2011.
- F. Zwicky. Die Rotverschiebung von extragalaktischen Nebeln. *Helv. Phys. Acta*, 6:110–127, 1933. doi: 10.1007/s10714-008-0707-4. [Gen. Rel. Grav.41,207(2009)].
- F. Zwicky. On the Masses of Nebulae and of Clusters of Nebulae. *Astrophys. J.*, 86:217–246, 1937. doi: 10.1086/143864.

BIBLIOGRAPHY

Units

Abbreviation	Name	Equivalence
m	meter	
s	second	
kg	kilogram	
eV	electronvolt	$1.60 \times 10^{-19} \text{ kg m}^2 \text{ s}^{-2}$
M_{\odot}	solar mass	$1.989 \times 10^{30} \text{ kg}$
Hz	Hertz	1 s^{-1}
pc	parsec	$3.086 \times 10^{16} \text{ m}$
d	day	$8.64 \times 10^4 \text{ s}$
yr	year	$3.154 \times 10^7 \text{ s}$

Prefixes

Abbreviation	Prefix	Equivalence
E	Exa	10^{18}
P	Peta	10^{15}
T	Tera	10^{12}
G	Giga	10^9
M	Mega	10^6
k	kilo	10^3
-		10^0
c	centi	10^{-2}
m	mili	10^{-3}
μ	micro	10^{-6}
n	nano	10^{-9}
p	pico	10^{-12}

Prefixes

Abbreviation	Prefix	Equivalence
UHE	Ultra High Energy	$> \sim 10 \text{ TeV}$
VHE	Very High Energy	$> \sim 1 \text{ GeV}$
HE	High Energy	$> \sim 1 \text{ MeV}$